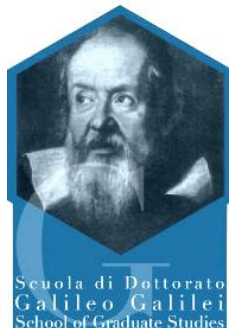




UNIVERSITÀ DI PISA



GRADUATE COURSE IN PHYSICS UNIVERSITY OF PISA

The School of Graduate Studies in Basic Sciences
"GALILEO GALILEI"

Ph. D. T H E S I S

Measurement of the inclusive jet cross section with the ATLAS detector at the LHC

Candidate:
Paolo FRANCAVILLA

Advisor:
Chiara Maria Angel RODA

Jury :

<i>Reviewers :</i>	Franco BEDESCHI	- INFN - Pisa
	Jonathan BUTTERWORTH	- University College London
	Gavin SALAM	- CERN; Princeton University; LPTHE, UPMC Univ. Paris 6 and CNRS
<i>Advisor :</i>	Chiara Maria Angel RODA	- University of Pisa and INFN - Pisa
<i>President :</i>	Kenichi KONISHI	- University of Pisa
<i>Examinators :</i>	Elisabetta BARBERIO	- University of Melbourne
	Franco BEDESCHI	- INFN - Pisa
	Mauro DELL'ORSO	- University of Pisa
	Peter LOCH	- University of Arizona

Contents

1 The ATLAS experiment at the Large Hadron Collider	5
1.1 The Large Hadron Collider at CERN	5
1.1.1 A brief history	5
1.1.2 The accelerator chain	6
1.1.3 Delivered luminosity	7
1.2 The ATLAS detector	11
1.2.1 Inner Detector	12
1.2.2 Calorimetric system	15
1.2.3 The muon spectrometer	20
1.2.4 Trigger and Data acquisition	21
1.2.5 Monte Carlo simulation of the ATLAS detector	24
1.2.6 The data samples collected in 2010	24
2 Jet production at hadron colliders:	
Theoretical predictions	27
2.1 Fundamental interactions: the Standard Model	27
2.2 The Strong interactions: the Quantum Chromo-Dynamics (QCD)	30
2.2.1 Structure of pQCD predictions	30
2.2.2 From the soft divergences to the jet algorithms	33
2.2.3 Beyond the fixed order predictions: the parton shower and non perturbative effects	38
2.2.4 Different strategies to get a predictions	41
2.3 Inclusive jet cross section: Theoretical prediction	43
2.3.1 Fixed order pQCD	44
2.3.2 Total theoretical uncertainties for the fixed order predictions	50
2.3.3 NLO Matrix Element + Parton Shower	51
3 Measuring jets:	
Reconstruction and Calibration	53
3.1 Jet reconstruction	53
3.1.1 Jet inputs	54
3.1.2 Jet calibration procedure: EM+JES	54
3.2 Jet algorithms: back to definitions	60
3.2.1 Reconstruction efficiency and purity	60
3.2.2 Picking up all the high energy objects: the dark clusters	63
4 Measuring jets:	
Performances	69
4.1 Jet cleaning	70
4.2 Jet reconstruction efficiency and purity	72

4.3	Jet energy calibration	75
4.3.1	Jet energy scale: from the calorimetric response to an isolated hadron to the final estimate of the uncertainty	75
4.3.2	Jet energy resolution	99
5	The inclusive jet cross section:	
	Measurement with 37 pb^{-1}	103
5.1	Trigger and luminosity	104
5.1.1	Trigger strategy	104
5.1.2	Luminosity	108
5.2	Event and jet selection	110
5.2.1	Jet selection	111
5.2.2	Data stability	111
5.3	Correcting the detector effects: unfolding	111
5.3.1	Monte Carlo samples for the unfolding	112
5.3.2	Detector level shape: improving the Monte Carlo descriptions	113
5.3.3	Unfolding strategy	115
5.3.4	Computing the statistical uncertainty with the IDS unfolding	116
5.3.5	Systematic uncertainty on the unfolding procedure	117
5.3.6	Comparison between IDS and bin-by-bin unfolding	118
5.4	Systematic uncertainties	120
5.4.1	Uncertainty on the jet energy scale	120
5.4.2	Uncertainty on the jet energy resolution	123
5.4.3	Total systematic uncertainty	124
5.4.4	Correlations	125
5.5	Results	129
6	Conclusions	145
A	Comparison of the 2010 Summer result and the complete 2010 data analysis	147
B	Additional material to Chapter 2	151
C	Additional material to Chapter 4	159
C.1	Jet cleaning	159
D	Additional material to Chapter 5	169
	Bibliography	197

Introduction

The measurement of the inclusive jet cross section is one of the test of perturbative quantum chromo-dynamics par excellence. The jets, sprays of particles, are copiously produced in the high-energy proton-proton collisions, such at the one at the Large Hadron Collider. They are the footprints of the interactions of quarks and gluons, under the influence of the strong force. The measurement of the inclusive jet cross section depends on the value of the strong force coupling constant, on the structure of the proton, and on the dynamics of the strong force in a large variety of regimes.

The major distinctive features of the inclusive jet cross section reported in this thesis with respect to previous measurements carried out at other high energy colliders are:

- the measurement can profit of the unprecedented collision intensity and center-of-mass energy of $\sqrt{s} = 7$ TeV provided by the Large Hadron Collider, overcoming the highest transverse jet momentum measured in previous experiments by a factor larger than two;
- the wide solid angle coverage of the ATLAS experiment allows the measurement of the cross section in uncharted angular regions;
- the quality of the ATLAS measurement of jets at low energies allows the extension of the cross section measurement to really low energy;
- the jet cross section profits of the new anti- k_t jet definition developed in the last couple of years. The choice of this jet algorithm overcomes the problems in the data-prediction comparison caused by previously used jet algorithms.

All these features make the presented jet cross section, one of the more extensive and detailed measurement of the jet physics at hadron colliders. The ATLAS Collaboration prepared a first public result on the inclusive jet cross section, reported in Reference [[ATLAS Collaboration 2011k](#)]. These preliminary results have been used as a starting point for the analysis discussed in this thesis, that has largely improved the previous result.

The inclusive jet cross section presented in this thesis is the double-differential cross section, measured in bin of transverse momentum p_T and rapidity $|y|$. The jet transverse momentum p_T is the component of the jet momentum perpendicular to the direction of the colliding particles. The jet rapidity is defined as:

$$y = \frac{1}{2} \ln\left(\frac{E + p_z}{E - p_z}\right) \quad (1)$$

where E is the jet energy and p_z is the jet momentum along the direction of the colliding particles. The double-differential inclusive jet cross section is given by:

$$\frac{d^2\sigma}{dp_T dy} = \frac{N}{\Delta p_T \Delta y L} \quad (2)$$

as a function of p_T and y . Here N is the number of jets measured in a bin in p_T (with a bin width Δp_T), and y (with a bin width Δy), and L is the total integrated luminosity. The inclusive jet cross section is measured for $20 \text{ GeV} < p_T < 1500 \text{ GeV}$, and for $-4.4 < y < 4.4$, which is the wider range reached so far at hadron collider. The data sample used in this analysis amounts to an integrated luminosity L of almost 37 pb^{-1} . This is the total statistics collected in 2010.

The easy definition of the cross section hides the several studies performed in the last years to define a jet, to check the precision of the jet calibration, to correct for the detector effects and finally to take into account in the most complete way all the different sources of systematic uncertainties. These aspects will be discussed along the thesis. It must be clear from the beginning of this report that the list of studies needed to get the final measurement of the inclusive jet cross section, with the detailed and mature results presented in this thesis, represents a challenge not only for a single person, but for a group of people.

The author of this thesis had the possibility to participate to most of the discussions, having a leading role in the measurement of this cross section. The next lines will introduce the structure of the thesis, and the personal contribution to the different parts.

Structure of the thesis and personal contribution

The thesis is divided in 5 Chapters. Chapter 1 is a short introduction to the Large Hadron Collider, and to the ATLAS experiment. The author participated to some special operation of the detector as shifter of the hadronic calorimeter TileCal. In particular, he was on shift for the first beams circulating in the Large Hadron Collider in 2008 and for the first collisions at $\sqrt{s} = 900 \text{ GeV}$ in 2009. Since May 2011 he is participating to the TileCal operations as run coordinator.

Chapter 2 is divided into two parts. The first one (Sections 2.1 and 2.2) is an introduction to the Standard Model of particle physics and to the quantum chromo-dynamics, heavily inspired to the clear, complete and concise description in Reference [Dissertori 2010]. The second one (Section 2.3) is the theoretical estimate of the inclusive jet cross section. In this section, the author contributed as a responsible for defining the guidelines for the ATLAS Collaboration to estimate the jet cross sections (not only the inclusive jet cross section). In the ATLAS Collaboration, he did the first tests of the NLO predictions with the anti- k_t jet algorithm and the first tests of the Powheg formalism for the jet production. The major contributions for the inclusive jet cross section have been the cross checks of the theoretical predictions (the fixed order NLO prediction, the non-perturbative correction and the Powheg results). In particular, the author developed part of the code used to derive the non-perturbative corrections.

Chapter 3 is an introduction to the jet reconstruction in ATLAS. This is divided into two parts. The first part (Section 3.1) defines the strategy adopted to reconstruct jets in ATLAS for the 2010 data. On this part, the author gave a contribution to the design of the JetPerformance package (see Reference [Doglioni 2011b]) in the ATLAS software, used to derive the performances of the jet reconstruction in ATLAS. The second part (Section

3.2) describes some experimental aspects in the jet definition, which drove the ATLAS Collaboration to select the anti- k_t jet algorithm as the default jet algorithm for the first period of data taking. The studies on this topic, done by the ATLAS Collaboration in 2009, cover several aspects. In the section reported in this thesis, only some of the relevant tests, done by the author, are reported.

Chapter 4 describes the performances and the uncertainties in the jet reconstruction. The Chapter is mostly devoted to the uncertainty on the jet energy scale. In particular, the author gave a contribution in checking the background contribution on the measurement of the calorimeter response to single particles. Another important contribution consists in the development of the selection criteria of events to be used for the multi-jet balance technique. This technique has been used to have an alternative cross check of the precision on the calibration of very high-energy jets.

Chapter 5 gives a detailed description of the measurement of the inclusive jet cross section. These results would have not been possible without the contributions of almost thirty people participating at the INCLUSIVE JET AND DIJET CROSS SECTION WORKING GROUP in the ATLAS Collaboration.

The author played a relevant and leading role in this group. He gave a fundamental contribution in defining the binning of the measurement in p_T , especially in the high- p_T region, by checking the impact of the jet energy resolution. He had a leading role in organizing the cut flow and the stability cross checks of the measurement. He provided the detector level spectra in the central region in rapidity used for the unfolded final results. He gave an important contribution on the techniques to propagate the systematics errors on the jet energy scale to the final cross section, cross checking the final bands, and combining the different contribution on the final measurement. He combined the contributions from INCLUSIVE JET AND DIJET CROSS SECTION WORKING GROUP on the measurement of the inclusive jet cross section for the ATLAS Collaboration. He was one of the fundamental authors of the measurement reported in Reference [ATLAS Collaboration 2011k]. He has been author and editor both of the public note of the measurement reported in Reference [ATLAS Collaboration 2011j] and of the paper (in preparation) containing the results of this thesis.

CHAPTER 1

The ATLAS experiment at the Large Hadron Collider

Contents

1.1	The Large Hadron Collider at CERN	5
1.1.1	A brief history	5
1.1.2	The accelerator chain	6
1.1.3	Delivered luminosity	7
1.2	The ATLAS detector	11
1.2.1	Inner Detector	12
1.2.2	Calorimetric system	15
1.2.3	The muon spectrometer	20
1.2.4	Trigger and Data acquisition	21
1.2.5	Monte Carlo simulation of the ATLAS detector	24
1.2.6	The data samples collected in 2010	24

This chapter takes a closer look at the Large Hadron Collider located at CERN, the European Organization for Nuclear Research, and at one of the detectors placed along its ring: ATLAS, A Toroidal Lhc ApparatuS (described in detail in Reference [[ATLAS Collaboration 2008a](#)]).

1.1 The Large Hadron Collider at CERN

The Large Hadron Collider (LHC) is a circular accelerator located at CERN and designed to collide beams consisting of protons or heavy-ions. It is currently the highest energy collider in the world since it collided proton-beams at a center of mass energy of $\sqrt{s} = 7$ TeV. This section describes the LHC in some more details, and the operation conditions in 2010. A detailed description of the LHC can be found in References [[Bruning 2004a](#), [Bruning 2004b](#), [Benedikt 2004](#)].

1.1.1 A brief history

The LHC circulated its first beams on 10 September 2008, working as a particle storage ring. After nine days, a failure in an electrical connection led to serious damage, stopping the operations until 2009. CERN has spent over a year repairing and consolidating the

machine to ensure that such an incident cannot happen again. The recommissioning of the LHC began in the summer 2009, and successive milestones have regularly been passed since then. The beams have been re-established in LHC in November 2009, after more than one year of stop.

In 2009 LHC produced for the first time collisions at the center of mass energy of $\sqrt{s} = 900 \text{ GeV}$. The data recorded in the period of the accelerator commissioning was important to test the performances of the detector, in preparation of the higher energy collisions.

In March 2010, LHC accelerated and collided protons at $\sqrt{s} = 3.5 \text{ TeV}$, reaching the highest beam and collisions energy in the world. The LHC is designed to accelerate and collide particles grouped in trains of bunches. In the first days, only two bunches of protons were injected in the machine, colliding on the four interaction points. The experience gained with the operation and analysis of the first data recorded in 2010 has been mainly directed to the commissioning of the trigger and data acquisition systems and to the understanding of the detector and accelerator performances allowing to set a solid ground for the physics analysis.

The evolution of the accelerator performances rapidly evolved since March 2010, allowing the collaboration to record an integrated luminosity of about 20 nb^{-1} in the summer 2010, almost 40 pb^{-1} at the end of 2010, and 5 fb^{-1} at the end of 2011.

This rapid evolution in the integrated luminosity is due to the increasing number of protons per bunch, to the squeezing of the beams in the interaction points, to the increasing number of bunches per beam and to the reduced inter-bunch latency time. All these improvements, aimed at reaching as soon as possible the design operation conditions, pushed the experimental collaborations to face always new conditions, affecting the detector operations, and to some extent the quality of the data.

1.1.2 The accelerator chain

The accelerator complex at CERN is an ensemble of machines capable of accelerate particles at increasingly higher energies. Each machine injects the beam into the next one, which takes over to bring the beam to a higher energy, and so on. The accelerator complex is schematically shown in Figure 1.1

The very first step in the chain is the proton source. The protons, extracted from Hydrogen gas, are fed into a linear accelerator (LINAC2). The LINAC2 accelerates the protons to an energy of 50 MeV. At the end of the LINAC2, the protons are injected in the Proton Synchrotron Booster (PSB), a circular accelerator in which the protons reach an energy of 1.4 GeV. At this energy, the protons are ready to be injected in a second circular accelerator, the Proton Synchrotron (PS), in which they are accelerated up to 25 GeV. After the PS, the protons are injected in a third circular accelerator, the Super Proton Synchrotron (SPS), in which their energy arises to 450 GeV, which is the injection energy for the Large Hadron Collider.

The LHC is the last and more powerful step of acceleration, which boosts the proton to 3.5 TeV. It is located in a circular tunnel 27 km in circumference. The tunnel is buried about 50 to 175 meters underground. It straddles the Swiss and French borders on the outskirts of Geneva.

The beams move around the LHC ring inside a continuous vacuum guided by magnets. The magnets are superconducting and are cooled by a cryogenics system, which makes the LHC, not only the highest-energy collider in the world, but also the largest cryogenic system.

The accelerator is made of eight arcs and eight "insertions". Each arc contains 154 dipole magnets. An insertion consists of a long straight section plus two (one at each end) transition regions. The exact layout of the straight section depends on the specific use of the insertion: physics (beam collisions within an experiment), injection, beam dumping, beam cleaning. The important parameters that characterize the LHC with the designed values and the values reached at the end of 2010 are listed in Table 1.1.

Once the proton bunches are injected and accelerated, the beams are stored at high energy for hours. During this time collisions take place in the interaction points inside the four main LHC experiments.

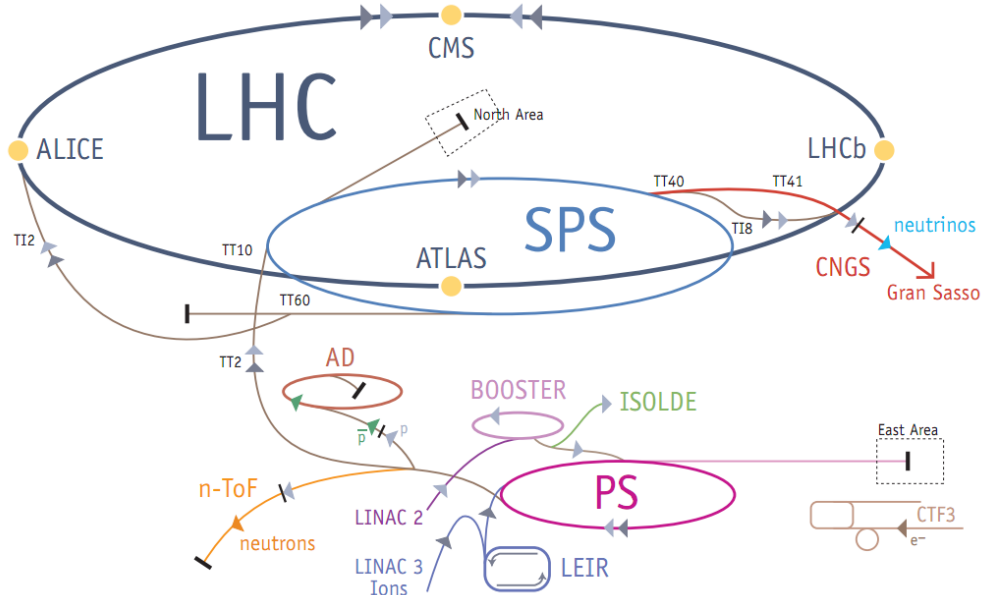


Figure 1.1: The accelerator complex at CERN.

1.1.3 Delivered luminosity

An important figure of merit for the accelerator performance is the luminosity. The rate of collisions is directly proportional to the luminosity. The rate R for a certain process with cross section σ is in fact proportional to the number of particles in each bunch (N_1 and N_2), the circulation frequency (f), the number of bunches (n) and to the inverse of the beam cross-section (A):

$$R = f \times n \frac{N_1 \times N_2}{A} \times \sigma = \mathcal{L} \times \sigma \quad (1.1)$$

where \mathcal{L} is the instantaneous luminosity.

Table 1.1: Important parameters for the LHC. The detailed description of the LHC operations in 2010 can be found in References [Ferro-Luzzi 2011, Meddahi 2011].

General aspects	Designed	End 2010
Circumference	26659 m	
Number of arcs (2450 m long)	8	
Momentum at collision	7 TeV/c	3.5 TeV/c
Momentum at injection	450 GeV/c	
Bunch spacing	25 ns	150 ns
Peak Luminosity	$10^{34} \text{ cm}^{-2}\text{s}^{-1}$	$2 \cdot 10^{32} \text{ cm}^{-2}\text{s}^{-1}$
No. of bunches per proton beam	2808	368
No. of protons per bunch (at start)	$1.15 \cdot 10^{11}$	
Stored beam energy	360 MJ	28 MJ
Stored energy in magnets	11 GJ	
Beam lifetime	10 h (average)	30 h (longest)
Emittance ϵ_n	$3.75 \mu\text{rad}$	2.5-3.5 μrad
Beta function β^*	0.55 m	3.50 m
<hr/>		
Magnets		
Number of magnets		
(dipoles, quadrupoles ... dodecapoles)	9300	
Number of dipoles	1232	
Number of quadrupoles	858	
Dipole operating temperature	1.9 K	
Peak magnetic dipole field	8.33 T	
Current in main dipole	11800 A	
<hr/>		
Superconducting alloy		
Composition of the superconducting alloy	Ni_Ti	
Maximum current with NO resistance (1.9 K - 8.33 T)	17000 A	
Maximum current with NO resistance (1.9 K - 0 T)	50000 A	
<hr/>		
RF System		
Main RF System	400.8 MHz	
Voltage of 400 MHz RF system at 7 TeV	16 MV	
Number of RF cavities	8 per beam	

During the course of a fill (the period the beams are kept colliding) the instantaneous luminosity drops as the beams loose intensity. For this reason, the peak instantaneous luminosity is reached at the beginning of a fill.

By integrating the rate for a process in a certain period of time, one gets the estimate of the total number of events (N_{tot}) recorded in that period:

$$N_{tot} = \int dt \mathcal{L} \times \sigma \quad (1.2)$$

The quantity $L = \int dt \mathcal{L}$ is the integrated luminosity. Figure 1.2 shows how the instantaneous and integrated luminosity have increased in the period March-November 2010. The delivered luminosity in 2010 is of about 40 pb^{-1} , and at the end of 2011, the luminosity integrated from 2010 is of about 5 fb^{-1} .

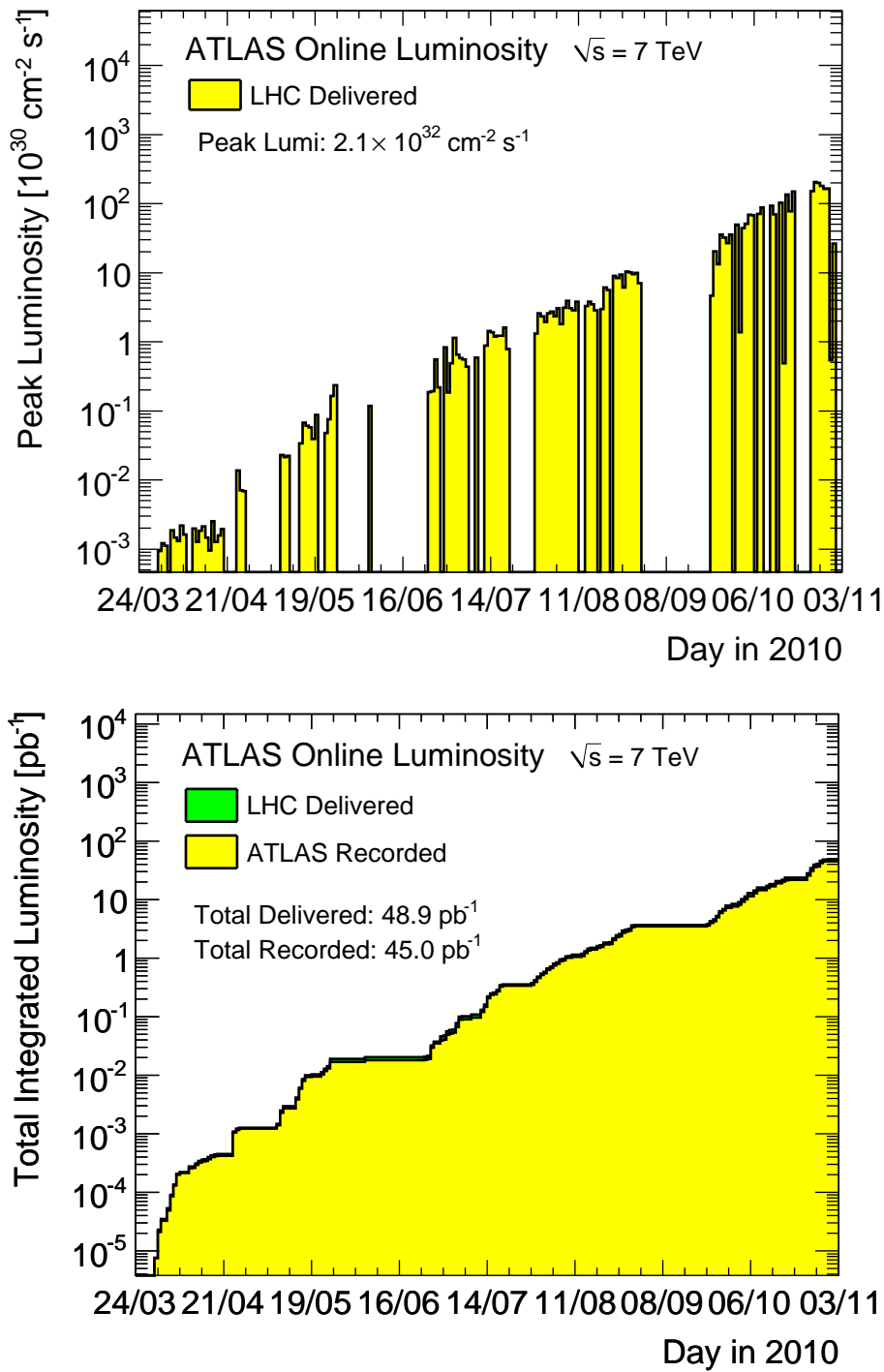


Figure 1.2: (Top) Development of the LHC peak luminosity in 2010. (Bottom) Integrated luminosity in 2010 delivered to (green) and recorded by ATLAS (yellow) during stable beams and for pp collisions at 7 TeV centre-of-mass energy.

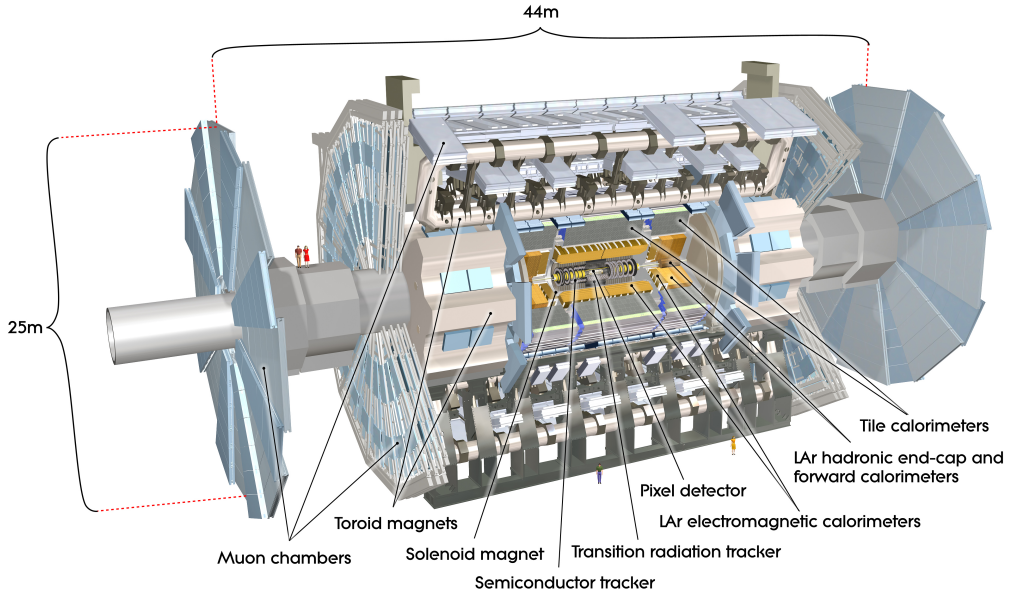


Figure 1.3: Scheme of the ATLAS detector.

1.2 The ATLAS detector

The ATLAS Collaboration is an international collaboration, spanning the whole globe. It was born in 1992 by merging two proto-collaborations, and the detector concept was basically settled by the time of the preparation of the ATLAS Technical Proposal in 1994. The ATLAS detector was designed to cover the widest possible range of physics studies, from the search for the Higgs boson to supersymmetry (SUSY) and extra dimensions. The detector is designed for the study of high energy proton-proton and ion-ion high energy collisions. Of particular interest for the physics at LHC are the collisions that produce energetic particles emerging roughly perpendicular to the axis of colliding beams, the so called high transverse momentum (p_T) phenomena.

To cover a wide range of physics, the ATLAS detector was designed with a cylindrical layout, and with a forward-backward symmetry with respect to the interaction point. A precision tracking system (Inner Detector) surrounds the interaction region, operating in a solenoidal magnetic field. The inner detector is surrounded by a system of calorimeters, followed by a muon tracking system with a dedicated toroidal magnetic field. The fundamental choice of two separate magnetic systems, one for the internal tracking, and one for the outer muon tracker, has driven the design of the rest of the detector. The present layout has been designed to fulfill the following requirements:

- very good electromagnetic calorimetry for electron and photon identification and measurement, complemented by full-coverage hadronic calorimetry for accurate jet and missing transverse energy (E_{Tmiss}) measurement;
- high precision muon momentum measurement with the capability to guarantee ac-

curacy at the highest luminosity using the external muon spectrometer alone;

- efficient tracking at high luminosity for high- p_T lepton momentum measurement, electron and photon identification, tau lepton and heavy flavor identification, and full-event reconstruction capability at lower luminosity;
- triggering and measurement of particles at low- p_T threshold, providing high efficiency for most physics processes of interest at the LHC;
- fast and radiation hard detectors due to the experimental conditions at the LHC, and high detector granularity to handle the particle fluxes and to reduce the influence of overlapping events.

The next sections describe the subsystems of the ATLAS detector, with more emphasis on the most relevant systems used to measure the inclusive jet cross section. A general and detailed description of the ATLAS detector, and of its performances is provided in References [ATLAS Collaboration 2008a, ATLAS Collaboration 2009b]. As an introduction to the geometrical coordinates used in this Chapter, the ATLAS reference system is described in the following lines.

Coordinate system in ATLAS

ATLAS uses a right-handed coordinate system with its origin at the nominal interaction point in the center of the detector. The z -axis is defined along the beam pipe direction, which defines the longitudinal direction, and the transverse (x, y)-plane as the plane perpendicular to the beam direction. The x -axis points from the interaction point to the center of the LHC ring, and the y -axis points upward. For the transverse plane, the cylindrical coordinates (r, ϕ) are used. The azimuthal angle ϕ is the azimuthal angle around the beam pipe, referred to the x -axis. The angle with respect to the beam pipe, θ is used to define the pseudo-rapidity $\eta = -\log \tan \theta/2$. Zero pseudo-rapidity corresponds to the plane perpendicular to the beam-line through the interaction point. Closer to the beam axis, the pseudo-rapidity grows towards positive (negative) infinity. The pseudo-rapidity is a geometrical quantity which corresponds, in the limit of 0 mass particles, to the rapidity, defined as $y = 1/2 \log (E + p_z)/(E - p_z)$. The rapidity y (and as a consequence the pseudo-rapidity η) is an important variable in hadronic colliders. The center of mass frame of the hard scattering can have a longitudinal boost with respect to the laboratory. The difference of two rapidities (Δy) is invariant under longitudinal boost, making the rapidity an important variable in hadron colliders, and making the pseudo-rapidity more suitable than θ to describe the angles along the beam direction.

1.2.1 Inner Detector

The central tracking system in ATLAS, discussed in detail in References [ATLAS Collaboration 1997a, ATLAS Collaboration 1997b, ATLAS Collaboration 2010m], is designed to measure the track and the momentum of the charged particles produced in the collisions. To achieve the momentum and vertex

resolution, in the very large track density, high precision measurement must be made with fine detector granularity. The detector has been designed to be able to make high quality measurement assuming approximately 1000 particles emerging from the collision every 25 ns within $|\eta| < 2.5$ for the designed energy and luminosity. By measuring the positions of the hits of the charged particles with different radial layers of detectors, it is possible to reconstruct the direction of the outgoing particle, and through the curvature due to the magnetic field, the momentum of the track. The central tracking detector in ATLAS consists of three different technologies: the internal pixel detector, the silicon micro-strip semiconductor tracker (SCT) and the transition radiation tracker (TRT) surrounded by a super conducting solenoid providing a 2 T magnetic field. The inner detector has a cylindrical geometry, with a radius $R=1.15$ m and a longitudinal length of 6.20 m.

The strategy is to combine few high precision measurements close to the interaction point with a large number of lower precision measurements in the outer layer.

- Pixels: the pixel system consists of three concentric layers of semi-conductive pixels in the central region, and eight wheels in the region $|\eta| > 1.7$. A track typically hits three layers of Pixel, which measure both the $r - \phi$ and the z coordinates.
- SCT: the SCT consists of four layers of semi-conductive strips in the central region. In the end-cap they are arranged in wheels. A track typically hits four layers of SCT, which precisely measure the $r - \phi$ coordinate, and coarsely the z coordinate.
- TRT: the TRT provides a large number of hits (36). It consist of straw tubes parallel arranged to the beam axis in the barrel region, and in wheels in the end-cap. It only provides information in the azimuthal direction. The reduced resolution with respect to the inner detectors is compensated by the higher radius, and by the number of measured points.

The combination of precision trackers at small radii, with the TRT at larger radii, gives a very robust and precise measurement of tracks in all the detection directions. The internal semiconductor trackers also measure the part of the tracks closest to the interaction point, allowing the reconstruction of the possible primary and secondary vertexes, as introduced in the following lines.

Figure 1.4 shows two schematic views of the inner detector, with the geometrical position of the different technologies.

Vertexes

The analysis of the inclusive jet cross section uses the knowledge of the position of the primary interaction point, (primary vertex) of the proton-proton collision. The reconstruction of the interaction vertex is based on the reconstruction of charged particle tracks in the ATLAS inner detector. It is divided in two steps: (a) the primary vertex finding algorithm, dedicated to associate reconstructed tracks to the vertex candidate, (b) the vertex fitting algorithm, dedicated to reconstruct the vertex position and its corresponding error matrix. The measurement of the position of the primary vertex has a resolution of about 0.05-1 mm depending on the number of associated tracks and of the p_T of the tracks. The

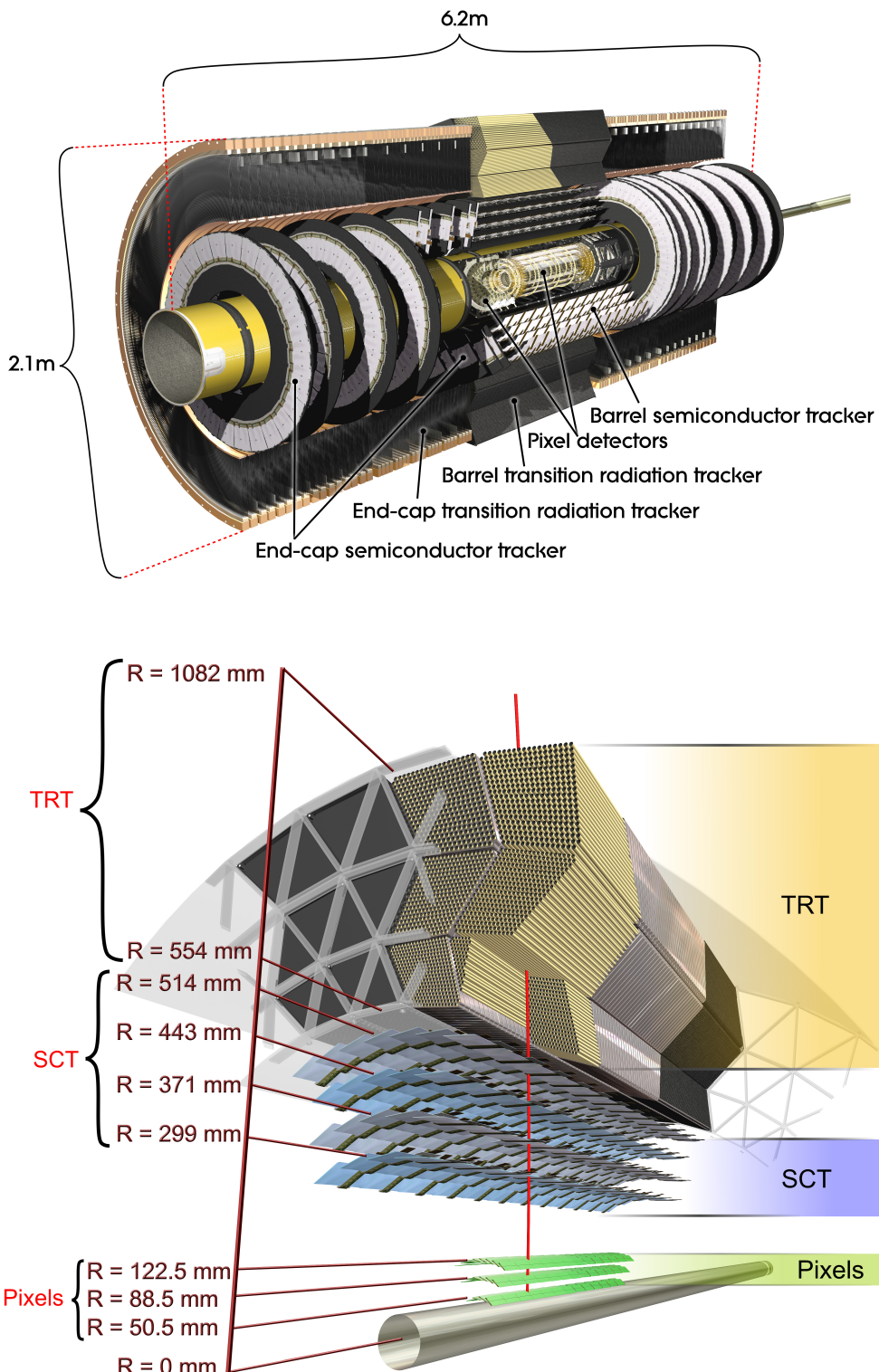


Figure 1.4: Overall view of the inner detector.

position of the vertex depends of the accelerator conditions. It can cause a shift of 0.5 mm in the transverse plane, and fluctuations of about 30-50 mm in the longitudinal direction. For this reason, during physics runs the luminous region (named beam spot) is determined by using the distribution of the recorded primary vertexes typically every 10 minutes. A detail description of the vertex reconstruction performances can be found in References [[ATLAS Collaboration 2010b](#), [ATLAS Collaboration 2010i](#)].

The analysis of the inclusive jet cross section used the information of the primary vertex for two porposes: (a) to reject the non-collision background contribution, such as those due to the cosmic rays, by selecting events with at least one primary vertex; (b) to monitor the number of primary vertexes in the events, to properly correct for the particles produced by the additional proton-proton interactions per bunch crossing.

1.2.2 Calorimetric system

The calorimetric system selected for the ATLAS experiment consists of different technologies, adopted to obtain the best performance in each geometrical region while maintaining a sufficient radiation resistance. The calorimetric system covers a wide range in pseudo-rapidity ($\eta < 4.9$), and is completely hermetic in ϕ . This allows to obtain an accurate measurement of the jets in a large phase-space, and a good measurement of the missing transverse energy.

Given the difference in the shower development for electrons/photons and hadrons, the calorimetric system is divided into two different sections: the electromagnetic section (EM), described in References [[ATLAS Collaboration 1996a](#), [ATLAS Collaboration 2010j](#)], and the hadronic section (HAD) described in References [[ATLAS Collaboration 1996b](#), [ATLAS Collaboration 2010k](#)]. The EM section must provide a good measurement and containment of the electromagnetic showers. The hadronic shower are instead measured by the ensemble of the EM and HAD sections that together contain at best the whole shower and limit the punch-through (i.e. particles leaking out of the calorimeter).

Thicker calorimeters improve the containment of the showers, however this has to be balanced against the increased material and dimension of the device. The two parameters which describe the thickness of a calorimeter, for the electromagnetic showers, and for the hadronic showers, are the radiation length X_0 and the interaction length λ_I . The first one is both (a) the mean distance over which a high-energy electron loses all but $1/e$ of its energy by bremsstrahlung, and (b) 7/9 of the mean free path for pair production by a high-energy photon. The second one is the mean distance traveled by a hadron before undergoing an inelastic nuclear interaction. The total thickness of the EM calorimeter is more than $22 X_0$, and for the containment of the hadronic shower, the calorimetric system has a thickness of $9.7 \lambda_I$.

To achieve the required performance in a widely varying radiation environment the ATLAS calorimetric system uses radiation-hard liquid Argon (LAr) technology for the EM barrel and end-cap, for the hadronic end-cap (HEC), for the forward calorimeter (FCal). In the barrel region, the cryostat is shared with the super conducting solenoid, while the EM end-cap, the HEC and the FCal share the same cryostat in the forward region. In the

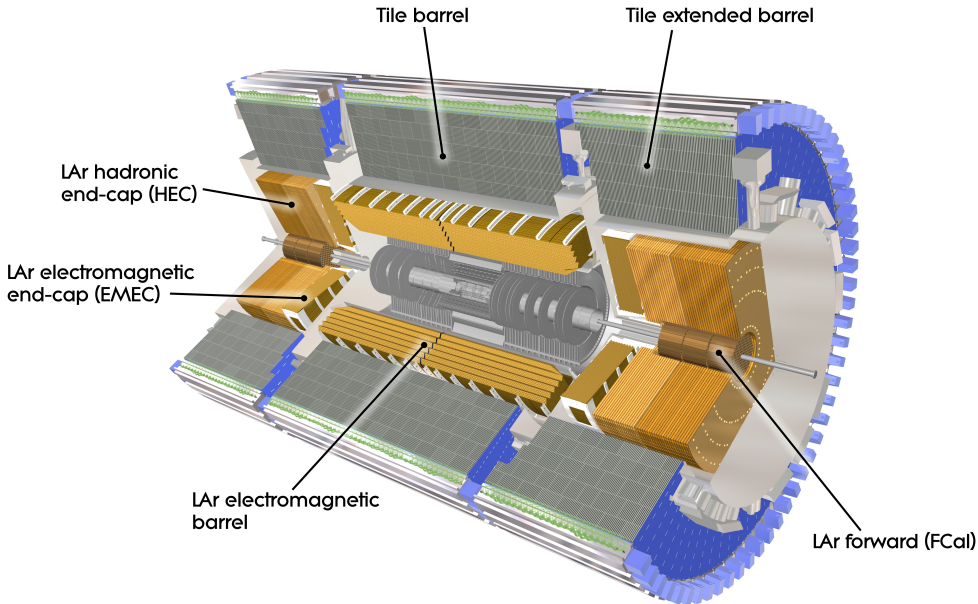


Figure 1.5: Overall view of the ATLAS calorimetric system.

barrel region, the tile calorimeter (TileCal) provides a good solution to precisely measure the energy loss by hadrons, with a relatively cheap technology. Scintillating tiles are used as active material, while the passive material is steel. The TileCal is divided in a barrel ($|\eta| < 1$) and two extended barrels ($0.8 < |\eta| < 1.7$). Figure 1.5 shows an overall view of the ATLAS calorimetric system. The calorimeters are divided in different radial layers of cells, which allow us to follow the longitudinal development of the electromagnetic and hadronic showers produced by the impinging particles. The design parameters for the different ATLAS calorimeters are shown in Table 1.2. The division in cells coarsely follows a projective geometry, in which the detector is divided by different region of fixed pseudo-rapidity.

1.2.2.1 The electromagnetic calorimeters

The electromagnetic calorimeter is divided into a barrel part ($|\eta| < 1.475$) and two end-cap components ($1.375 < |\eta| < 3.2$). The barrel consists of two identical half-barrels separated at $z=0$ by a 6 mm gap between them. The two end-caps are divided in two coaxial wheels. The absorber consist of lead, with an accordion geometry, which provide a complete symmetry in ϕ without azimuthal cracks. The active material is the liquid Argon. Charged particles that cross the liquid Argon produce by ionization a current which is measured in electrodes. The electrodes which collect the signals envelop the absorber.

The barrel is divided in three longitudinal samples. The first one ($4.3 X_0$ long) has a fine segmentation in η , to precisely determine the pseudo-rapidity direction of the impinging particles. The second layer, the largest one ($16 X_0$ long), is designed to measure the bulk

Table 1.2: Design parameters of the ATLAS calorimeter.

EM CALORIMETER (LAr)	Barrel	End-cap
Coverage	$ \eta < 1.475$	$1.375 < \eta < 3.2$
Long. segmentation	3 samplings	3 samplings 2 samplings
Granularity ($\Delta\eta \times \Delta\phi$)		$1.5 < \eta < 2.5$ $2.5 < \eta < 3.2$
Sampling 1	0.003×0.1	0.025×0.1 0.003×0.1 0.004×0.1 0.006×0.1 0.1×0.1
Sampling 2	0.025×0.025	0.025×0.025 0.1×0.1
Sampling 3	0.05×0.025	0.05×0.025
PRESAMPLER	Barrel	End-cap
Coverage	$ \eta < 1.52$	$1.5 < \eta < 1.8$
Granularity ($\Delta\eta \times \Delta\phi$)	0.025×0.1	0.025×0.1
Hadronic Tile (TileCal)	Barrel	Extended Barrel
Coverage	$ \eta < 1.0$	$0.8 < \eta < 1.7$
Long. Segmentation	3 sampling	3 sampling
Granularity ($\Delta\eta \times \Delta\phi$)		
Sampling 1 and 2	0.1×0.1	0.1×0.1
Sampling 1 and 2	0.2×0.1	0.2×0.1
Hadronic LAr (HEC)		End-cap
Coverage		$1.5 < \eta < 3.2$
Long. Segmentation		4 sampling
Granularity ($\Delta\eta \times \Delta\phi$)	0.1×0.1	$1.5 < \eta < 2.5$ $2.5 < \eta < 3.2$
FCal		Forward
Coverage		$3.1 < \eta < 4.9$
Long. Segmentation		3 sampling
Granularity ($\Delta\eta \times \Delta\phi$)		0.2×0.2

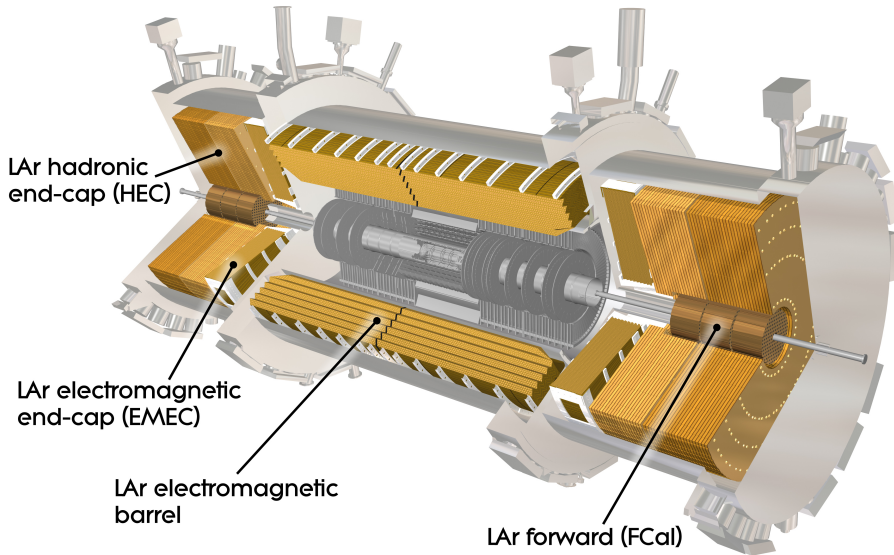


Figure 1.6: Overall view of the liquid argon calorimetric system.

of the energy loss by electrons and photons. The third layer, with a coarser segmentation, is used to measure the energy loss in the last part of the longitudinal development of the electromagnetic showers.

Figure 1.6 shows an overview of the liquid argon calorimeters.

The signals generated in the different cells are shaped, amplified and digitized by the front-end electronics, located in the gap between the TileCal barrel and the TileCal extended barrel. The shaped signals are sampled five times at a frequency of 40 MHz. The digitized samples are transmitted to the Read Out Drivers (RODs) that contains Digital Signal Processors that reconstruct the amplitude and time of the original signal using a linear combination (Optimal Filter - OF) [Cleland 1992] of the samples s_i . The energy in each channel is given by:

$$E_{cell}(\text{MeV}) = F \sum_{i=1}^5 a_i(s_i - P) \quad (1.3)$$

where F is the conversion factor between ADC counts and MeV, P is the cell pedestal and a_i are the optimal filtering coefficients. The linearity of the EM calibration has been verified with test-beam electrons in the range 10-350 GeV. The scale of the calorimeter has also been verified with collision data using Z^0 decays into an electron-positron pair.

1.2.2.2 Hadronic calorimeters

The hadronic calorimeters enclose the EM calorimeter. Together they measure the energy deposition of the hadronic showers. Given the small thickness in terms of λ_l of the EM calorimeter, the hadronic calorimeters are designed to give, to the complete calorimetric system, a good containment of the hadronic showers. Furthermore, they are designed to be hermetic in ϕ and to cover a wide range in pseudo-rapidity ($|\eta| < 4.9$). These features allow the ATLAS experiment to perform an accurate measurement of the jets in a large phase-space, and a good measurement of the missing transverse energy.

There are three types of hadronic calorimeters in ATLAS: the tile calorimeter, the hadronic end-cap calorimeter and the forward calorimeter.

The tile calorimeter

The central part of the hadronic calorimeter, TileCal, differs from the rest of the ATLAS calorimetry because it does not use the LAr as active material. The calorimeter is made by steel absorbers and scintillating tiles within the iron structure. The structure is periodical in z , and the tiles are oriented perpendicular to the beam axis. The tiles are read out by two wave length shifting (WLS) fibers, one for each side. The WLS fibers are grouped to reach the desired cells granularity, reported on Table 1.2.

Their signals are read by photo-multipliers located on the radial periphery of the calorimeter. Each cell is read out by two photo-multipliers to obtain a double readout.

The TileCal is subdivided into one barrel region ($|\eta| < 1.0$), and in two extended barrels ($0.8 < |\eta| < 1.7$, one on each side of the barrel). The gap between them provides space for the services for the inner detector and the front-end electronics of the EM calorimeter. Both the barrel and the two extended barrels are subdivided in 64 modules, one for each ϕ slice ($\Delta\phi \sim 0.1$). It is segmented in depth in three layers, approximately 1.5, 4.1 and $1.8 \lambda_l$ thick for the barrel, and 1.5, 2.6 and $3.3 \lambda_l$ for the extended barrel.

The front-end electronics of one TileCal module is placed on its external edge. The pulse produced by the photo-multipliers are shaped, amplified and digitized at 40 MHz with fast ADCs that provide, for each signal, seven samples. The signal is than processed using the optimal filtering technique [Fullana 2005] to obtain the signal amplitude and time. In this case however for all the signals above a predefined threshold it is also possible to save the complete digitized information.

The hadronic end-cap

Each one of the two hadronic end-cap consists of two independent wheels which cover the pseudo-rapidity interval $1.5 < |\eta| < 3.2$. Both wheels consist of an array of copper plates, with a thickness of 25 mm in the first wheel, and 50 mm in the second one. The active material is the liquid Argon, which generates the currents read out by the electrodes. The gap between the plates is split by three electrodes into four drift spaces. The central electrode is the read-out electrode, while the side ones are the HV carries. Each wheel is divided into two longitudinal layers. In Figure 1.6 the position of the two wheels is shown.

The signals in the cells, are sent to the preamplifier boards located at the wheel periphery, and the energy is reconstructed with a dedicated optimal filtering procedure.

The forward calorimeter

The radiation hardness of the liquid Argon technology is particularly important for the forward calorimeter (FCal, described in detail in Reference [[ATLAS Collaboration 2008b](#)]). This sub-detector is in fact facing an high level of radiation. Its front face is about 4.7 m from the interaction point, and it is really close to the beam pipe. Its position is shown in Figure 1.6. It provides clear benefits both in terms of uniformity of the calorimetry coverage, and in terms of radiation background for the muon spectrometer in the forward direction.

The FCal consists of three longitudinal sections: the first one is made of copper, while the other two are made by tungsten. The liquid Argon is the active material, and the currents produced by the ionization are collected in electrodes for the measurement of the energy deposition. The main difference between the forward calorimeter and the other liquid Argon calorimeters in ATLAS is the geometry adopted to collect the signals. In each section, the calorimeter is made by a metal matrix with regularly spaced longitudinal channels filled with concentric rods and tubes. The rods are at positive high voltage, while the tubes and the matrix are grounded. Rods are grouped for the readout totaling about 3500 channels.

The signals from the electrodes define the energy measured in each cells, by using a peculiar optimal filtering algorithm.

1.2.3 The muon spectrometer

The muon spectrometer is based on the magnetic deflection of muon tracks in the large superconducting air-core toroid magnets. The magnet configuration provides a field mostly perpendicular to the muon trajectory, while minimizing the degradation of resolution due to multiple scattering because the muons travel mainly through the air.

The muon spectrometer has been instrumented to have the possibility to perform a precise standalone measurement of the muon momentum. A detailed description of the muon spectrometer can be found in Reference [[ATLAS Collaboration 1997c](#)].

In the barrel region ($|\eta| < 1.0$), the muon chambers are arranged in three cylindrical layers (sectors), while in the end-cap ($1.4 < |\eta| < 2.7$) they form three vertical walls. The transition region ($1.0 < |\eta| < 1.4$) is instrumented with four layers.

The azimuthal layout follows the magnet structure: there are 16 sectors. The large sectors lie between the coils, and they overlap with the small sectors placed next to the coils. Figure 1.7 shows an overall view of the geometry of the muon sectors, and of the different technologies used to detect and measure the muons.

The choice of different types of chambers has been driven by criteria of rate capability, granularity, aging and radiation hardness. The measurement of the track bending is provided in most of the η regions by the Monitored Drift Tubes (MDT), while at large η , the higher granularity Cathode Strip Chambers (CSC) are used. The chambers for the

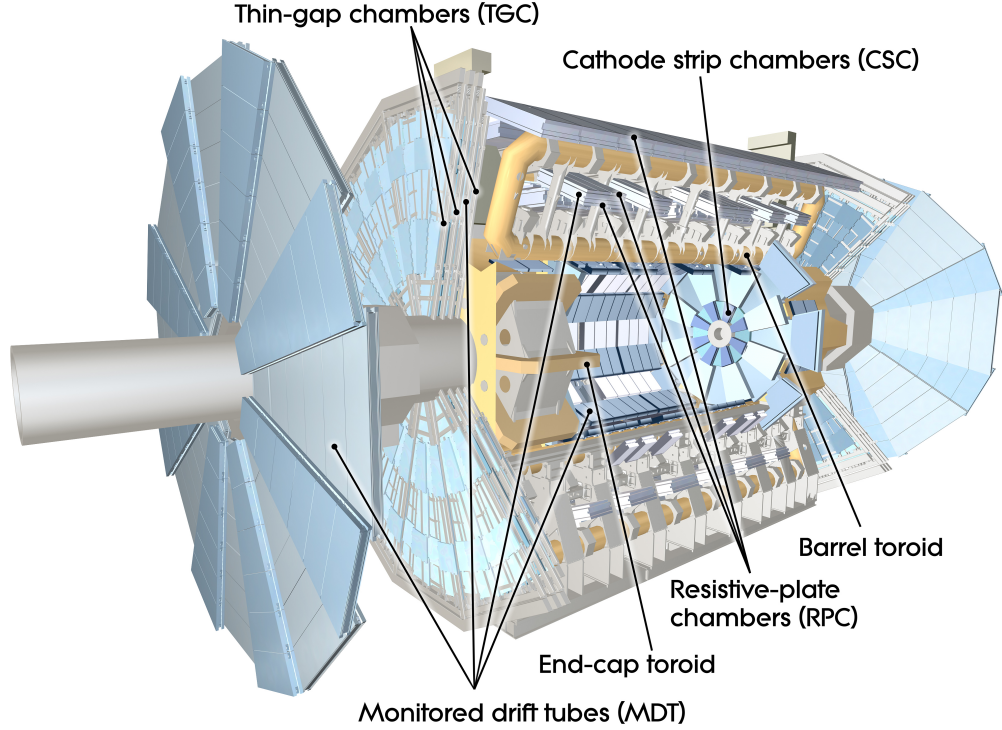


Figure 1.7: Overall view of the muon chamber system in ATLAS.

first level of the trigger system need a very fast response. They covers the region $|\eta| < 2.4$. The Resistive Plate Chambers (RPC) are used in the barrel region, while the Thin Gap Chambers (TGC) are used in the end-cap.

The overall performance over the large area involved depends on the alignment of the muon chambers with respect to one another, and to the overall detector. The internal deformations and relative positions of the MDT chambers are monitored by precision-mounted alignment sensors. The magnetic field is continuously monitored, to be able to properly determine the bending power along the muon trajectory.

1.2.4 Trigger and Data acquisition

The ATLAS trigger and data-acquisition is based on three levels of on-line event selection. Each trigger level refines the decision of the previous one. A detailed description of these systems can be found in References [[ATLAS Collaboration 1998](#), [ATLAS Collaboration 2003](#)]. Starting from an initial bunch crossing rate of 40 MHz, the rate of selected events must be reduced to about 100 Hz for permanent storage. The strong rejecting factor must match the need of an excellent efficiency for the rare physics processes of interest. The Level-1 trigger takes its decision based on a reduced granularity information from a subset of detectors. Objects searched by the calorimeter triggers are high transverse momentum electrons, photons, jets, hadronically decayed taus, as well as the missing transverse energy and the total transverse energy. The muons are identified

by the trigger chambers in the muon spectrometer. All the Level-1 trigger decisions are taken by logically combined requirements on these objects. No tracking information is used by the Level-1 trigger, due to the timing restrictions. The maximum rate at which the ATLAS front-end system can accept Level-1 triggers is limited to 70-80 kHz, but in the last year several tests to reach 100 kHz have been performed. Due to the geometrical size of the experiment (in some cases the time of flight to arrive to a sub detector is of the same order of magnitude of the bunch crossing period), and to the time in which the detector signals extend, all the detector signals are stored in pipelines. Events accepted by the Level-1 are read-out from these pipeline in the front-end electronics. The allowed Level-1 latency, measured from the proton-proton collision until the trigger decision is available to the front-end electronics, should be less than 25 μ s.

All the detector data, selected by the Level-1 trigger, are collected from the different part of the detector to the Read Out System (ROS), until the event is processed by the High Level Trigger (HLT). The HLT consists of two different levels, the Level-2 and the Event Filter (EF).

The Level-2 trigger processors make use of the complete granularity information from the complete ATLAS detector. However, only data from a small geometrical portion of the detectors are used in the Level-2. These regions, called Regions of Interest (RoIs), are selected by the Level-1 trigger. The final Level-2 rate is expected to be about 1-2 kHz.

The Event Filter is the last step of the chain. It uses off-line algorithms, adapted for the on-line time requirements, to reconstruct the objects, and to take its decision. The Event Filter has about 1 second to take the decision, and the output rate is of about 100 Hz. The events selected by the Event Filter are written to mass storage for the subsequent off-line analysis.

In the next subsections, the relevant triggers used in the measurement of the inclusive jet cross section are presented.

Minimum bias trigger scintillators

The Minimum Bias Trigger Scintillators (MBTS) are 32 scintillator plates connected to different photo-multipliers. They are divided in two wheels, situated on the positive and negative LAr end-caps, covering the pseudo-rapidity range $2.1 < |\eta| < 3.8$. For each wheel, there are 2 segments in η (inner and outer) and 8 segments in ϕ .

The MBTS were used to trigger on Minimum Bias events at early days running. Figure 1.8 shows a picture of the position of the MBTS system.

The light produced in the scintillators is sent, via wave length shifting fibers to some of the TileCal photo-multipliers. After an amplification step, the signals of the 32 photo-multipliers are sent to discriminators. If there is at least one signal above the discriminator threshold, the event is accepted by the Level-1 system. The name of the trigger which fires in this configuration is L1_MBTS_1, and it has been extensively used for the analysis of the very first collisions, for the analysis of the minimum bias events and for the measurement of low transverse momentum jets.

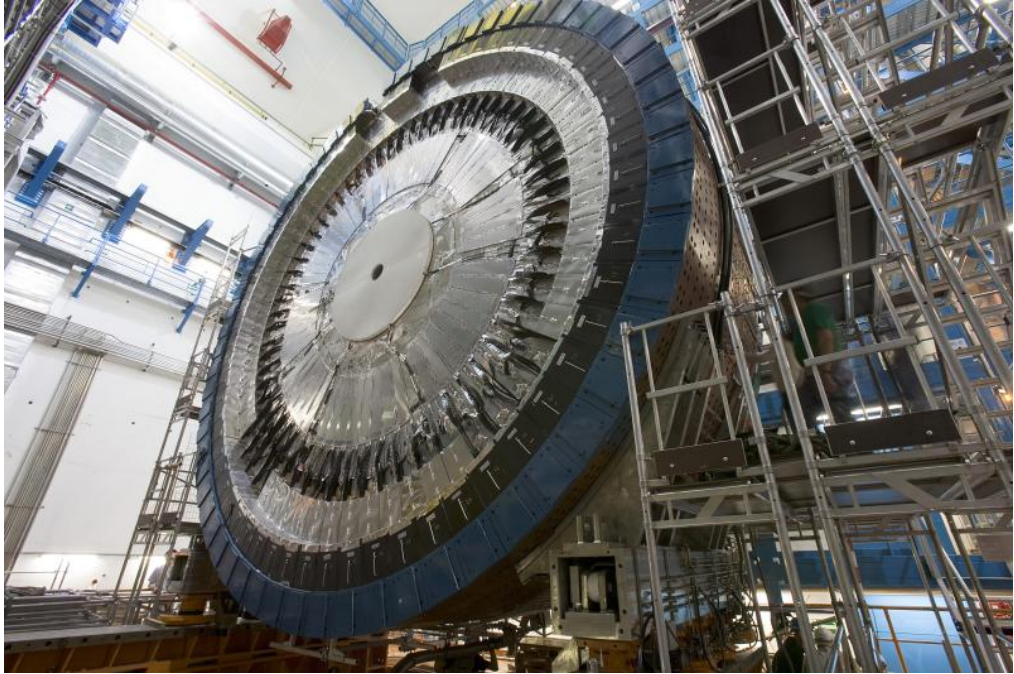


Figure 1.8: Photo of MBTS mounted on LAr end-cap cryostat. MBTS is the gray annulus divided in 8 visible tiles. Fibers from MBTS go radially to photo-multipliers in TileCal.

Jet triggers

The important units for the jet trigger algorithm are the jet RoIs and the Jet Windows. The energy in the electromagnetic and the energy in the hadronic calorimeters are summed in projective towers of $\Delta\eta \times \Delta\phi = 0.1 \times 0.1$. These towers are summed in RoIs to give a granularity of $\Delta\eta \times \Delta\phi = 0.4 \times 0.4$ (4×4 towers per jet element). They are used to indicate the position of the candidate jet.

The Jet Windows are windows of size 4×4 , 6×6 and 8×8 projective towers, which slide in steps of two towers in both the η and ϕ directions. They are used to measure the jet E_T .

The requirements for the Level-1 single jet trigger are:

- The ROI cluster must be a local E_T maximum compared to its neighbors;
- The jet window E_T , for the granularity under consideration, must be greater than the selected jet threshold.

Several sets of trigger E_T thresholds are available in the ATLAS trigger menu. Each threshold set is a combination of a threshold for jet E_T (on which no hadronic calibration procedure is applied) and a choice of jet window size.

In the first period of data taking the measurement of the inclusive jet cross section is based on events selected by the Level-1 jet trigger. In this period, in fact, the higher trigger levels were under commissioning and not used to reject the data. The list of the used trigger items are shown in Tables 5.1-5.4 in Section 5.1.1.

Similar strategies are used to select the jets in the central region (up to $|\eta| < 3.2$), by the central jet trigger and in the forward region ($3.2 < |\eta| < 4.9$), by the forward jet trigger. The measurement of jet in the region around 3.2 can be done using the OR combination of the central and the forward jet trigger, as described in Section 5.1.1.

The Level-2 jet trigger algorithm accesses calorimeter data that lies in a rectangular region centered around the Level-1 jet RoI position. The position and transverse energy of each detector element that falls into the chosen region are read-out by the algorithm. The elements are clustered in cone-shaped object in the (η, ϕ) plane with a given radius $R_{cone} = \sqrt{\Delta\eta^2 + \Delta\phi^2}$. The jet energy and position are found through an iterative algorithm, which runs N times. In the first step the center of the jet is the position of the Level-1 jet RoI (η_0, ϕ_0) . In the $i+1$ iteration the position of the cone (η_{i+1}, ϕ_{i+1}) is defined as the the centroid of the cone opened around the center (η_i, ϕ_i) in the i iteration.

The requirements for the Level-2 single jet trigger is that at least one of the jets in the event passes a threshold in E_T .

The subsequent trigger selection is done by the Event Filter. This algorithm was under commissioning in 2010, and it was used in pass-through (even if the decision of the Event Filter was evaluated, it was not taken into account for the data acquisition). A detailed description of the algorithms used in the Event Filter can be found in Reference [ATLAS Collaboration 2009c].

1.2.5 Monte Carlo simulation of the ATLAS detector

The ATLAS sub-detectors have been exposed to beams in several test in the last 20 years. These tests were aimed at proofing the expected performances of the technological solutions adopted by the experiment, and to improve the Monte Carlo description of the detector. The ATLAS detector simulation software [ATLAS Collaboration 2010n] is based on GEANT4 [Agostinelli 2003], and it uses the GEANT4 physics list QGSP_BERT [A.Ribon 2010]. The simulations have been widely used in the last years, not only to check the performances of the detector, but also to develop techniques for the analysis of the data. Part of the ATLAS event reconstruction depends on the accuracy of the Monte Carlo description of the geometry and of the defects of the detector. The accuracy of these descriptions have been studied with several dedicated analysis using the first proton-proton collisions.

1.2.6 The data samples collected in 2010

The quest for higher and higher luminosity has implied to work with continuously changing accelerator and detector conditions especially from the point of view of the trigger system. The data recorded in 2010 have been divided in various periods. Within each period the accelerator and the detector conditions can be considered uniform. The general description of the operation conditions and the integrated luminosity collected in each period are shown in Table 1.3. The list of data indicated in Table 1.3 has been used for the measurement of the inclusive jet cross section. The analysis strategy is designed to take into account the peculiarities of the different periods, and a cross check of the data stability has been done

Table 1.3: 2010 data periods for proton-proton running

Period	Description	Integrated luminosity (nb ⁻¹)
A	Unsqueezed stable beam data ($\beta^*=10$ m): typical beam spot width in x and y is 50-60 μm .	0.4
B	First squeezed stable beams ($\beta^*=2$ m): typical beam spot width in x and y is 30-40 μm .	9.0
C	More bunches in the machine	9.5
D	Bunches with 0.9×10^{11} p/bunch - $\beta^*=3.5$ m Pileup: 1.3 interactions per bunch crossing (was <0.15 before) Larger z -vertex distribution.	320
E	New trigger menu, with operation for the trigger commissioning	1118
F	36 colliding bunches in ATLAS	1980
G	Bunch trains with 150 ns spacing from LHC	9070
H	233 colliding bunches in ATLAS	9300
I	295 colliding bunches in ATLAS	23000

and presented in Section 5.2.

Detector status at the end of 2010

The subsystems have a natural evolution, partially due to the natural aging of the sub-detectors, partially due to the different conditions in the accelerator. In 2010 the ATLAS collaboration was able to record high quality data from all the subsystems, with an high fraction of good channels. The approximate fraction of operating channels at the end of 2010, shown in Table 1.4, is in general higher than 97 %.

The efficiency integrated (and weighted by the weekly luminosity) over this data taking period is 93.6%. The inefficiency accounts for the turn-on of the high voltage of the Pixel, SCT and some of the muon detectors (2.0%) and any inefficiencies due to dead-time or due to individual problems with a given sub-detector that prevented the ATLAS data taking to proceed (4.4%).

Table 1.4: ATLAS detector status at the end of 2010

Subdetector	Number of channels	Approximate operational fraction
Pixels	80 M	97.3%
SCT Silicon Strips	6.3 M	99.2%
TRT Transition Radiation Tracker	350 k	97.1%
LAr EM Calorimeter	170 k	97.9%
Tile calorimeter	9800	96.8%
Hadronic endcap LAr calorimeter	5600	99.9%
Forward LAr calorimeter	3500	100%
LVL1 Calo trigger	7160	99.9%
LVL1 Muon RPC trigger	370 k	99.5%
LVL1 Muon TGC trigger	320 k	100%
MDT Muon Drift Tubes	350 k	99.5%
CSC Cathode Strip Chambers	31 k	98.5%
RPC Barrel Muon Chambers	370 k	97.0%
TGC Endcap Muon Chambers	320 k	98.4%

CHAPTER 2

Jet production at hadron colliders: Theoretical predictions

Contents

2.1	Fundamental interactions: the Standard Model	27
2.2	The Strong interactions: the Quantum Chromo-Dynamics (QCD)	30
2.2.1	Structure of pQCD predictions	30
2.2.2	From the soft divergences to the jet algorithms	33
2.2.3	Beyond the fixed order predictions: the parton shower and non perturbative effects	38
2.2.4	Different strategies to get a predictions	41
2.3	Inclusive jet cross section: Theoretical prediction	43
2.3.1	Fixed order pQCD	44
2.3.2	Total theoretical uncertainties for the fixed order predictions	50
2.3.3	NLO Matrix Element + Parton Shower	51

2.1 Fundamental interactions: the Standard Model

The experimental observations and the theoretical developments in the last century drastically changed the description of the deepest properties of the matter, and of its fundamental constituents. The fundamental constituents of the matter are the particles, which interact via different forces: the electromagnetic force, the weak force, the strong force and the gravitational force. All the fundamental particles and their interactions (but the gravity) are described by the Standard Model theory of the fundamental interactions. A detailed introduction to the Standard Model of particle physics can be found in References [Aitchison 2003, Aitchison 2004]. The particles and the forces are described by relativistic quantum fields, developed by the fruitful unification of the classical fields, the quantum mechanic and the special relativity.

The particles are divided in quarks and leptons depending on their interactions. In the Standard Model description, the quarks can interact through electromagnetic, weak, and strong interactions, with the strong interactions being the dominant one. Six different flavors of quarks are foreseen by the model and have been experimentally found: down, up, strange, charm, bottom and top. The leptons include charged leptons and neutrinos. The charged leptons are the electron, muon and tau. The corresponding neutrinos are known

Three Generations of Matter (Fermions)				
	I	II	III	
mass→	2.4 MeV	1.27 GeV	171.2 GeV	
charge→	$\frac{2}{3}$	$\frac{2}{3}$	$\frac{2}{3}$	
spin→	$\frac{1}{2}$	$\frac{1}{2}$	$\frac{1}{2}$	
name→	u up	c charm	t top	
Quarks	d down	s strange	b bottom	
	4.8 MeV	104 MeV	4.2 GeV	
	$-\frac{1}{3}$	$-\frac{1}{3}$	$-\frac{1}{3}$	
	$\frac{1}{2}$	$\frac{1}{2}$	$\frac{1}{2}$	
Leptons	ν_e electron neutrino	ν_μ muon neutrino	ν_τ tau neutrino	Z^0 weak force
	<2.2 eV	<0.17 MeV	<15.5 MeV	91.2 GeV
	0	0	0	0
	$\frac{1}{2}$	$\frac{1}{2}$	$\frac{1}{2}$	1
Bosons (Forces)	e electron	μ muon	τ tau	W^\pm weak force
	0.511 MeV	105.7 MeV	1.777 GeV	80.4 GeV
	-1	-1	-1	± 1
	$\frac{1}{2}$	$\frac{1}{2}$	$\frac{1}{2}$	1

Figure 2.1: The elementary particles in the Standard Model.

as the electron neutrino, muon neutrino and tau neutrino. Charged leptons can interact electromagnetically and weakly. The neutrinos can only interact weakly. At each particle correspond an anti-particle with equal mass and opposite charge.

The six quarks and the six leptons can be split up into three generations of particles with similar properties, but with different masses. The three generations contain (d, u, e, ν_e), (s, c, μ, ν_μ), and (b, t, τ, ν_τ). The "normal" matter is made of up quarks, down quarks and electrons. The quarks are "glued" together by the gluons, to form the nucleons and the atomic nuclei, and the electron interact with the nuclei via electromagnetic interactions, carried by photons, to form atoms and molecules.

The second and third generation of quarks and charged leptons have a short lifetime. The general properties of the fundamental particles of the Standard Model are reported in Figure 2.1.

These particles in the Standard Model are described by relativistic quantum fields. The general structure of the quantum mechanics and of the special relativity forces the fields to be invariant under fundamental symmetries. The interactions between different fields

are introduced by requiring the invariance under an additional symmetry: the local gauge symmetry. The symmetry group that produces the interactions in the Standard Model is $U(1) \times SU(2) \times SU(3)$. The $U(1)$ is a complex phase and $SU(2)$ and $SU(3)$ are unitary matrices with determinant one and rank two and three respectively. The detailed description of this symmetry, and its implication on high energy interactions is beyond the scope of this document, and can be found in References [Aitchison 2003, Aitchison 2004]. The requirement of maintaining the gauge additional invariance introduces a specific set of dynamics.

The invariance under $U(1)$ and $SU(2)$ leads to the theory of the electroweak interactions. Four particles mediate the electroweak interactions: the photon (γ), the W^+ , the W^- and the Z^0 . The photon is responsible for all the electromagnetic interactions and has no mass. The other electroweak gauge particles are massive and are seen in much rarer processes.

The invariance under $SU(3)$ is responsible for generating the strong interaction. The strong charge is called color and it can take three values (usually called red, green and blue) and their anti-values (anti-red, anti-green, anti-blue). The sum of the three colors is charge neutral. The strong interaction has one massless mediator, the gluon, which also carries color and anti-color charge. An important peculiarity of the strong interaction is that the force gets stronger at large distances. This has profound consequences. One of them is that strongly interacting particles can only be observed in color-neutral bound states (the hadrons). This property is known as confinement. Any attempt to separate a quark or gluon from its bound state results in the production of new color-neutral particles rather than a free quark or gluon. The protons and the neutrons are the "common" bound states of strongly interacting up and down quarks.

The final piece of the Standard Model is the Higgs particle. The Higgs particle is the footprint of a mechanism which provides the masses to the W^\pm , to the Z^0 and to all the fundamental particles within the Standard Model (including itself). So far the Higgs particle is only a postulate and has not been confirmed experimentally. One of the goal of the Large Hadron Collider experiments is to investigate the presence of the Higgs boson and its dynamics.

2.2 The Strong interactions: the Quantum Chromo-Dynamics (QCD)

The Quantum Chromo-Dynamics (QCD) is produced by the invariance under the $SU(3)$ local gauge symmetry. It is the Standard Model description of the dynamics of the strong interactions. A complete introduction to the QCD can be found in References [Dissertori 2010, Salam 2010]. This section is an introduction to some of the important aspects involved in the determination of the theoretical prediction for the inclusive jet cross section at the LHC.

There are different first-principles approaches to solve QCD. The most complete approach is lattice QCD [Gupta 1997]. It involves a discretization of the space-time. The values of the quark and gluon fields are considered at all the vertices/edges of the resulting 4-dimensional lattice. The method is fruitful to calculate static quantities, such as the hadron mass spectrum, but at present it is not suitable to carry out a complete lattice calculations of the LHC physics.

The approach used in hadron colliders to describe the strong interactions is through the perturbative QCD (pQCD). In this approach, the important parameter is the coupling which determines the strength of the force. Perturbative QCD relies on the idea of an order-by-order expansion in a small coupling.

The couplings in the Standard Model have a dependence on energy or distance. For the electromagnetic and the weak force the coupling gets stronger as one goes to higher energies or shorter distances, while for the strong force the opposite is true. The coupling for the QCD is named α_s and Figure 2.2 shows the decreasing of the strong coupling constant α_s as a function of the scale of the process, as obtained from the measurements in several experiments (Reference [Bethke 2009]).

The strong force is weaker at small distances and high energies and gets stronger as the distance between particles increases. The fact that in QCD the force is weak at small distances is known as asymptotic freedom. The property of asymptotic freedom means that in the high energy regime ($Q \gtrsim 5\text{-}10 \text{ GeV}$), physics can be described well by perturbation theory.

Colliders like the LHC are mainly investigating phenomena involving high energy scales, in the range 50 GeV to 5 TeV. For these values the QCD coupling is small and the perturbation theory can be applied.

2.2.1 Structure of pQCD predictions

The strong coupling

In the framework of perturbative QCD, the predictions of observables are expressed in powers of the renormalized coupling $\alpha_s(\mu_r^2)$, a function of an (unphysical) renormalization scale μ_r . Renormalization is a way to remove infinities from the theoretical predictions, absorbing some terms in the coupling which acquires a scale dependence. The value of α_s is not calculable in perturbative QCD, but the value measured at a certain scale (usually the mass of the Z^0 boson) can be evolved to another scale μ_r , thanks to the renormalization

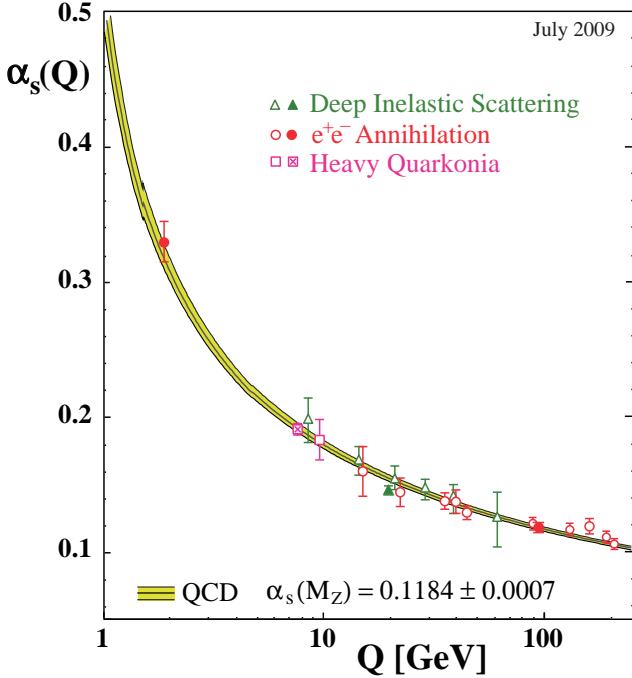


Figure 2.2: Summary of measurements of the strong coupling constants α_s as a function of the process energy scale Q . The plot is taken from Reference [Bethke 2009].

group equation (RGE):

$$\mu_r^2 \frac{d\alpha_s}{d\mu_r^2} = - \sum_i b_i \alpha_s^{2+i} \quad (2.1)$$

The coefficients b_i , which determine the running of the coupling constant, can be calculated in pQCD. When one takes μ_r close to the scale of the momentum transfer Q in a given process, $\alpha_s(\mu_r^2 \sim Q)$ is indicative of the effective strength of the strong interaction in that process.

The partons

Even if the high energy hadron colliders accelerate hadrons (i.e. protons), the fundamental interacting particles in pQCD are the quarks and the gluons (named partons).

In the cross sections involving initial state hadrons (such as in proton-proton collisions), a mapping between the kinematic properties of the initial hadrons to the initial partons is needed. This mapping is provided by the non-perturbative parton distribution functions (PDFs). The PDF $f_{i|h}(x, \mu_f^2)$ is the probability density of partons of type i inside a fast-moving hadron h to carry a fraction x of the hadron longitudinal momentum. The scale μ_f is the factorization scale. Its role is to handle the parton emissions which are collinear with the initial parton. The majority of the emissions that modify a parton's momentum are actually collinear (parallel) to that parton, and do not depend on the fact that the parton is destined to interact in the hard process. It is natural to view these emissions as modifying the structure of the proton rather than being part of the hard partonic interaction. The separation between the two categories is somewhat arbitrary and parametrized by a factorization scale μ_f . When one takes μ_f close to the scale of the momentum transfer Q in a given process,

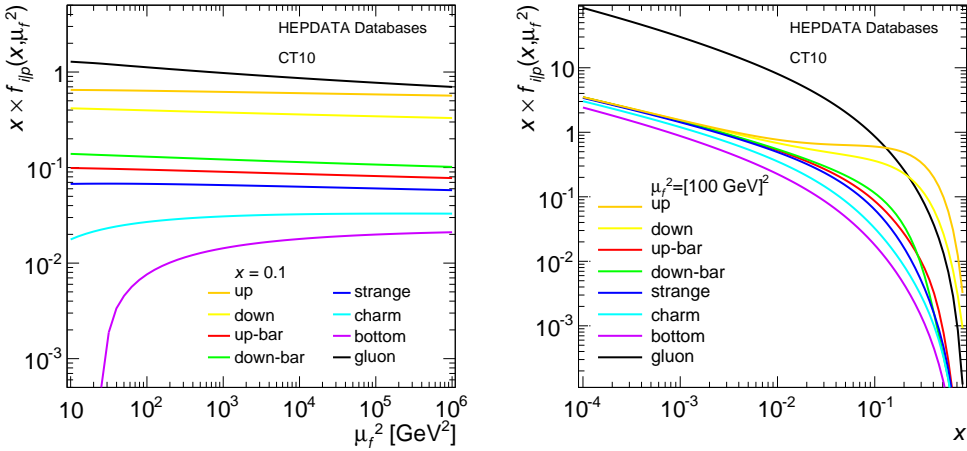


Figure 2.3: Dependence of the proton PDFs on the scale μ_f^2 and on the fraction of longitudinal momentum x , for the CT10 fit. Values extracted from Reference [<http://durpdg.dur.ac.uk/>].

$f_{i|h}(x, \mu_f^2 \sim Q^2)$ becomes indicative of the effective parton density function which enters in the hard process.

The value of $f_{i|h}$ can be measured in different experiments (usually in deep inelastic proton-electron scattering) and it can be evolved to other scales μ_f , thanks to the Dokshitzer-Gribov-Lipatov-Altarelli-Parisi (DGLAP) equation, which at leading order is:

$$\frac{\partial f_{i|h}(x, \mu_f^2)}{d\mu_f^2} = \sum_j \frac{\alpha_s(\mu_f^2)}{2\pi} \int_x^1 \frac{dz}{z} P_{i \leftarrow j}^{(1)}(z) f_{j|h}\left(\frac{x}{z}, \mu_f^2\right) \quad (2.2)$$

The coefficients $P_{i \leftarrow j}^{(1)}(z)$ describe the probability for a parton j to emit a parton i which carries a fraction z of his momentum. These coefficients, known as splitting functions, can be calculated in pQCD. Figure 2.3 show the proton PDFs $f_{i/p}(x, \mu_f^2)$, for the CT10 fits (see Reference [Lai 2010]). The two plots show the dependence of the PDFs for the different partons on the x and μ_f^2 values.

pQCD predictions at hadron colliders

Once defined the strength of the strong force (α_s) and how to evolve the hadron (proton)-parton mapping for the initial state, one can calculate the cross section of a certain final state X . The cross section factorizes in two terms: the probability of having a certain partonic configuration in the initial state (i, j) , and the partonic cross section ($\hat{\sigma}_{i,j \rightarrow X}$) that, given the partonic initial state (i, j) , describes the production of the final state X . This second part can be expanded in power of α_s : $\hat{\sigma}_{i,j \rightarrow X} = \sum_{n=0}^{\infty} \alpha_s^n \hat{\sigma}_{i,j \rightarrow X}^{(n)}$. The master equation to calculate the pQCD cross sections in proton-proton colliders is:

$$\sigma(pp \rightarrow X) = \sum_{n=0}^{\infty} \alpha_s^n(\mu_r^2) \sum_{i,j} \int dx_1 dx_2 f_{i/p}(x_1, \mu_F^2) f_{j/p}(x_2, \mu_F^2) \hat{\sigma}_{i,j \rightarrow X}^{(n)}(x_1, x_2, \mu_r^2, \mu_f^2) \quad (2.3)$$

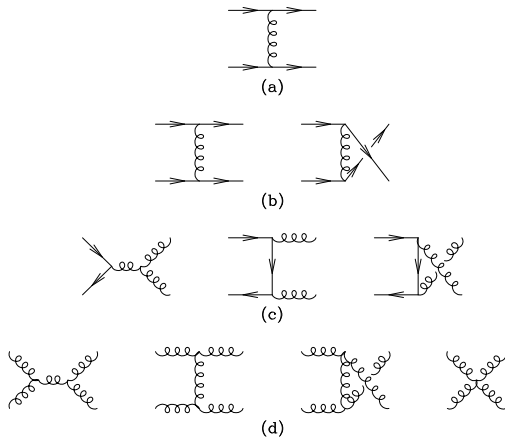


Figure 2.4:
Diagrams for
the $2 \rightarrow 2$ processes.
The diagrams are
divided in different
sub-processes
depending on the
initial and final state.
This figure is taken
from Reference
[Ellis 1996].

Only the perturbative expansion of the partonic cross section is process dependent. The strong coupling constant and the PDFs are universal, and they can be measured in a wide variety of processes, in different experiments, and for different scales. The first non trivial order in the perturbative expansion of $\hat{\sigma}_{i,j \rightarrow X}$ is named leading order (LO). The expansion to the first two orders is named next to leading order (NLO). The perturbative expansion of the partonic cross section can (in principle) be calculated from first principles, but there are still many challenges that remain to be solved before we have a complete understanding of perturbative QCD.

2.2.2 From the soft divergences to the jet algorithms

The easiest QCD partonic processes are the $2 \rightarrow 2$ production: the scattering of two incoming partons producing two outgoing partons. Figure 2.4 shows some Feynman diagrams for these QCD partonic processes. The leading order is proportional to α_s^2 . It sums over all the tree matrix elements $|M_2^2|$ with two incoming partons and two outgoing partons:

$$d\hat{\sigma}_2^{(LO)} = \alpha_s^2 |M_2^2| d\Phi_2. \quad (2.4)$$

where $d\Phi_2$ is the phase space integration measure. By looking at the process $2 \rightarrow 3$, which is the natural continuation after the $2 \rightarrow 2$, one can notice a general property of the pQCD calculations in the limit of collinear and soft emission. The first order in the perturbative expansion is proportional to α_s^3 :

$$d\hat{\sigma}_3^{(LO)} = \alpha_s^3 |M_3^2| d\Phi_3 \quad (2.5)$$

but if one of the final state gluon becomes collinear (parallel) to another particle i (the inter-parton angle $\theta_{ig} \rightarrow 0$) and its energy tends to zero (it becomes "soft", $E_g \rightarrow 0$) the equation 2.5 becomes:

$$\lim_{\theta_{ig} \rightarrow 0, E_g \rightarrow 0} d\hat{\sigma}_3^{(0)} \propto d\hat{\sigma}_2^{(0)} \alpha_s \frac{d\theta_{ig}^2}{\theta_{ig}^2} \frac{dE_g}{E_g} \quad (2.6)$$

This equation shows non-integrable divergences both for small θ_{ig} and for small E_g . They are known as infra-red and collinear divergences, and are general properties of the pQCD predictions. These divergences are important because they determine which observables can be calculated within the pQCD framework.

After the LO $2 \rightarrow 2$ and $2 \rightarrow 3$ processes, one can investigate the interference of a 2-particle tree-level and 2-particle 1-loop amplitude loop diagrams ($2\text{Re}(M_2 M_{2,1-\text{loop}}^*)$). This term is proportional to α_s^3 and mirror the structure of soft and collinear divergences in the $2 \rightarrow 3$ leading order calculation.

A way to handle them is necessary to have a finite prediction for the pQCD.

2.2.2.1 Jet definition: theoretical requirements

The fact that the real emission of a gluon and the interference term in the expansion diverge, is an indication that the four-momenta of the partons are not good observables for the pQCD. To overcome the divergences, one can introduce a mapping of the m four-momenta of the outgoing particles (p_1, \dots, p_m) to a set of l four-momenta (q_1, \dots, q_l):

$$\text{JDef}_{(l,m)}(q_1, \dots, q_l | p_1, \dots, p_m) \quad (2.7)$$

This mapping is named jet definition, and the goal is to simplify the description of the final state by associating close-by partons. Each of the l objects is named jet.

To be able to properly calculate the perturbative expansion of the cross section, the jet definition has to allow the cancellation of the soft and collinear divergences of the real emission (introduced in the description of the $2 \rightarrow 3$ case above) and the virtual term (the interference term). This is done by satisfy the following criteria:

- Infra-red safety: the list of jets and their kinematic properties should not change if a really soft parton is added in the final state:

$$\text{JDef}_{(l,m+1)}(q_1, \dots, q_l | p_1, \dots, p_g, \dots, p_m) \rightarrow \text{JDef}_{(l,m)}(q_1, \dots, q_l | p_1, \dots, p_m) \text{ if } p_g \rightarrow 0 \quad (2.8)$$

This condition is needed to overcome the divergence generated by the term dE_g/E_g in the equation 2.6.

- Collinear safety: the list of jets and their kinematic properties should not change if a parton splits in a collinear pair of partons:

$$\begin{aligned} \text{JDef}_{(l,m+1)}(q_1, \dots, q_l | p_1, \dots, p_i, p_j, \dots, p_m) &\rightarrow \\ \text{JDef}_{(l,m)}(q_1, \dots, q_l | p_1, \dots, p_i + p_j, \dots, p_m) &\text{ if } p_i \parallel p_j \end{aligned} \quad (2.9)$$

This condition is needed to overcome the divergence produced by the term $d\theta_{ig}^2/\theta_{ig}^2$ in the equation 2.6.

If a jet definition follows the two rules above, it is named infra-red and collidear safe. In order to completely fix a jet definition two aspects must be specified: the rules to determine which objects should be merged together (jet algorithm) and the method to calculate the jet four-momentum from the ensemble of the objects belonging to the jet (jet recombination).

The idea of associate close-by objects in jets is consolidated by the phenomenology of particles produced in collider physics. Sprays of particles have been measured in the last 30 years in all the high energy colliders. The jet definition becomes a fundamental aspect to be able to compare the measured cross sections with the state-of-art theoretical predictions. This is guaranteed if the jet definition in use in the experimental measurements fulfills the theoretical requirements of the infra-red and collinear safety. Experimental requirements have been added to the theoretical one, to make a good choice of a jet algorithm in the modern particle physics. These requirements drove the development of different recombination schemes and jet algorithms. In the following lines, an introduction to some of the recombination schemes and jet algorithms tested by the ATLAS Collaboration will be described.

Recombination scheme

The most natural way to recombine the jet constituents is the vectorial sum of their four-momenta:

$$q_k = \sum_i p_i$$

This is independent of the jet algorithm and it provides a meaningful single-jet mass, and conserves energy and momentum. This strategy has been used for the theoretical prediction of the inclusive jet cross section, and for the measurement of jets with the ATLAS detector, as reported in Section 3.1.1.

Jet algorithms

Given the different requirements to be fulfilled by the jet algorithm, and the long history of improvements in the last 30 years, several jet algorithms have been developed and used in collider physics. In particular, they can be divided in two families: cone algorithms and sequential recombination algorithms.

- **Cone algorithms:** The term “cone algorithm” is applied to the wide range of jet algorithms which broadly aim to maximize energy (or p_T) in a geometric cone. The cone gives a circle when projected in $y - \phi$ space, and the radius of the circle, R , is a key parameter of the algorithm. The circularity or otherwise of the eventual jets depends upon details of the algorithm, in particular upon how overlapping jets are treated.

Most frequently used cone algorithms are “iterative”. When a candidate cone is identified, its momentum vector is calculated and the cone is redrawn around the new center. The process is repeated until it converges on a stable cone.

The question arises in cone algorithms as to what to do when energy deposits exist which are spread over a larger area than a single cone; or alternatively, what happens if two stable cones overlap. Generally one of two different approaches is adopted.

Progressive removal: The highest p_T jet is identified, all energy associated with it is removed, and the algorithm is rerun to identify the next highest p_T jet.

Split/Merge: All stable cones are identified. Cones which share energy are either split into two jets or merged into a single jet based upon the fraction of their energy which is in common. Typically an overlap fraction (OLF) parameter is defined such that if two cones share more than a fraction OLF (usually between 0.5 and 0.75) they are merged. Otherwise, they are split into two jets, with the overlap energy being assigned to the higher p_T of the two.

For a clear and detailed discussion and bibliography of cone algorithms and their use in older experiments, see Reference [[Salam 2009](#)] and references therein.

- **ATLAS cone:** The ATLAS Cone is of the split/merge type. Different radius have been studied for the different physics analysis. This algorithm was used in old ATLAS studies and it relies upon a seed in order to initiate the first candidate cones. The seed is usually a calorimeter tower or cluster (introduced in Section 3.1.1), a parton or a particle with a p_T above some threshold. This has been shown to be an infrared and collinear unsafe procedure [[Seymour 1998](#)] and thus such cone algorithms cannot be used in NLO QCD calculations. Various attempts to improve the situation, by using for example the midpoints between all seeds as additional seeds, have culminated in the development of a seedless infra-red safe cone (SIScone) algorithm [[Salam 2007](#)], which is one of the algorithms evaluated in Section 3.2.1.
- **Seedless infra-red safe cone (SIScone):** The seedless infra-red safe cone algorithm, SIScone, is described in detail in Reference [[Salam 2007](#)]. Here a briefly summary of the main features is given. The algorithm identifies a list of all the possible stable protojets by finding all cones which contain a unique combination of the input objects. Stability in this context means that the cone centred on the summed four-momentum of the constituents contains all and only those constituents.

The protojets are identified by considering circles in $y - \phi$ space of radius R drawn through pairs of the input objects. Two such circles can be drawn for each pair, and for each circle there are four permutations of whether both, one or neither of the points is considered to be within the circle. Once all stable protojets have been identified, a split/merge procedure is applied to obtain the final list of jets. Several important subtleties are required in order to ensure infrared safety. These are all detailed in Reference [[Salam 2007](#)] and there it is also shown numerically that the algorithm is infrared safe to better one event in 10^{-9} .

- **Sequential recombination algorithms:** The algorithms most commonly used in lepton colliders, and also at the electron proton collider HERA, are based upon pairwise clustering of the initial constituents. In general, the algorithms define a distance measure between objects, and also some conditions upon which clustering should be terminated. The two algorithms considered here are all of the type in which for each

object i , the quantities, d_{ij} and d_{iB} are evaluated as follows:

$$d_{ij} = \min(p_{Ti}^{2p}, p_{Tj}^{2p}) \frac{\Delta R_{ij}^2}{R^2} \quad (2.10)$$

$$d_{iB} = p_{Ti}^{2p}, \quad (2.11)$$

where

$$\Delta R_{ij}^2 = (y_i - y_j)^2 + (\phi_i - \phi_j)^2$$

and y_i is the rapidity of object i . A list of all the d values is compiled. If the smallest entry is of the d_{ij} type, objects i and j are combined and the list is remade. If the smallest entry is of the d_{iB} type, this object is considered a complete “jet” and is removed from the list. In the sense defined by the algorithm, the d_{ij} is the distance between two objects, and d_{iB} is the distance between the object and the beam. The variable R is a parameter of the algorithm setting the resolution at which jets are resolved from each other as compared to the beam. For large values of R , the d_{ij} are smaller, and thus more merging takes place before jets are completed.

Historically, implementations of these algorithms have been prohibitively slow. This issue has been solved [Cacciari 2006] in the FastJet [Cacciari] implementations used here.

The variable p takes different values for each of the two algorithms discussed in the following sections.

- **k_\perp jet algorithm:** For the k_\perp algorithm, described in References [Catani 1993, Ellis 1993], $p = 1$ in Equation 2.11.

The symbol k_\perp indicates the transverse momentum of the lower p_T object relative to the direction of the higher p_T object of a pair (i, j) :

$$k_\perp \sim \min(p_{Ti}, p_{Tj}) \sqrt{(y_i - y_j)^2 + (\phi_i - \phi_j)^2} \quad (2.12)$$

By comparing the Equation 2.12 with the Equations 2.11, one can notice that the objects with low relative k_\perp are merged first. This means that within a jet, the final merge is the hardest, and this information can be exploited to interrogate the substructure of the jets, looking for scales associated with the decays of massive particles [Butterworth 2002, Brooijmans 2008, Butterworth 2007, ATLAS Collaboration 2009a, ATLAS Collaboration 2009b, ATLAS Collaboration 2009d]. Note that if the transverse momentum p_T of an object (relative to the beam direction) is lower than its k_\perp relative to anything else (divided by R), it will not be merged any further. Thus soft objects are either merged with nearby hard objects, or left alone with low p_T , effectively “merged” with the beam.

- **anti- k_t jet algorithm:** For the anti- k_\perp (anti- k_t) algorithm [Cacciari 2008], $p = -1$ in Eq. 2.11. This means that in the vicinity $\Delta R < R$ of a hard object, all softer objects will be merged with the harder object in order of their closeness

in ΔR . In the situation in which an hard object is surrounded by a uniform high density of soft objects, the catchment area of the jet will have, with some approximation, a circle shape, of radius R . Thus the jet boundary is unaffected by soft radiation. If two comparably hard objects are within $R < \Delta R < 2R$ of each other, the energy of the surrounding soft objects will be shared between them depending upon their relative k_\perp and distance. For hard objects within $\Delta R < R$ of each other, a single jet will be formed containing both hard objects and the soft objects within their vicinity. The ordering of the merging is not meaningful for this algorithm. However, the constituents may be reclustered using one of the other algorithms to recover subjet information [Schwartz].

A detailed study of the performance of the jet reconstruction with different jet definitions is reported in Section 3.2. This detailed study, performed by the ATLAS Collaboration in 2009, and aimed at the selection of a candidate jet definition to be used in the first period of data taking, pointed on the robustness of the anti- k_t jet algorithm in reconstructing jets in different event topology. As a result, the anti- k_t jet algorithm has been adopted for the measurement of the inclusive jet cross section reported here.

2.2.3 Beyond the fixed order predictions: the parton shower and non perturbative effects

The perturbative QCD calculations provide accurate predictions as long as the observables are infra-red and collinear safe (i.e. jets), but it does not describe the production of particles (i.e. pions or kaons) in the jets.

The divergences in the real emission of an extra partons in Formula 2.6 can be interpreted as the footprint of the high probability to emit gluons in the collinear and soft regions. With this idea, one can perform an approximated sum over all the perturbative orders to calculate the probability to emit collinear or soft gluons. Whereas the real emission of extra collinear or soft gluons have a "bare" infinity, in the approximated calculation, the emission probability of gluons is simply bounded to be between 0 and 1.

Several code were proposed and used to simulate this approximated emission of partons, described in References [Sjostrand 2006, Sjostrand 2008, Corcella 2001, Bahr 2008a, Lönnblad 1992, Hoeche 2009]. These codes recursively simulate the emission of multiple partons, producing a multi parton final state. This gives a parton shower event. The parton shower can be merged/matched with the LO or the NLO matrix elements to estimate the cross section for different processes.

In the case of the LO or the NLO pQCD calculations, the final state usually consists of few partons. For the parton shower events, the multiplicity of final state parton can be really high and the use of a jet algorithm really simplify the description of the final state, reducing the number of final state objects. At this level of simulation, the jets become complex QCD observables, and the choice of the jet definition starts to play an important role. Furthermore, the high parton multiplicity improve the description of the jet substructure.

Even if the production of the extra partons by the parton shower is a natural consequence of the QCD, the final goals of the measurements is to be sensitive to the processes

at high energy (i.e. a new colorless resonance decaying into two quarks), reducing the impact of the lower scale parton emission in the parton shower. Having this in mind, the selection of the jet definition should reduce the impact due to the parton shower and other effects which are marginally related with the high energy scattering.

2.2.3.1 Non-perturbative effects

To complete a realistic simulation of the proton proton collisions, the Monte Carlo codes need to address the two points:

- how the final state partons transform into the real final state particles measured by the detector (hadronization model);
- how the proton remnants, that are those partons that do not participate to the hard scattering, evolves (underling event model).

These two effects go beyond the possibility of the pure pQCD description, and different models have been developed - following observation of the dynamics of the strong interactions.

Hadronization models

The emissions of gluons in the parton showers are usually ordered in a sequence of decreasing scaled of energies, relative transverse momentum or angles.

At the typical scale of the hadron mass - 1 GeV - where the pQCD starts to be less appropriate, other models are needed to move from the partons to the list of final state hadrons. The most common models used to simulate the "hadronization" are the string model and the cluster model.

- String model: in this model, introduced in Reference [Andersson 1983], when a positive colored quark-antiquark pair moves apart, their self interaction collapses in a string, with a certain tension. The evolution of these strings, which can break up in smaller segments, determines the production of the hadrons.
- Cluster model: the motivation for the cluster model is the pre-confinement property in pQCD proved in References [Amati 1979, Bassetto 1980, Marchesini 1981]. At the end of the parton shower, the gluons are forcibly split into light quark-antiquark pairs, and the color singlet clusters spanned by all the quark-antiquark pairs have a universal distribution which can be used as starting point for "decays" of the clusters in hadrons.

Both the models need to be tuned to the measured data, in order to reproduce realistic results.

Underlying event models

The physics of the proton remnant is of special interest because it affects the reconstruction of the objects created in the hard scattering (such as the jets) in a non trivial way. Most of the models hypothesizes the presence of extra partonic interactions at low scale, assuming $2 \rightarrow 2$ partonic process, driven by the pQCD description (Section 2.2.2).

These extra interactions are usually characterized by three main parameters. The first one determines the geometrical distribution of the partons over the transverse area associated to the proton. The denser this distribution is, the easier the multiple partonic interaction happens.

The second important parameter is an energy scale ($p_T^{min} \sim 2 - 6$ GeV) which define the range in which the pQCD cross section for the $2 \rightarrow 2$ process should be replaced by a model driven cross section. This replacement is motivated by the divergence of the $2 \rightarrow 2$ pQCD cross section when the transfer momentum of the two outgoing partons goes to 0. This divergence can be interpreted as an higher probability of multiple interactions. Different models use different approaches to suppress this divergence.

The simulation of the extra parton interactions plays an important role in the inclusive jet production. In fact the hard scattered process and the softer ones are driven by the same physics. The only distinction between them is the "artificial" p_T ordering used to allow an optimization in simulating high- p_T jets. For this reason, the cross section used for the hard scattering in the jet production must be coherently replaced by the model used in the extra parton interaction. This is not crucial for high p_T jet (above 100 GeV), but it could give significant contributions at lower p_T , where an incoherency could generate a sort of double counting of the soft physics.

A third common aspect in most of the Monte Carlo codes is the way in which the extra partonic interactions are connected with the rest of the event. Since the partons produced in the multiple partonic interactions are colorful, they are color connected with the high scale process. Different models have different strategies to simulate this connection. In some cases the connection happens only in the rearrangement of the final state partons before the hadronization. In other cases, the evolution of the parton shower is affected by these multiple interactions.

The complexity of these models and the high flexibility to reproduce different scenario, require a fine tune of the parameters. The tuning tries to reproduce at best the measured distributions. This has been done in several experiments, and it is a crucial step to be able to reach high precision on the measurement of the hard scattered processes.

The ATLAS Collaboration used the first measured distribution to prepare different tunes for the Monte Carlo simulation. These tunes are divided into two classes. The first one is obtained in optimizing the Monte Carlo description of the minimum bias data (ATLAS MinBias Tunes, or AMBT). The second one used the measured distributions of the soft particles in events with high- p_T objects (ATLAS Underlying Event Tunes, or AUET).

In this thesis several tunes have been used to estimate the effect of the non-perturbative physics on the inclusive jet cross section. The list of tunes used in this measurement are listed in Table 2.1. They are used for two different propose. the first one is to estimate the non perturbative correction for the inclusive jet cross section, as introduced in the following Sections. The second one is to generate events used to simulate the detector response, as a tool to estimate the performances of the detector.

Table 2.1: Set of tunes used in the measurement of the inclusive jet cross section. A description of the tunes can be found in References [Skands 2009, Skands 2010, Buckley 2010b, ATLAS Collaboration 2011m, ATLAS Collaboration 2011b, Bahr 2008b, ATLAS Collaboration 2011b, ATLAS Collaboration 2010e, Corcella 2002, Butterworth 1996, Mangano 2003, Sjostrand 2006].

Generator	Tune	Use
PYTHIA 6.421	AMBT1 LO*	Baseline event generation for the detector simulation and non-pert. corrections
	Perugia 2010	Event generation for the detector simulation
HERWIG++ 2.4.2	ATLAS MC10	Event generation for the detector simulation
ALPGEN +HERWIG + JIMMY	ATLAS MC10	Event generation for the detector simulation
PYTHIA 6.425	AUET2B CTEQ6L1	Baseline for the non-per. corrections and tune for the Powheg predictions
	Perugia 2011 [PYTUNE=350]	Non-per. corrections and tune for the Powheg predictions
	AUET2 LO**	Non-pert. corrections
	AUET2B LO**	Non-per. corrections
	AMBT2B CTEQ6L1	Non-per. corrections
PYTHIA 8.150	Perugia 2010	Non-per. corrections
	4C	Non-per. corrections
HERWIG++ 2.5.1	UE7000-2	Non-per. corrections

2.2.4 Different strategies to get a predictions

There are different strategies to get theoretical predictions at hadron colliders. The first approach is to use a NLO (or NNLO if available) calculation, and correct it for the non-

perturbative effects. In this case, usually two different kind of programs are used. The first one calculates the fixed order pQCD prediction. The second one, usually a Monte Carlo, simulates the parton shower, the hadronization and the underlying event with some specific model. These simulations are used to extract a factor to correct the pQCD predictions for the non-perturbative effects. Since different models are available, different factors can be derived and used to estimate the stability of this correction (or in other words the uncertainty due to the different models).

A second strategy, developed in the last years, is to merge the NLO pQCD prediction to a parton shower Monte Carlo. In this way, the parton shower, the hadronization and the underlying event are still described by some model, but all the different aspects are handled by the same program in a coherent way.

For the inclusive jet cross section, both the approaches are available, and have been used in this study.

2.3 Inclusive jet cross section: Theoretical prediction

Jet cross sections can only be defined for specific jet algorithms. In this analysis jets are identified using the anti- k_t jet algorithm [Cacciari 2008, Cacciari 2006, Cacciari]. The anti- k_t jet algorithm is described in Section 2.2.2. The comparison between the experimental performances of the anti- k_t jet algorithm, the k_{\perp} jet algorithm, the SISCone jet algorithm and the ATLAS cone jet algorithm will be discussed in detail in Section 3.2. These comparisons resulted in the selection of the anti- k_t jet algorithm as the default jet algorithm to be used in the first period of data taking by the ATLAS Collaboration. A detailed description of the experimental performances of the anti- k_t jets for the 2010 data is reported in Section 4. From the theoretical point of view, the anti- k_t jet algorithm is an interesting algorithm because it is infra-red and collinear safe at all the order in the perturbative expansion. Two different values are used for the clustering parameter R (0.4 and 0.6), which can be seen intuitively as the radius of a cone jet in the plane (ϕ, y) of azimuthal angle and rapidity. The jet cross section measurements are corrected for all experimental effects, and so refer to the ideal “truth” final state of a proton-proton collision (see, for example [Buttar 2008]). Here “truth jets” are identified using the anti- k_t algorithm and are built from stable particles, i.e. those with a proper lifetime longer than 10 ps. This definition includes muons and neutrinos from hadron decays. By applying the jet definition to the cross section calculations, one can obtain the inclusive jet cross section.

The measurement is done in the following bins of absolute rapidity ($|y|$): [0.0-0.3], [0.3-0.8], [0.8-1.2], [1.2-2.1], [2.1-2.8], [2.8-3.6], [3.6-4.4]. They are selected to be regions with uniform technology, with only two special transition regions: [1.2-2.1] around the transition region from the central calorimetry to the end-cap calorimeter, and [2.8-3.6] in the transition between the end-cap calorimeter and the forward calorimeter. The binning in p_T is the result of several studies, on the trigger and on the detector performance. The low p_T regions are measured with several prescaled trigger chains. Each chain is completely efficient in a different range of p_T . In the region where two or more chains are completely efficient, only the less prescaled one is used. This strategy optimizes the statistical precision in each region, while it avoids the double counting of jets. These different regions have been used as binning for $p_T < 400$ GeV. In the high- p_T regions, the bins have been selected by studying of the p_T smearing of the detector, simulating the impact of the jet- p_T resolution on the expected spectra. The bin widths have been selected to avoid big bin migrations due to this smearing. The final binning is a good compromise which avoid big bin migrations, while optimizing the statistical precision due to the peculiar trigger strategy in the low- p_T region. Furthermore, the same p_T binning is used in all the different rapidity regions. This helps in studying the $|y|$ dependence of the cross-section. The edges of the selected bins are (in GeV): [20-30], [30-45], [45-60], [60-80], [80-110], [110-160], [160-210], [210-260], [260-310], [310-400], [400-500], [500-600], [600-800], [800-900], [900-1000], [1000-1500].

The measurement reported is the double differential inclusive jet cross section:

$$\frac{1}{\Delta p_T \Delta |y|} \int_{y \text{ bin}} d|y| \int_{p_T \text{ bin}} dp_T \frac{d^2 \sigma}{dp_T d|y|} \sim \frac{d^2 \sigma}{dp_T d|y|} \quad (2.13)$$

2.3.1 Fixed order pQCD

For the theoretical prediction, a fixed order NLO calculation has been used. This prediction has been corrected for the non-perturbative effects, and it has been used as baseline for the comparison of the measured inclusive jet cross section, and for the comparison with other theoretical predictions. The next section describes the peculiarities of a NLO calculation, and its uncertainties.

Leading order and next to leading order

The need of an accurate prediction requires the use of the calculation at the higher order available in the perturbative expansion. Even if in the last years, several fundamental steps towards the Next to Next to Leading Order predictions have been done, a Next to Leading Order (NLO) calculation has been used for the inclusive jet production . The prediction at NLO involves supplementing the LO result with the 3-particle tree-level matrix element ($|M_3^2|$), and the interference of a 2-particle tree-level and 2-particle 1-loop amplitude ($2\text{Re}(M_2 M_{2,1-\text{loop}}^*)$). The NLOJet++ 4.1.2 [Nagy 2003] program along with the CT10 [Lai 2010] NLO PDFs is used for all baseline NLO calculations.

The accuracy of the NLO prediction is mainly affected by the uncertainties on the PDFs, by the size of the contribution of the neglected higher orders in the perturbative calculation (evaluated by varying the renormalization and factorization scales), and by the uncertainty on the value of the strong coupling constant α_S . To allow for fast and flexible evaluation of PDF and scale uncertainties, an ad hoc software has been used (AP-PLGRID [Carli 2010]). It is interfaced with NLOJet++ in order to calculate the perturbative coefficients once, and store them in a lookup table. This allows to "re-use" the perturbative calculation with different PDFs or different α_S values.

Baseline NLO predictions for the inclusive jet spectrum, corrected for the non-perturbative effects, are shown in Figure 2.5 for the anti- k_t jets with $R = 0.6$, and for all the considered rapidity regions. A similar plot for the anti- k_t jets with $R = 0.4$ is shown in the Appendix.

Uncertainty due to the neglected higher terms

To estimate the uncertainty on the NLO prediction due to neglected higher-order terms, each observable was recalculated while varying the renormalisation scale by a factor of two with respect to the default choice, defined for the inclusive jet cross section to be the p_T of the hardest jet in the event in each specific rapidity region. Similarly, to estimate the sensitivity to the choice of scale where the PDF evolution is separated from the matrix element, the factorisation scale was separately varied by a factor of two. To avoid the appearance of large logarithms, the two scales are not simultaneously varied by a factor 2 in opposite directions. Thus the total set of renormalisation and factorisation scales used is:

$$\left(\frac{\mu_F}{p_T^{\max}}, \frac{\mu_R}{p_T^{\max}}\right) = (x_F, x_R) == \left(\frac{1}{2}, 1\right), \left(2, 1\right), \left(1, \frac{1}{2}\right), \left(1, 2\right), \left(\frac{1}{2}, \frac{1}{2}\right), \left(2, 2\right)$$

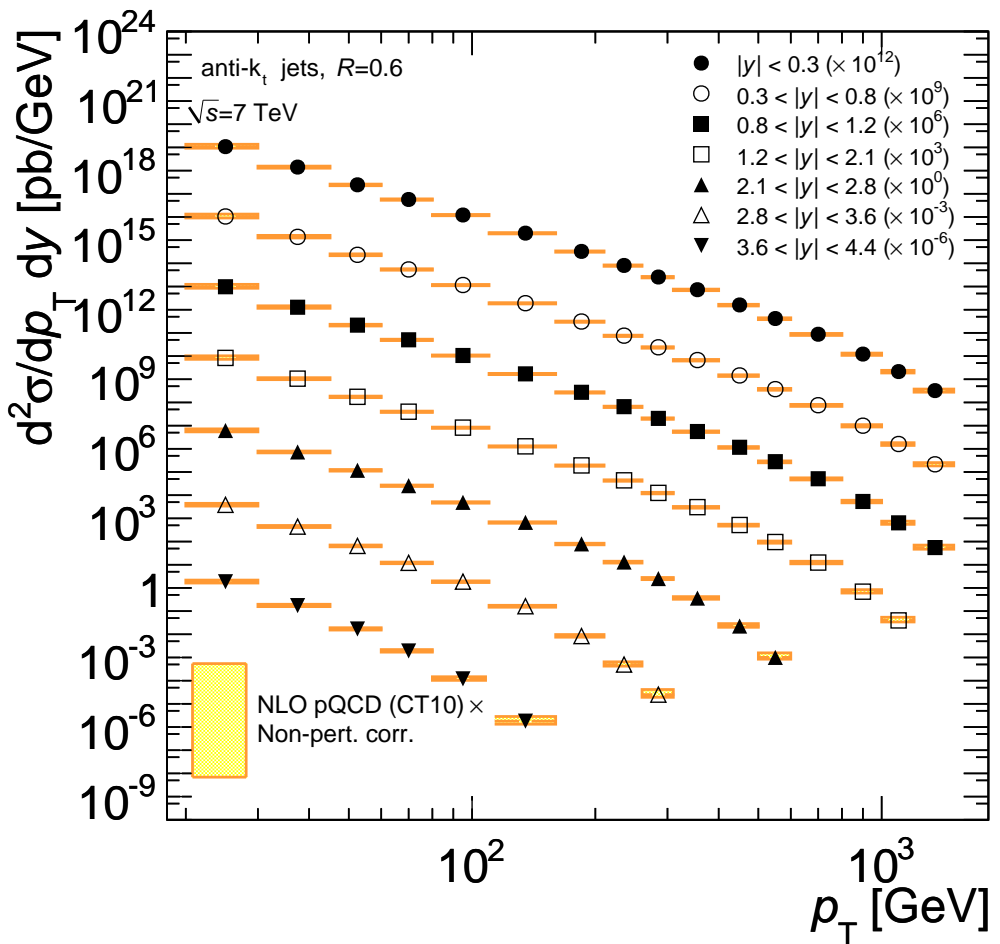


Figure 2.5: Prediction for the the inclusive jet cross section as a function of p_T at $\sqrt{s} = 7$ TeV for the anti- k_t jet algorithm with $R=0.6$. The theoretical prediction is derived by correcting with the non perturbative factors, the fixed order NLO calculation. To distinguish the cross section in the different rapidity regions, multiplicative factors have been used. The PDF used for the perturbative calculation are the CT10.

The envelope of the variation of the observables was taken as the systematic uncertainty due to scale choice. Another way to estimate the impact of the scale variation starts from the observation of the dependence of the cross section, in a certain bin of p_T and $|y|$ in the plane (x_F, x_R) (as described in Reference [Olness 2010]). Four representative $(p_T, |y|)$ regions (a central low- p_T region, and three different rapidity regions with $p_T \sim 100$ GeV) are shown in Figure 2.6. A more detailed selection of $(p_T, |y|)$ regions can be found in the Appendix. In this Figure, the values of the cross section have been normalized by the value in the point $(x_F, x_R) = (1, 1)$. The red lines show the variation of the scales adopted in this analysis. The cross section has a saddle point, which usually is not distant from (1,1) in the bins of the estimated inclusive jet cross section. An alternative choice for the baseline estimate of the cross section, instead of (1,1) is to use the value of the cross section on the saddle point. Given the fact that for all the bins in the measured spectra, the saddle points are close to (1,1), and that the scale variation used in this study is usually bigger than the distance to the saddle point, the baseline selection in this analysis has been derived with the usual choice selection $(x_F, x_R) = (1, 1)$.

Uncertainty due to the parton distribution functions

Different PDF sets have been used to estimate the inclusive jet cross section. They differ for the data used to extract the distributions, for the parametrization used to describe the PDF functions, and for the strategy adopted to perform the fit to the data. The families reported in this study are the CT10, the MSTW 2008 (NLO) [Martin 2009], the HERAPDF 1.5 [H1 and ZEUS Collaborations] and the NNPDF 2.1 [Ball 2010, Forte 2010]. All these families have special sets of PDFs which can be used to evaluate the uncertainty due to their determination.

Figure 2.7 shows the PDF sets for different partons for the CT10, and the comparison of the gluon PDF for the different families used in this analysis, normalized to the CT10 gluon distribution. The comparisons for the other partons can be found in the Appendix. CT10 seems to prefer an higher probability of having an initial gluon with large x .

The used PDF sets account for correlations by expressing the PDF parameters in terms of an orthogonal basis, where each eigenvector is associated with a positive and negative error. The total error on an observable is obtained by taking the RMS of the predictions from 100 replicas (NNPDF 2.1), or the asymmetric uncertainty given by the following formulas(all other approaches). This asymmetric uncertainty on a given observable for these PDFs is given by:

$$\Delta X^+ = \sqrt{\sum_{i=1}^{N_{\text{vect}}} [\max(X_i^+ - X_0, X_i^- - X_0, 0)]^2} \quad (2.14)$$

$$\Delta X^- = \sqrt{\sum_{i=1}^{N_{\text{vect}}} [\max(X_0 - X_i^+, X_0 - X_i^-, 0)]^2} \quad (2.15)$$

where X_0 and X_i^\pm are the observables calculated using the central prediction and \pm variations, respectively. This equation gives a 90% confidence estimate for MSTW 2008 and

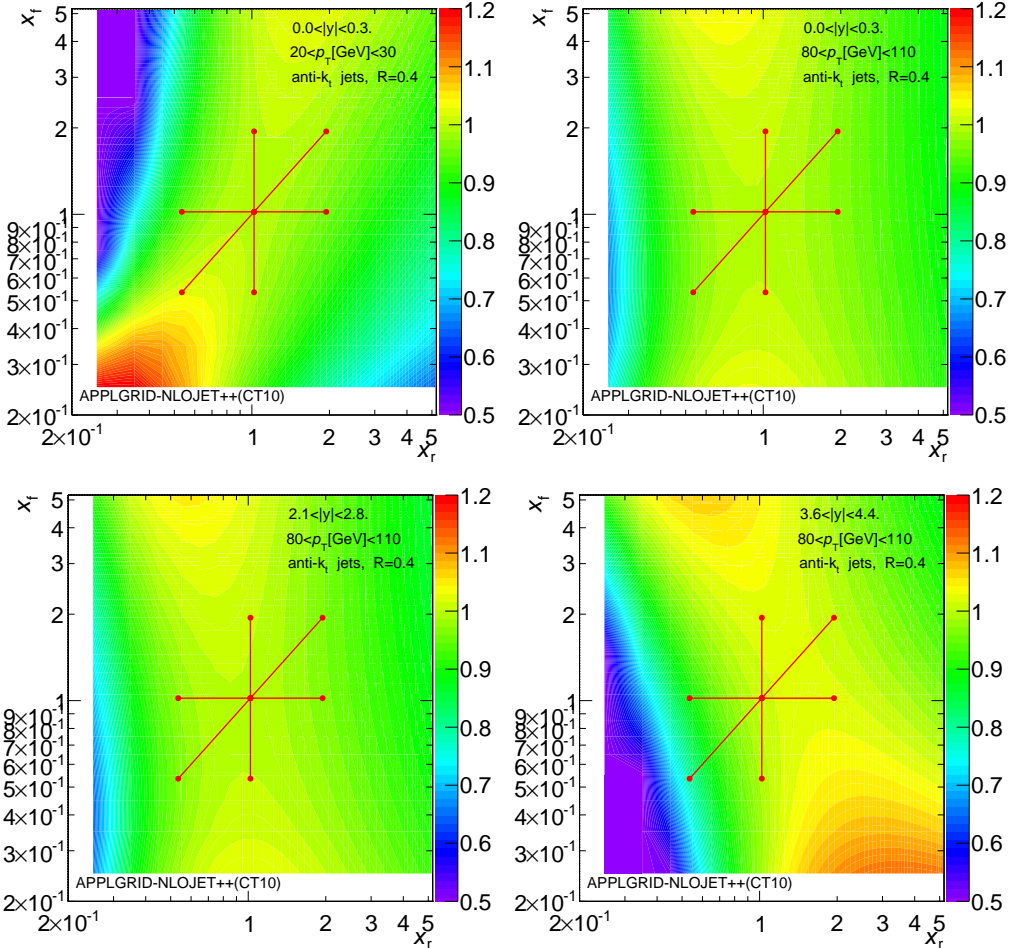


Figure 2.6: Scale dependence for the inclusive jet cross section for the anti- k_t jet algorithm with $R = 0.4$, for some representative bins in p_T and rapidity. The scale dependence, shown following the color scheme on the right, is normalized to the cross section in the point (1,1). The red lines show the scale variation adopted for the estimate of the uncertainty due to the neglected higher orders.

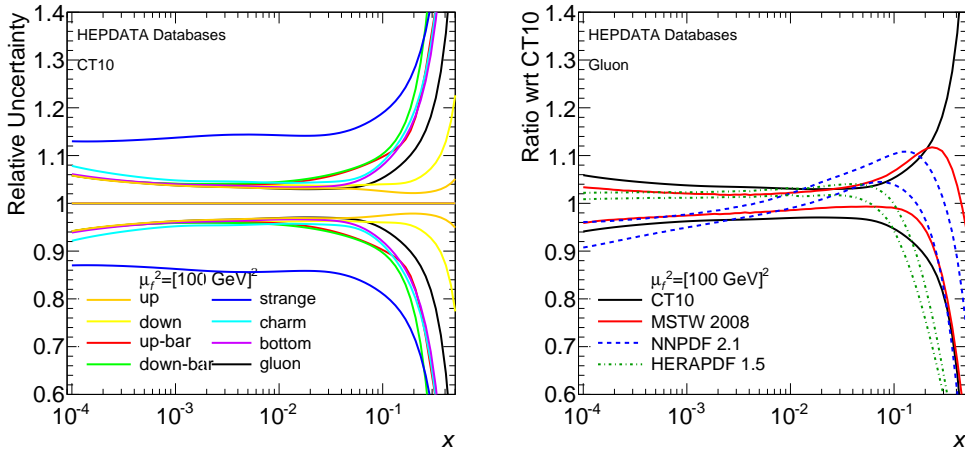


Figure 2.7: Left: Relative uncertainty on the parton distribution functions as a function of the fractional longitudinal momentum x for the CT10. Right: Comparison of gluon distribution functions as a function of the fractional longitudinal momentum x in different PDF families: CT10, MSTW 2008, HERAPDF 1.5, NNPDF 2.1. Values extracted from Reference [<http://durpdg.dur.ac.uk/>].

CT10 PDFs and 1σ uncertainties for HERAPDF 1.5. Therefore, the uncertainty estimates for MSTW 2008 and CT10 were scaled down by the factor $C_{90} \equiv 1.64485$ in order to get comparable values for all PDFs.

To evaluate the uncertainty on an observable calculated with the NNPDF 2.1 set, the formula

$$\Delta X = \sqrt{\frac{1}{N_{\text{rep}} - 1} \sum_{k=1}^{N_{\text{rep}}} [X_k - \langle X \rangle]^2},$$

was used, where N_{rep} is the number of replicas used in the calculation.

The PDF uncertainty on the inclusive jet cross section is of the order of $\sim 3\%$ at low p_T , but it increases with transverse momentum and becomes the dominant theoretical uncertainty for jet $p_T \gtrapprox 200 \text{ GeV}$ in the central rapidity region.

Uncertainty on the strong coupling constant

The value of the strong coupling constant should be used coherently to the PDF set adopted in the calculation. In fact, as it has been shown in Reference [Lai], the result of the PDF fit depends on the value of α_s . To properly take into account the effect of the strong coupling uncertainty, the cross section has been estimated using different PDF sets derived using positive and negative variations of α_s from its best estimate. The cross section uncertainty is then estimated as:

$$\Delta\sigma_{\alpha_s} = \frac{1}{2} \sqrt{(d\sigma(\alpha_s^+))^2 - (d\sigma(\alpha_s^-))^2}. \quad (2.16)$$

where the values for α_s^- , α_s^0 and α_s^+ are shown in Table 2.2.

Table 2.2: Values of the α_s strong running coupling constant for $\mu_r = M_Z$ used in fitting the different PDF sets.

PDF sets	α_s^-	α_s^0	α_s^+
CT10	0.116	0.118	0.120
MSTW 2008	0.116	0.120	0.123
HERAPDF 1.5	0.1156	0.1176	0.1196
NNPDF 2.1	0.117	0.119	0.121

These values all refer to the strong coupling constant α_s evaluated at the mass of the Z boson, $M_Z = 91.2$ GeV, and the PDF sets have been fitted with these values of α_s .

This uncertainty is $\sim 4 - 5\%$ and almost flat in jet p_T , but goes down to $2 - 3\%$ for low p_T jets.

Non-perturbative corrections

The fixed-order NLO calculations predict parton-level cross sections, which must be corrected for non-perturbative effects to be compared with data. This is done by using leading-logarithmic parton shower generators to evaluate the ratio of cross sections with and without hadronisation and underlying event, and multiplying bin-by-bin the parton-level cross sections by this ratio.

The correction is evaluated, bin-by-bin, by taking the ratio of the cross section at hadron level ($\sigma_{had=ON,ue=ON}$), divided by the cross section in which the hadronization and the underlying event are switched off ($\sigma_{had=OFF,ue=OFF}$):

$$c = \frac{\sigma_{had=ON,ue=ON}}{\sigma_{had=OFF,ue=OFF}} \quad (2.17)$$

The baseline correction is evaluated using the AUET2B CTEQ6L1 tune. The uncertainty on this correction is estimated as the maximum spread of the correction factors obtained from PYTHIA 6.425 [Sjostrand 2006] using the AMBT2B CTEQ6L1, AUET2 LO**, AUET2B LO**, AMBT1, Perugia 2010, Perugia 2011 (PYTUNE=350) tunes and PYTHIA 8.150 [Sjostrand 2008] tune 4C as well as those obtained from the HERWIG++ 2.5.1 [Bahr 2008b] tune UE7000-2.

All the distribution for the truth-jets at particle and parton-level have been obtained from these generators using the RIVET package [Buckley 2010a].

As expected, the corrections depend strongly on the jet size, so separate sets of corrections and uncertainties have been developed for jets with radius 0.4 and 0.6. The correction factors and their uncertainties depend on the interplay of the hadronization and the underlying event for the different jet sizes, and they have a significant influence at low p_T .

An example of the correction factors for the inclusive jet spectrum is shown in Figure 2.8. The errors are the envelope of the correction factors derived using the alternate

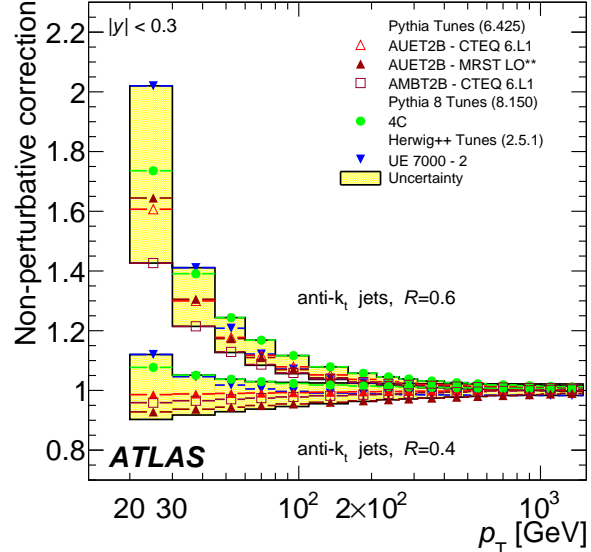


Figure 2.8: Non-perturbative corrections, evaluated with different Monte Carlo generators and tunes for the inclusive jet cross section of anti- k_t jets with $R = 0.6$ for the central rapidity region $|y| < 0.3$.

tunes listed. For $R = 0.4$, the non-perturbative correction factor is dominated by hadronization and is approximately 0.95 at jet $p_T = 20$ GeV, increasing closer to unity at higher p_T . For $R = 0.6$, the correction factor is dominated by the underlying event and is approximately 1.5 at jet $p_T = 20$ GeV, decreasing to between 1.0 and 1.1 for jets above $p_T = 100$ GeV. The complete list of plots of the correction factors can be found in the Appendix.

Comparisons of the correction factors for $R = 0.4$ and $R = 0.6$ jets reveal the different dominant non-perturbative effects for the two jet sizes. The correction for the smaller jet size is dominated by the effect of hadronization spreading energy outside the jet area. The correction for the larger jet size is dominated by underlying event adding inside of the jet area. Thus comparisons of the measurements with two jet radii at low p_T will provide additional information on the correct modeling of non-perturbative effects for jet production at $\sqrt{s} = 7$ TeV.

2.3.2 Total theoretical uncertainties for the fixed order predictions

The overall uncertainty for the fixed order prediction is calculated as the quadratic sum of all the components discussed so far: neglected higher orders, PDFs, α_s and non-perturbative effects.

An example of the total uncertainty, split in the different components, is shown in Figures 2.9. A complete list of figures for the total theoretical uncertainty in the different rapidity regions, for the two values of R can be found in the Appendix.

At low- p_T , the uncertainty for the non-perturbative effects is higher. This is suggesting that a good measurement of the inclusive jet cross section in this region could be used to improve the understanding of the interplay between the perturbative QCD, and the non-perturbative effects.

At higher- p_T , the PDF uncertainty become dominant. A precise measurement in this

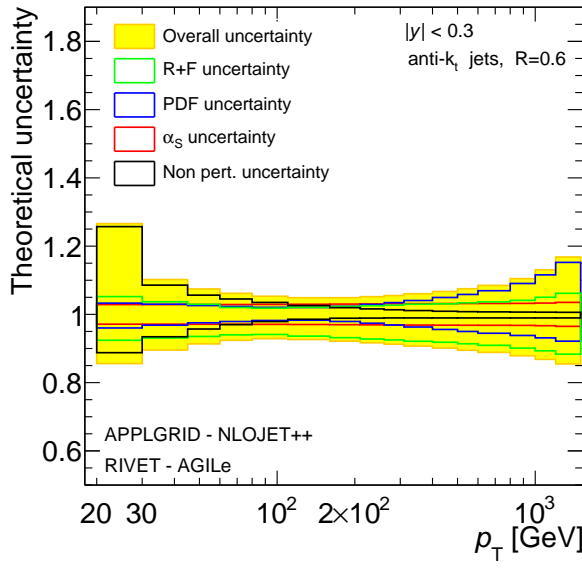


Figure 2.9: Total uncertainty on the fixed order theoretical prediction, corrected with the non-perturbative factors, for the central region of rapidity ($|y|<0.3$) for the inclusive jet cross section of anti- k_t jets with $R=0.6$. The different sub-components are shown in the figure.

region can give information on the parton structure, or eventually, on the presence of new physics.

2.3.3 NLO Matrix Element + Parton Shower

Several methods to construct NLO event generators are available [Frixione 2002] for a considerable number of hadron collider processes [Bahr 2008b, Frixione 2010, Hoche 2011]. The use of an event generator with NLO matrix elements (ME), including the simulation of the parton shower, the hadronisation, and the underlying event, creates a more coherent theoretical prediction and overcomes the need for separate non-perturbative corrections.

A NLO parton shower Monte Carlo prediction for inclusive jet and dijet production has only recently become available through the Powheg formalism [Alioli 2011a]. Powheg, which uses the Powheg Box package [Nason 2004, Frixione 2007, Alioli 2010], and it is interfaced to both PYTHIA and HERWIG [Corcella 2002]+JIMMY [Butterworth 1996]. to simulate the parton shower, the hadronization and the underlying event.

The AUET2B for PYTHIA¹ and the AUET2 for HERWIG +JIMMY have been derived from the standalone version of these event generators, with no optimisation for the Powheg predictions. The showering portion of Powheg events uses the PDFs from PYTHIA or HERWIG as part of the specific tune chosen.

In addition to the ATLAS underlying event tunes, the PYTHIA Perugia 2011 (PYTUNE=350) tune have used for the theoretical prediction.

In the Powheg algorithm, each event is built by first producing a QCD 2→2 partonic scattering. The renormalization and factorization scales are set to be equal to the transverse momentum of the outgoing partons (p_T^{Born}), before proceeding to generate the hardest par-

¹To limit the scale of the multiple partonic interactions (MPI) to the hardness of the primary process, the parameter `mstp(86)` in PYTHIA is set to 1.

tonic emission in the event². The CT10 PDF is used in this step of the simulation. Once the hardest partonic emission is simulated, the events can be evolved to the hadron level using parton-shower event generators.

One important parameter in the simulation of the partonic events is the cut on the minimum $p_T^{Born}:\text{bornktmin}$. If the cut is approximately at few GeV, the partonic cross section becomes larger than the total proton-proton cross section (due to the divergence at low- p_T , as discussed in Section 2.2.3.1). This unphysical cross section should only affect the very low p_T bins in the inclusive jet cross section, but the simulation of multiple partonic interactions for the underlying event could produce a migration to higher p_T . Preliminary studies, with $\text{bornktmin}=5$ GeV and $\text{bornktmin}=10$ GeV shown some differences in the inclusive cross section in the p_T -bin 60-80 GeV and higher, which should be investigated.

For this analysis, the cut $\text{bornktmin}=5$ GeV has been used for the Powheg theoretical predictions. The preliminary predictions used in this study do not show the detailed analysis of the uncertainties done for the fixed order predictions, but only a comparison of different Monte Carlo generators and tunes.

²The folding parameters used are 5-10-2. A number of different weighting parameters are used to allow coverage of the complete phase space investigated: 25 GeV, 250 GeV and 400 GeV. The minimum Born p_T is 5 GeV. For all the samples the leading jet transverse momentum is required to be no more than seven times greater than the leading parton's momentum. Furthermore, the HERWIG +JIMMY showered samples requires that the p_T of the additional MPI scatters are less than the hard scatter generated by Powheg. A similar effect is achieved with PYTHIA samples by setting `mstp(86)=1`. See Reference [[Alioli 2011b](#), [Nason 2007](#)] for a detailed explanation.

CHAPTER 3

Measuring jets: Reconstruction and Calibration

Contents

3.1	Jet reconstruction	53
3.1.1	Jet inputs	54
3.1.2	Jet calibration procedure: EM+JES	54
3.2	Jet algorithms: back to definitions	60
3.2.1	Reconstruction efficiency and purity	60
3.2.2	Picking up all the high energy objects: the dark clusters	63

The electronic signals measured by the different sub-detectors introduced in Section 1.2 are used to obtain quantitative information on the physics objects, like leptons, photons or jets. The procedure to extract such information is named reconstruction of the physics objects. Several jet reconstruction procedures have been developed in the last years by the ATLAS Collaboration. This Chapter gives an overview of the jet reconstruction procedure used for the inclusive jet cross section measurement. In the second part of this Chapter, particular emphasis will be given to the studies on the experimental performances of different jet definitions, introduced in Section 2.2.2.1. These studies contributed to the choice of the anti- k_t jet algorithm as the default jet algorithm used in the first ATLAS measurements.

3.1 Jet reconstruction

The performance of identification and reconstruction of a particular physics object is defined considering a reference truth object. In the case of electron or muons, the definition of the reference truth object is quite straightforward. In the case of jets, this definition is not so clear and unique. Because of the multiple collimated particles which belong to a jet, the jets have an intrinsic complexity, and they are not elementary objects. The strategy adopted by the ATLAS Collaboration is to define truth-jets. As anticipated in Section 2.3, the truth jets are identified using a jet definition and are built from stable particles, i.e. those with a proper lifetime longer than 10 ps. The fundamental properties of a jet depend on how the elementary particles are merged in jets, and on how the kinematic properties of these elementary particles are used to determine the jet kinematic. Different jet definitions give different jets. The truth jets used for the standard ATLAS jet reconstruction are identified

with the anti- k_t jet algorithm. These truth jets are used to study, in the Monte Carlo simulations, the performances of the reconstructed calorimeter jets (or just reconstructed jets). In these studies, the goal of the jet reconstruction procedure is to combine the calorimetric signals to get a "view" of the events as similar as possible to the one given from the truth jets. For this reason, the jet algorithm used in the reconstructed jets is coherent with the one for the truth jets: the anti- k_t jet algorithm.

3.1.1 Jet inputs

The calorimetric system has an high granularity of cells. To reduce the impact of the noise induced by the high multiplicity of cells, the ATLAS Collaboration developed a procedure which groups cells in clusters. A sketch of a cluster is shown in Figure 3.1. The cells are associated following a geometrical closeness criteria in the 3D space, and the clusters extend to the different radial layers of the calorimeter system.

These "topological" cell clusters are basically an attempt to reconstruct three-dimensional "energy blobs" representing the showers developing for each particle entering the calorimeter. The clustering starts with seed cells (SEED in Figure 3.1) with a signal-to-noise ratio, or signal significance $G = E_{\text{cell}}/\sigma_{\text{noise}}$, cell , above a certain threshold S , i.e. $|G| > S = 4$. All directly neighboring cells of these seed cells, in all three dimensions, are collected into the cluster. Neighbors of neighbors are considered for those added cells which have G above a certain secondary threshold N ($|G| > N = 2$, NEIGHBOR in Figure 3.1). Finally, a ring of guard cells (CELL in Figure 3.1) with signal significances above a basic threshold $|G| > P = 0$ is added to the cluster. After the initial clusters are formed, they are analyzed for local signal maximums by a splitting algorithm, and split between those maximums if any are found.

The cluster variables which are relevant for the jet definition are the direction with respect to the interaction point, and the sum of the energy in its cells. From these variable, a 0 mass four-vector is associated to each single cluster, and the list of these four-vectors is used as input to the jet definition which merges the clusters in jets.

Once the jet algorithm has performed the association of the inputs to the final jets, the recombination scheme defines how to determine the energy and momentum of the jets. Energy and momenta of the clusters are added into the four-momentum of the final jet. As anticipated in Section 2.2.2, the four-vector recombination scheme is used :

$$p^k = \sum_i p^i$$

The result of the jet clustering, is a list of jets, at the so called electro-magnetic (EM) scale. A calibration procedure is used to restore the p_T of the jets.

3.1.2 Jet calibration procedure: EM+JES

The EM scale is the baseline jet energy scale measured by the calorimeters. The EM energy scale is established using test-beam measurements for electrons and muons in the electromagnetic and hadronic calorimeters (a detailed description can be found in References [ATLAS Collaboration 2010f, Collaboration 2010, Adragna 2009, Cojocaru 2004,

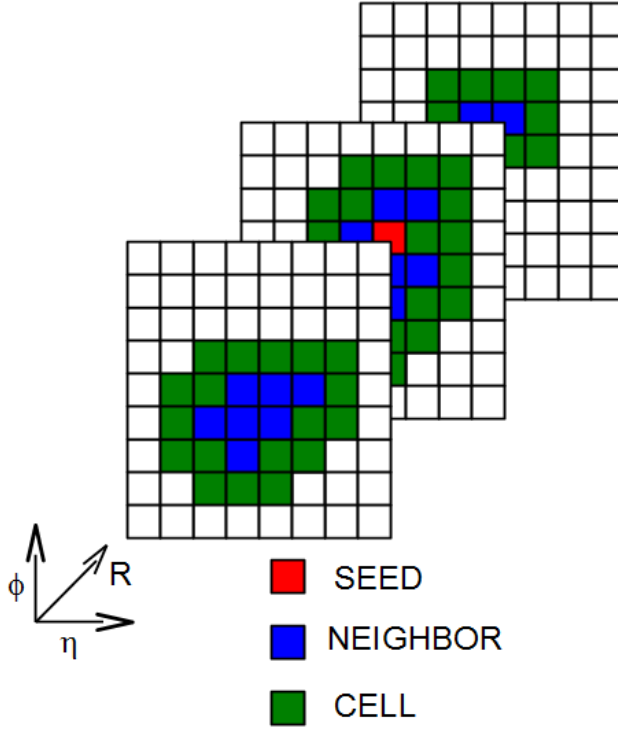


Figure 3.1: Sketch of the cluster formation in three subsequent radial layers of the ATLAS calorimetric system.

[Pinfold 2008]). This energy scale accounts correctly for the energy of photons (γ) and electrons (e^\pm), but it does not correctly estimate the energy of pions (π) and it does not correct for instrumental (detector) effects. Due to non-compensation, the ATLAS calorimeter system has a lower response to hadron showers than to electromagnetic showers. The jet calibration corrects for this difference, and for the other instrumental effects, such as the energy deposits in non instrumented regions (also known as "dead material"), or the effect of the bending of the magnetic field. As a result, $p_T^{\text{truth}} > p_T^{\text{EM}}$ with large nonlinearities and non-uniformities. An effect of about $R = p_T^{\text{EM}}/p_T^{\text{truth}} \sim 70\%$ is expected for p_T^{truth} of 100 GeV.

The jet calibration procedure is divided into three steps. In the first one it corrects for the energy deposited by particles produced in the multiple proton-proton collisions during the same bunch crossing (pile-up). The second step corrects the p_T of the jet for the shift in the position of the primary vertex. The third one applies a correction to the p_T^{EM} to recover the p_T^{truth} scale, for the calorimeter non compensation, energy losses in inactive regions and out-of-cone showering effects. In the next lines, this calibration scheme, adopted by the ATLAS experiment is described:

Pile-up correction: The energy scale of jets at the electromagnetic scale can include energy that does not come from the hard scattering process, and it is instead due to multiple proton-proton collisions within the same bunch crossing (pile-up). An average offset correction to subtract this additional energy is derived from minimum bias data and applied at the electromagnetic scale as the first step of the calibration scheme. The correction is derived from minimum bias data and is a function

of the number of reconstructed primary vertexes N_{PV} and jet η . It takes into account the average additional energy per jet. The correction is derived for the two jet sizes $R=0.6/0.4$. Further details on the pile-up offset correction can be found in Reference [ATLAS Collaboration 2011e].

Origin correction: The jet reconstruction uses $(x, y, z) = (0, 0, 0)$ (the center of the detector and origin of the ATLAS coordinate system) as reference to calculate the direction and p_T of the input jet constituents. If the primary vertex is shifted with respect to the detector center, the origin of the jet differs from the one assumed by the reconstruction, and, as a consequence, the jet p_T is biased. The jet origin correction is the second step of the calibration chain. The direction of each cluster of cells forming the jet is corrected to point back to the primary vertex with the highest $\sum p_T^2$ track of the event. The kinematics of each cluster is recalculated using the vector from the primary vertex to the cluster centroid as its direction. The raw jet four momentum is finally redefined as the four-vector sum of the clusters four-vectors.

Final jet energy scale: The final step of the jet calibration is the "EM+JES" calibration, which corrects for calorimeter non-compensation, energy losses in inactive regions, out-of-cone showering effects and inefficiencies in the calorimeter clustering and jet reconstruction. The correction factors depend on the jet energy and direction, due to the changing calorimeter technology and to the varying amounts of dead material in front of the calorimeters.

The EM+JES calibration is derived from simulated events. To derive the correction factors, isolated¹ calorimeter reconstructed jets are associated to truth jets requiring a and angular distance between the two jets, $\Delta R < 0.3$. An average correction, function of the jet p_T and η , is than obtained to restore the calorimeter jet energy to that one of the corresponding truth jet. Figure 3.2 shows the corrections derived for the anti- k_t jet algorithm with $R=0.6$ as a function of p_T of the jet, in different pseudo-rapidity regions, and the simulated jet energy response at the *EM* scale as a function of pseudo-rapidity η for different jet energies E .

Following the energy correction, a small η -dependent correction is applied to remove a bias in the reconstructed η of jets that occurs when jets fall in poorly instrumented regions of the calorimeter (especially the transition region between the hadronic endcap and forward calorimeter).

The η -correction is parameterized vs jet E and η_{det} , and is very small ($\Delta\eta < 0.01$) for most regions of the calorimeter but larger in the crack regions (up to $\Delta\eta = 0.07$ for low p_T jets in the HEC-FCal transition region).

Figure 3.3 shows the average response of the calibrated jets in energy and in p_T and for various region of η . The energy response is defined as the ratio $E^{\text{reco}}/E^{\text{truth}}$, and the p_T response as $p_T^{\text{reco}}/p_T^{\text{truth}}$. It can be noticed from this Figure, that the calibration for $p_T < 40$

¹An isolated jet is defined as a jet that has no other jets within $\Delta R = 2.5R$, where R is the distance parameter of the jet algorithm.

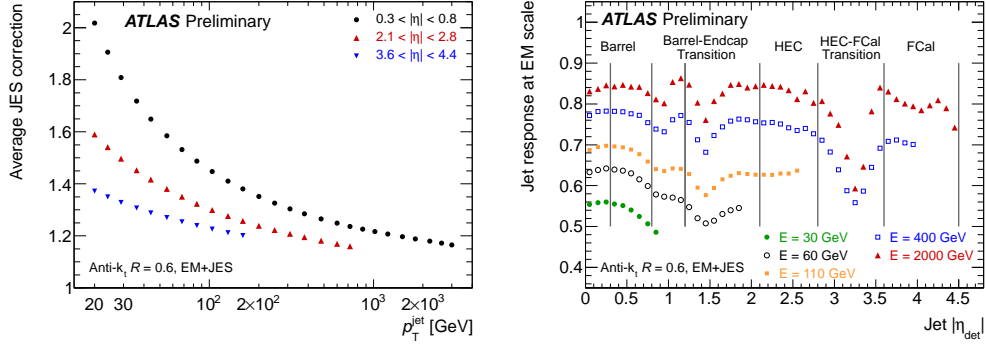


Figure 3.2: (left) Average jet energy scale correction for anti- k_t jets with $R=0.6$ as a function of calibrated jet transverse momentum for three representative $|\eta|$ -intervals. (right) Simulated jet energy response at the electromagnetic scale as a function of the detector pseudo-rapidity η_{det} for several EM+JES calibrated jet energies E . These Figures are taken from Reference [ATLAS Collaboration 2011h].

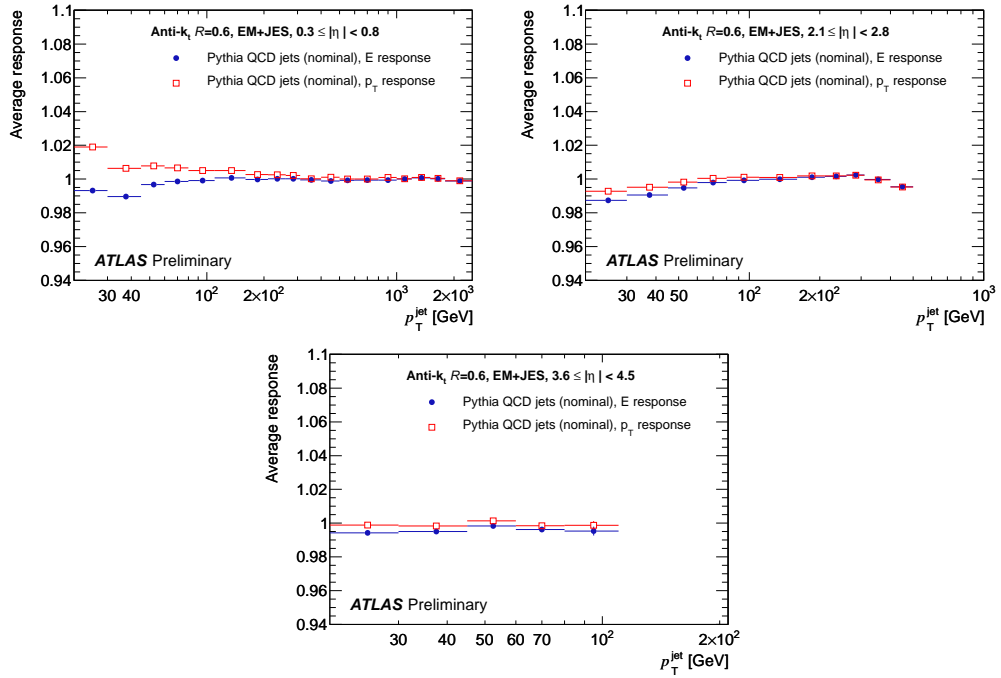


Figure 3.3: Average response of the reconstructed anti- k_t jets with $R=0.6$ in different regions of rapidity. These Figures are taken from Reference [ATLAS Collaboration 2011h].

GeV has a small bias of the order of 2%, which is incorporated in the source of systematic errors of the inclusive jet cross section measurement.

3.1.2.1 Alternative calibrations

Alternative strategies to calibrate jets have been developed by the ATLAS Collaboration. The main difference with respect to the calibration described above, is the attempt to use the complete shower shape information. The goal is to restore the linearity while improving the energy resolution. Two calibration concepts have been implemented for ATLAS. Both the cell energy density calibration (Global Cell Weighting Calibration) and the local topocluster calibration (Local Hadron Calibration) are based on the same idea: in the ATLAS calorimeters the radiation length X_0 is much smaller than the hadronic interaction length λ_I , so electromagnetic showers are shorter, narrower, and have higher energy density than hadronic ones. For the Global Cell Weighting Calibration the weights depend on the cell energy density and are tuned by comparing truth jets and reconstructed jets. For the Local Hadron Calibration multiple variables at cell and cluster level are considered in a modular approach, treating independently the various effects.

Global Cell Weighting: The Global Cell Weighting Calibration depends only on the energy density in the calorimeter cells that belong to the reconstructed jet. Electromagnetic-like cascades generate more concentrated showers than hadronic-like cascades with the same energy. In the first step, the Global Cell Weighting calibration applies a weight which depends on the cells energy density (Reference [[Salvachua 2009](#)]) to the energy in each cell. In a second step, a jet energy scale correction is applied. This correction improves the linearity of the response, see Reference [[ATLAS Collaboration 2009b](#)] for more details.

Local Hadron Calibration: The Local Hadron Calibration method applies classification and calibration steps to clusters which are then used as input to jets. The clusters correspond roughly speaking to individual particles although in denser jet environments several particles could contribute to a single cluster. The effects of non-compensation, missing energy due to noise thresholds in the clustering, and energy deposits lost outside the calorimeters are dealt with in independent steps. The classification and calibration constants, derived from single pion simulations, utilize cluster shape variables as well as the cell energy density and the cluster energy in their parameterizations. A final jet-level correction on top of the local hadron calibration is used to correct for global effects. These include particles never producing a cluster in the calorimeter either due to the noise thresholds or due to absorption in upstream material and those bent outside the jet acceptance area by the magnetic field.

These calibration procedures improve the jet energy resolution, as shown in Figure 3.4. This Figure shows the jet energy resolution measured with the first data in 2010. The relative resolution in p_T ($\sigma(p_T)/p_T$) is shown as a function of p_T . The measurement is obtained with the method described in Section 4.3.2. The Figure compares the resolutions of the standard jet calibration (EM+JES) with some of the alternative calibrations, such as

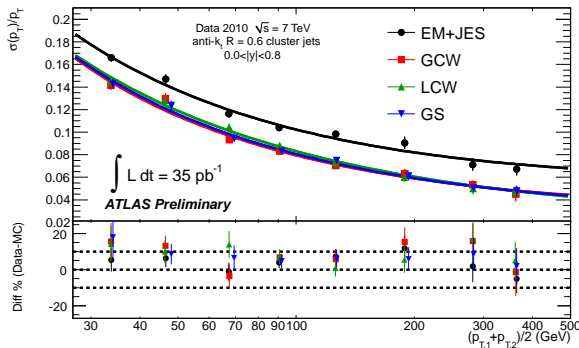


Figure 3.4: Comparison of the jet energy resolution for the different calibration procedures for the anti- k_t jets with $R=0.6$. The resolutions are measured with the di-jet method, introduced in Section 4.3.2. The measured resolutions are compared to the resolutions obtained with the same method on simulated data. The Figure is taken from Reference [ATLAS Collaboration 2011d].

the Local Hadron Calibration (LHC) and the Global Cell Weighting (CGW). In Figure 3.4 an additional calibration termed GS is also shown but it is not discussed here.

The alternative calibrations show a better resolution. For the 2010 data, the calibration EM+JES, described in the previous section, has been chosen because it allows a direct evaluation of the systematic uncertainty and is therefore suitable for first physics analyses.

3.2 Jet algorithms: back to definitions

The nature of a jet depends on the definition adopted to associate the elementary objects and to calculate the final kinematic properties. As reported above, a jet is not a fundamental particle, but a complex QCD observable, and different definition are sensitive to different aspects. The definition to be used in a measurement must follow the needs of that specific measurement. This means that an ultimate jet algorithm does not exist. On the other hand, for the first physics analyses in an experiment it is preferred to find a unique definition that can accommodate the needs of different scenario. Several studies have been done by the ATLAS Collaboration to select a good candidate. Important aspects are the efficiency and the purity in reconstructing jets in different topologies and for different jet multiplicity, the performance of the jet calibration and the capability of the jet algorithm to collect all the high energy elementary objects in the event. On top of these requirements, others experimental needs were checked, as the CPU-time needed to perform the merging of the objects (important for the offline event reconstruction and for the jet reconstruction in the High Level Trigger). In this selection the theoretical requirements play a very important role. The use of an infra-red unsafe or collinear unsafe jet algorithm in a measurement prevents from having precise calculation with the state-of-art theory, and to extract the important physics information from the measurement. In this optic, it is really fundamental the choice of an infra-red safe jet algorithm for the measurement at the LHC.

In this section, the description will focus on two different aspects: the efficiency/purity in reconstructing jets and the capability of the jet algorithm to pick-up all the high p_T constituents. These aspects are deeply related to the capability of the jet algorithm to consistently reproduce the same picture at truth level and at the reconstructed level. The results shown in this section were an important part of the studies done by the ATLAS Collaboration in 2009, aimed at the definition of the default jet algorithm. The Monte Carlo samples were simulated for proton collisions at $\sqrt{s} = 10$ TeV, the jet have been calibrated with the Global Cell Weighting Calibration. They have been generated with a PYTHIA di-jet sample interfaced to the 2009 ATLAS detector simulation, based on GEANT4. Even if the generated samples are not updated, and the calibration scheme is different from the one used in the measurement of the inclusive jet cross section, the general results of these studies marginally depend on these details.

3.2.1 Reconstruction efficiency and purity

The jet algorithm under study are the ATLAS Cone (with cone radius $R = 0.4$, and split and merge parameter equal to 0.5), the SISCone (with cone radius $R = 0.4$, and split and merge parameter equal to 0.75), the k_\perp (with parameter D equal to 0.4) and the anti- k_t (with parameter D or R equal to 0.4), introduced in Section 2.2.2. The ATLAS cone is disfavored from the theoretical point of view because it is infra-red unsafe [Seymour 1998].

The first figure-of-merit under investigations is the correspondence of the reconstructed jet view with the truth jet view of the event. The correspondence between the two levels demonstrate that, as it is desirable, the jet algorithm is insensitive to the type of input object. This aspect can be investigated studying the reconstruction efficiency and purity.

The definition of these two quantities depends on the matching truth jets - reconstructed jets. A truth jet and a reconstructed jet are matched if their distance ΔR is less than 0.3. The efficiency and the purity are defined as:

$$\text{efficiency} = \frac{\# \text{ matched truth jets with reconstructed jets}}{\# \text{ truth jets}} \quad (3.1)$$

$$\text{purity} = \frac{\# \text{ matched reconstructed jets with truth jets}}{\# \text{ reconstructed jets}} \quad (3.2)$$

The efficiency and the purity are studied in an inclusive sample of simulated di-jet events. These events are divided in different sub-samples, according to the hard scale of the simulated event. This artificial division gives some increased sensibility to the correspondance of the jet reconstruction for p_T close to the hard scale of the event. Of particular interest is the splitting and merging of the second and third jets ordered in p_T .

The efficiency (purity) as a function of the p_T of the truth jet (reconstructed jet) is shown in Fig. 3.5.a (3.5.b) for various jet algorithms. The error bars represent the statistical uncertainties. The main differences are in the low p_T region ($p_T < 100$ GeV). In this range, the best efficiency and purity are obtained using the anti- k_t jet algorithm, and the ATLAS Cone jet algorithm shows the worst behavior.

This is a first indication that the anti- k_t jet algorithm is stable (even at low- p_T) under the presence of low- p_T objects, such as underlying event particles or calorimeter noise fluctuation.

Different hard scales: incoherences for the close-by jets

The jet reconstruction efficiency and purity are studied in more detail for events with at least one of the hard scattered partons having a \hat{p}_T in the interval [560, 1120] GeV. The results for the efficiency and purity are shown in Figs. 3.5.c and 3.5.d, respectively. The efficiency and the purity exhibit a drop for jet transverse momenta between 100 GeV and 500 GeV. This last value is very close to the lower value of the \hat{p}_T of the hard scattered partons used to select the events ($\hat{p}_T^{\text{low}} = 560$ GeV). The drop is more prominent for the ATLAS Cone and for the SISCone jet algorithms, and the maximum effect is around $p_T \sim 300$ GeV ($\sim \hat{p}_T^{\text{low}}/2$). Similar efficiency and purity losses are observed in other intervals of \hat{p}_T . The losses are observed in the range $p_T \leq \hat{p}_T^{\text{low}}$, and are maximal for $p_T \sim \hat{p}_T^{\text{low}}/2$. This artifact, introduced by the event selection, can be used as a starting point for deeper investigations on the stabilities in the efficiency and purity for the different jet algorithms.

An explanation for the drop in efficiency and purity, which is not shown in Figures 3.5.a and 3.5.b, can be due to the fact that the merging or splitting of close-by jets at particle level and at reconstructed level behave differently. Naively, if the procedure to split two close-by-jets is sensitive to the low p_T objects, one truth jet could be split in two close-by reconstructed jets and vice versa. In the first case (one truth jet versus two close-by reconstructed jets), one of the reconstructed jets will fail the association with the truth jet, resulting in a drop of the purity at $p_T^{\text{reco}} \sim p_T^{\text{truth}}/2$ (because the two reconstructed jets are sharing the energy of the truth jet). In the second case, (one reconstructed jet versus two close-by truth jets), only one of the two truth jets will be associated with the reconstructed

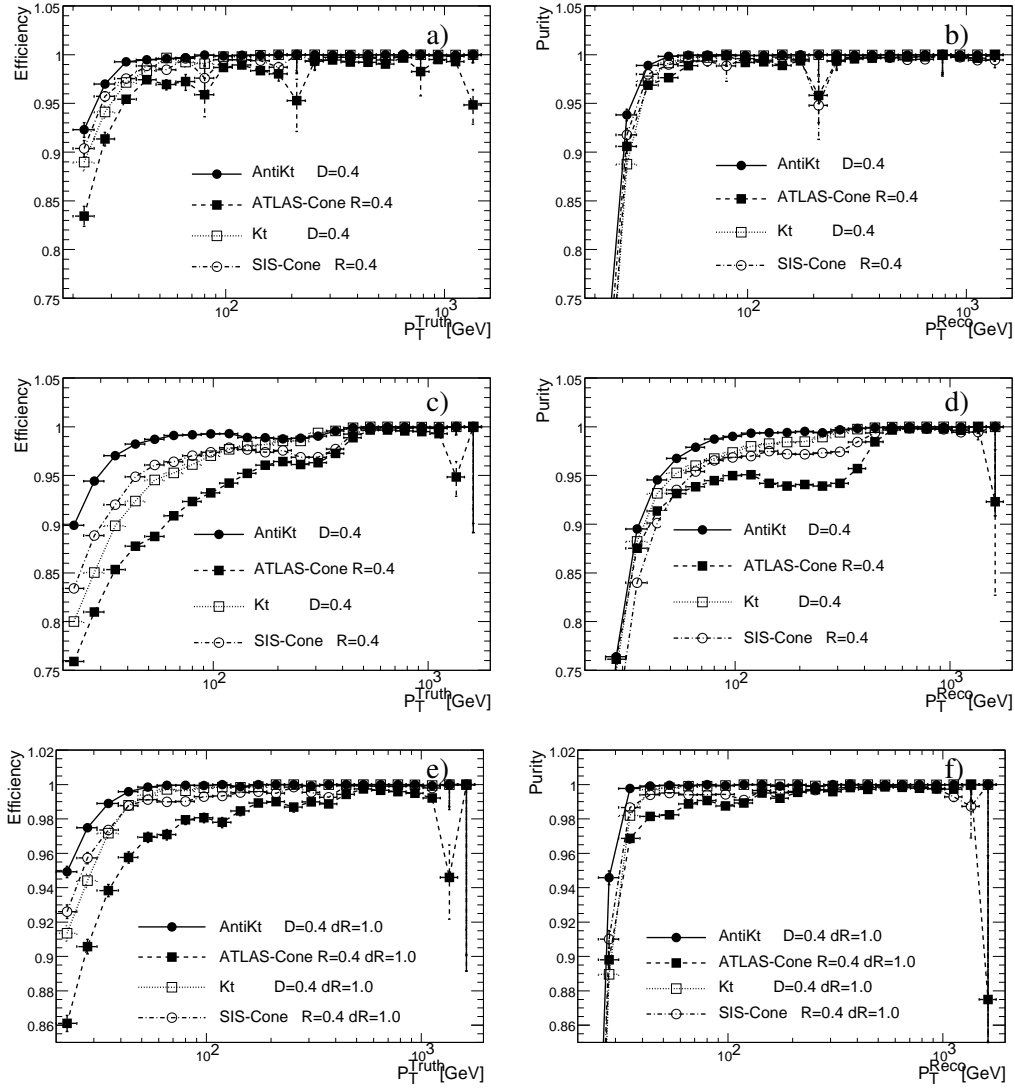


Figure 3.5: Calorimetric jet reconstruction efficiency (a, c, e) and purity (b, d, f) for jets in $|\eta| < 0.4$. Efficiency (a) and purity (b) for simulated QCD di-jet events with \hat{p}_T in the interval [8, 1120] GeV; efficiency (c) and purity (d) for simulated QCD di-jet events with \hat{p}_T in the interval [560, 1120] GeV; efficiency (e) and purity (f) for isolated jet in simulated QCD di-jet events with \hat{p}_T in the interval [560, 1120] GeV.

jet, resulting in a drop of the efficiency at $p_T^{\text{truth}} \sim p_T^{\text{reco}}/2$. Due to the steeply-falling shape of the cross-section the jets with $p_T \sim \hat{p}_T^{\text{low}}$ are artificially increased by the selection applied on \hat{p}_T , and the effect of the mis-behavior in merging or splitting the close-by jets is expected to be at $p_T \sim \hat{p}_T^{\text{low}}/2$.

The instabilities on merging or splitting the close-by jets are confirmed by the absence of the drop in the efficiency and purity in Figs. 3.5.e and 3.5.f which show the efficiency and the purity for isolated jets. The truth jets (reconstructed-jets) are taken into account for the efficiency (purity) only if the closest truth jet (reconstructed jet) has a distance $\Delta R > 1.0$.

These drops in the jet reconstruction efficiency and purity arise from the impact of the calorimetric showers in the reconstruction of systems of close-by jets. The anti- k_t jet algorithm is more stable against such effects than the other algorithms considered here.

Leading and sub-leading jets

Studies of the jet reconstruction efficiency and purity for leading and sub-leading jets can also be used to investigate the differences between the jet algorithms. After sorting the truth jets into descending order in p_T , the reconstruction efficiencies for the first, the second and the third jet are evaluated. By sorting the reconstructed jets, the reconstruction purities are estimated for the first, the second and the third jet. The results in this subsection are obtained using the events with at least one of the hard scattered partons having a \hat{p}_T in the interval [560,1120] GeV, in order to be consistent with the results of the previous subsection.

The reconstruction of the first jet in these events is fully efficient and pure for all the studied algorithms. A drop in the efficiency and in the purity for the cone-like jet algorithms is shown in Figures 3.6.a and 3.6.b for the second jet. The ranges in p_T for the drops are the same as those in Figures 3.5.c and 3.5.d. Similar drops are shown in Figures 3.6.c and 3.6.d for the third jet.

The explanation given above of the instabilities in the calorimetric reconstruction of close-by jets is consistent with these results. In particular, studies on the isolated leading and sub-leading jets (avoiding the systems of nearby jets) show that the efficiency and the purity are restored for at least the first four jets. As an example of the impact of the isolation requirement, in Figures 3.6.e and 3.6.f, the efficiency and the purity for the third isolated jet are shown. In these last plots the efficiency and purity are restored.

These analyses indicate that the reconstruction of hadronic activity in the calorimeter can lead to a single truth jet being reconstructed as more than one jet in the calorimeter, or to two truth jets being merged into a single jet in the calorimeter. That is, the jet algorithms have an undesirable sensitivity to the details of the hadronic shower reconstruction. The algorithm which minimises this sensitivity, and it thus has the highest and most robust efficiency and purity, is the anti- k_t jet algorithm.

3.2.2 Picking up all the high energy objects: the dark clusters

Investigations carried out by previous experiments [S. D. Ellis 2001] have shown large calorimetric energy depositions not belonging to any jet for some specific jet algorithm.

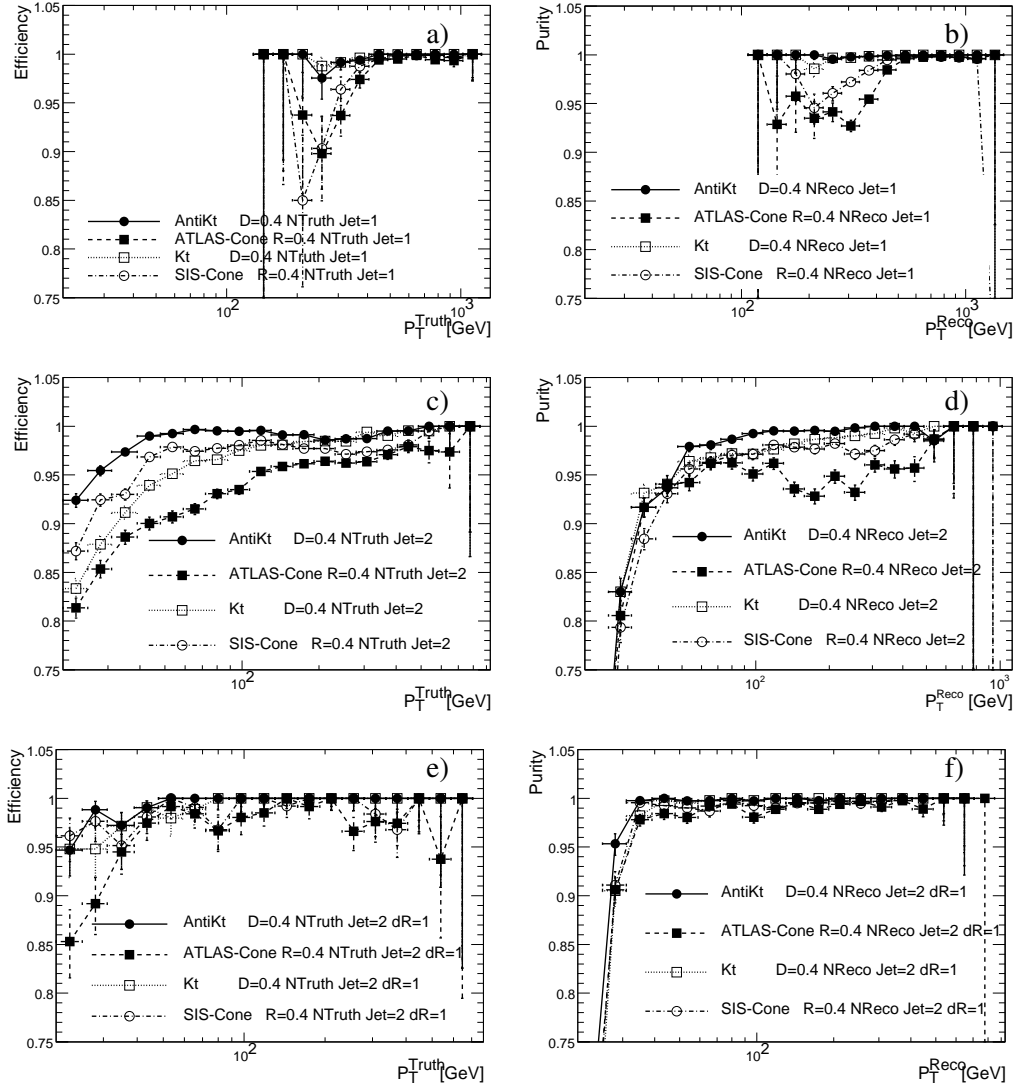


Figure 3.6: Reconstruction efficiency (a, c, e) and purity (b, d, f) for jets in $|\eta| < 0.4$. Efficiency (a) and purity (b) for the second jet sorted by descending p_T ; efficiency (c) and purity (d) for the third jet sorted by descending p_T ; efficiency (e) and purity (f) for the third isolated jet sorted by descending p_T .

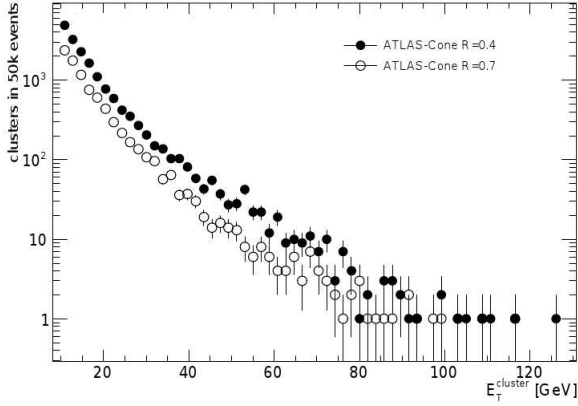


Figure 3.7: Transverse cluster energy distribution for clusters left out of the jets (ATLAS-Cone with a cone radius of $R = 0.4$ and $R = 0.7$) simulated in 50000 Pythia di-jet events with \hat{p}_T in the interval $[560, 1120]$ GeV. The transverse energy of the cluster is the calibrated energy obtained using the local hadron calibration.

This is usually the case of the iterative cone algorithms. These sizable energy depositions outside jets have been called “Dark Towers”. The presence of energetic objects not belonging to any jet is a feature which causes the loss of part of the event information and it should be avoided.

Given the fact that the inputs for the jet reconstruction in ATLAS are clusters, and not towers, to avoid any confusion, the clusters not associated to any jet will be called in this section “dark clusters”. The presence of dark clusters in the ATLAS jet reconstruction is investigated in this section.

All the clusters with $E_T > 10$ GeV are expected to belong to a jet with $E_T > 10$ GeV. Dark clusters with $E_T > 10$ GeV have been found for the ATLAS Cone jet algorithm. The SISCone jet algorithm, the k_\perp jet algorithm, and the anti- k_t jet algorithm do not show any dark cluster.

To check the dependence of the rate of dark clusters from the size of the radius of the ATLAS Cone jet algorithm, two different radii ($R = 0.7$ and $R = 0.4$) have been used. Figure 3.7 shows the transverse cluster energy ($E_T^{Cluster}$) distribution of the clusters left out of the jets by the ATLAS Cone jet algorithm with two different radii.

The two spectra highlight that the phenomenon is more important for smaller cone radius. The existence of unclustered energy depositions is a feature of the jet algorithm, and occurs both for calibrated and uncalibrated objects, and Figure 3.7 shows clusters calibrated using the Local Hadron Calibration [ATLAS Collaboration 2009e].

The rate of dark clusters per event for the ATLAS-Cone is shown in Table 3.1 for QCD di-jet events divided in exclusive samples of \hat{p}_T .

To study the problem in more detail, the clusters not belonging to any jet were associated to the closest jet in $\Delta R = \sqrt{(\phi^{jet} - \phi^{cluster})^2 + (\eta^{jet} - \eta^{cluster})^2}$. The idea behind this association is discussed in the following lines.

The ATLAS-Cone jet algorithm opens a cone of radius $R = 0.4$ or $R = 0.7$ around the position of a seed, and then calculates the centroid of that cone according to the energy depositions inside the cone. A new cone is opened around the position of the centroid, and the procedure continues iteratively until the position of the centroid is stable. All the clusters in consideration a seed for the ATLAS-Cone, but, in some special spatial configurations,

QCD di-jet Pythia Sample	Events with dark clusters ATLAS Cone R=0.4 (%)	Event with dark clusters ATLAS Cone R=0.7 (%)
\hat{p}_T in [1120,2240] GeV	47.6 ± 0.2	25.5 ± 0.2
\hat{p}_T in [560,1120] GeV	33.5 ± 0.2	17.0 ± 0.2
\hat{p}_T in [280,560] GeV	15.0 ± 0.2	7.8 ± 0.1
\hat{p}_T in [140,280] GeV	3.7 ± 0.1	1.8 ± 0.1

Table 3.1: Rate of energy deposition above 10 GeV that are not clustered to any jets per event. The result are shown for different Pythia di-jet samples with increasing jet transverse momenta.

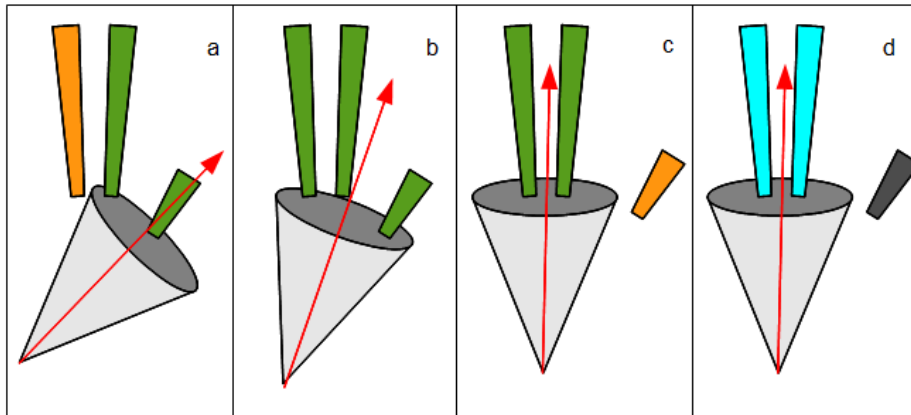


Figure 3.8: Sketch of the iterative procedure in the ATLAS cone algorithm that leads to the problem of dark clusters. The gray cones represent the jet that is being formed. The colored trapeziums represent the towers: orange/green for outside/inside the forming jet and gray/blue for outside/inside the stable jet. The height is proportional to the deposited energy.

some of the seeds could be left out of the final cone. This happens for instance in the configuration of Figure 3.8, when a low- E_T seed has two or more large energy depositions next to it. The steps for the ATLAS Cone are:

1. a cone is open around a seed (a);
2. the centroid is calculated and the center of the cone is shifted to the centroid (b);
3. a second centroid is calculated and the cone is shifted (c);
4. the last configuration is stable, but the initial seed is left out (d). This seed is left out as dark cluster.

Following this sketch, the dark clusters are expected to be close to a jet having a large energy with respect to the cluster ($E^{\text{cluster}}/E^{\text{jet}}$). The distribution of ΔR versus $E^{\text{cluster}}/E^{\text{jet}}$ is shown in Figure 3.9. In this figure, jets with $638 < E_T^{\text{jet}} < 767$ GeV and

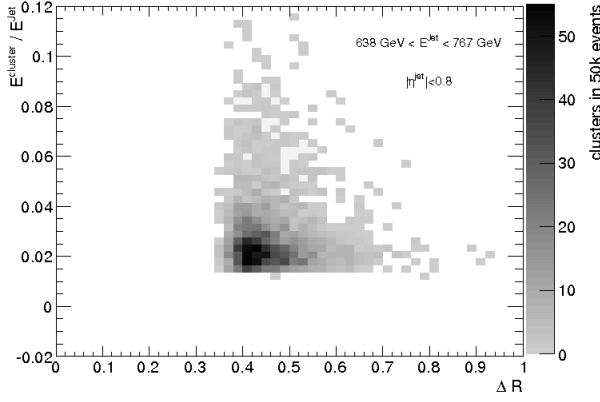


Figure 3.9: Two dimensional distribution of the angular distance between dark clusters and the closest jet (ΔR) versus $E^{cluster}/E^{jet}$ for one bin in η^{jet} and E^{jet} . The plot is obtained with 50k events of the J6 dijet sample simulated with Pythia.

$|\eta^{jet}| < 0.4$ are shown. Similar distributions have been found in other bins of $(E_T^{jet}, |\eta^{jet}|)$. The effect does not depend on the energy and direction of the jet (different directions are covered by different calorimetric technologies). As expected, the dark clusters are close to a jet. The ratio shows that usually they have a small fraction of the jet energy.

The phenomenon of the dark clusters, which affects only the ATLAS Cone, severely affects the study of the properties of jets. It leaves unclustered energetic objects that can cause calibration difficulties; one example is the calibration of the missing transverse energy that treats unclustered energy depositions in a special way.

As a result, the ATLAS Cone is strongly disfavored for the analysis of the data at the LHC.

CHAPTER 4

Measuring jets: Performances

Contents

4.1 Jet cleaning	70
4.2 Jet reconstruction efficiency and purity	72
4.3 Jet energy calibration	75
4.3.1 Jet energy scale: from the calorimetric response to an isolated hadron to the final estimate of the uncertainty	75
4.3.2 Jet energy resolution	99

Many analyses at hadron colliders are based on final states containing jets therefore a good understanding of the jet performances is an important input for most of these studies. The jet measurement in ATLAS strongly relies on the Monte Carlo simulation. For this reason a huge effort has been dedicated to develop detailed checks of the expected reconstruction and calibration performances using data. The goal of these studies is to control the agreement between the measured data and the simulated events. The observed discrepancies between data and MC are used to estimate the systematic uncertainties on the jet performances. These uncertainties are propagated to the final measurements with jets, and, in our case, to the inclusive jet cross section measurement.

For the inclusive jet cross section, the important reconstruction performances are :

- the jet reconstruction efficiency;
- the jet reconstruction purity;
- the jet energy scale;
- the jet energy resolution;
- the jet angular resolution.

These quantities are evaluated with Monte Carlo simulations while their uncertainties are estimated using dedicated studies carried out with collision data. The relevant studies to propagate the performances of the jet reconstruction to the inclusive jet cross section measurement are summarized in the following Chapter.

The dominant contribution to the final uncertainty on the inclusive jet cross section measurement is that given by the jet energy scale. The inclusive jet production as a function

of the transverse momentum is steeply falling and a small deviation of the jet scale results as a large change on the number of measured jets for a certain p_T range and for a certain integrated luminosity.

This means that the measurement of the inclusive jet cross section is a natural benchmark for the accuracy with which the jet energy scale has been assessed. The studies used to determine the jet energy and its uncertainty are described in this chapter. This part is not intended to be a detailed description of all the techniques used to measure the jet energy scale and its uncertainty, but a coherent introduction to the reconstruction performances and to the evaluation of the systematic uncertainties which are affecting the measurement. For each study here described, an exhaustive list of references is also given.

Datasets corresponding to different periods of the 2010 data taking have been used for different studies, depending on the accelerator condition (i.e. the level of pile-up), and the quality of the dataset. In all the studies jets are required to have $p_T > 20$ GeV and cleaning cuts are used to reject jets produced by sporadic detector problems as discussed in the following pages.

4.1 Jet cleaning

The first analyses of the collision data showed that some of the reconstructed jets were generated by sporadic noisy signals in the calorimeter or to energy deposition not related to collisions (cosmic-rays or LHC beam background). These jets are indicated as fake-jets. A series of selection cuts were developed to reject these fake-jets, as described in Reference [[ATLAS Collaboration 2011g](#)]. Fake-jets have been classified in three families, according to the problem that is causing them, and removed by applying the requirements described hereafter.

- **Jets from noisy hadronic end-cap (HEC) calorimeter electronics:**

A jet is rejected if the majority of the jet energy is collected in HEC cells with bad pulse shape compared to a reference shape, or if the absolute value of cell energies below 0 GeV in a given jet is greater than 60 GeV. This second cut has great discriminating power in rejecting jets reconstructed due to noise fluctuations.

- **Jets from noisy electromagnetic (EM) calorimeter electronics:**

A central jet ($|\eta| < 2.8$) is rejected if the majority of the jet energy is collected from the EM calorimeter cells with bad pulse shape compared to a reference shape.

- **Jets from non-collision background:**

A jet is rejected if 95% of the jet energy is released in the hadronic calorimeter and, in the central region ($|\eta| < 2.0$, inside the tracking acceptance), the fraction of the total jet p_T carried by charged particles (measured with the inner detector) is smaller than 10%. These cut are efficient in rejecting the energy loss by cosmic particles, which usually deposit most of their energy in the outer calorimeters (the hadronic part). Furthermore, the fake jets from cosmic background are rejected by requiring a time coincidence for the measured jet (allowing a window of 10 ns).

The fake jets affected from beam backgrounds are mostly induced by two phenomena: the beam-gas interaction, and the beam halo. In the first one, the particles are produced along the beam axis, in the vicinity of the ATLAS cavern. Their contribution is suppressed by rejecting a jet if 95% of its energy is deposited in the electromagnetic calorimeter, but the fraction of p_T carried by charged particles is small. The beam halo is composed mostly by muons parallel to the beam direction, which are generated, for instance, from the interaction of the protons lying on the beam boundary with the LHC collimators. Given the radial geometry of the ATLAS Calorimetric system, the fake jets originated by the beam halo parallel to the beam axis, are rejected if the fraction of energy in one of the radial layer is bigger than 99%.

The detailed list of cuts is summarized in the Appendix.

These cuts were developed to optimize the rejection of the identified problems while being very efficient in selecting real jets. The Monte Carlo simulation does not incorporate the description of these problems. This means that the performance of these cuts in selecting real jets has to be studied on real data.

The efficiency in selecting real jets is measured using a tag-and-probe method in which the cleaning selection is applied on a representative and (as much as possible) unbiased set of real jets. These jets are named "probe" jets.

To reduce the bias on the probe jet, this set is chosen with specific conditions on the event topology, reducing the direct requirement on the probe jets. Events with the two leading jets, ordered in p_T , back to back ($\Delta\phi > 2.6$) and well balanced ($\frac{|p_{T,1} - p_{T,2}|}{p_{T,\text{avg}}} < 0.4$ where $p_{T,\text{avg}} = \frac{(p_{T,1} + p_{T,2})}{2}$) are chosen. Furthermore, one of the two leading jet is required to be within $|\eta| < 2.0$ and to pass a tightened version of the quality selections stated above. These jets are termed "tag" jets. The jets balancing a tag jet in the selected dijet events, are used as probe.

The cleaning cuts have been applied to the probe sample, measuring as a function of $|y|$ and p_T the fraction of jets not being rejected. For the final efficiencies a fit has been performed to remove statistical fluctuations and to extrapolate into uncovered phase space regions. In order to assess the systematic uncertainty, the selection cuts have been varied to apply a looser or tighter criteria. The maximum deviation from the nominal value was assigned as the systematic uncertainty. In addition, the method was cross-checked using jets from Monte Carlo events, which simulate real jets from collision events. The difference in the efficiency measured using the tag-and-probe method and the one measured by taking the fraction of rejected jets in the whole Monte Carlo jets sample is within 0.2%, which is well within the quoted systematic uncertainties. Figure 4.1 shows in white dots the measured efficiency in the central rapidity region ($|y| < 0.3$) for the anti- k_t jets with $R=0.4$. The efficiency estimated with the fit, and used in the measurement of the inclusive jet cross section, is in black, and the systematic uncertainty on the efficiency is shown as a red band. The efficiency is usually bigger than 99%, and only at low p_T in the central region, it becomes almost 97%. No significant differences have been found between the anti- k_t jets with $R=0.4$ and $R=0.6$. A complete list of figure for the cleaning efficiency can be found in the Appendix.

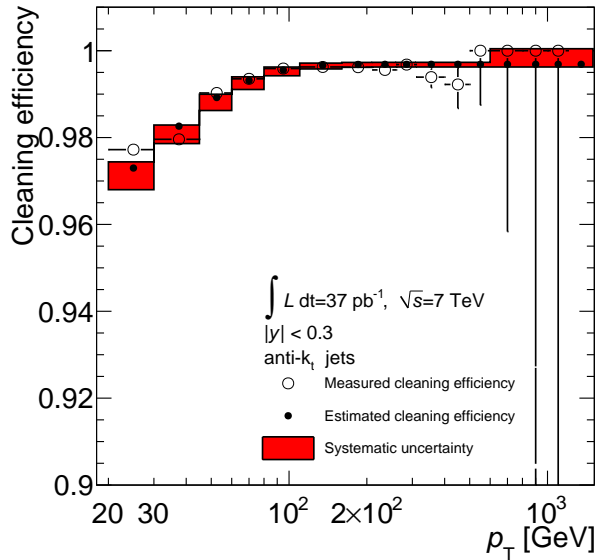


Figure 4.1: Measured cleaning efficiencies in bins of p_T in the central rapidity region $|y| < 0.3$ for the anti- k_t jets with $R=0.4$. The black dots are the result of a fit performed on measured values marked as white points. The red uncertainty band is the systematic uncertainty obtained from variations of the tag jet selection.

4.2 Jet reconstruction efficiency and purity

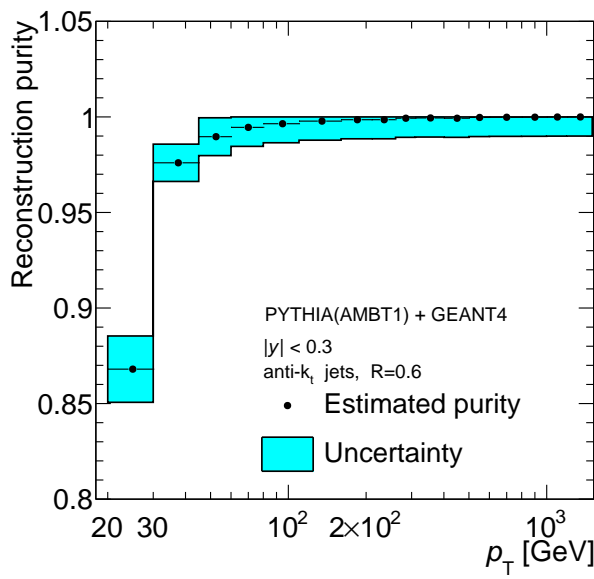
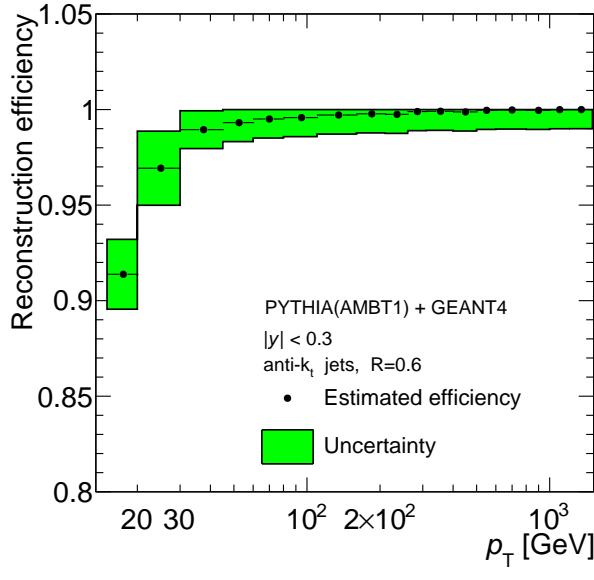
The capability to identify a jet in the detector is one of the general property which directly affects the measurement of the inclusive jet cross section. This capability is well quantified by the efficiency and purity variables introduced in Section 3.2.1. The calorimeters are completely efficient in measuring jets at high p_T , but they may have small inefficiencies at low p_T . Also the purity, at small p_T , can be different from the ideal value of one because some low p_T calorimeter jets are not matched to truth jets. The most frequent source of this problem is a small fluctuation of the jet energy measurement that increases the measured p_T above the minimum p_T threshold used to define a jet, and resulting as an extra jet.

The estimate of these two quantities is done in Monte Carlo simulations. The reconstruction efficiency and purity for the anti- k_t jet algorithm with $R=0.6$ are shown in Figures 4.2 and 4.3 as a function of p_T in the central rapidity region ($|y| < 0.3$). Both the efficiency and the purity are higher than 95% above 30 GeV. A complete list of plots, for the the anti- k_t jet algorithm with $R=0.6$ and $R = 0.4$ can be found in the Appendix.

Measuring the reconstruction efficiency

The efficiency and purity described above are estimated from the MC only. It is therefore highly desirable to find a method to check this evaluations with collision data. This is possible only for the efficiency and it is done using jets reconstructed from tracks. Tracks jets are obtained using tracks as input objects for the anti- k_t jet algorithm. A tag-and-probe method is than implemented to measure the jet reconstruction efficiency relative to track jets. This technique allows to determine the efficiency to match calorimeter jets to track jets in events with a di-jet back-to-back topology.

The highest p_T track jet in the event is defined as the tag object and a second track jet balancing this in ϕ is considered the probe object.



A matching efficiency can be defined by searching for calorimeter jets matched to the probe track jet. The selections on the tag jets are done to suppress the bias in the method. The tag track jet is required to have $p_T \geq 15$ GeV. The measured estimator for the efficiency at low probe track jet p_T was found to be dependent on the tag track jet p_T when the latter is smaller than 15 GeV, becoming stable for a tag track jet p_T greater than 15 GeV.

Because track jets and calorimeter jets are reconstructed by independent ATLAS sub-detector, a good agreement of data and Monte Carlo for this matching efficiency means that the absolute jet reconstruction efficiency can be estimated from the simulation with a good accuracy.

Calorimeter jets with $p_T > 7$ GeV are matched to probe track jets if $\Delta R < 0.4$. Due to the $|\eta| < 1.9$ reconstruction region of track jets, the measurement is only valid for calorimeter jets with $|\eta| < 2.3$. The track jet performance has been studied on data and found to be in good agreement with the performance in the Monte Carlo simulation, as reported in Reference [ATLAS Collaboration 2010h].

Figure 4.4.(a) shows the efficiency to match calorimeter jets to probe track jets in data and simulation. The total error is the quadratic sum of the statistical and systematic error. Systematic errors are obtained by varying the minimum p_T of the tag jet, the $\Delta\phi$ window for the probe jet (the selection is $\Delta\phi > 2.8$) and the ΔR matching radius between the probe track jet and the calorimeter jet. The ratio between the efficiency relative to track jets for data and for Monte Carlo is shown in Figure 4.4.(b). The Monte Carlo is describing properly the efficiency of reconstructing jets at low p_T , with deviation of the order of 1-2% in the very low- p_T region used for the analysis of the inclusive jet cross section.

An uncertainty of 2% is assumed for the bin in p_T [20-30] GeV. The uncertainty decreases to 1% in the other bins.

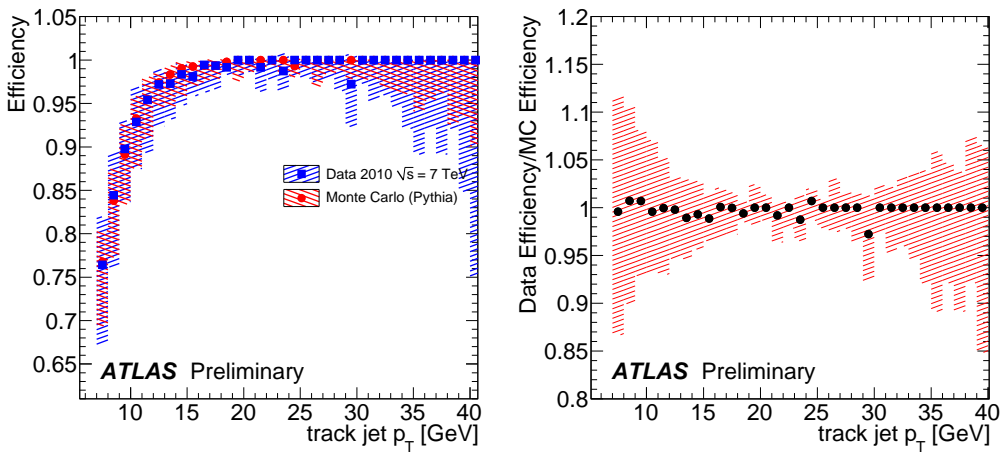


Figure 4.4: Left: efficiency to match calorimeter jets to probe track jets as a function of p_T for $|\eta| < 2.3$. Right: ratio between the measured efficiency and the Monte Carlo description. Plots taken from Reference [ATLAS Collaboration 2010h].

4.3 Jet energy calibration

The method to calibrate the jets, introduced in Section 3.1.2, is reported in detail in Reference [ATLAS Collaboration 2011h]. The systematic error on the jet energy calibration is the dominant experimental uncertainty for numerous physics results and in particular for the cross-section measurement of the inclusive jets, as shown in Section 5.4. In this part, some of the measurements performed to determine the accuracy of the jet energy scale (JES) and resolution (JER) are reported.

The studies are divided in two parts. The first part collects the checks to determine the accuracy on the JES. The second one discusses the check on the JER, and its uncertainty. In particular, the finite jet energy resolution is responsible for the jet migrations between close-by bins in the final measurement of the inclusive jet cross section. The final measurement must be corrected for this migration, and the unfolding methods adopted by the ATLAS Collaboration for the measurement of the inclusive jet cross section, are reported in Section 5.3.

The effects of the JES and JER uncertainties on the measurement of the inclusive jet cross section are different, and can be decoupled. The effect of the systematic error on the JES can be seen as a global shift of the measured p_T , and it strongly affects the cross section. A systematic error on the JER affects the accuracy of the Monte Carlo description of the migration matrix, and, as a consequence, the stability of the unfolding procedure, as described in Section 5.3.

4.3.1 Jet energy scale: from the calorimetric response to an isolated hadron to the final estimate of the uncertainty

The jet calibration strategy adopted by ATLAS relies on the good Monte Carlo description of the calorimeter response. Different studies were performed to check the correctness of this strategy, and to assess the accuracy on the JES. The systematic uncertainty, which comes from these studies, have been divided in seven components:

- Calorimeter response:

The description of the energy deposition of single charged hadrons impinging on the calorimeter has been measured with proton-proton and test-beam data. The difference between the data and the Monte Carlo is the dominant contribution to the JES uncertainty in the central pseudo-rapidity region, and it is reported in detail in Section 4.3.1.1.

- Detector description (additional dead material):

The uncertainty due to possible deviations in the material description is evaluated using specific Monte Carlo samples where the material budget is varied. Even if this component is taken into account in the previous item for the single charged hadrons in proton-proton data used in the studies of the calorimeter response, a bias of 1% at $p_T < 30 \text{ GeV}$ in the region $0.3 < |\eta| < 0.8$, and smaller than 1% for higher p_T , as been found for the other particles, such as the neutral particles, forming a jet.

- **Signal selection (noise threshold):**

The selection of the signals in the calorimeter is based on the signal-to-noise ratio of calorimeter cells, where the noise refers to the RMS of the measured cell energy distribution in events with no energy deposition from collisions events. This value depends on the accelerator and the detector conditions, and any discrepancy with respect to the nominal RMS used in the detector simulation introduces a bias in the signal selection and in the final JES. The impact on the JES uncertainty from this discrepancy is estimated to be between 1% and 2% for $p_T < 45 \text{ GeV}$, and negligible for higher p_T .

- **Physics models in the Monte Carlo generators:**

The contribution to the JES uncertainty due to the modeling of the fragmentation and underlying event, and to other parameters of the Monte Carlo event generators has been estimated by using an ALPGEN +HERWIG +JIMMY sample¹, and the PYTHIA Perugia 2010 tune² (the complete list of generators and tunes used to generate dijet events for performance studies is shown in Table 2.1). The impact on the JES uncertainty is of the order of 4% for $p_T < 30 \text{ GeV}$, decreasing to $\sim 2\%$ for $45 < p_T < 100 \text{ GeV}$, becoming smaller for higher p_T .

- **Calibration method:**

The calibration factors are derived to restore the energy and the pseudo-rapidity of the jet. Since the jet has a mass, the p_T is not directly proportional to the energy (for which the calibration is derived). For this reason, in case of massive jets, the p_T calibration has a bias. This error is estimated directly on the Monte Carlo simulation, and it results in a bias of 2% at $p_T < 30 \text{ GeV}$ in the region $0.3 < |\eta| < 0.8$, and smaller than 1% for higher p_T . Figure 3.3 shows the non linearity due to this effect.

- **Uncertainty on the relative calibration for jet with $|\eta| > 0.8$:**

The different calorimeter technologies and the varying amounts of dead material in front of the calorimeters for different regions of pseudo-rapidity are taken into account in the calibration procedure. The relative uncertainty due to a mis-modeling of the detector in the forward region, in which the direct calorimeter response cannot be studied for the absence of the inner tracker, has been performed using the balance in p_T in di-jet events. This uncertainty gives a dominant uncertainty for the forward region, and for this reason is reported in detail in Section 4.3.1.2.

- **Pile-Up:**

Particles produced by multiple soft proton-proton interactions in the same bunch crossing additional to the event of interest (in-time pile-up) can produce additional energy deposits that are reconstructed within the jet. As described in Section 3.1.2, an average offset correction is applied to account for the average increase of the jet

¹This sample differs from the nominal sample for the multi leg leading order matrix elements, for the PDF set used, for the ordering in the parton shower and for the models of fragmentation and underlying events.

²This sample differs from the nominal sample for an increased final state radiation, and for changes in the parameters of the fragmentation model.

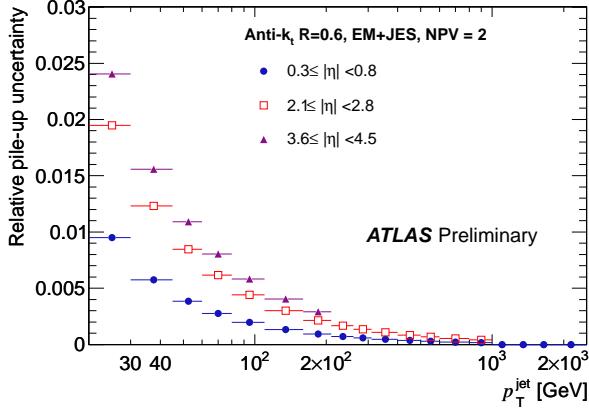


Figure 4.5: Relative pile-up uncertainty for anti- k_t jets with $R=0.6$ in the case of two measured primary vertexes, $N_{PV} = 2$, for three rapidity regions as a function of jet p_T . Figure taken from Reference [[ATLAS Collaboration 2011h](#)].

energy due to pile-up. This correction is parameterized as a function of the measured primary vertexes N_{PV} . The estimate of the remaining uncertainty on the jet energy scale after applying the pile-up correction is based on the studies described in Section 5 of Reference [[ATLAS Collaboration 2011e](#)]. The uncertainty is derived as a function of the number of reconstructed vertexes. This allows the correction and its uncertainty to be valid also for data periods where the number of reconstructed primary vertexes is higher than the period where the correction is derived. Figure 4.5 shows the relative uncertainty due to pile-up in the case of two measured primary vertexes. In this case, the uncertainty due to pile-up for central jets with $p_T = 20$ GeV and pseudo-rapidity $| \eta | < 0.8$ is about 1%, while it amounts to about 2% for jets with pseudo-rapidity $2.1 < | \eta | < 2.8$ and to less than 2.5% for all jets with $| \eta | < 4.5$. The uncertainty increases with the number of primary vertexes, becoming, with four primary vertexes, for central, endcap and forward jets less than 3%, 6% and 8%, respectively.

These components are used to estimate the jet energy scale uncertainty for the jet reconstructed with the anti- k_t jet algorithm with distance parameter $R=0.6$ and $R=0.4$. The method to combine the different components is reported in Section 4.3.1.3. In the same section, a first detailed study of the correlations is introduced.

Data driven checks of the Jet Energy scale uncertainty

The most prominent components in the determination of the jet energy scale uncertainty are derived from the comparison of the calorimeter response in collision data. In particular, in the central region ($|y| < 0.8$), the dominant component is the uncertainty on the description of the calorimeter response to isolated hadrons. In the other rapidity regions, the uncertainty due to the relative $| \eta |$ inter-calibration becomes the dominant component. In the following sections, the techniques used to determine these components are described.

4.3.1.1 Calorimeter response: isolated single particles

The calorimeter response to isolated hadrons has been checked with the first collisions at $\sqrt{s} = 900$ GeV and $\sqrt{s} = 7$ TeV. This response has been studied by comparing the energy deposited in the calorimeter (E) to the momentum (p) measured by the tracker for well isolated hadrons. The calorimeter energy is measured as the sum of the energy deposited in cones of $\sqrt{\Delta\phi^2 + \Delta\eta^2} < 0.2$ around the hadron. The ratio $$ is studied as a function of the track momentum in regions of pseudo-rapidity for collision data and for MC samples. Figure 4.6(a) shows a sketch of the analysis selection for the measurement of E/p .

The comparison of $$ gives a direct estimate of the correctness of the simulation of the energy deposits of single charged particles in the Monte Carlo simulation. The discrepancy is used as one of the input to estimate the uncertainty on the JES, as described in the second part of this Subsection.

Figure 4.6(c) shows the distribution of the ratio E/p for a specific region in pseudo-rapidity and momentum ($0 < |\eta| < 0.6$, $2.2 < p < 2.8$ GeV).

A detailed description of the studies performed by the ATLAS Collaboration on the calorimetric response to single isolated hadrons can be found in References [[ATLAS Collaboration 2010I](#), [ATLAS Collaboration](#), [ATLAS Collaboration 2011a](#)].

The important aspects for this analysis are:

- The statistical significance of the test:

The statistics in the analysis is limited to an integrated luminosity of $866 \mu\text{b}^{-1}$ in proton-proton collisions at $\sqrt{s} = 7$ TeV. This sample corresponds to the first period of data taking in which the pile-up was absent, and the minimum bias triggers were not prescaled out from the data acquisition. This statistics allows us to measure the E/p distribution in the range $2 \text{ GeV} < p < 20 \text{ GeV}$.

- The quality of the tracks in the Inner Detector measurement:

The tracks satisfy the basic quality criteria and are consistent with being originating from the primary vertex.

- The isolation of the track from charged and neutral particles:

The charged particles are required to be isolated. All the tracks which, extrapolated to the calorimeter surface, have a second track closer than $\sqrt{\Delta\phi^2 + \Delta\eta^2} < 0.4$, are rejected. This requirement is really efficient in rejecting other charged particles producing an energy deposit in the selected calorimetric region, but it is not able to reject the neutral particles, mostly photons produced in the $\pi^0 \rightarrow \gamma\gamma$ decays.

The neutral background contributing to the calorimeter deposit is responsible for the tails at $E/p > 1$, shown in Figure 4.6(c).

The method used to estimate and subtract the background is discussed in the following part.

The tails in Figure 4.6(c) are simulated by the Monte Carlo³, which could be, in principle, used to estimate their contribution.

³The Monte Carlo simulation consists of a sample of proton-proton collisions at $\sqrt{s} = 7$ TeV pro-

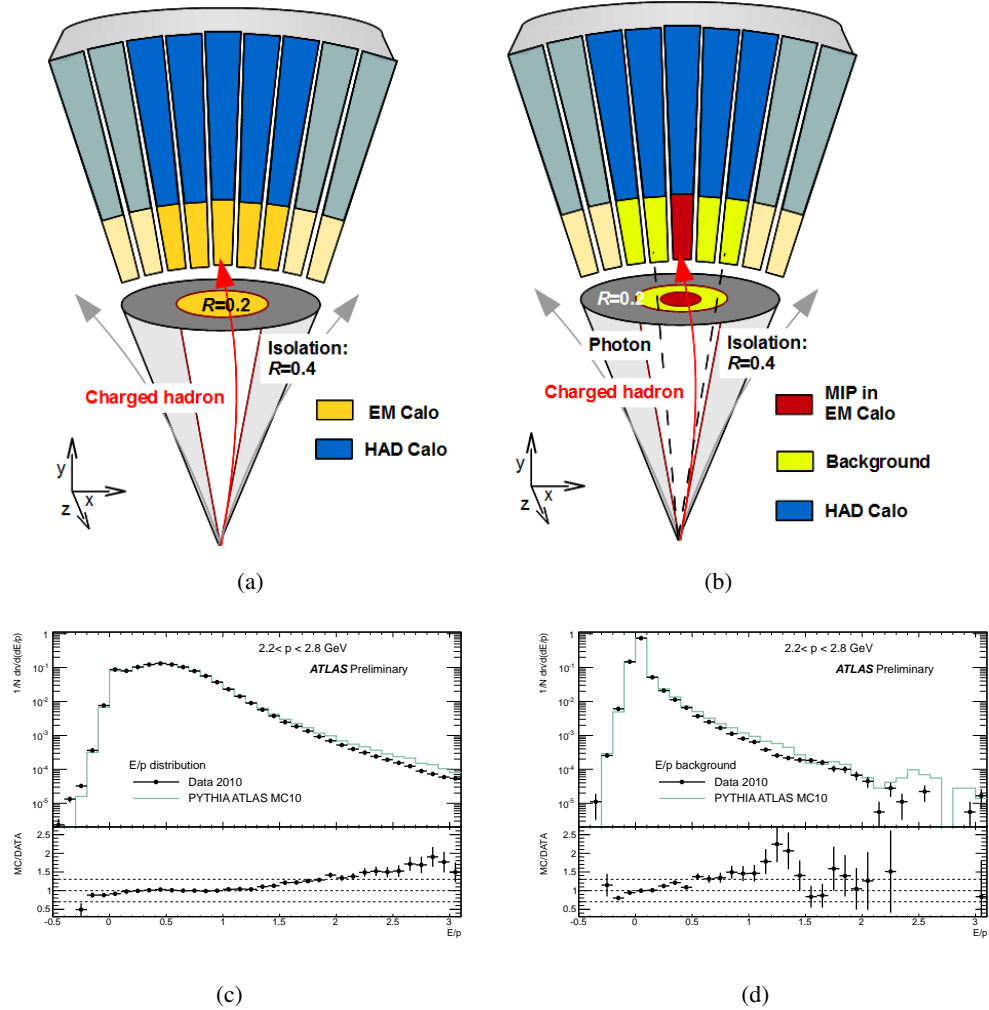


Figure 4.6: (a) Sketch of the analysis selection to study the E/p distribution. (b) Strategy to select special events for the measurement of contribution of the neutral background. (c) E/p distribution for isolated tracks with an impact point in the region $0 < \eta < 0.6$ and with a momentum in the range $2.2 < p < 2.8 \text{ GeV}$. (d) The same as (c) for the background selection in the cone annulus between $R=0.2$ and $R=0.1$ in the EM calorimeter. Figures (c) and (d) are taken from Reference [ATLAS Collaboration 2011a].

The shape of the tail in the E/p distribution depends on the probability to produce neutral particles in the direction of an isolated charged particle. This strongly depends on the model adopted to simulate the hadronization and the underlying event in PYTHIA. To limit the dependence on the modeling of the background, the estimate of the contribution of the neutral background is obtained from collision data.

In the Monte Carlo simulation, the impact of the neutral hadrons not decaying in photons, such as neutrons, is estimated to be small with respect to the contribution of the γ . For this reason, the measurement of the background in data has been designed to be efficient in measuring the contribution of the additional photons. The idea is to select a subset of tracks which show a late start of the hadronic shower in the calorimeter, and to measure in the electromagnetic calorimeter the contribution from the neutral particles. These isolated tracks are minimum ionizing particle in the electromagnetic calorimeter ($E_{\text{EM}}^{0,1} < 1.1 \text{ GeV}$ in the EM calorimeter in a cone of $\Delta R = 0.1$), and have an important energy deposit in the hadronic calorimeter ($E_{\text{HAD}}^{0,1}/p > 0.4$ in the hadronic calorimeter in a cone of $\Delta R = 0.1$). As example, a sketch of the background selection is shown in Figures 4.6(b).

In this sample of isolated tracks, the measurement of the background is done with the electromagnetic calorimeter in the annulus $0.1 < R < 0.2$, where the contribution of the impinging charged track is expected to be negligible. In this region, the measured energy is expected to come from energy deposition of γ .

This estimate, rescaled by the geometrical factor, can be used to subtract the average neutral background contribution from the average energy deposition of charged hadrons.

The background contribution from neutral hadrons depositing their energy in the Tile calorimeter was estimated in Reference [ATLAS Collaboration] and found to be small⁴. Figure 4.6(d) shows the E/p distribution in the annulus between $R=0.1$ and $R=0.2$ in the EM calorimeter for isolated tracks satisfying the background selection. The background $\langle E/p \rangle_{BG}$ is about $3.5 - 4.5\%$ for $p < 10 \text{ GeV}$ and decreases to $\sim 3\%$ for track momenta of $\sim 20 \text{ GeV}$. The general trend is confirmed by the MC simulation. However, a significant discrepancy between the MC predictions and the data is observed. This corresponds to a $\sim 1\%$ difference on $\langle E/p \rangle$ and is taken as a systematic uncertainty.

Figure 4.7 shows $\langle E/p \rangle$, corrected for the neutral background, as a function of the track momentum in two different η bins up to $\eta = 1.1$. The green shaded area corresponds to the MC simulation prediction and the black points to the collision data.

duced by non-diffractive processes. The event generation was done with PYTHIA 6.421 (see Reference [Sjostrand 2006]) using the AMBT1 tune (ATLAS Minimum Bias Tune 1, described in Reference [ATLAS Collaboration 2010e]), introduced in Tables 2.1. The ATLAS detector simulation software [ATLAS Collaboration 2010n], which is based on GEANT4 [Agostinelli 2003] has been used to process the generated events. The Geant4 physics list used is QGSP_BERT [A.Ribon 2010].

⁴The measured background correction to the $\langle E/p \rangle$ is found to be roughly 10% of the raw $\langle E/p \rangle$. This takes into account only energy deposited by π^0 and other neutral hadrons (mainly n and K_L^0) in the EM calorimeter, but not that deposited by n and K_L^0 in the hadronic calorimeter. Roughly speaking, n and K_L^0 carry about 1/3 of the total energy carried by neutral hadrons. About 2/3 of this energy is deposited in the EM calorimeter, which is about one interaction length long in the central calorimeter region. Therefore, the fraction of background not taken into account is about $1/3 \cdot 1/3 \sim 10\%$, or $\sim 1\%$ of the raw $\langle E/p \rangle$. Even assuming a 50% discrepancy between data and MC concerning the n and K_L^0 energy deposit in the hadronic calorimeter, the $\langle E/p \rangle$ will only be affected at the 0.5% level.

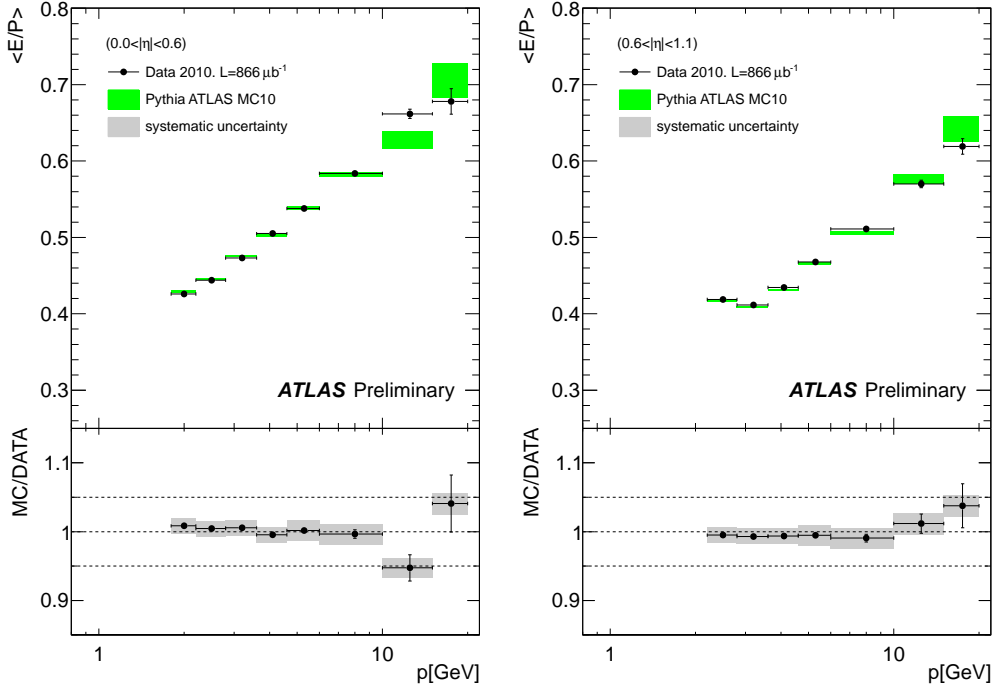


Figure 4.7: $\langle E/p \rangle$ after background subtraction as a function of the track momentum in different $|\eta|$ bins. The black dots represent the collision data, while the green rectangles represent the MC prediction. The lower part of the figures shows the ratio between the MC simulation prediction and collisions data. The gray band indicates the size of the systematic error on the ratio data to MC. The dotted lines are placed at $\pm 5\%$ of unity. Figures taken from Reference [ATLAS Collaboration 2011a].

The lower part of the Figure shows the ratio between Monte Carlo simulation and data. The agreement between data and Monte Carlo simulation is within 2% for particles with momentum up to 10 GeV and it is around 5% for momentum in 10–20 GeV range. The systematic uncertainties, taken into account in the comparison, are shown in gray. The systematic errors taken into account are discussed in References [ATLAS Collaboration , ATLAS Collaboration 2011a]. Usually they are smaller than 1%, dominated by the background subtraction uncertainty ($\sim 1\%$). The calorimeter uncertainty is 2–5% on central isolated hadrons.

Calorimeter response: jets

The response uncertainty of single charged particles and the expected uncertainty for neutral particles are used to propagate the uncertainty on the calorimeter jet energy scale.

The analysis is performed with inclusive di-jet Monte Carlo events simulated with PYTHIA. Jets are selected requiring a separation of $\Delta R > 2.0$ to any other jet with $p_T^{\text{EM}} > 7$ GeV. The jet energy is first decomposed into the energy of the constituent par-

ticles of the jet. The uncertainty on the jet energy scale is then determined by convolving the uncertainty on the single particle response with the jet particle composition.

The numerical evaluation of the uncertainty on the jet energy scale is performed with Monte Carlo pseudo-experiments. In each pseudo-experiment, the jet energy scale is calculated after randomly changing the Monte Carlo single particle energy response within the appropriate uncertainty range given by the measured data/MC ratio. The final uncertainty on the jet energy scale is then given by the spread of the distribution of the jet energy scale over all pseudo-experiments. More details on the method are given in Reference [[ATLAS Collaboration](#)].

The E/p measurements only cover the response of charged hadronic particles with momenta less than ~ 20 GeV. However, depending on the jet momentum, on average, between 35% and 90% of the energy in jets is carried by particles that are not measured in-situ using the isolated track analysis (mostly photons from π^0 decays, neutral hadrons and high momentum charged hadrons). Hence, the uncertainty on the energy response to these particles is needed in order to obtain the total calorimeter uncertainty on the jet energy scale and is addressed in the following. The uncertainty for the high momentum charged particles (up to 350 GeV) is obtained by the study of the ATLAS Combined Test Beam (CTB), carried out at CERN in 2004 (see References [[ATLAS Collaboration 2010a](#), [Cojocaru 2004](#), [Dowler 2002](#)] for a detailed description). From these measurements (References [[ATLAS Collaboration 2010a](#)]), the ratio between data and Monte Carlo simulation predictions is used to supplement the E/p measurements in the previous pages with a larger energy range. However, since these measurements are not taken in the same detector, additional systematic uncertainties from the test beam have to be taken into account.

For single particle momenta above 400 GeV no direct measurements in a test beam or in-situ exist. Therefore a conservative additional uncertainty of 10% on top of the 350 GeV measurement uncertainty is used in order to cover possible effects from calorimeter nonlinearities at high energy densities and longitudinal leakage.

The absolute electromagnetic energy scale in ATLAS has been established using $Z \rightarrow ee$ decays for the electromagnetic LAr calorimeters and using the energy loss of minimal ionizing muons in the Tile calorimeter. For the bulk of the electromagnetic LAr barrel calorimeter a 1.5% uncertainty on the cell energy measurement is found and a 5% uncertainty on the LAr presampler cell energy. For the Tile calorimeter a scale uncertainty of 3% is found.

This uncertainty does not affect charged particles measured in-situ with E/p , but needs to be considered for all other particles contributing to jets. A special treatment of barions and neutral hadronic particles is used to propagate a conservative uncertainty on the final calorimeter jet energy scale reported in Reference [[ATLAS Collaboration 2011a](#)]. On average, approximately 10-12% of the jet energy is carried by neutral hadrons. The uncertainty on the calorimeter response to these particles was estimated conservatively resulting in a $\sim 1\%$ contribution to the total JES uncertainty.

The total calorimeter uncertainty on the jet energy scale is shown in Figure 4.8 for anti- k_t jets with $R = 0.6$ in the pseudo-rapidity range $0 < |\eta| < 0.8$. The maximum expected shift in the jet energy scale is $\sim 1\%$ with an uncertainty of 1–3%. The envelope of the

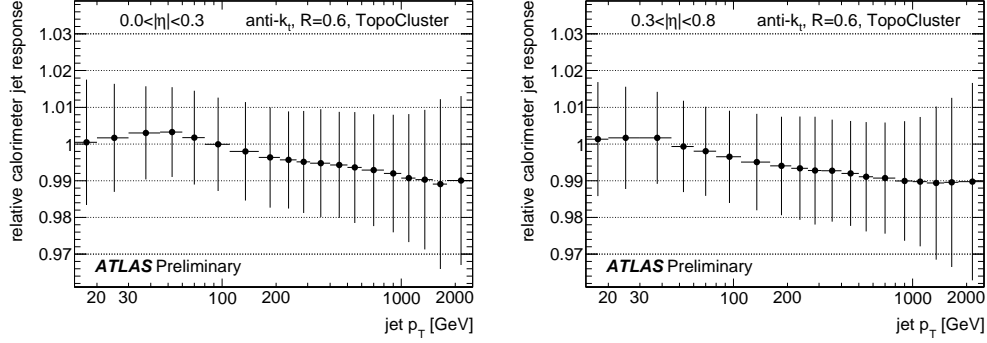


Figure 4.8: Expected shift (black dots) and total uncertainty (error bars) on the relative calorimeter jet response with respect to the MC simulation for jets reconstructed with the anti- k_t algorithm ($R = 0.6$) in the range $0.0 < |\eta| < 0.3$ and $0.3 < |\eta| < 0.8$ as function of the transverse jet momentum. The x -axis is the jet transverse momentum calibrated with the EM-JES calibration. The Figures are taken from Reference [[ATLAS Collaboration 2011a](#)].

shift and uncertainty on the calorimeter JES is taken as the contribution to the total JES uncertainty discussed in Reference [[ATLAS Collaboration 2011h](#)].

The use of pseudo-experiments for the determination of the JES uncertainty allows a direct extraction of the correlation of uncertainties between different jet momenta, rapidities or algorithms by correlating fluctuations of different quantities within one pseudo-experiment.

Figure 4.9 shows the correlation of the JES uncertainty between different pseudo-rapidity and momentum bins. As expected, the correlation between neighboring bins in $|\eta|$ and p_T is almost 100%, while widely separated bins show only a $\sim 30\%$ correlation. This remaining $\sim 30\%$ correlation is mostly caused by the calorimeter energy scale and neutral hadron uncertainty, which contribute identically to all jets.

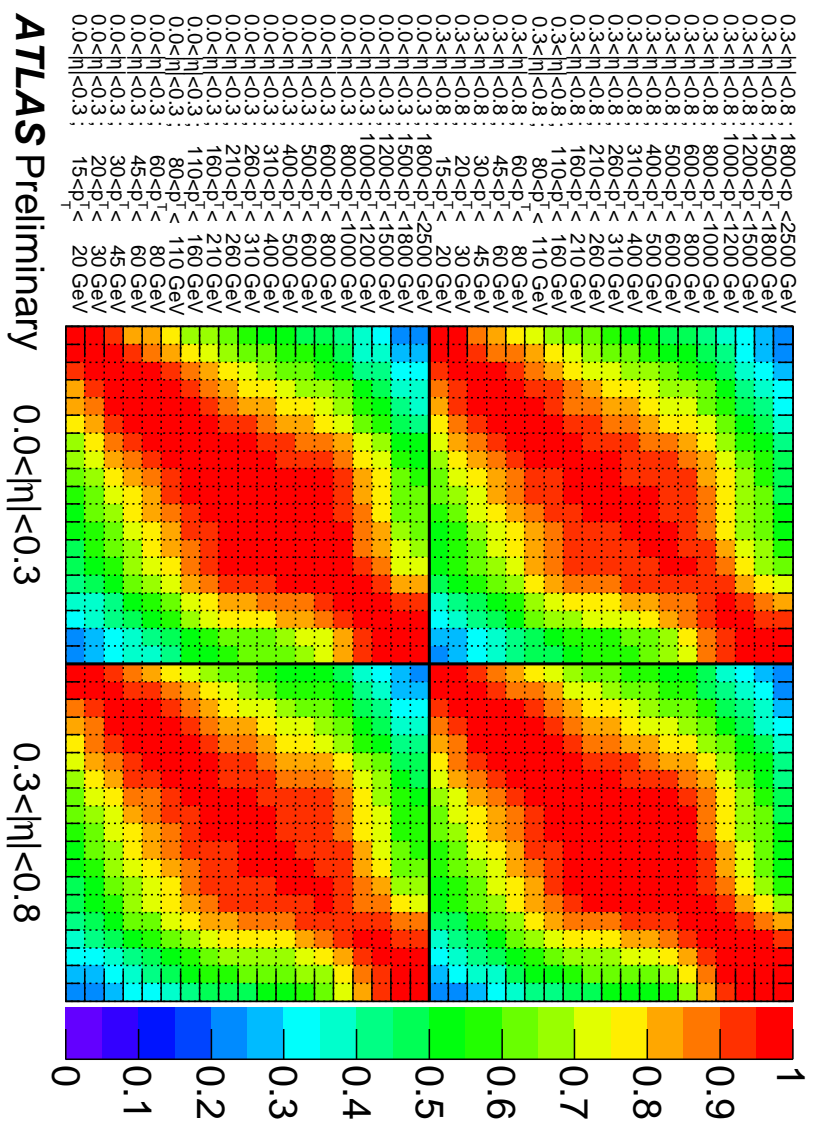


Figure 4.9: Correlation coefficient of the total uncertainty on the calorimeter jet response for jets reconstructed with the anti- k_t jet algorithm ($R = 0.6$) in the range $0.0 < |\eta| < 0.8$ and transverse jet momenta between $15 \text{ GeV} < p_T < 2.5 \text{ TeV}$. The bins on the x-axis are identical to the bins on the y-axis. A red color indicates $\sim 100\%$ correlated uncertainties, a blue color almost uncorrelated uncertainties. Figure taken from Reference [ATLAS Collaboration 2011a].

4.3.1.2 Calibrating the forward region: Di-jet balance

Due to the changing calorimeter technology and to the varying amounts of dead material in front of the calorimeters, the response of the ATLAS calorimeters to jets is dependent on the jet direction. A calibration is therefore needed to ensure a uniform calorimeter response to jets. This is achieved by applying correction factors derived from Monte Carlo simulations. Such corrections have been validated in-situ. A detailed description of the methods developed by the ATLAS Collaboration to validate the jet calibration in different rapidity regions can be found in the References [[ATLAS Collaboration 2010g](#), [ATLAS Collaboration 2011f](#)].

The standard approach for η intercalibration with dijet events is to use the central region of the calorimeters as the reference region. The relative calorimeter response of jets in other calorimeter regions is quantified by the p_T balance between the reference jet and the probe jet, exploiting the fact that these jets are expected to have equal p_T due to transverse momentum conservation. The central region of the barrel ($|\eta| < 0.8$) has been chosen as reference region. In this region the study of the calorimeter response to single isolated tracks can profit from the presence of the inner tracker and from a more uniformity in the calorimeter technology.

The data collected in 2010, with a total integrated luminosity of 35 pb^{-1} was used to validate the pseudo-rapidity inter-calibration. The trigger strategy is chosen such that the trigger efficiency, for a specific region of $p_T^{\text{avg}} = [p_T(j_1) + p_T(j_2)]/2$, is greater than 99% and approximately flat as a function of the pseudo-rapidity.

These events were required to contain a single vertex with at least five good tracks with $p_T > 0.5 \text{ GeV}$ and to pass detector, trigger and reconstruction quality criteria.

Events were also requested to have at least two jets above the jet reconstruction threshold of 7 GeV. The event was rejected if either of the two leading jets did not satisfy the standard jet cleaning criteria, introduced in Section 4.1.

To enhance events which have a $2 \rightarrow 2$ topology, the following selection criteria are applied:

- $p_T^{\text{avg}} > 20 \text{ GeV};$
- $\Delta\phi(j_1, j_2) > 2.6 \text{ rad};$
- $p_T(j_3) < \max(0.15 p_T^{\text{avg}}, 7 \text{ GeV});$

where j_i denotes the i^{th} highest p_T jet in the event and $\Delta\phi(j_1, j_2)$ is the azimuthal angle between the two leading jets.

As example, the event topology used in this analysis is shown in Figure 4.10.

The recorded di-jet events are used to measure an η -intercalibration factor c of the probe jet, or its response relative to the reference jet $1/c$, using the relation

$$\frac{p_T^{\text{probe}}}{p_T^{\text{ref}}} = 1/c. \quad (4.1)$$

A disadvantage of requiring events with a jet in the central reference region is the significant loss of event statistics, especially in the forward region where the dijet cross

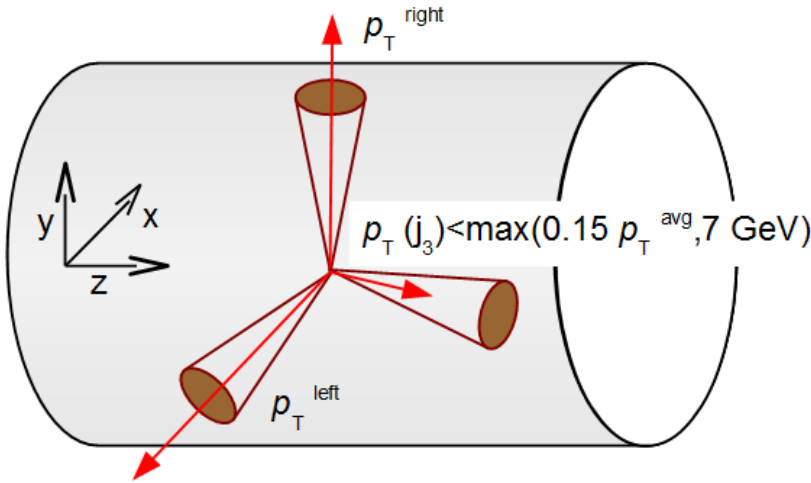


Figure 4.10: Sketch of the event topology used for the di-jet balance technique.

section drops steeply as the rapidity interval between the jets increases. In order to use the full statistics, one can divide the jets in “left” and “right” jets defined from $\eta^{\text{left}} < \eta^{\text{right}}$. The equation (4.1) then becomes:

$$\frac{p_T^{\text{left}}}{p_T^{\text{right}}} = \frac{c^{\text{right}}}{c^{\text{left}}} = \mathcal{R} \quad (4.2)$$

where the term \mathcal{R} denotes the ratio of the responses, and c^{left} and c^{right} are the η intercalibration factors for the left and right jets, respectively.

By dividing the samples in bins of p_T^{avg} , indexed with k , in bins of η^{left} , indexed with i and η^{right} , indexed with j , one can rewrite the equation 4.2:

$$\frac{c_{ik}}{c_{jk}} = \langle \mathcal{R}_{ijk} \rangle \text{ or } c_{ik} = \langle \mathcal{R}_{ijk} \rangle c_{jk} \quad (4.3)$$

where $\langle \mathcal{R}_{ijk} \rangle$ is the average value of \mathcal{R}_{ijk} in the bin (i, j, k) . For each c_{ik} , the second relation 4.3 corresponds to a set of linear equations, which can be used to get the estimate of the relative correction factor c_{ik} . This is obtained by minimizing the expression:

$$S(c_{1k}, \dots, c_{Nk}) = \sum_{j=1}^N \sum_{i=1}^{j-1} \left(\frac{1}{\Delta \langle \mathcal{R}_{ijk} \rangle} (c_{ik} \langle \mathcal{R}_{ijk} \rangle - c_{jk}) \right)^2 + X(c_{ik}), \quad (4.4)$$

where N are the number of η -bins, $\Delta \langle \mathcal{R} \rangle$ is the statistical uncertainty of $\langle \mathcal{R} \rangle$ and the function $X(c_{ik})$ is used to quadratically suppress deviations from unity of the average corrections⁵. The minimization (Eq. 4.4) is done separately for each p_T -bin k , and the resulting

⁵ $X(c_{ik}) = K \left(N_{\text{bins}}^{-1} \sum_{i=1}^{N_{\text{bins}}} c_{ik} - 1 \right)^2$, with K being a constant and N_{bins} being the number of η -bins (number of indices i). This term prevents the minimization from choosing the trivial solution: all c_{ik} equal to zero. The value of the constant K does not impact the solution as long as it is sufficiently large ($K \approx 10^6$).

calibration factors c_i (for each jet η -bin i) are scaled such that the average calibration factor in the reference region $|\eta| < 0.8$ equals unity.

The agreement between the Monte Carlo description and the measured distribution is generally good. Figure 4.11 shows the relative response obtained with the matrix method as a function of the jet pseudorapidity for data and the Monte Carlo event generator simulations. The Monte Carlo simulation consists of a sample of proton-proton collisions at $\sqrt{s} = 7$ TeV produced by di-jet production processes. The event generation was done with PYTHIA 6.421 [Sjostrand 2006] using the AMBT1 tune (ATLAS Minimum Bias Tune 1) [ATLAS Collaboration 2010e], HERWIG++ [Bahr 2008b] and ALPGEN [Mangano 2003]⁶.

Four different p_T^{avg} regions are shown: $20 \leq p_T^{\text{avg}} < 30$ GeV, $30 \leq p_T^{\text{avg}} < 45$ GeV, $60 \leq p_T^{\text{avg}} < 80$ GeV and $80 \leq p_T^{\text{avg}} < 110$ GeV. The response in data is reasonably well reproduced by the Monte Carlo simulations for $p_T > 60$ GeV, with the MC and data agreeing typically better than the 2% level in the central region ($|\eta| < 2.8$) and better than 5% in the forward region ($|\eta| > 2.8$). At lower values of p_T , the data do not agree as well with the MC simulations and the MC simulations themselves show a large spread around the data. For $20 < p_T^{\text{avg}} < 30$ GeV, the MC deviates from the data by about 10% for $|\eta| > 2.8$, with the different MC simulations predicting both higher and lower responses than that observed in the data. The main differences could reflect a difference in physics modeling between the event generators.

The uncertainty on the relative jet response must reflect this disagreement because there is no *a-priori* reason to believe one theoretical prediction over another. The uncertainty on the relative response is taken to be the RMS deviation of the MC predictions from the data. At high p_T , where the spread of MC predictions is small, the uncertainty mainly reflects the true difference between the response in data and simulation. At low p_T and large $|\eta|$, the uncertainty mainly reflects the physics modelling uncertainty, although the detector-based differences between data and simulation is also accounted for. Figure 4.12 shows the uncertainty in the jet response, relative to jets in the region $|\eta| < 0.8$, as a function of the jet p_T and $|\eta|$.

⁶ ALPGEN provides LO matrix elements for up to six partons in the final state and is linked to HERWIG 6 [Corcella 2002] and JIMMY [Butterworth 1996] to provide parton showering, hadronization and multiple partonic interactions.

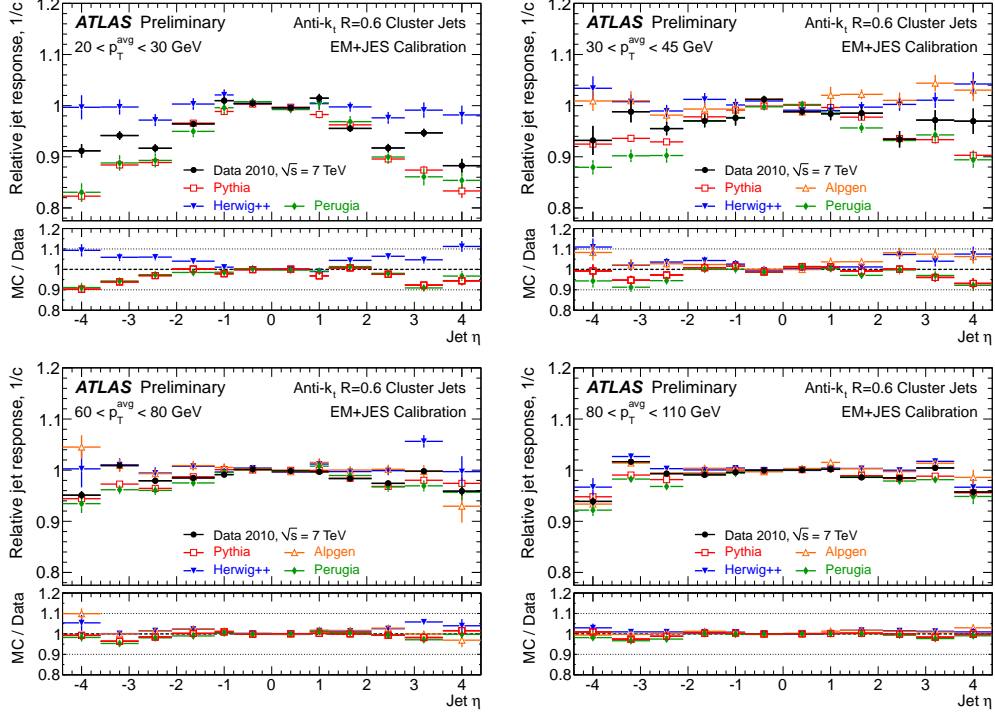


Figure 4.11: Relative jet response, $1/c$, as a function of the jet pseudo-rapidity found using the matrix method for $20 < p_T^{\text{avg}} < 30 \text{ GeV}$, $30 < p_T^{\text{avg}} < 45 \text{ GeV}$, $60 < p_T^{\text{avg}} < 80 \text{ GeV}$ and $80 < p_T^{\text{avg}} < 110 \text{ GeV}$.

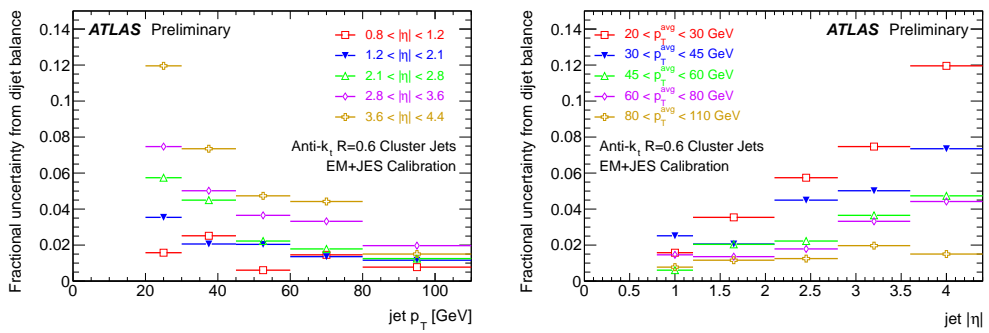


Figure 4.12: (a) Uncertainty in the jet response as a function of jet p_T for various regions of the calorimeter. (b) Uncertainty in the jet response as a function of jet $|\eta|$ for various values of jet p_T .

4.3.1.3 Determination of the jet energy scale uncertainty and correlation

The total jet energy scale uncertainty has been derived by considering all the individual contributions described in Section 4.3.1. A detailed description can be found in Reference [ATLAS Collaboration 2011h]. In the central region ($|\eta| < 0.8$), the estimate proceeds as follows:

1. For each p_T and η bin, the uncertainty due to the calibration procedure is calculated for both jet energy and p_T response. For each bin, the maximum deviation from unity between the energy and p_T response is taken as the final non-closure uncertainty.
2. The calorimeter response uncertainty is estimated as a function of jet η and p_T from the propagation of single particle uncertainties to the jets, as detailed in Section 4.3.1.1.
3. Sources of uncertainties estimated using special Monte Carlo samples generated with ad-hoc variations with respect to the standard configuration are accounted as follows:
 - (a) the response in the test sample \mathcal{R}_{var} and the response in the nominal sample \mathcal{R}_{nom} are considered as a starting point for the estimate of the JES uncertainty. The deviation of this ratio from unity is defined as:

$$\Delta_{\text{JES}}(p_T, \eta) = \left| 1 - \frac{\mathcal{R}_{\text{var}}(p_T, \eta)}{\mathcal{R}_{\text{nom}}(p_T, \eta)} \right|. \quad (4.5)$$

This deviation is calculated from both the energy and p_T response, leading to $\Delta_{\text{JES}}^E(p_T, \eta)$ for the deviation in the energy response, and to $\Delta_{\text{JES}}^{p_T}(p_T, \eta)$ for the deviation in the transverse momentum response.

- (b) In each bin, the largest value between Δ_{JES}^E and $\Delta_{\text{JES}}^{p_T}$ is considered as the contribution to the final JES systematic uncertainty due to the specific systematic effect:

$$\Delta_{\text{JES}}(p_T, |\eta|) = \max(\Delta_{\text{JES}}^E(p_T, \eta), \Delta_{\text{JES}}^{p_T}(p_T, \eta)). \quad (4.6)$$

For each p_T , η bin, the contributions from the calorimeter, non-closure, Monte Carlo variations and dead material listed above are added in quadrature.

For pseudo-rapidities beyond $|\eta| > 0.8$, the η inter-calibration contribution is estimated for each pseudo-rapidity bin in the End-Cap region as detailed in Section 4.3.1.2. The inter-calibration contribution is added in quadrature to the total JES uncertainty determined in the $0.3 \leq |\eta| < 0.8$ region to estimate the JES uncertainty for jets with $|\eta| > 0.8$, with the exception of the non-closure term that is retained for the specific η region.

The non-closure term gives an important contribution of about 1-2% to the total JES in the for $p_T < 40$ GeV, and becomes smaller than 1% for $p_T > 100$ GeV.

The contribution to the uncertainty due to the description of the pile-up, described in Section 4.3.1, is to be added separately, depending on the number of primary vertexes in the event. In the following, only the uncertainty in the case of a single proton-proton interaction is shown in detail.

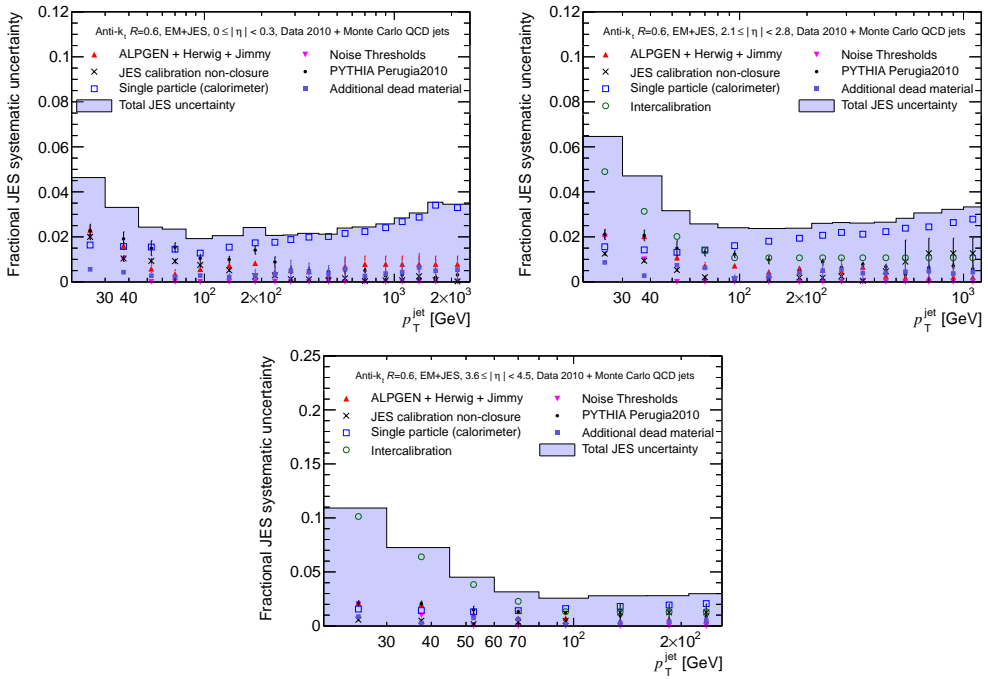


Figure 4.13: Jet energy scale uncertainty in bins of p_T and y for the anti- k_t jets with $R=0.6$. The different components used to estimate the uncertainty are shown. Figures taken from Reference [Doglioni 2011a].

Total jet energy scale systematic uncertainty

Figures 4.13 shows the final fractional jet energy scale systematic uncertainty as a function of jet p_T for three representative pseudo-rapidity regions. On the figure the contribute to the total uncertainty given by the various sources is also shown. The complete list of plots can be found in the Appendix.

The fractional JES uncertainty in the central region amounts to 2 to 4% for $p_T < 60$ GeV, and it is between 2 and 2.5% for $60 \text{ GeV} < p_T < 800 \text{ GeV}$. For jets with $p_T > 800$ GeV, the uncertainty goes from 2.5 to 4%, due to the larger uncertainties for particles with momentum beyond 400 GeV comprised in these jets. The uncertainty amounts to up to 7% and 3%, respectively, for $p_T < 60$ GeV and $p_T > 60$ GeV in the endcap region, where the central uncertainty is taken as a baseline and the uncertainty due to the relative calibration is added. In the forward region, a 13% uncertainty is present for $p_T < 60$ GeV: the increase in the uncertainty is dominated by the modelling of the soft physics in the forward region that is accounted for in the $|\eta|$ -intercalibration contribution, as discussed in the previous Section.

Correlations on the jet energy scale uncertainty

The jet energy scale uncertainty is the dominant uncertainty on the measurement of the inclusive jet cross section. To make a test of the agreement of the measured cross section with the theoretical prediction, one should try to profit as much as possible of the correlations on the sources of the uncertainty.

The most important component in the central pseudo-rapidity region comes from the calorimeter response to jets, shown in Figure 4.8. For this component, the method discussed in Section 4.3.1.1 provides the correlation matrix shown in Figure 4.9 in the central rapidity region $|\eta| < 0.8$ in the different p_T bins⁷.

Given the difficulty of propagating a covariance matrix to the final measurement, another equivalent strategy have been selected to describe this uncertainty.

This strategy divides the covariance matrix in completely uncorrelated sources, which are 100% correlated in p_T . This is convenient because each single component can be propagated to the final measurement, and the final covariance matrix can be calculated for the inclusive jet cross section. This approach is the favored method for fitting the measured spectra to extract the values of the PDFs or the value of the strong coupling constant (see for example Reference [Pumplin 2002]).

In this method, each single component α can be associated to a nuisance parameter λ_α . When propagated to the final measurement, a statistical test can be done minimizing the χ^2 :

$$\chi^2 = \sum_{i=1}^{N_{\text{bins}}} \frac{1}{s_i^2} \left(D_i - T_i - \sum_{\alpha=1}^{N_{\text{sources}}} \lambda_\alpha \sigma_{i\alpha} \right)^2 - \sum_{\alpha=1}^{N_{\text{sources}}} \lambda_\alpha^2, \quad (4.7)$$

where D_i are the data measurements, T_i the theoretical predictions, s_i the statistical error (uncorrelated between the bins), $\sigma_{i\alpha}$ is the systematic uncertainty from source α for the p_T -bin i , and λ_α is a random nuisance parameter. As can be seen from Equation 4.7, it is assumed that all uncertainty sources are uncorrelated with respect to each other, since the penalty term, $\sum_{\alpha=1}^{N_{\text{sources}}} \lambda_\alpha^2$, does not contain off-diagonal elements. However the uncertainty associated with each nuisance parameter is fully correlated across the bins.

An alternative way to express the χ^2 is by taking the inverse of the uncertainty covariance matrix C :

$$\chi^2 = \sum_{i=1}^{N_{\text{bins}}} \sum_{j=1}^{N_{\text{bins}}} (D_i - T_i) C_{ij}^{-1} (D_j - T_j). \quad (4.8)$$

It can be shown (see pages 4-5 of Reference [Nadolsky]) that the full covariance matrix used in Equation 4.8 can be constructed from the uncertainty components $\sigma_{i\alpha}$ by

$$C_{ij} = s_i s_j \delta_{ij} + \sum_{\alpha=1}^{N_{\text{sources}}} \sigma_{i\alpha} \sigma_{j\alpha}. \quad (4.9)$$

The nuisance parameter representation (Equation 4.7) is usually technically easier to deal with and also has the advantage that it may indicate which uncertainty source is responsible for any discrepancy between data and theory. This approach is hence preferred.

⁷The method described in Section 4.3.1.1 has been used to derive the correlation matrix for the anti- k_t jets with $R=0.4$ and with $R=0.6$.

However, as previously mentioned, it requires each uncertainty source to be fully correlated across all bins.

The uncertainty on the calorimeter response, responsible for the covariance in Figure 4.9, is split into seven subcomponents that each have the desired property of being fully correlated versus p_T and η while being uncorrelated with respect to each other. These components are shown in Figure 4.14.

To see how well the correlations are described when using these seven components, the (p_T, p_T) correlation matrix from these components has been compared with the original one in Figure 4.9. All correlations are preserved within 2% for jets above 30 GeV.

Other six components of the JES uncertainty have been introduced in the first part of Section 4.3.1. These components are shown in Figure 4.13, labeled as "ALPGEN +HERWIG +JIMMY ", "JES calibration non-closure", "Noise Thresholds", "PYTHIA Perugia2010", "Additional dead material", "Intercalibration".

Table 4.1 summarizes all 13 JES uncertainty components (seven from the calorimeter response - seen in Figure 4.14 - and six from other sources as previously explained).

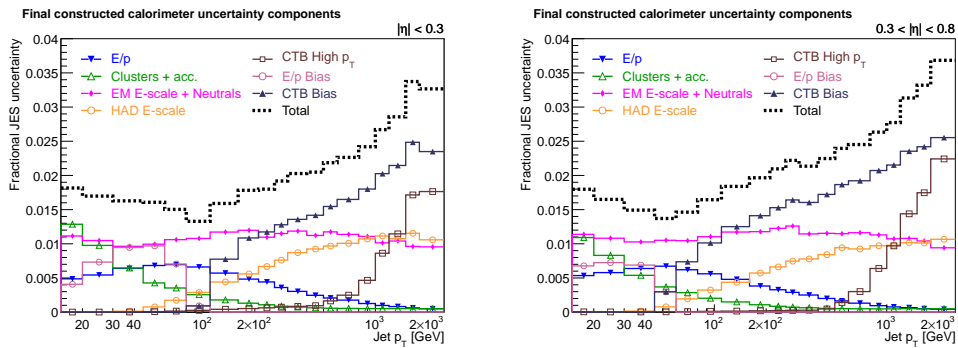


Figure 4.14: Generated subcomponents of the calorimeter jet energy scale uncertainty. As desired, the sum in quadrature of these uncertainties is equal to the original calorimeter uncertainty labeled as “Single particle (calorimeter)” in Figure 4.13, and the covariance between any two bins is consistent with the corresponding value in Figure 4.9. Plot taken from Reference [Gillberg 2011].

Table 4.1: Summary of the jet energy scale uncertainty components. Components 7-13 are artificially constructed from a covariance matrix, and hence do not directly correspond to a source. The descriptions of these components are therefore only interpretations. The total uncertainty of components 1-6 can be seen in Figure 4.13, and components 7-13 in Figure 4.14.

Source	Approximate description
JES component 1	Uncertainty due to the noise suppression threshold used for reconstruction of calorimeter clusters
JES component 2	Uncertainty of the modelling of the underlying event (Default PYTHIA AMBT1 tune vs the Perugia2010 tune)
JES component 3	Uncertainty from the parton showering, hadronization and parton density functions (default PYTHIA AMBT1 tune vs ALPGEN dijet using HERWIG for showering and hadronization, JIMMY for the underlying events, and different pdf: CTEQ6L1)
JES component 4	“Non-closure” of calibration (residual deviation after applying the MC derived calibration to nominal MC)
JES component 5	Uncertainty due to dead material description in MC
JES component 6	Relative uncertainty of forward jets ($ \eta > 0.8$) measured from dijet balance.
JES component 7	Largest part of this uncertainty comes from the theoretical modelling of forward jets
JES component 8	Systematic uncertainty of E/p single particle measurements
JES component 9	Cluster thresholds and acceptance cuts (of the single particle response analysis)
JES component 10	E -scale of the EM calorimeter and calorimeter response to neutral hadrons
JES component 11	Hadronic calorimeter energy scale
JES component 12	High p_T jet response from combined test beam
JES component 13	Data-MC discrepancy of E/p for single isolated hadrons
	Data-MC discrepancy of the response measured in the combined test beam

4.3.1.4 In-situ checks of the jet energy scale

With the method adopted for the first data in ATLAS, the uncertainty for the high p_T jets (above 600 GeV) is estimated extrapolating the measurement at lower scales (the calorimeter response to single pions have been studies for $p_T < 350$ GeV). Since the uncertainty on the jet energy scale is the dominant uncertainty in the measurement of the inclusive jet cross section, a direct check of the goodness of the JES is necessary. With the integrated luminosity used in this analysis, the absolute transverse momentum of jets has been probed with photon-jet events up to a few hundred GeV.

With this events the jet p_T scale can be assessed exploiting the p_T balance constraint of the jet against the precisely measured photon (see Reference [[ATLAS Collaboration 2011c](#)]). The multi-jet balance technique allows the extension of the in-situ test up to the TeV-scale using the abundant multi-jet events. A complete description of the method can be found in Reference [[ATLAS Collaboration 2011n](#)].

High energy jets: Checks on the energy scale stability

The multi-jet balance technique has been developed to verify the energy scale of jets of very high transverse momentum.

The method exploits the p_T balance in events where the highest- p_T jet (leading jet) is produced back-to-back to a multi-jet system. The leading jet is required to have significantly larger transverse momentum than other jets in the event. In this way the leading jet is at a higher p_T scale compared to other reconstructed jets, termed non-leading jets. The ensemble of the non-leading jets (passing the selection cuts) is referred to as a recoil-system. As example, the event topology used in this analysis is shown in Figure 4.15. The vectorial sum of the transverse momenta of all non-leading jets defines the transverse momentum of the recoil-system ($\vec{p}_T^{\text{Recoil}}$) that is expected to approximately balance the transverse momentum of the leading jet. Thus a correlation between the momentum scale of the leading jet, and the scale of the non-leading jets can be established.

If the absolute JES is well known for all non-leading jets, the JES of the leading jet can be verified by studying the multi-jet balance (MJB) that is defined as the ratio:

$$\text{MJB} = \frac{|\vec{p}_T^{\text{Leading}}|}{|\vec{p}_T^{\text{Recoil}}|}. \quad (4.10)$$

Moreover the $\vec{p}_T^{\text{Recoil}}$ is a good estimator of the true leading jet p_T (on average, the ratio of the reconstructed $\vec{p}_T^{\text{Recoil}}$ to the leading jet truth p_T is consistent with one to better than 1%), and it is therefore interesting to study MJB as a function of p_T^{Recoil} .

In the ideal case MJB should be equal to one, however various effects such as the presence of close-by jets, of soft gluon emission, or pile-up or the analysis cuts themselves may introduce a bias. Even more important than the particular value of MJB is the comparison between the balance measured in the simulation (MJB^{MC}) and data (MJB^{Data}). Any discrepancy in the description of the multi-jet balance should be interpreted as a source of systematic uncertainty and therefore the ratio $\text{MJB}^{\text{Data}}/\text{MJB}^{\text{MC}}$ can be used to assess the high- p_T JES uncertainty. The jets belonging to the recoil-system must be confined to a

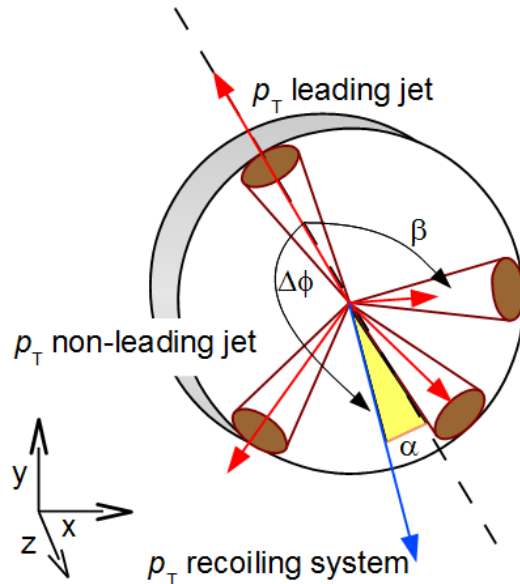


Figure 4.15: Sketch of the event topology used for the multi-jet balance technique.

lower jet energy scale with respect to the leading jet in order to ensure that the multi-jet balance is testing the absolute high p_T scale and not only the inter-calibration between jets. There are various analysis methods to constrain the leading jet to a higher p_T scale with respect to the jets in the recoil-system [Ruehr 2009]. In this analysis this is done by setting a maximum limit on the ratio between the transverse momentum of second highest- p_T jet ($p_T(J2)$) and the p_T^{Recoil} ($p_T(J2)/p_T^{\text{Recoil}} < 0.6$).

The jets belonging to the recoil-system are required to have a $p_T > 20 \text{ GeV}$ and $|y| < 2.8$. Events with leptons or photons, with jets which do not pass the jet cleaning criteria in Section 4.1, or with less than two jets in the recoil-system are rejected. To reduce the bias from the trigger and jet selection, events with $p_T^{\text{Recoil}} < 80 \text{ GeV}$ have been rejected. Other two important topological variables have been used to suppress the unbalance due to the emission of soft radiation in the event. The first variable is $\alpha = |\Delta\phi - \pi|$, where $\Delta\phi$ is the azimuthal opening angle between the highest- p_T jet and the recoil-system. It is used to select events in which the leading jet and the recoil-sum are back-to-back ($\alpha < 0.3 \text{ radian}$). The second variable, β , is the azimuthal opening angle of the non-leading jet that is closest to the leading jet in ϕ , measured with respect to the leading jet itself. This variable is used to reject the events in which part of the jets in the recoil-system is in the direction of the leading jet ($\beta > 1 \text{ radian}$), reducing the contribution of the soft radiation in the direction of the leading jet.

Several Monte Carlo samples of QCD jet events produced with all the generators and tunes listed in the first part of Table 2.1 have been used to study the MJB^{MC}. The different generators and tunes have been used to check the stability of the MJB estimator, when changing PDF, parton shower, underlying event models and hadronization models. None of the samples include multiple proton-proton collisions in the simulation. However, in order to evaluate the systematic uncertainty introduced by the pile-up collisions, a PYTHIA

sample that includes pile-up has been used. In this case events have been weighted in order to reproduce the correct vertex multiplicity. All generated samples are then passed through a full GEANT4 [Agostinelli 2003] simulation of the ATLAS detector. Finally, the MC simulated events are reconstructed and analyzed with the same analysis chain as the data.

The multi-jet balances obtained from the selected events for the anti- k_t jet algorithm with $R = 0.6$ and $R = 0.4$ are shown in Figure 4.16(a) and (b) for the data and Monte Carlo. The uncertainties shown in the Figure 4.16(a) and (b) are statistical only.

The transverse momentum of the recoil-system ranges from 80 GeV up to 1.0 TeV (1.2 TeV) for the anti- k_t jets with $R = 0.6$ (0.4). The multi-jet balance at low p_T^{Recoil} values shows a bias towards values lower than one. This is a consequence of the binning of p_T^{Recoil} . The effect is in fact observed already at truth level and, after reconstruction, is correctly reproduced by the MC. The ratios between the distributions obtained from the data and the MC for the two jet sizes are also shown in the lower part of Figure 4.16(a) and (b). The agreement between the data and MC, evaluated as the average value of the data over MC ratio, is achieved within 3 % up to the TeV region.

The data/MC ratio provides an estimate of the uncertainty on the leading jet p_T scale. However in order to correctly constrain this estimate, the systematic uncertainties need to be addressed.

Two main categories of sources of systematic uncertainties have been considered: 1) those that affect the reference p_T of the recoil-system, and 2) those that affect the variable MJB used to probe the leading jet p_T , due to analysis cuts or a imperfect MC modeling of the event.

The systematic uncertainty on the recoil-system has been calculated taking into account the following effects:

- the standard JES uncertainty on the p_T of each jet composing the recoil-system;
- the dependence of the jet response on the angular distance to the closest jet for the recoiling system as discussed in Reference [ATLAS Collaboration 2011h];
- the dependence of the jet response on the flavor composition of the recoil-system as discussed in Reference [ATLAS Collaboration 2011h].

The systematic uncertainty on MJB due to the uncertainty on the p_T^{Recoil} has been estimated by calculating the multi-jet balance shifting the p_T of all jets in the recoil-system up and down by the systematic uncertainties. The total systematic uncertainty is obtained by summing in quadrature the contribution of each source.

The second category of systematic uncertainty includes sources that affect the MJB variable which is used to probe the high- p_T jet scale and that are due to the analysis cuts or to the imperfect MC modeling. In the following the various sources considered are discussed.

- The imperfect description given by the MC for the variables used to select the events might induce a systematic uncertainty on the multi-jet balance. All relevant analysis

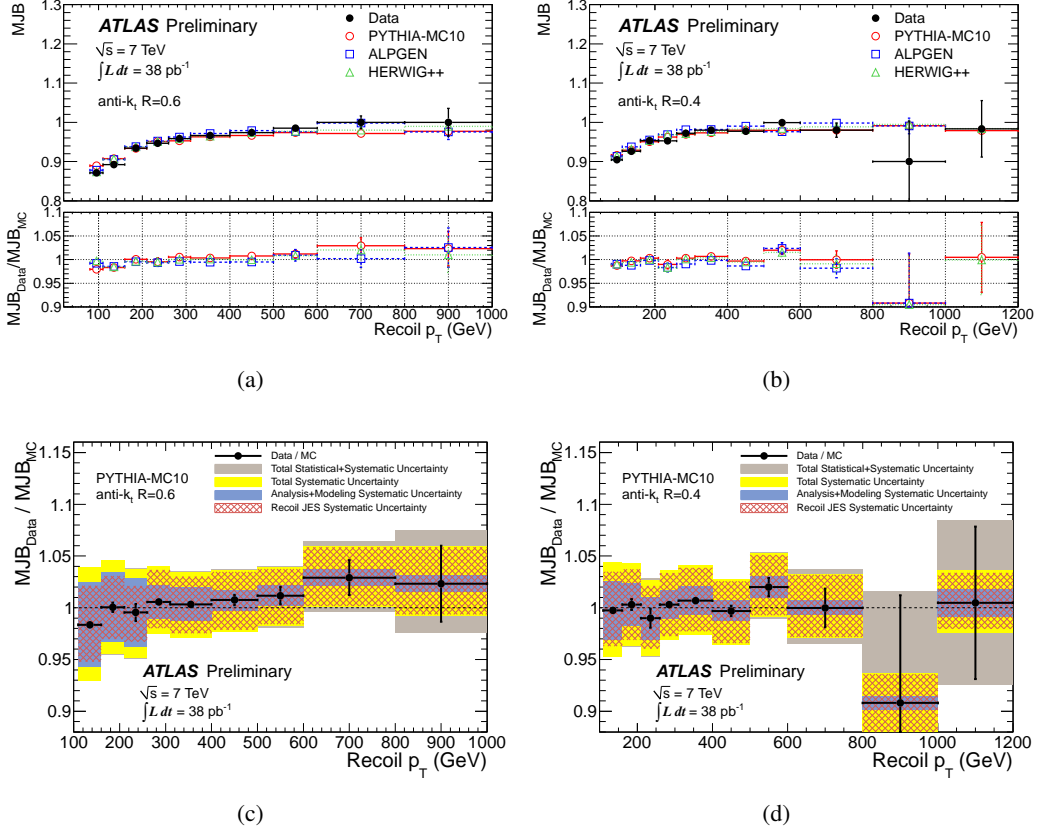


Figure 4.16: (top) MJB as a function of the recoil-system p_T for data and MC for the anti- k_t algorithm with distance parameter 0.6 (a) and 0.4 (b). The transverse momentum of the recoil-system ranges from 80 GeV up to 1.0 TeV (1.2 TeV) for the anti- k_t jets with $R = 0.6$ (0.4). (bottom) Ratio of the data to MC for MJB as a function of the recoil-system p_T for anti- k_t jets with $R = 0.6$ (c) and $R = 0.4$ (d). The colored regions show the total uncertainty (grey - dark) obtained as the squared sum of the total systematic uncertainty (yellow - light) and of the statistical uncertainty (error bars). Also displayed are the contributions to the systematic uncertainty due to analysis cuts and event modeling (blue - darkest) and to the jet energy scale for jets in the recoil-system (hatched band). These Figures are taken from Reference [ATLAS Collaboration 2011n].

(bottom) Ratio of the data to MC for MJB as a function of the recoil-system p_T for anti- k_t jets with $R = 0.6$ (c) and $R = 0.4$ (d). The colored regions show the total uncertainty (grey - dark) obtained as the squared sum of the total systematic uncertainty (yellow - light) and of the statistical uncertainty (error bars). Also displayed are the contributions to the systematic uncertainty due to analysis cuts and event modeling (blue - darkest) and to the jet energy scale for jets in the recoil-system (hatched band). These Figures are taken from Reference [ATLAS Collaboration 2011n].

Source	anti- k_t R = 0.6/0.4
Jet energy scale of the recoil-system	4 %
Flavor composition	$\simeq 1$ %
Close-by jets	2 %
Jet p_T threshold	< 2 %
α cut	< 1 %
β cut	< 1 %
$p_T(J2)/p_T^{\text{Recoil}}$ cut	3 %
Underlying event modeling	2 %
Fragmentation modeling	1.5 %
Pile-up	< 1 %

Table 4.2: Maximum values of the systematic uncertainties in the whole p_T^{Recoil} range, for all effects considered.

cuts have been varied in a range where the corresponding kinematic variables are not strongly biased;

- The impact of the jet rapidity acceptance. This selection could cause an additional systematic uncertainty, if the fraction of jets produced outside the rapidity range differs in the data and MC, and the difference can affect the MJB constructed from jets inside the range.
- Effect of the underlying event, fragmentation and ISR/FSR modeling.
- Effect of the description of the Pile-up on the Monte Carlo simulation.

A summary of all the systematic uncertainties are shown in Table 4.2. At high transverse momentum the main contribution to the systematic uncertainty is due to the standard jet energy scale uncertainty.

The summary of all systematic uncertainties from the two categories and the total systematic uncertainty obtained by adding them in quadrature, overlaid on the data to MC ratio of the multi-jet balance, is presented in Figure 4.16(c) and (d) for anti- k_t jets with $R = 0.6$ and $R=0.4$.

The systematic uncertainty due to the knowledge of the recoil-system transverse momentum amounts to about 4 % for jets of $p_T = 1$ TeV. The presently collected data sample allows the validation of the high- p_T JES within 5% up to 1 TeV for anti- k_t jets with $R = 0.6$ and up to 800 GeV for $R = 0.4$. In this range the statistical uncertainty is roughly equivalent to or smaller than the systematic uncertainty.

4.3.2 Jet energy resolution

The estimate of the jet energy resolution is important to validate the fluctuation in the jet simulation in the Monte Carlo. For the inclusive jet cross section, this has an impact on the unfolding procedure, used to minimize the effects of the detector from the measured cross section. Two in-situ methods have been used by the ATLAS Collaboration to check the correctness of the jet energy resolution: the di-jet balance method (discussed in Reference [Abbott 2001]) and the bi-sector method (discussed in Reference [Bagnaia 1984]). In the analysis of the inclusive jet cross section, the transfer matrix used to perform the unfolding correction for the detector effects (discussed in Section 5.3) have been derived from the Monte Carlo with the nominal simulated resolution. The results of these methods discussed in this Section have been used to estimate the uncertainty on Monte Carlo description of the jet energy resolution.

These methods involve different assumptions that can be validated in data, and are sensitive to different sources of systematic uncertainties. The use of two independent measurements of the jet energy resolution gives more robustness to the estimate of the resolution. The jets, measured in the 2010 data, are binned in different regions of pseudo-rapidity, with a binning which mimic the final binning for the measurement of the inclusive jet cross section.

The di-jet balance method for the determination of the jet p_T resolution is based on momentum conservation in the transverse plane. The asymmetry between the transverse momenta of the two leading jets $A(p_T(jA), p_T(jB))$ is defined as:

$$A(p_T(jA), p_T(jB)) = \frac{p_T(jA) - p_T(jB)}{p_T(jA) + p_T(jB)} \quad (4.11)$$

where the jA and jB identify the first two leading jet ordered in p_T . The distribution of A has a spread σ_A which is:

$$\sigma_A \sim \frac{\sigma_{p_T}}{\sqrt{2} < p_T >} \quad (4.12)$$

if the two jets are in the same region of the detector and have the same resolution σ_{p_T} .

In order to be less sensitive to the soft radiation effects, events with additional jets with $p_T^{EM} > 10$ GeV are discarded, and an extra correction is applied to correct for it.

The bi-sector method is based on the definition of an imbalance (transverse) vector p_T , which is defined as the vector sum of the two leading jets in the di-jet event. This vector is projected along an orthogonal coordinate system in the transverse plane (ψ, η) where η is chosen in the direction that bisects $\Delta\phi_{1,2} = \phi_1 - \phi_2$, the angle formed by the two leading jets in the transverse plane. This is illustrated in Figure 4.17. For a perfectly balanced di-jet system, the vectorial sum of the p_T of the first two jets is equal to 0. In the real case, if both the jets belong to the same y region, so they have the same average energy resolution, it can be shown that:

$$\frac{\sigma_{p_T}}{p_T} = \frac{\sqrt{\sigma_\psi^2 - \sigma_\eta^2}}{p_T \sqrt{2} |\cos \Delta\phi_{1,2}|} \quad (4.13)$$

where σ_ψ and σ_η are the measured resolutions in the ψ and η directions. In this case, soft radiation effects are removed by subtracting in quadrature σ_ψ and σ_η .

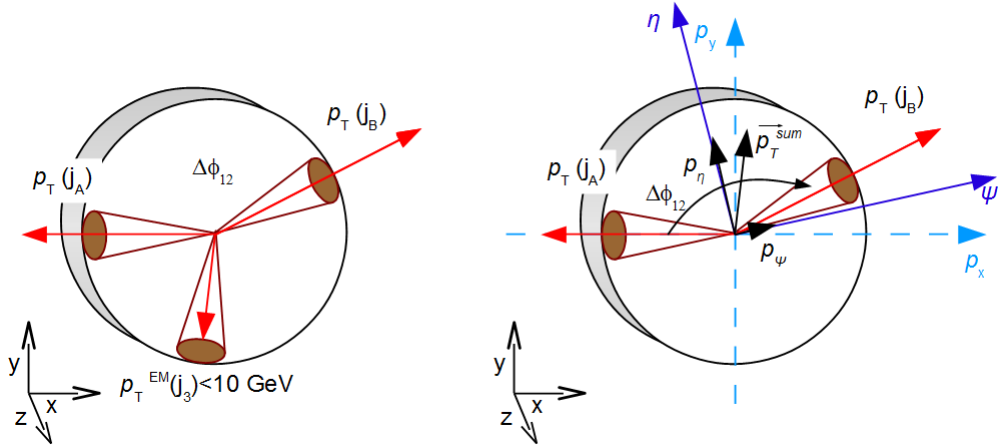


Figure 4.17: Sketch with the variables used in dijet balance and the bi-sector techniques.

By using these two methods, the jet energy resolution has been estimated with a sample of 35 pb^{-1} of data. Data and Monte Carlo simulation distributions are in agreement for both the methods, and the Monte Carlo simulation describes the jet energy resolution measured in data within 10% for jets between 30 and 500 GeV in p_T and $|y| < 2.8$. For the other regions used in the inclusive jet cross section, the estimate of the uncertainty is extrapolated in a conservative way, assuming $\sim 30\%$ uncertainty at $p_T = 20 \text{ GeV}$.

The jet resolution in p_T for the different rapidity regions, as a function of p_T , with the systematic uncertainty coming from the in-situ measurements, are shown in Figure 4.18, for the anti- k_t jet algorithm with $R=0.6$ in some representative rapidity regions. The complete list of figures can be found in the Appendix.

These uncertainties have been propagated to the final inclusive jet cross section measurement, via the unfolding procedure, as discussed in Section 5.3.

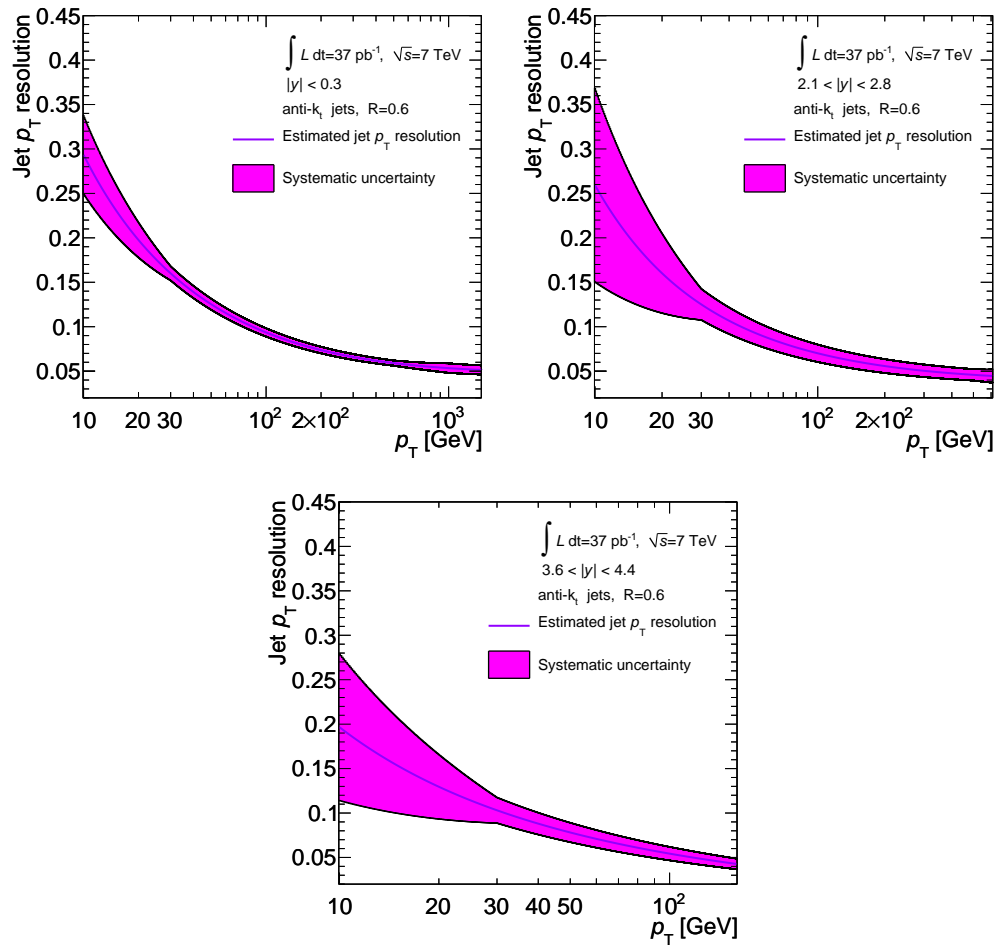


Figure 4.18: Jet energy resolution as a function of p_T in three representative regions of y for anti- k_t jets with $R=0.6$.

CHAPTER 5

The inclusive jet cross section: Measurement with 37 pb^{-1}

Contents

5.1	Trigger and luminosity	104
5.1.1	Trigger strategy	104
5.1.2	Luminosity	108
5.2	Event and jet selection	110
5.2.1	Jet selection	111
5.2.2	Data stability	111
5.3	Correcting the detector effects: unfolding	111
5.3.1	Monte Carlo samples for the unfolding	112
5.3.2	Detector level shape: improving the Monte Carlo descriptions	113
5.3.3	Unfolding strategy	115
5.3.4	Computing the statistical uncertainty with the IDS unfolding	116
5.3.5	Systematic uncertainty on the unfolding procedure	117
5.3.6	Comparison between IDS and bin-by-bin unfolding	118
5.4	Systematic uncertainties	120
5.4.1	Uncertainty on the jet energy scale	120
5.4.2	Uncertainty on the jet energy resolution	123
5.4.3	Total systematic uncertainty	124
5.4.4	Correlations	125
5.5	Results	129

The jet cross section measurements detailed in this thesis are obtained from the full 2010 dataset of proton-proton collisions at $\sqrt{s} = 7 \text{ TeV}$, with the exceptions of the low- p_T region $20 \leq p_T < 60 \text{ GeV}$, and the forward region $|y| > 2.8$. For low- p_T jets, only data taken up to the beginning of June are considered since the instantaneous luminosity of the accelerator was low enough that pile-up contributions were negligible, and the majority of the bandwidth was allocated to the Minimum Bias trigger that is used to collect low- p_T events. For forward jets in $|y| > 2.8$, the first data taking period was not used because the forward jet trigger was not yet commissioned.

Since the life time of the LHC colliding beams strongly depends on the conditions of the accelerator (it could be from few hours to more than one day), the acquired data is

divided in different blocks termed runs. The runs are usually as long as a the beam life time. In order to select periods in which the detector is in a good status, the runs are further divided in subset termed luminosity blocks (LB) corresponding to data taking periods of about 1 minute. Only the luminosity blocks with a good status for the L1 central trigger processor, solenoid magnet, inner detectors (Pixel, SCT, and TRT), calorimeters (barrel, endcap, and forward), luminosity measurement, as well as tracking, jet, and missing energy reconstruction performance are used. In addition, good data quality was required for the high-level trigger during the periods when this device was used. No requirement was placed on the muon spectrometer, which was not used in these measurements.

The runs in 2010 have been divided into 9 periods, summarized in Section 1.2.6. Within each period, the accelerator and the detector conditions can be considered uniform. A check of the stability of the measurement of the inclusive jet cross section in the different periods will be discussed in Section 5.2.2.

5.1 Trigger and luminosity

Three different triggers have been used in this measurement: the Minimum Bias Trigger Scintillators (MBTS); the central jet trigger, covering $|\eta| < 3.2$; and the forward jet trigger, spanning $3.1 < |\eta| < 4.9$.

The MBTS trigger (L1_MBTS_1) requires at least one hit in the minimum bias scintillators located in front of the endcap cryostats, covering $2.09 < |\eta| < 3.84$ (see Section 1.2.4). It has been demonstrated to have negligible inefficiency for the events of interest for this analysis [ATLAS Collaboration 2010c] and is used to select events with jets having transverse momentum between 20-60 GeV.

The central and forward jet triggers are composed of three consecutive levels: Level 1 (L1), Level 2 (L2) and Event Filter (EF) (see Section 1.2.4). Up to summer 2010 only L1 information was used to select events, while L2 was used from the summer to the end of the year. The jet trigger did not reject events at the Event Filter stage in 2010. The central and forward jet triggers independently select data using several jet E_T^{EM} thresholds that each require the presence of a jet with sufficient E_T^{EM} at the electromagnetic (EM) scale (see Section 3.1.2). For each L1 threshold ($E_T^{\text{EM}} > 5 \text{ GeV}$, $E_T^{\text{EM}} > 10 \text{ GeV}$, $E_T^{\text{EM}} > 15 \text{ GeV}$, $E_T^{\text{EM}} > 30 \text{ GeV}$, $E_T^{\text{EM}} > 55 \text{ GeV}$, $E_T^{\text{EM}} > 75 \text{ GeV}$, $E_T^{\text{EM}} > 95 \text{ GeV}$ and $E_T^{\text{EM}} > 115 \text{ GeV}$), there is a corresponding L2 threshold that is generally placed 15 GeV above the L1 value¹. Each such L1+L2 combination is referred to as a L2 trigger chain.

5.1.1 Trigger strategy

As the instantaneous luminosity increased throughout 2010, it was necessary to prescale triggers with lower E_T^{EM} thresholds, while the triggers with the highest E_T^{EM} thresholds remained unprescaled. A trigger is prescaled if only one event every P (the value of the prescale) triggered events is saved on the disk. The final measurement must correct for the effect of the prescale. For each p_T -bin considered in this analysis, a dedicated trigger

¹The exception is the lowest threshold, for which the difference between L1 and L2 is 10 GeV.

Central $ y < 2.8$, except for crack p_T range	Period A*-F	Period G-H
20-30	L1_MBTS_1	n/a
30-45	L1_MBTS_1	n/a
45-60	L1_MBTS_1	n/a
60-80	$L1 E_T^{\text{EM}} > 5 \text{ GeV}$	$L2 E_T^{\text{EM}} > 15 \text{ GeV}$
80-110	$L1 E_T^{\text{EM}} > 15 \text{ GeV}$	$L2 E_T^{\text{EM}} > 30 \text{ GeV}$
110-160	$L1 E_T^{\text{EM}} > 30 \text{ GeV}$	$L2 E_T^{\text{EM}} > 45 \text{ GeV}$
160-210	$L1 E_T^{\text{EM}} > 55 \text{ GeV}$	$L2 E_T^{\text{EM}} > 70 \text{ GeV}$
210-260	$L1 E_T^{\text{EM}} > 75 \text{ GeV}$	$L2 E_T^{\text{EM}} > 90 \text{ GeV}$
260-310	$L1 E_T^{\text{EM}} > 95 \text{ GeV}$	$L1 E_T^{\text{EM}} > 95 \text{ GeV}$
310+	$L1 E_T^{\text{EM}} > 95 \text{ GeV}$	$L1 E_T^{\text{EM}} > 115 \text{ GeV}$

Table 5.1: The trigger chains used for the inclusive jet analysis in the region $|y| < 2.8$, except for the crack in the region $1.2 \leq |y| < 2.1$. The measurement for $20 \text{ GeV} < p_T < 60 \text{ GeV}$ over the range $|y| < 2.8$ is done using only the Periods A-C, to limit the impact of the pile-up. The L1_MBTS_1 trigger is used in this p_T -range. Due to mis-timings in the Level-1 central jet trigger hardware, L1_MBTS_1 was also used to trigger all jets before run 152777. The period after this timing change is here denoted as “A**”.

threshold is chosen that is fully efficient ($> 99\%$) while having as small a prescale factor as possible. In the following lines the association (p_T -bin,Trigger) is discussed. As an example, in an event triggered only by the chain $T1$, associated to the p_T range $60 \text{ GeV} - 80 \text{ GeV}$ in the central rapidity region, only the jets in this interval are used for the measurement, discarding all the other jets in the event. In this way, one can simplify the correction for the prescales.

Given the complexity of the trigger strategy in the HEC-FCal transition region $2.8 < |y| < 3.6$ where neither the central nor the forward trigger is fully efficient, the discussion of this region will be postponed at the end of this Section.

Central jet trigger efficiency

The L2 trigger efficiencies as a function of the reconstructed jet p_T (at calibrated energy scale), for the anti- k_t jets with $R=0.6$, are shown in Figure 5.1 for the central (top left) and for the crack (top right) regions. The crack region, lying between the barrel and endcap calorimeters ($1.2 \leq |y| < 2.1$), shows, as expect, a lower efficiency. Similar performances are obtained for anti- k_t jets with $R=0.4$. Tables 5.1-5.2 summarize which triggers are used for each p_T bin of the cross section measurement and for each period of data for the central and crack regions ($|y| < 2.8$). The trigger chains corresponding to the two highest p_T thresholds do not apply the L2 selection, therefore in these cases the L1 thresholds are listed.

Central crack $1.2 \leq y < 2.1$ p_T range	Period A*-F	Period G-H
20-30	L1_MBTS_1	n/a
30-45	L1_MBTS_1	n/a
45-60	L1_MBTS_1	n/a
60-80	$\text{L1 } E_T^{\text{EM}} > 5 \text{ GeV}$	$\text{L2 } E_T^{\text{EM}} > 15 \text{ GeV}$
80-110	$\text{L1 } E_T^{\text{EM}} > 5 \text{ GeV}$	$\text{L2 } E_T^{\text{EM}} > 15 \text{ GeV}$
110-160	$\text{L1 } E_T^{\text{EM}} > 15 \text{ GeV}$	$\text{L2 } E_T^{\text{EM}} > 30 \text{ GeV}$
160-210	$\text{L1 } E_T^{\text{EM}} > 30 \text{ GeV}$	$\text{L2 } E_T^{\text{EM}} > 45 \text{ GeV}$
210-260	$\text{L1 } E_T^{\text{EM}} > 55 \text{ GeV}$	$\text{L2 } E_T^{\text{EM}} > 70 \text{ GeV}$
260-310	$\text{L1 } E_T^{\text{EM}} > 75 \text{ GeV}$	$\text{L2 } E_T^{\text{EM}} > 90 \text{ GeV}$
310-400	$\text{L1 } E_T^{\text{EM}} > 95 \text{ GeV}$	$\text{L1 } E_T^{\text{EM}} > 95 \text{ GeV}$
400+	$\text{L1 } E_T^{\text{EM}} > 95 \text{ GeV}$	$\text{L1 } E_T^{\text{EM}} > 115 \text{ GeV}$

Table 5.2: The trigger chains used for the inclusive jet analysis in the crack region $1.2 \leq |y| < 2.1$. The measurement for $20 \text{ GeV} < p_T < 60 \text{ GeV}$ over the range $1.2 \leq |y| < 2.1$ is done using only the Periods A-C, to limit the impact of the pile-up. The L1_MBTS_1 trigger is used in this p_T -range. Due to mis-timings in the Level-1 central jet trigger hardware, L1_MBTS_1 was also used to trigger all jets before run 152777. The period after this timing change is here denoted as “A*” (n/a indicates not assigned).

Forward jet trigger efficiency

The trigger efficiency for the most forward rapidity region $3.6 \leq |y| < 4.4$, where jets are fully contained in the forward calorimeter, is shown in Figure 5.1 bottom left. Due to a known problem with a dead trigger tower in a region of the FCal, the asymptotic efficiency of some chains does not reach 100%. Since this effect is very small (smaller than 1%), and the per-event efficiency definition is used, such that an offline jet in the bad trigger tower can be recorded because there was another jet in the event, a systematic uncertainty has been applied rather than a restriction of the phase-space of the measurement. For triggers not reaching 100% efficiency (but 99% or more), the plateau value is defined as the point where the trigger efficiency reaches the asymptotic value.

Table 5.3 summarizes the triggers that are used for each bin of the cross section measurement for each period of data used for the forward regions ($3.6 \leq |y| < 4.4$).

Trigger efficiency in the transition region

For inclusive jets in the HEC-FCal transition region $2.8 < |y| < 3.6$, neither the central nor the forward trigger is fully efficient. Instead the logical OR of the triggers is used, which is fully efficient at sufficiently high jet p_T , as can be seen in Figure 5.1 bottom right.

Table 5.4 summarizes the triggers that are used for each bin of the cross section measurement for each period of data used for the forward regions ($2.8 \leq |y| < 3.6$).

p_T range Forward region $3.6 \leq y < 4.4$	Period A-C	Period E5-F	Period G-H
20-30	L1_MBTS_1	n/a	n/a
30-45	n/a	$L1 E_T^{EM} > 10 \text{ GeV}$	n/a
45-60	n/a	$L1 E_T^{EM} > 10 \text{ GeV}$	n/a
60-80	n/a	$L1 E_T^{EM} > 10 \text{ GeV}$	$L2 E_T^{EM} > 25 \text{ GeV}$
80-110	n/a	$L1 E_T^{EM} > 30 \text{ GeV}$	$L2 E_T^{EM} > 25 \text{ GeV}$
110-160	n/a	$L1 E_T^{EM} > 55 \text{ GeV}$	$L2 E_T^{EM} > 45 \text{ GeV}$
160+	n/a	$L1 E_T^{EM} > 55 \text{ GeV}$	$L2 E_T^{EM} > 70 \text{ GeV}$

Table 5.3: The trigger chains used for this analysis in the very forward region of $3.6 \leq |y| < 4.4$ (n/a indicates not assigned).

p_T range Transition region $2.8 \leq y < 3.6$	Period A-C	Period E5-F	Period G-H
20-30	L1_MBTS_1	n/a	n/a
30-45	L1_MBTS_1	n/a	n/a
45-60	L1_MBTS_1	n/a	n/a
60-80	n/a	$L1 E_T^{EM} > 10 \text{ GeV}$ (central OR forward)	n/a
80-110	n/a	$L1 E_T^{EM} > 10 \text{ GeV}$ (central OR forward)	$L2 E_T^{EM} > 25 \text{ GeV}$ (central OR forward)
110-160	n/a	$L1 E_T^{EM} > 30 \text{ GeV}$ (central OR forward)	$L2 E_T^{EM} > 45 \text{ GeV}$ (central OR forward)
160-210	n/a	$L1 E_T^{EM} > 55 \text{ GeV}$ (central OR forward)	$L2 E_T^{EM} > 45 \text{ GeV}$ (central OR forward)
210-260	n/a	$L1 E_T^{EM} > 55 \text{ GeV}$ (central OR forward)	$L2 E_T^{EM} > 70 \text{ GeV}$ (central OR forward)
260+	n/a	$L1 E_T^{EM} > 55 \text{ GeV}$ (central OR forward)	$L2 E_T^{EM} > 70 \text{ GeV}$ (central OR forward)

Table 5.4: The trigger chains used for this analysis in the region $2.8 \leq |y| < 3.6$ (n/a indicates not assigned).

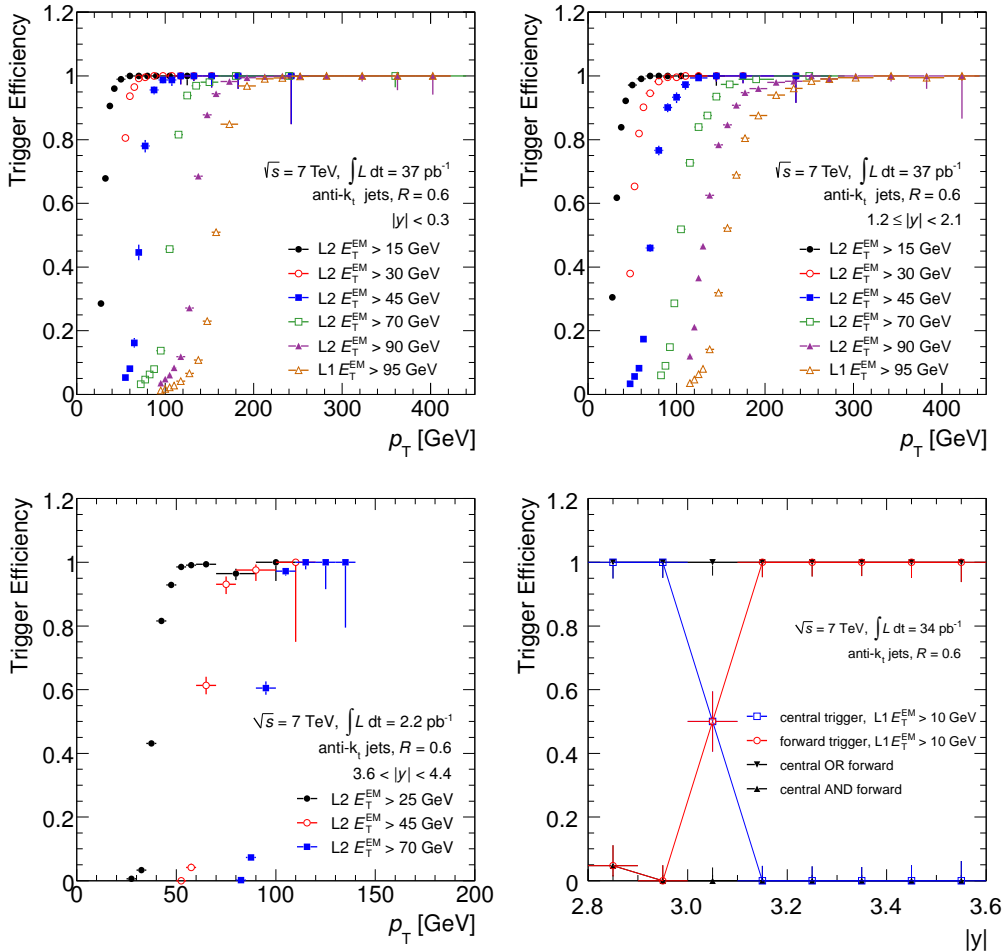


Figure 5.1: - Efficiency of the trigger system of the anti- k_t jets with $R=0.6$. The four plots show the L2 trigger chain in different regions of the detector. On bottom right: trigger efficiency in the transition region.

A specific strategy to take into account the different prescale combinations for the inclusive jet cross section in this transition region have been used, as introduced in the next Section.

5.1.2 Luminosity

The luminosity is independently determined using several detectors and algorithms, each having different acceptances, systematic uncertainties and sensitivity to background. A detailed description of the techniques used for the luminosity measurement of their performances can be found in References [[ATLAS Collaboration 2011i](#), [ATLAS Collaboration 2011o](#)]. In the following a brief description of the most important concepts used for the luminosity measurements is given. By using the Equation 1.1, the

luminosity can be expressed as:

$$\mathcal{L} = \frac{R_{vis}}{\sigma_{vis}} \quad (5.1)$$

where R_{vis} is the observed interaction rate measured by a particular detector and algorithm, and σ_{vis} is the total inelastic cross section multiplied by the efficiency of a particular detector and algorithm. Since R_{vis} is an experimental observable, the calibration of the luminosity scale for a particular detector and algorithm is equivalent to determining the visible cross section σ_{vis} . As reported in Reference [ATLAS Collaboration 2011o], the calibration of σ_{vis} is performed using dedicated Van der Meer scans, where the absolute luminosity can be inferred from direct measurement of the machine parameters, as reported in Equation:

$$\mathcal{L} = f \times n \frac{N_1 \times N_2}{A} \quad (5.2)$$

The Van der Meer scan measured the transverse size of the beams (to determine A). The other variables in Equation 5.2 are precisely measured with dedicated accelerator detectors. The direct measurement of the luminosity in a dedicated run is used to have a precise estimate of σ_{vis} for the different detectors and algorithms.

The total systematic uncertainty on the measurement of the luminosity is of 3.4%, which takes into account all the uncertainties on the determination of σ_{vis} , and the uncertainties in R_{vis} .

During normal ATLAS operation, the luminosity is determined about once per second. The total integrated luminosity is then recorded for every luminosity block of an ATLAS run. The final luminosity used in any analysis, though, depends on the trigger that is used to select events and its associated prescale. If the prescale is equal to 1, the estimate of the cross section σ is straightforward: $\sigma = N_{jet} / \int dt \mathcal{L} = N_{jet} / \mathcal{L}^{int}$. With a prescale p , only one jet every P is saved, and the estimate of the cross section becomes: $\sigma = N_{jet} \times P / \mathcal{L}^{int}$. The quantity $\mathcal{L}_{eff} = \mathcal{L}^{int} / P$ is the effective integrated luminosity, corrected for the prescale of a given trigger. An off-line luminosity calculator is therefore used to correct the total luminosity for the prescale of a given trigger, as well as any dead time of the data acquisition system. This returns an effective luminosity, defined as:

$$\mathcal{L}_{eff} = \sum_{LB} \frac{\mathcal{L}_{LB}^{int}}{P_{LB}^{trig}} \quad (5.3)$$

where \mathcal{L}_{LB}^{int} is the integrated luminosity in a specific luminosity block LB (excluding any dead time of the data acquisition system), and P_{LB}^{trig} is the prescale of a given trigger for the same luminosity block.

The total achieved luminosity in 2010, used in this analysis, is $(37.3 \pm 1.2) \text{ pb}^{-1}$.

The calculation of the total luminosity per bin follows the inclusive jet trigger scheme (see Tables 5.1-5.3 in Section 5.1.1). The luminosity calculation for most bins is straightforward, since only one trigger is used to fill each bin of p_T and $|y|$.

For the region in rapidity $2.8 < |y| < 3.6$, the use of the luminosity requires a specific treatment. The strategy used to account for different prescale combinations for inclusive jets in the HEC-FCal transition bin, which can be accepted by the central jet trigger, by the forward jet trigger, or by both, is described as the “Inclusive method for fully efficient

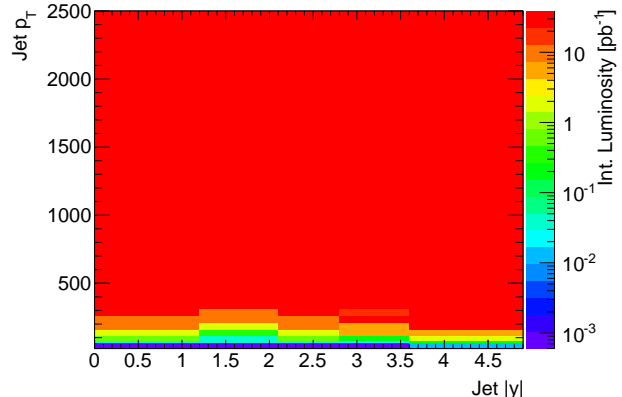


Figure 5.2: Effective integrated luminosity for various rapidity bins and data-taking periods.

combinations” in Reference [Lendermann 2009]. To avoid double counting in taking the OR of central and forward chains, jets in that bin are divided in three classes, according to their having passed (before prescale) the central threshold, the forward one or both. For each class, an equivalent luminosity is calculated summing over all luminosity blocks. The luminosity for jets selected by the central trigger is

$$\mathcal{L}_J^{int} = \Sigma_{LB} \frac{\mathcal{L}_{LB}^{int}}{P_{LB}^J}$$

where P_{LB}^J is the prescale of the central trigger for each luminosity block, and \mathcal{L}_{LB}^{int} its luminosity; for jets selected by the forward trigger the equivalent luminosity will be

$$\mathcal{L}_{FJ}^{int} = \Sigma_{LB} \frac{\mathcal{L}_{LB}^{int}}{P_{LB}^{FJ}}$$

Finally, for events taken, before prescale, by both central and forward trigger, the equivalent luminosity is

$$\mathcal{L}_{JFJ}^{int} = \Sigma_{LB} \frac{\mathcal{L}_{LB}^{int}}{P_{LB}^J P_{LB}^{FJ} / (P_{LB}^J + P_{LB}^{FJ} - 1)}$$

Let N_J , N_{FJ} and N_{JFJ} denote respectively the number of events taken by the central trigger, by the forward trigger, and by both triggers. The cross section before any other correction is given by

$$\sigma = \frac{N_J}{\mathcal{L}_J} + \frac{N_{FJ}}{\mathcal{L}_{FJ}} + \frac{N_{JFJ}}{\mathcal{L}_{JFJ}}$$

ensuring that events passing two triggers are properly treated in a separate category and not double-counted.

Figure 5.2 shows the effective integrated luminosity per bin. The low- p_T regions have a lower effective integrated luminosity, which corresponds to higher prescales.

5.2 Event and jet selection

In coincidence with a bunch crossing, a cosmic-ray muon, or particles from other background beam activities (such as beam-gas collisions), could release energy in the calorimeter. These type of backgrounds are rejected by requiring that events contain at least one

primary vertex consistent with the mean position of the interaction points (which depends on the accelerator conditions) and that has at least five tracks associated to it. This vertex definition is consistent with that used to evaluate pile-up vertexes in the offset correction, as detailed in Sec. 3.1.2. The efficiency for collision events to pass these vertex requirements, as measured in a sample of events passing all selections of this analysis, is well over 99%.

Background contributions from non-proton-proton-collision sources were evaluated by investigating events from trigger streams in which no real collision candidates are expected. These events are taken in periods with unpaired or empty proton bunches. In this data sample, only one jet that satisfies the selection criteria was found, and the background rates across the entire data period can be assumed to be negligibly small.

5.2.1 Jet selection

For the inclusive jet measurements, jets are required to have $p_T > 20 \text{ GeV}$ and to be within $|y| < 4.4$. They must also pass the specific fully-efficient trigger for each p_T and $|y|$ bin, as detailed in Section 5.1.

The jets must pass the quality criteria described in Section 4.1, that are derived to suppress fake jets originated by cosmic ray interactions or by sporadic noise bursts in the calorimeters. Since the selection is not completely efficient for the real jets, the final cross sections must be corrected by the efficiency reported in Figure 4.1.

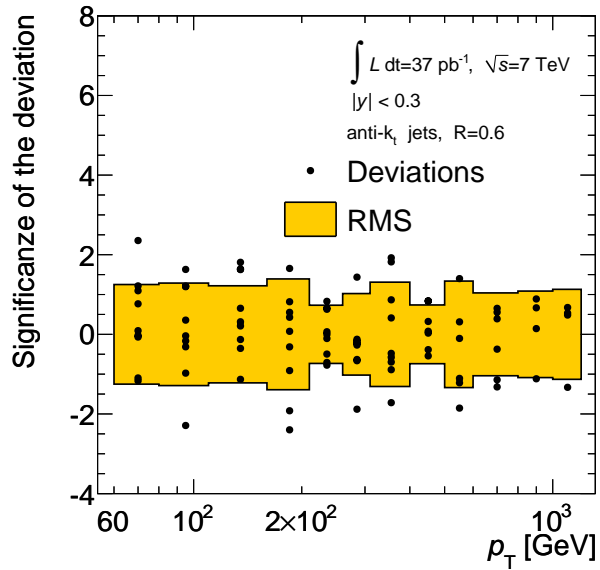
5.2.2 Data stability

Since the analyzed data sample has been acquired on a quite long period of time and with many changes in the beam conditions, the jet cross section was measured for all runs to ensure that the observed variations were consistent with statistical fluctuations. The jet production cross section is found to be stable within statistical errors across the whole data taking period. Figure 5.3 shows the stability of the measurement performed in different periods of data taking. Only the central region for anti- k_t jets with $R=0.6$ is shown in this Figure. Figures for several other regions can be found in the Appendix. In this Figure, each single point is the significance of the deviation of the measurement performed in one of the 9 periods of data taking, with respect to the final cross section. Only the statistical uncertainty is used to define the significance. In each bin, the distribution of this points is expected to be gaussian, with a RMS equal to 1. The measured RMS in each bin is shown as a yellow band. No significant deviation is evident from this plots, showing that the variations over the different periods of data taking, with different conditions for the LHC and different conditions of the experiment, are consistent with statistical fluctuations. The effect of the changes in the LHC and in the ATLAS detector did not strongly affect the capability to perform the measurement of the inclusive jet cross section.

5.3 Correcting the detector effects: unfolding

The goal of the studies on the jet cross section described in this thesis is to report a measurement which can be easily compared with the state-of-art theoretical prediction. For

Figure 5.3: Stability of the inclusive jet cross section measured in each period of data taking for the anti- k_t jets with $R=0.6$ in the central rapidity region. The cross section measured in each period is compared to the measurement performed on the complete statistics. Each point in the p_T bins shows the significance of the deviation of the measurement in each period, from the measurement done with the complete dataset. Only the statistical uncertainty is taken into account to define the significance. The yellow band is the RMS measured from the black points, which is expected to be at 1.



this purpose, all the detector effects have been corrected with a detector unfolding, and the measurement are defined at "truth-level". Truth-level jets in the Monte Carlo simulation are identified using the anti- k_t jet algorithm and are built from stable particles, which are defined as those with a proper lifetime longer than 10 ps. The unfolding correction have been derived from Monte Carlo simulations, as described in the next Section.

5.3.1 Monte Carlo samples for the unfolding

Several Monte Carlo generators were used to simulate QCD di-jet and multi-jet production in proton-proton collisions at $\sqrt{s} = 7 \text{ TeV}$. For the correction of the detector effects, PYTHIA 6.421 generator with the MRST 2007 LO* [Martin 2009, Sherstnev 2008] PDFs was used. This generator is based on leading-order perturbative QCD matrix elements for $2 \rightarrow 2$ processes, along with a leading-logarithmic parton shower, an underlying event simulation with multiple parton interactions, and the Lund string model for hadronisation. Samples were generated using the ATLAS Minimum Bias Tune 1 (AMBT1) set of parameters [ATLAS Collaboration 2010d], in which the non-diffractive model has been tuned to ATLAS measurements of charged particle production at $\sqrt{s} = 900 \text{ GeV}$ and $\sqrt{s} = 7 \text{ TeV}$.

The simulation of the inclusive jet production have been divided in one MinBias sample and eight jet samples (named J1, J2, J3, J4, J5, J6, J7, J8, or shortly Jx samples), in order to efficiently simulate with high statistics the high p_T tails of the distribution. The variable used to split the Monte Carlo production in Jx samples is the partonic p_T of the born $2 \rightarrow 2$ process (\hat{p}_T).

Since the Jx cover the region $\hat{p}_T > 17 \text{ GeV}$, the MinBias sample, restricted to $\hat{p}_T < 17 \text{ GeV}$ is used to simulate the jet production at lower scales. The main goal of the MinBias sample is to simulate the production of particles at low p_T , and depends on the models

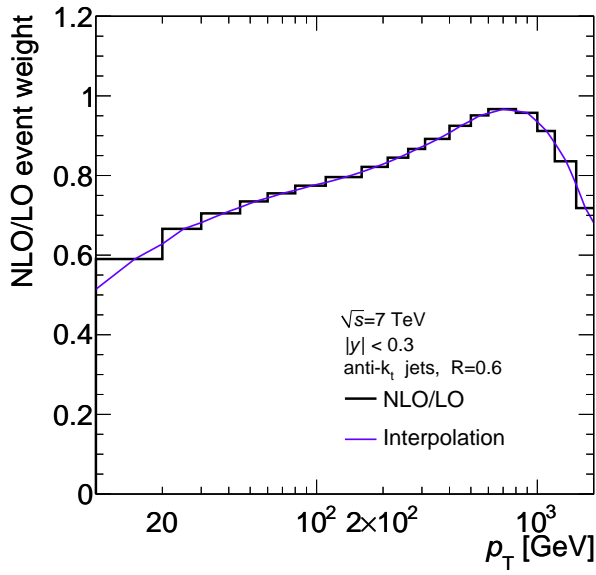


Figure 5.4: Weights for the anti- k_t jets with $R=0.6$ used to correct for the difference in the shape of the Monte Carlo simulation due to the MRST 2007 LO* PDFs and to the missing NLO terms. These weights are used to improve the agreement between the Monte Carlo detector level shapes and the measured shapes in order to reduce the unfolding systematic uncertainties, especially for the bin-by-bin unfolding.

adopted by PYTHIA to simulate the soft physics.

The particle four-vectors from these generators were passed through a full simulation [ATLAS Collaboration 2010n] of the ATLAS detector and trigger that is based on GEANT4 [Agostinelli 2003]. Finally, the simulated events were reconstructed and jets were calibrated using the same version of the ATLAS software as used to process the data.

5.3.2 Detector level shape: improving the Monte Carlo descriptions

The Monte Carlo simulation have been used to estimate the impact of the detector, and to correct for it. Even if the single jets are described with an high accuracy by the Monte Carlo simulation (Section 4), a possible bias in the unfolding procedure could come from the shape of the estimated cross sections in the event generators. To improve the agreement with the shape of the measured detector level spectra , the Monte Carlo spectra have been reweighted by a NLO/LO coefficient.

These coefficients, shown in Figure 5.4 in the central rapidity region for the anti- k_t jets with $R=0.6$, are derived from NLOJET++, by dividing the NLO prediction with the MSTW 2008 (NLO) PDF, by the LO prediction with the MRST 2007 LO* PDF (to apply a smooth correction, a linear interpolation, shown in the Figure, has been used). The goal of these weights is to change the shape of the cross section (the total normalization is irrelevant for the unfolding procedure). A complete set of plots can be found in the Appendix.

One could argue that the proper LO prediction to calculate the weights to get a proper re-weighted shape should be the result of the Monte Carlo at the parton level. Given the fact that this re-weighting is not aimed at the estimate of the cross section but to improve the Monte Carlo shape, the fixed LO in NLOJET++ have been used. Any re-weighting which brings the Monte Carlo closer to the data, but which is not using the information from the data, is improving the solidity of the unfolding results.

The weights have been applied to the single truth jets, as a function of the jet p_T and

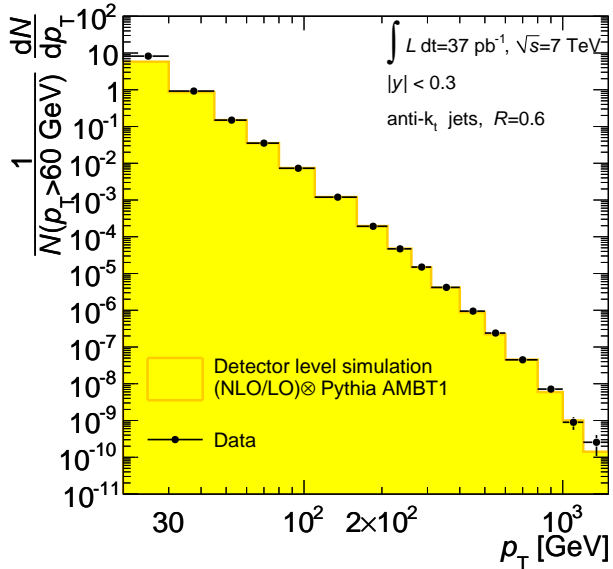


Figure 5.5: Observed inclusive p_T distribution (black dots) for jets with $p_T > 20 \text{ GeV}$ and $|y| < 0.3$ for anti- k_t jets with $R=0.6$. Only statistical uncertainties are included and the distributions are normalized to the integral from $p_T > 60 \text{ GeV}$. The data are compared to Monte Carlo predictions, re-weighted for the NLO/LO coefficients.

rapidity. In order to propagate this re-weighting on the reconstructed jet spectra, a geometrical association of truth jets and reconstructed jets has been used. The jets are associated if their distance in $\Delta R = \sqrt{\Delta\phi^2 + \Delta\eta^2}$ is less than 0.3. This association is really efficient at high p_T , but it drops at low p_T ². For the non matched jets, the weights are used to maintain the correct fraction of unmatched jets in the original Monte Carlo.

Figure 5.5 shows the spectrum of the measured jets, compared with Monte Carlo simulation corrected with the NLO/LO coefficients. This Figure shows only the central rapidity region for anti- k_t jets with $R=0.6$. The re-weighted Monte Carlo simulation properly describes the shape of the measured spectra (a complete set of plots can be found in the Appendix). Some discrepancy can be seen in the low- p_T region ($p_T < 30 \text{ GeV}$). The discrepancy in this p_T region has been investigated, and found to be consistent with a mis-calibration of the low- p_T jet, smaller than the JES uncertainty used in the analysis.

All the information on the jet smearing, available from the simulation, can be included in a transfer matrix of p_T^{reco} vs. p_T^{truth} . This matrix is obtained from Monte Carlo, using the geometrical matching (with maximal $\Delta R = 0.3$) between truth and reconstructed jets. Nine correlation matrices for each rapidity bin and for each jet algorithm size R are first derived from each of the eight JX samples (J1-J8) and the MinBias sample, and properly combined together.

An example of the matrices derived with this method is shown in Figure 5.6 for anti- k_t jets with $R = 0.6$. A complete set of transfer matrices can be found in the Appendix. In this Figure, one can notice that very low- p_T truth jets are associated with high- p_T reconstructed jets. The probability for this association is really low, so it is not affecting the final result of the unfolding procedure. It is in any case interesting to deeply investigate this jets. A calorimeter fluctuation, causing this effect seems to be unrealistic. This association is

²The main source of matching inefficiency is the p_T cut, which is set here at 10 GeV for both truth and reconstructed jets.

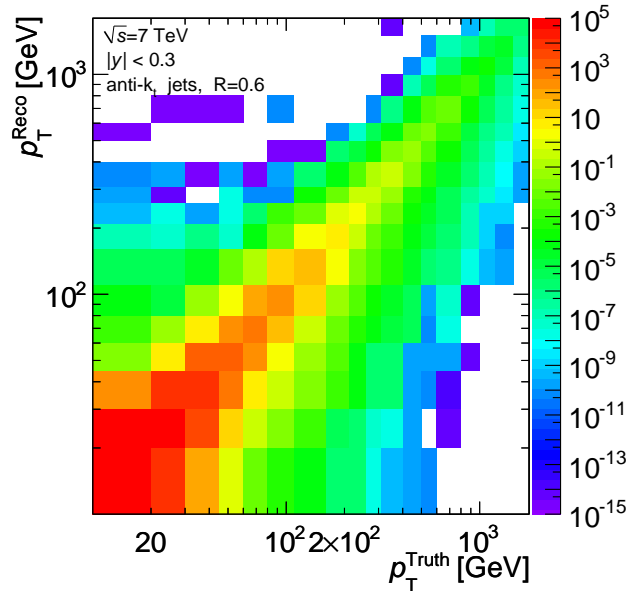


Figure 5.6: Transfer matrices derived by matching the truth jets to the reconstructed jets with the geometrical requirement $\Delta R < 0.3$ for the anti- k_t jets with $R=0.6$ in the central rapidity region.

probably due to a failure of the matching procedure in very crowded events.

The truth and reconstructed jets that fail the matching are saved in two different vectors for each Monte Carlo sample. The truth and reconstructed Monte Carlo spectra of the matched jets can be obtained by projecting the transfer matrix on one axis or the other. By dividing these spectra by the spectra of the unmatched jets, it is possible to calculate the matching efficiency (as a function of p_T) at the truth and reconstructed level (see Figures 4.2-4.3).

5.3.3 Unfolding strategy

The aim of the unfolding is to correct for detector effects in data, using a transfer matrix constructed as described in the previous section. Since the transfer matrix is computed using only matched jets (and not unmatched jets), the first step of the unfolding procedure is to account for unmatched reconstructed jets. This is done by multiplying the data by the matching efficiency obtained at the reconstructed level from the simulated samples (see Section 4.2). In the second step, the unfolding is performed using the matched jets. Since this step is the most important and delicate, three different methods have been tested by the ATLAS Collaboration: bin-by-bin, Singular Value Decomposition (SVD) method [Hocker 1996], and Iterative Dynamically Stabilized (IDS) method [Malaescu 2011].

The bin-by-bin correction involves multiplying the measured number of jets in a given bin in data, by the ratio of the number of truth jets over the number of reconstructed jets in the same bin of the Monte Carlo sample. This method fully relies on the MC shape when computing the correction factors to be applied to data. Any discrepancy between the shape of the MC and shape of the data introduces a bias in the unfolded spectra. This bias is usually acceptable if the migrations between bins are not very large. This method has been used as a default method in the past, but is used only as a cross-check here.

The SVD method uses a singular value decomposition in order to prevent fluctuations that a simple inversion of the transfer matrix would introduce. However, the regularization procedure in SVD also uses a constraint on the curvature of the unfolded spectrum, which introduces an artificial smoothing of the unfolded distribution and which can also cause biases. For this reason, it has been disfavored in this analysis.

The IDS method uses the MC transfer matrix to compute the matrix of unfolding probabilities, which encodes the probability for a jet reconstructed in a given bin i to be generated in bin j . The unfolding matrix is improved in a series of iterations, where the truth MC is re-weighted to the shape of the corrected data spectrum. The regularization, preventing statistical fluctuations from being amplified by the successive iterations, is provided by the use of the significance of the data-MC differences in each bin. The final unfolding matrix after the optimal number of iterations is used to correct the reconstructed spectrum for detector effects. Due to its advantages over the other methods, the IDS unfolding has been chosen as the default method for this measurement.

After the unfolded distribution for matched jets is found, using either the bin-by-bin, SVD, or IDS method, the third and final step of the unfolding is to divide this spectrum by the matching efficiency at the truth level in order to account for unmatched truth jets.

The corrections are applied in the first and third steps in a multiplicative way, as these corrections rely less on the MC shape than the corresponding corrections obtained by subtracting and then adding back the jets without matching.

Note that for the bin-by-bin correction, this three-step procedure gives a result which is identical to that obtained using a correction derived in one single step (one single multiplicative correction). Two main disadvantages are affecting the bin-by-bin: 1) the bias coming from a mis-modeling of the MC shape of the distributions; 2) the missing capability to properly propagate the statistical uncertainties, and their bin-to-bin correlations.

5.3.4 Computing the statistical uncertainty with the IDS unfolding

The statistical uncertainty is not the dominant error in the measurement of the inclusive jet cross section (only in the very high- p_T bins it becomes relevant), but one can profit of the IDS method to demonstrate with a good estimate, that even the statistical correlations are small. This is an important input for the QCD fits of the measurement. The unfolded cross section is the linear combination of the detector level distribution. This linear combination introduces the bin-to-bin correlation. The statistical uncertainties are determined by performing pseudo-experiments in Monte Carlo simulations. In each Monte Carlo simulation, all the bins of the transfer matrices for the MinBias and the eight JX samples are fluctuated following a Poisson distribution around their central values, and then recombined using the corresponding weights. The same procedure is applied for the spectra of jets without matching. The data spectra are also fluctuated, taking into account correlations due to the fact that several jets are produced in a given event. The unfolding is then performed for each toy, resulting in an unfolded spectrum. The errors are obtained from the covariance matrix of the resulting corrected spectra.

The correlation matrices for the unfolded spectra are shown in Figure 5.7 for some representative rapidity regions for the anti- k_t jets with $R=0.6$ (a complete set of correlations

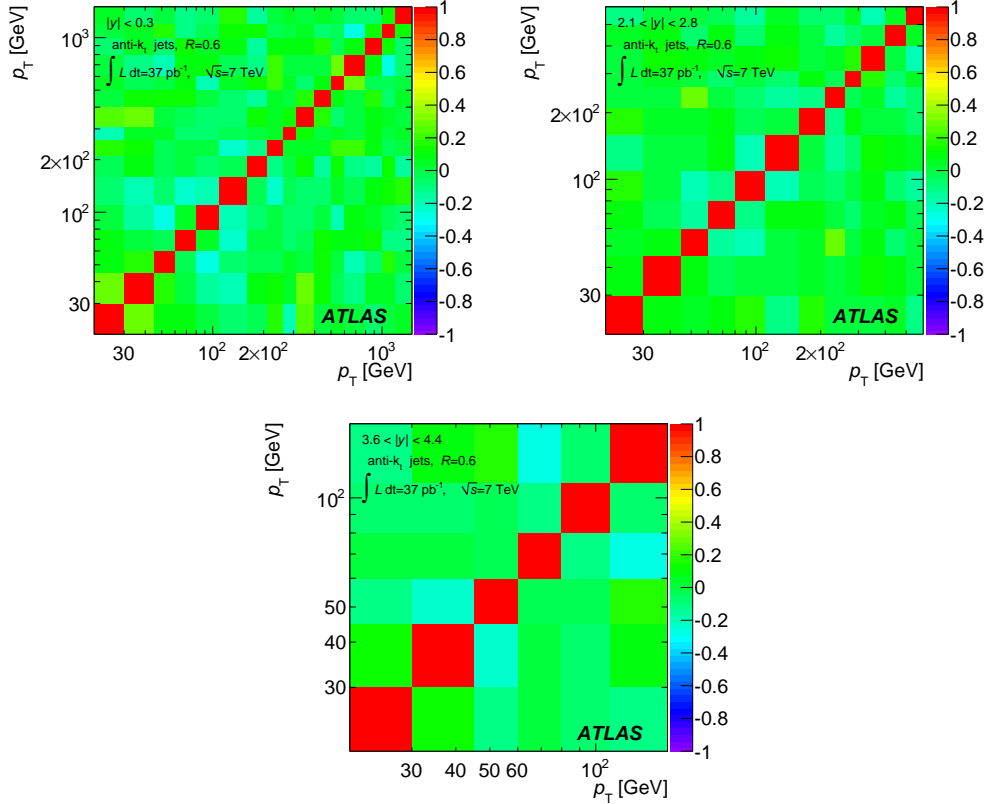


Figure 5.7: Correlation of the statistical uncertainty of the inclusive jet cross section after the unfolding procedure. The results are shown for anti- k_t jets with $R = 0.6$ in some representative slices of rapidity.

for the statistical uncertainty can be found in the Appendix). The bin-to-bin correlations are small, and the statistical covariances are negligible if compared with the systematic covariances.

5.3.5 Systematic uncertainty on the unfolding procedure

The systematic uncertainty for the bin-by-bin, SVD, and IDS methods are mainly due to the particular shape assumed for the generated spectrum. To reduce the impact of this difference, the Monte Carlo have been re-weighted as described in Section 5.3.1. On top of this change, an extra change is used to estimate the residual bias. The truth jets in the transfer matrices are re-weighted by multiplying each column of the matrix by a given weight. These weights are chosen to improve the agreement between the reconstructed Monte Carlo spectra and the data. Several different sets of weights have been tested. The reconstructed Monte Carlo spectra obtained with the modified truth spectra are unfolded using the original matrix and compared to the modified truth spectra. The resulting bias is interpreted as the systematic uncertainty, since it is defined as the difference between the unfolded result obtained using the *original* matrix and the unfolded result that would

have obtained using the *modified* reconstructed Monte Carlo as appropriate. In general, the smallest bias is obtained for the IDS method. This supports the choice of this algorithm as the default unfolding method. This uncertainty is smaller than 1% in most of the measured bins, becoming of the order of 1% in the high p_T range.

A second important uncertainty comes from the matching procedure, which is used to match truth and reconstructed jets in the transfer matrix for the unfolding. There is some freedom in the choice of the matching radius. The jet matching uncertainty is estimated by varying the matching radius used when building the transfer matrix. This variation changes both the transfer matrix and the spectra of jets without matching at the particle and reconstructed level.

The nominal matrix is built using a matching radius of $\Delta R < 0.3$. To estimate this uncertainty, two matrices using matching radii of 0.2 and 0.4 respectively have also been built. The two corresponding unfolding results are compared with the nominal unfolded spectrum, and their maximum deviation provides an estimate of the maximum matching systematic uncertainty.

The maximum effect is seen at low p_T due to the poor matching efficiency. The uncertainty is of the order of 1% in the range $p_T < 60 \text{ GeV}$, and smaller for higher p_T .

5.3.6 Comparison between IDS and bin-by-bin unfolding

The IDS and bin-by-bin unfolding procedures are expected to give compatible results within their uncertainties. Figure 5.8 shows a comparison of the two methods for anti- k_t jets with $R = 0.6$ in the central rapidity region. A complete set of plots can be found in the Appendix. This Figure compares the unfolded spectra, the statistical and the systematics errors obtained with the two different methods. The relative difference between the unfolded spectra using the two procedures (black points) is, in most bins, less than 1-2% and much smaller than the systematic uncertainties on the measurements (the two bands). Their respective statistical and systematic uncertainties are generally similar as well, though they differ at very low and high jet p_T ³.

³For the IDS method, a small improvement for the systematic errors in the forward rapidity regions is shown in the figures in the Appendix. This is not due to the unfolding procedure in itself, but to an improvement in the jet energy scale uncertainty in the forward region, not used for the bin-by-bin results.

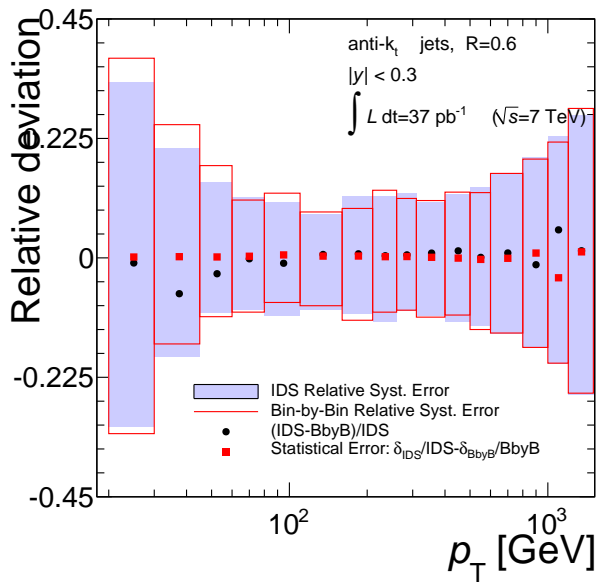


Figure 5.8: Comparison of the unfolded cross section using the bin-by-bin and the IDS methods. The relative difference with respect to the final (IDS) result is plotted as a function of jet transverse momentum in black dots. Red dots show the difference of the relative statistical uncertainties obtained in the two method. The two bands show the total systematic uncertainty for the IDS, and for the bin-by-bin methods. Agreement is observed at the per cent level or better precision. The results are shown for anti- k_t jets with $R = 0.6$ for the central rapidity region.

5.4 Systematic uncertainties

In this section the various sources of systematic uncertainty that influence the inclusive jet measurement are described. The leading source of uncertainty is the one affecting the jet energy scale.

5.4.1 Uncertainty on the jet energy scale

The uncertainty on the inclusive jet cross section from the jet energy scale is evaluated using the uncertainties described in Section 4.3.1 and in Reference [ATLAS Collaboration 2011h]. Each single component, reported in Table 4.1, is propagated to the final inclusive jet cross section.

The method uses the re-weighted Monte Carlo introduced in Section 5.3.1. It is a two step procedure. In the first step, each component α of the 13 reported in Table 4.1 is considered to vary the Monte Carlo shape in two ways. For a component α , the p_T of each single reconstructed jet in the Monte Carlo is shifted in the following way:

$$p_T(\sigma_\alpha^+) = p_T \cdot (1 + \sigma_\alpha) \text{ and } p_T(\sigma_\alpha^-) = p_T \cdot (1 - \sigma_\alpha) \quad (5.4)$$

where σ_α is the relative uncertainty for the component α . The results of these shifts are 26 set of spectra ($S_{\alpha,k}^\pm$ where k indicates the bin index, spanning all the bins in $p_T \times |y|$), which are used to estimate the final uncertainty.

A similar procedure has been applied to evaluate the effect of the jet energy scale uncertainty due to pile-up. This uncertainty depends on the number of primary vertexes measured in each event. Since each bin is measured with a different trigger, and it is therefore sensitive to different pile-up conditions, the propagation of the uncertainty due to the pile-up needed to correctly take into account the vertex multiplicity of each bin. Equation 5.4 has therefore been substituted by:

$$p_T(\sigma_{PU}^+(i)) = p_T \cdot (1 + \sigma_{PU}(i)) \text{ and } p_T(\sigma_{PU}^-(i)) = p_T \cdot (1 - \sigma_{PU}(i)) \quad (5.5)$$

where $\sigma_{PU}(i)$ is the relative uncertainty due to the pile-up in an event with i primary vertexes. A maximum number of 7 primary vertexes has been considered.

By measuring the primary vertex multiplicity distribution for each single bin k ($N_k(i)$), one can combine the 14 spectra in 2 final spectra ($S_{PU,k}^\pm$):

$$S_{PU,k}^\pm = \sum_i N_k(i) \cdot S_{PU,k}^\pm(i) \quad (5.6)$$

In the second step, the resulting 26+2 jet p_T spectra are unfolded in the same way as the data (see Section 5.3.3), and the relative differences Δ_α^\pm of the unfolded shifted jet spectra to the unfolded nominal spectra are taken as the uncertainty on the cross section.

The total relative uncertainty Δ_{JES}^\pm due to the jet energy scale uncertainty is obtained using the following equation:

$$\Delta_{JES}^+ = \sqrt{\sum_\alpha [\max(\Delta_\alpha^+, \Delta_\alpha^-, 0)]^2} \text{ and } \Delta_{JES}^- = -\sqrt{\sum_\alpha [\min(\Delta_\alpha^+, \Delta_\alpha^-, 0)]^2} \quad (5.7)$$

The errors, calculated in this way, are asymmetric. This procedure is repeated for each rapidity region and for the two radius R of the anti- k_t jets. The inclusive jet cross section systematic uncertainty due to the jet energy scale uncertainty is shown in Figure 5.9 for anti- k_t jets with $R=0.6$ in the central rapidity region. The light blue bands show the total uncertainty while the colored lines show the effect of the single components. Given the difficulties of plotting 14 components in the same Figure, for each region of rapidity, three different figures have been prepared. The complete set of figures can be found in the Appendix. The order of the sub-components in the plots has been selected for clarity. The largest effects at low- p_T in the central region comes from the uncertainty of modeling of the parton shower, hadronization and underlying event, from the "non-closure" of calibration, and from the uncertainty due to the noise suppression (components 1-4). At high- p_T , the uncertainty is dominated by the data-MC discrepancy of the calorimeter response measured in the combined test beam (component 13). In the rapidity region $|y| > 0.8$, the dominant contribution comes from the relative uncertainty on the jet inter-calibration (component 6).

The advantage of this procedure is to produce a set of 14 couples of uncertainties, which are internally 100% correlated in p_T , but which are uncorrelated to each other. These components are used to calculate the final correlation matrix, which can be used to statistically test the agreement of the theoretical prediction with the measurement, and to extract information on the proton structure or on the value of α_s with a QCD fit.

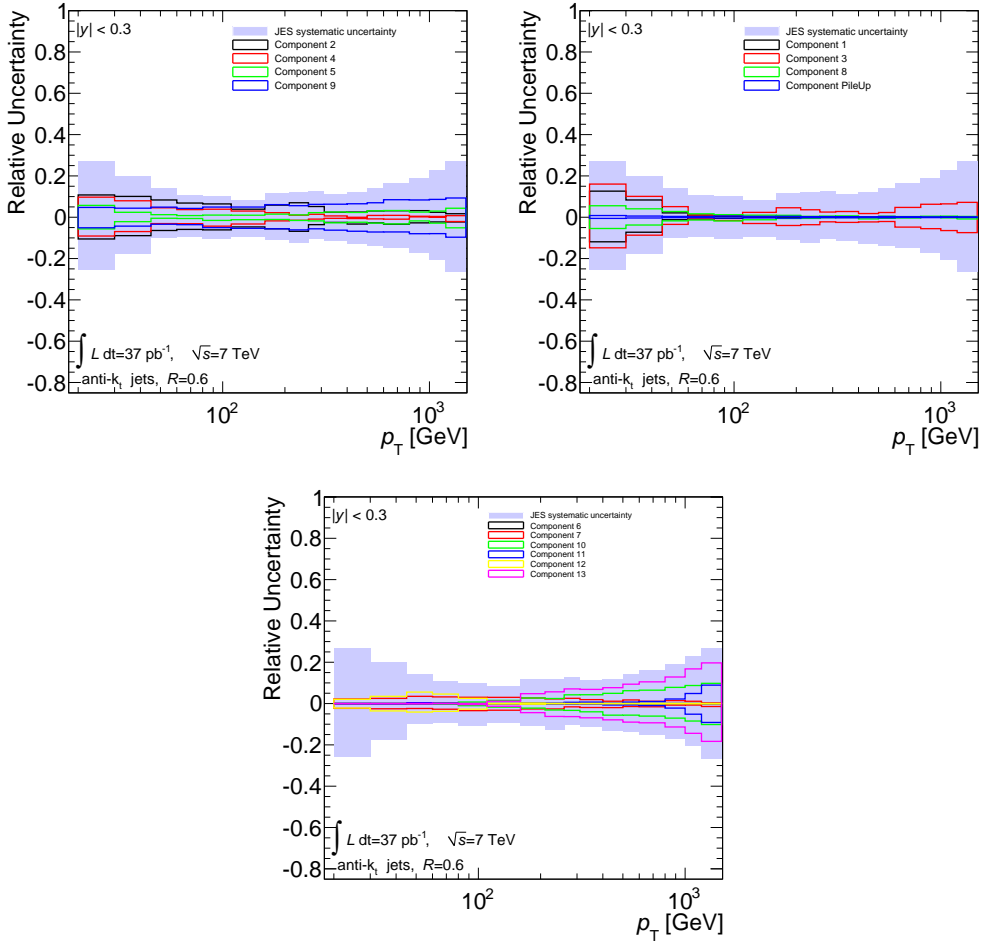


Figure 5.9: The colored lines show the relative systematic uncertainty on the inclusive jet cross section measurement due to the various components of the jet energy scale uncertainty for $|y|<0.3$ and anti- k_t jets with $R=0.6$. The association between the numbering and the meaning of each component is reported in Table 4.1. The light blue band shows the total uncertainty.

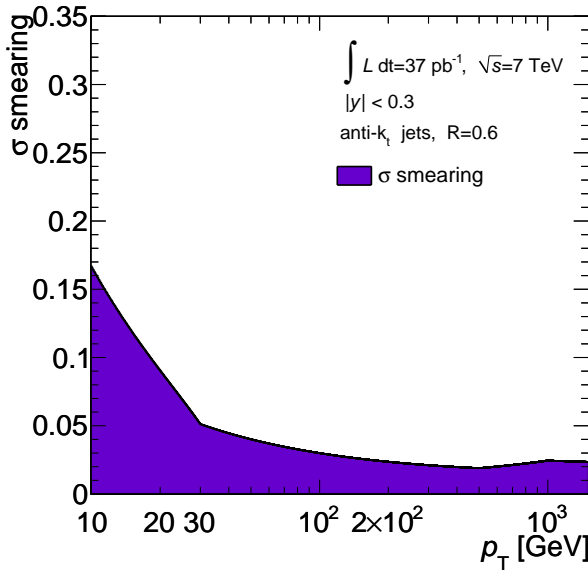


Figure 5.10: Additional smearing applied to the Monte Carlo reconstructed jets to estimate the impact of the uncertainty on the jet energy resolution on the final inclusive jet cross section for anti- k_t jets with $R=0.6$ in the central rapidity region.

5.4.2 Uncertainty on the jet energy resolution

The data/Monte Carlo studies detailed in Section 4.3.2 showed that the jet resolution is described in Monte Carlo within a 5-15% uncertainty. Fluctuations of the jet energy due to resolution effects are corrected for in the unfolding procedure (Section 5.3.3).

To evaluate the systematic uncertainty due to a potentially worse resolution with respect to the Monte Carlo simulation, the nominal jet energy resolution is worsened an amount equal to the measured systematic uncertainty. The p_T of each Monte Carlo jet is smeared by the factor σ_{smear} , calculated as:

$$\sigma_{\text{smear}}^2 + \sigma_{\text{nominal}}^2 = (\sigma_{\text{nominal}} + \Delta\sigma)^2 \quad (5.8)$$

where σ_{nominal} is the nominal fractional resolution (shown in Figure 4.18 for the anti- k_t jets with $R=0.6$ in some peculiar rapidity regions), and $\Delta\sigma$ the uncertainty on the nominal resolution.

The factor σ_{smear} used to smear the reconstructed jets by an amount equivalent to the jet energy resolution uncertainty is shown for anti- k_t jets with $R = 0.6$ in Figure 5.10 for the central rapidity region.

The smeared jets are used to derive a new transfer matrix with which the data are unfolded. The relative difference of the data spectrum unfolded with the smeared transfer matrix and the data spectrum unfolded with the nominal transfer matrix is taken as a symmetric systematic uncertainty. The impact of this uncertainty on the final cross section for anti- k_t jets with $R=0.6$ in the central rapidity region is shown in Figure 5.11 (a complete set of plots can be found in the Appendix).

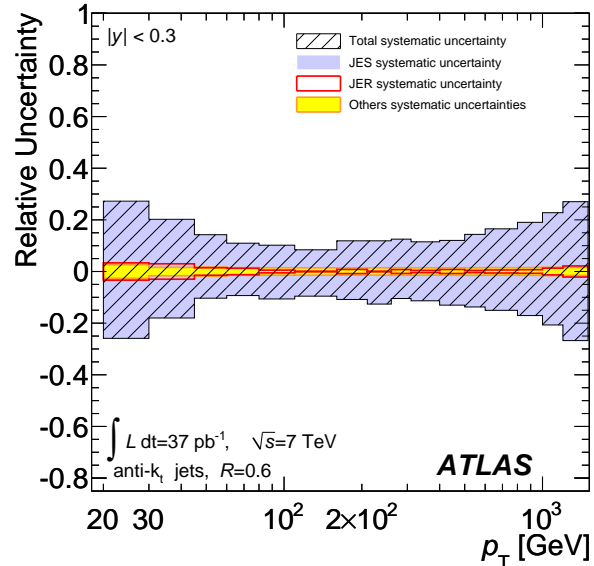


Figure 5.11: Relative systematic uncertainty on the final inclusive jet cross section for anti- k_t jets with $R=0.6$ in the central rapidity region. The contributions from the jet energy scale, the jet energy resolution and all the other sources are shown.

5.4.3 Total systematic uncertainty

Several systematic uncertainties have been estimated for the inclusive jet cross section measurement.

In the previous subsections, the 14 independent components for the jet energy scale uncertainty, and the strategy for the estimate of the error due to the uncertainty on the jet energy resolution have been introduced.

These uncertainties are the dominant one, but other important uncertainties have been estimated.

Figure 5.11 shows a summary of the total relative systematic uncertainty, and the contribution from the jet energy scale, the jet energy resolution, and the other components for the anti- k_t jets with $R=0.6$ in the central rapidity region. A complete set of plots can be found in the Appendix. The jet energy scale uncertainty is the the dominant uncertainty, and only at low- p_T the contribution from the jet energy resolution plays a role.

The other components taken into account play a small role in the determination of the total uncertainty, but they are important to properly calculate the systematics and the correlations to perform statistical tests of the measurement.

These components have been previously introduced in the relevant section, and will be only summarized here. They are:

- Jet angular resolution:

This component has been evaluated on the Monte Carlo, by shifting the angle of the jets according to the resolution in the Monte Carlo. This component has a small contribution, and it plays a role in the migration of jets between different regions of rapidity.

- Jet cleaning efficiency:

This uncertainty has been derived from the stability of the tag-and-probe method on

the collision data. This method has been used to estimate the cleaning efficiency, introduced in Section 4.1.

- Jet reconstruction efficiency and purity:

This component is conservatively estimated as 2% in the lower p_T bin, and 1% in the other regions. These values are used for the combination of the first and last corrections applied in the three step procedure adopted for the unfolding, introduced in Section 4.2.

- Unfolding uncertainty on the shape of the spectra:

This uncertainty is derived as discussed in Section 5.3.5, and it can be evaluated by the stability of the closure test of the unfolding procedure.

- Unfolding uncertainty on the matching procedure:

This uncertainty comes from the strategy adopted to generate the transfer matrices used for the unfolding. This strategy relies on the Monte Carlo matching of truth jets and reconstructed jets, and the uncertainty comes from the stability under the variation of the matching, as discussed in Section 5.3.5.

- Uncertainty on the trigger efficiency:

The trigger efficiency is used to associate at each single bin in $(p_T, |y|)$, a specific trigger chain. A conservative 1% uncertainty is assumed for the trigger efficiency.

- Luminosity:

The measurement of the luminosity has an uncertainty of 3.4% for the 2010 data. This uncertainty is not added in quadrature to the rest of other uncertainties, and is not shown in the plots. The effect is a completely coherent shift of the normalization of all the measured bins of the inclusive jet cross section.

The contribution to the relative systematic uncertainty from these components (but the luminosity, contributing with a 3.4%) are shown in Figure 5.12 for anti- k_t jets in the central rapidity region. A complete set of plots can be found in the Appendix.

5.4.4 Correlations

The systematic uncertainties of the measured jet cross section in the different p_T -bins summarized in the previous pages can be used to calculate the correlation and the covariance matrices of the systematic error. The systematic uncertainty is split into several components that are uncorrelated with respect to each other. Most of the components are completely correlated in p_T , and the formula to calculate the covariance matrix is the following:

$$\text{cov}(i, j) = \sum_{\alpha} \Delta_{\alpha,i} \Delta_{\alpha,j}, \quad (5.9)$$

where α runs over the different components, and $\Delta_{\alpha,i}$ is the uncertainty due to the component α in bin i .

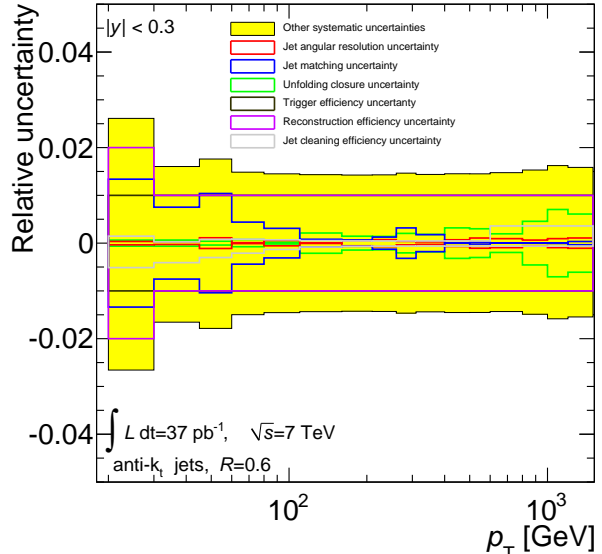


Figure 5.12: Contributions of the sub-dominant sources on the relative systematic uncertainty on the final inclusive jet cross section for anti- k_t jets with $R=0.6$ in the central rapidity region.

Once the covariance matrix is calculated, the correlation matrix is defined as usual:

$$\text{corr}(i, j) = \frac{\text{cov}(i, j)}{\sqrt{\text{cov}(i, i) \times \text{cov}(j, j)}} \quad (5.10)$$

A detailed discussion on which errors are assumed to be correlated in p_T and in $|y|$ is presented in Reference [Francavilla 2011]. In this section, only the summary table is presented. A summary of all the different nuisance parameters needed to perform a coherent fit of the data in all the different regions of rapidity is shown in Table 5.5. Bins with the same nuisance parameter in the Table are treated fully correlated, and bins with different nuisance parameters are uncorrelated.

Since the different systematic components have asymmetric errors, the definition of $\Delta_{\alpha i}$ is not straightforward. One can use the upper error, the lower error or symmetrise the error by taking the average of the two. Any of these choices generate slightly different correlation matrices, however the general aspect of the correlation matrix is the same. The systematic correlation matrix, calculated with symmetric errors, is shown in 5.13 for the anti- k_t jets in some representative rapidity regions.

Once the covariance matrix for the systematic uncertainties is calculated, one can estimate the complete covariance matrix by adding the statistical covariance matrix that is produced in the unfolding procedure (see Section 5.3.4). Since the statistical covariance matrix is dominated by the diagonal elements, and the size of the statistical uncertainty becomes dominant only in the last two bins at high- p_T , as a first approximation the impact of the off-diagonal elements of the statistical covariance can be assumed negligible.

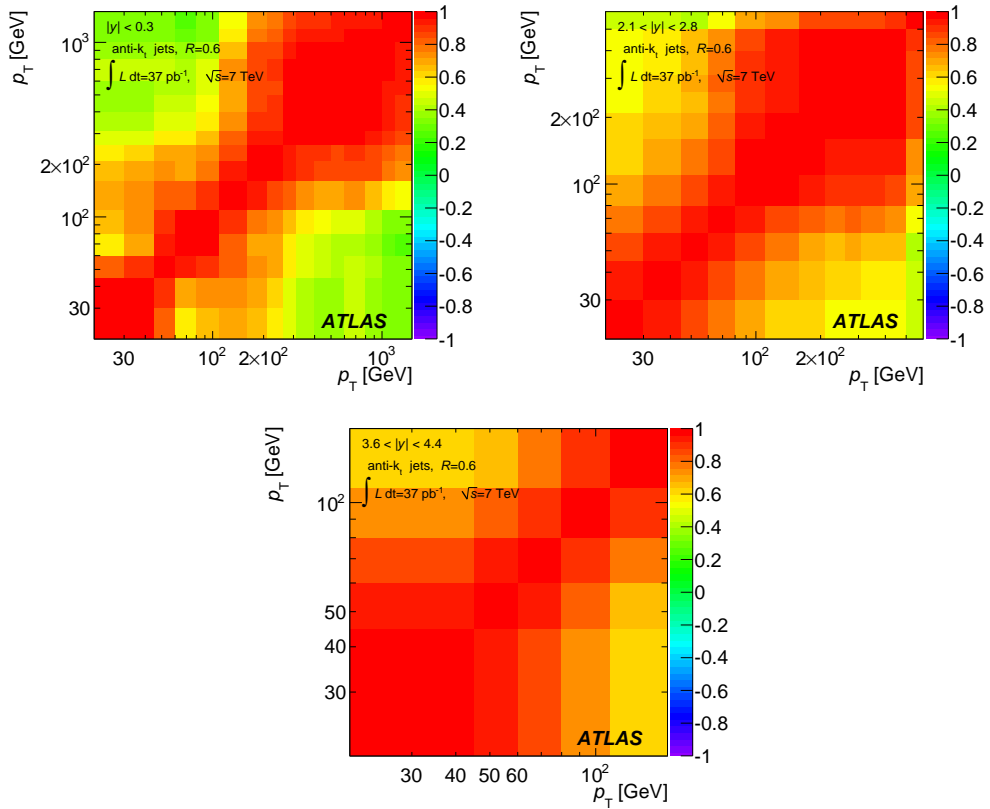


Figure 5.13: Correlation of the systematic uncertainty of the inclusive jet cross section at the end of the unfolding procedure. The results are shown for anti- k_t jets with $R = 0.6$ in some representative slices of rapidity.

Uncertainty Source	$ y $ -bins						
	0-0.3	0.3-0.8	0.8-1.2	1.2-2.1	2.1-2.8	2.8-3.6	3.6-4.4
JES 1:	1	1	2	3	4	5	6
JES 2:	7	7	8	9	10	11	12
JES 3:	13	13	14	15	16	17	18
JES 4:	19	19	20	21	22	23	24
JES 5:	25	25	26	27	28	29	30
JES 6:	31	31	31	31	31	31	31
JES 7:	32	32	33	34	35	36	37
JES 8:	38	38	39	40	41	42	43
JES 9:	44	44	45	46	47	48	49
JES 10:	50	50	51	52	53	54	55
JES 11:	56	56	57	58	59	60	61
JES 12:	62	62	63	64	65	66	67
JES 13:	68	68	69	70	71	72	73
Unfolding	74	74	74	74	74	74	74
Jet matching	75	75	75	75	75	75	75
JER	76	76	77	78	79	80	81
y -resolution	82	82	82	82	82	82	82
Trigger	u	u	u	u	u	u	u
Jet cleaning	u	u	u	u	u	u	u
Jet reco eff	83	83	83	83	84	85	86
Pile-up	u	u	u	u	u	u	u
Luminosity	87	87	87	87	87	87	87

Table 5.5: Description of bin-to-bin uncertainty correlation between $|y|$ -bins of the inclusive jet measurement. Each number corresponds to a nuisance parameter. Bins with the same nuisance parameter are treated fully correlated, and bins with different nuisance parameters are uncorrelated. All uncertainty sources listed here, but the one identified with u , are fully correlated versus p_T . The u means that the corresponding component is uncorrelated in p_T and in $|y|$.

5.5 Results

The double-differential inclusive jet cross section is shown in Figures 5.14 and 5.15 for jets reconstructed with the anti- k_t algorithm with $R = 0.4$ and $R = 0.6$, respectively. The measurement extends from jet transverse momentum of 20 GeV to almost 1.5 TeV, spanning two orders of magnitude in p_T and seven orders of magnitude in cross section. The measured cross sections have been corrected for all detector effects using the unfolding procedure described in Section 5.3. The final results are compared to NLO pQCD predictions (using the CT10 PDF set) corrected for non-perturbative effects, where the theoretical uncertainties from scale variations, parton distribution functions, and non-perturbative corrections have been accounted for. Some differences are observed at high jet p_T and $|y|$, but the data and theory predictions are generally in agreement within the experimental and theoretical uncertainties.

The ratio of the measured cross sections to the theoretical predictions from NLO pQCD corrected for non-perturbative effects, separated into different rapidity regions, are shown for $R = 0.4$ and $R = 0.6$ in Figs. 5.16-5.17 and 5.18-5.19, respectively. The data and theory predictions are in reasonable agreement within the experimental and theoretical uncertainties.

The data have also been compared with the predictions obtained with different PDF sets. In Figs. 5.20 -5.23, the theoretical error bands in the predictions obtained by using CT10, MSTW 2008, NNPDF 2.1, and HERAPDF 1.5 are shown compared to the measured cross sections, where data and theoretical predictions are normalized to the prediction obtained by using the CT10 PDF set. Agreement with data is observed for these PDF sets.⁴ The predictions with MSTW 2008, NNPDF 2.1, and HERAPDF 1.5 seem to have a better coherence with the measured cross sections, in particular in the forward region.

The comparison of the data with the Powheg prediction, using the CT10 PDF set, is shown for anti- k_t jets with $R = 0.4$ in different rapidity regions in Figs. 5.24 and 5.25. The markers show the comparison with the Powheg prediction showered using either PYTHIA (AUET2B tune and Perugia 2011) or HERWIG (AUET2 tune), as well as the NLO pQCD prediction derived by using the CT10 PDF set, which is used as common normalization. The same plots are shown for anti- k_t jets with $R = 0.6$, in Figs. 5.26 and 5.27.

Some differences exist between the Powheg prediction with PYTHIA and HERWIG parton showers. The NLO ME is the same for the two Powheg predictions, and it was found to be in good agreement with the pure parton-level ME calculation from NLOJet++ before non-perturbative corrections. Thus the difference between the two predictions of Powheg coupled to the two different parton shower implementations may be taken as an indication of the uncertainty due to the leading-logarithmic approximation used in the parton shower. Scale uncertainties are not shown for Powheg, but are assumed to be similar to those for NLOJet++. Within the present uncertainties, the Powheg predictions are consistent with both the data and NLOJet++ calculations. There is a trend for Powheg to predict larger cross sections than the data and NLOJet++ at low p_T , and smaller cross sections than

⁴Comparisons to CTEQ 6.6, NNPDF 2.0, and HERAPDF 1.0 were also performed, but they are not shown as they are fairly similar to those for CT10, NNPDF 2.1, and HERAPDF 1.5, respectively. In addition, comparisons to GJR08 VF and FF were performed but are not shown for brevity.

NLOJet++ (but closer to the data) in the high- p_T region. These are also the regions where the scale uncertainty in the fixed order corrected for the non-perturbative effects increases because the non-perturbative corrections, and their uncertainty, have a significant influence.

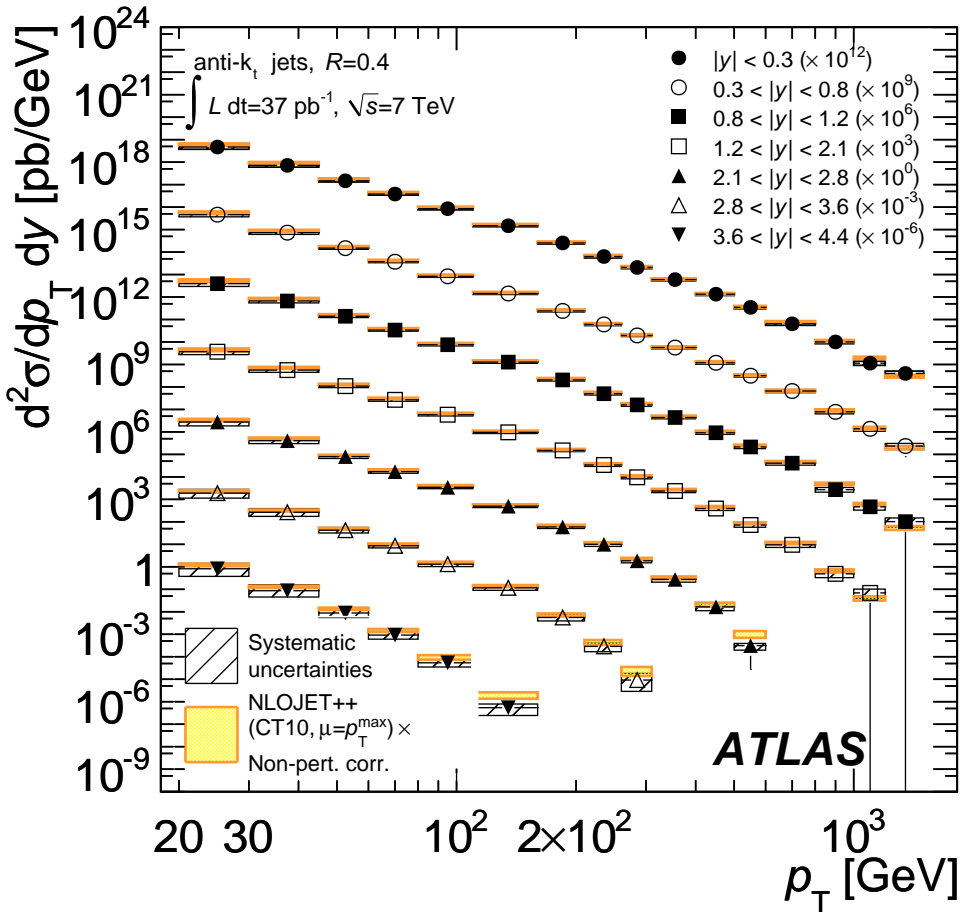


Figure 5.14: Inclusive jet double-differential cross section as a function of jet p_T in different regions of $|y|$ for jets identified using the anti- k_t algorithm with $R = 0.4$. For convenience, the cross sections are multiplied by the factors indicated in the legend. The data are compared to NLO pQCD calculations to which non-perturbative corrections have been applied. The error bars indicate the statistical uncertainty on the measurement, and the dark-shaded band indicates the quadratic sum of the experimental systematic uncertainties, dominated by the jet energy scale uncertainty. There is an additional overall uncertainty of 3.4% due to the luminosity measurement that is not shown. The theory uncertainty (light-shaded band) shown is the quadratic sum of uncertainties from the choice of renormalization and factorization scales, parton distribution functions, $\alpha_s(M_Z)$, and the modeling of non-perturbative effects, as described in the text.

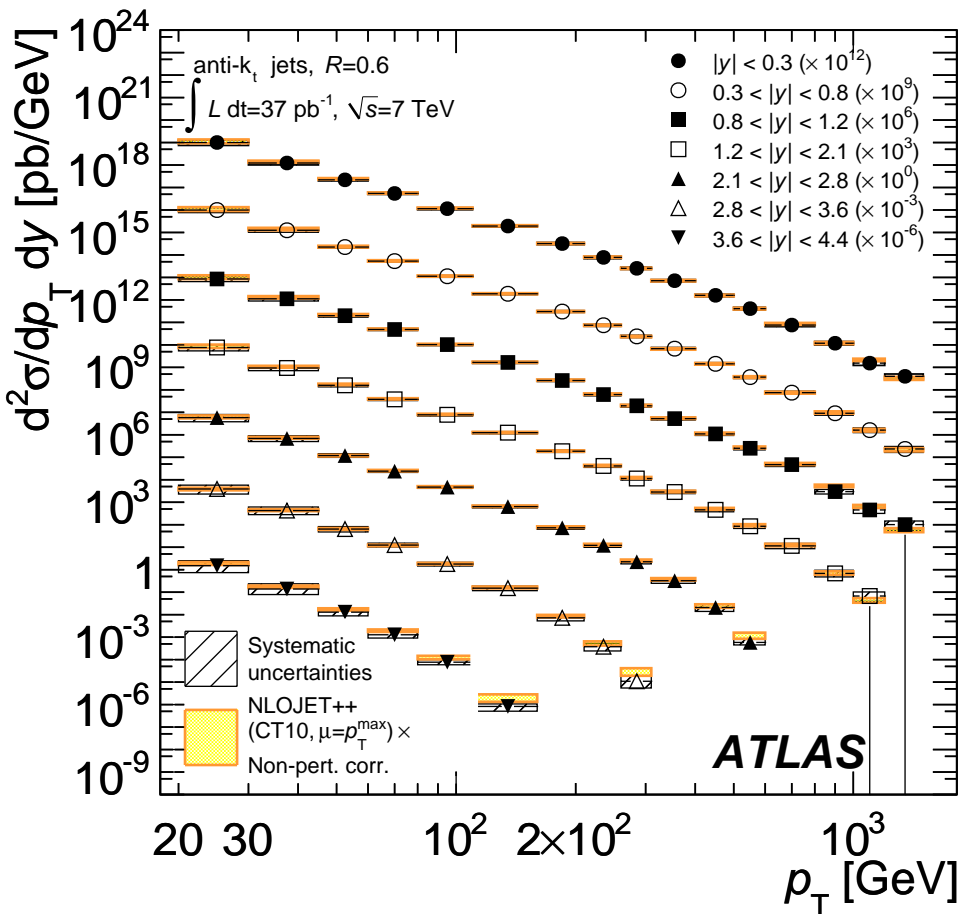


Figure 5.15: Inclusive jet double-differential cross section as a function of jet p_T in different regions of $|y|$ for jets identified using the anti- k_t algorithm with $R = 0.6$. For convenience, the cross sections are multiplied by the factors indicated in the legend. The data are compared to NLO pQCD calculations to which non-perturbative corrections have been applied. The theoretical and experimental uncertainties indicated are calculated as described in Fig. 5.14.

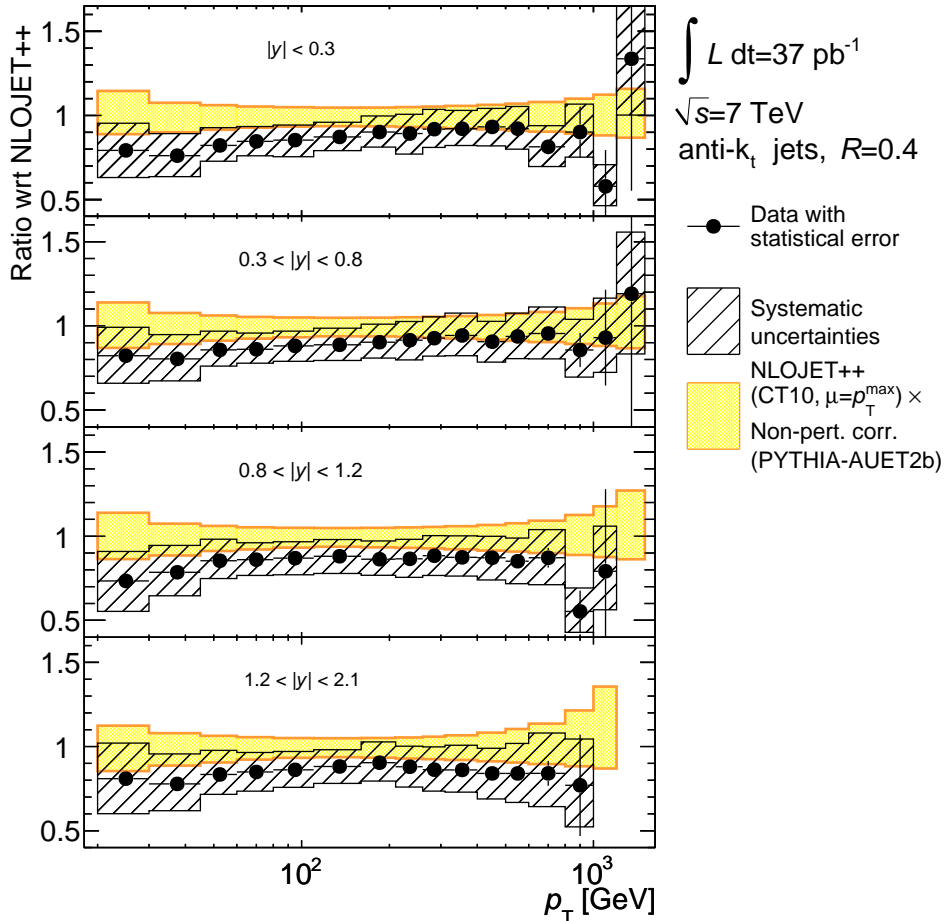


Figure 5.16: Inclusive jet double-differential cross section as a function of jet p_T in different regions of $|y|$ for jets identified using the anti- k_t algorithm with $R = 0.4$. The ratio of the data to the theoretical prediction is shown, and the total systematic uncertainties on the theory and measurement are indicated. The theoretical and experimental uncertainties are calculated as described in Fig. 5.14. Statistically insignificant data points at large p_T are omitted in the ratio.

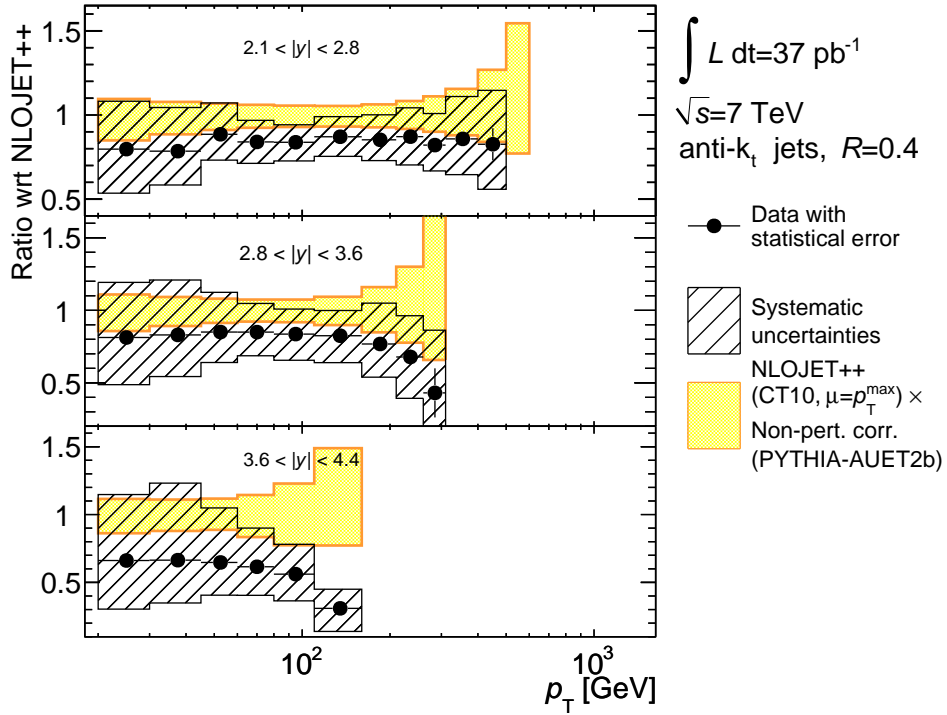


Figure 5.17: Inclusive jet double-differential cross section as a function of jet p_T in different forward regions of $|y|$ for jets identified using the anti- k_t algorithm with $R = 0.4$. The ratio of the data to the theoretical prediction is shown, and the total systematic uncertainties on the theory and measurement are indicated. The theoretical and experimental uncertainties are calculated as described in Fig. 5.14. Statistically insignificant data points at large p_T are omitted in the ratio.

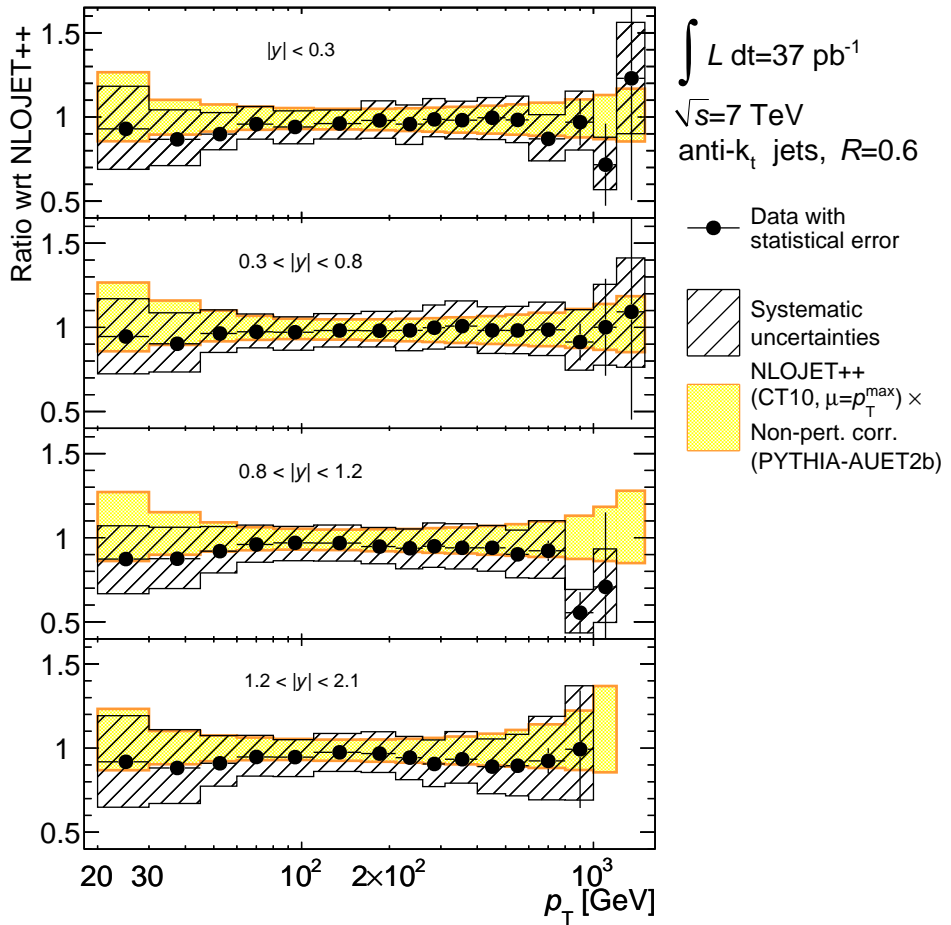


Figure 5.18: Inclusive jet double-differential cross section as a function of jet p_T in different regions of $|y|$ for jets identified using the anti- k_t algorithm with $R = 0.6$. The ratio of the data to the theoretical prediction is shown, and the total systematic uncertainties on the theory and measurement are indicated. The theoretical and experimental uncertainties are calculated as described in Fig. 5.14.

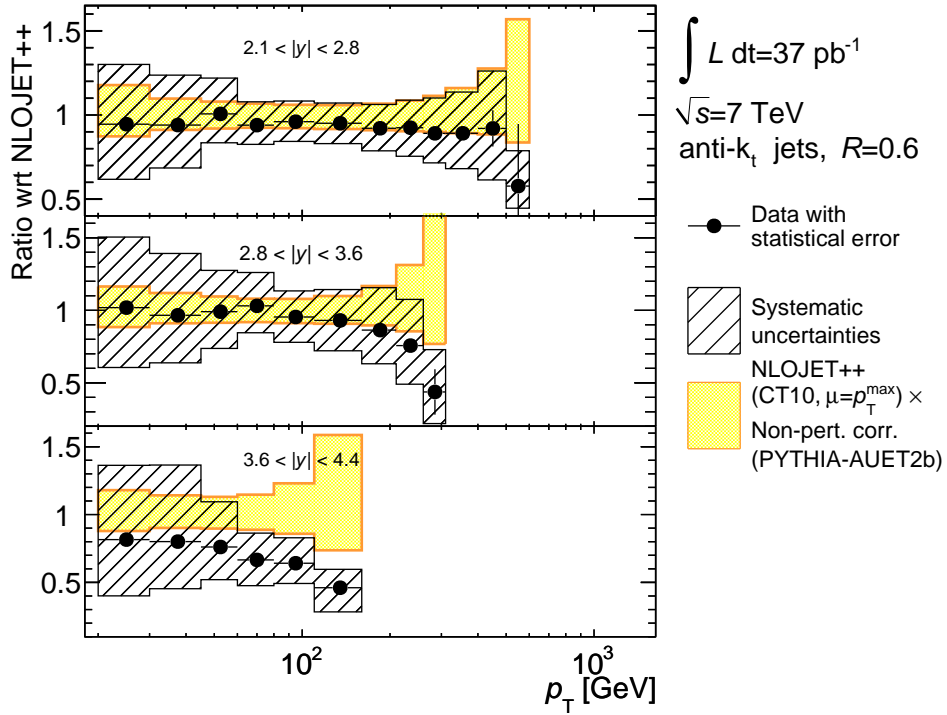


Figure 5.19: Inclusive jet double-differential cross section as a function of jet p_T in different forward regions of $|y|$ for jets identified using the anti- k_t algorithm with $R = 0.6$. The ratio of the data to the theoretical prediction is shown, and the total systematic uncertainties on the theory and measurement are indicated. The theoretical and experimental uncertainties are calculated as described in Fig. 5.14.

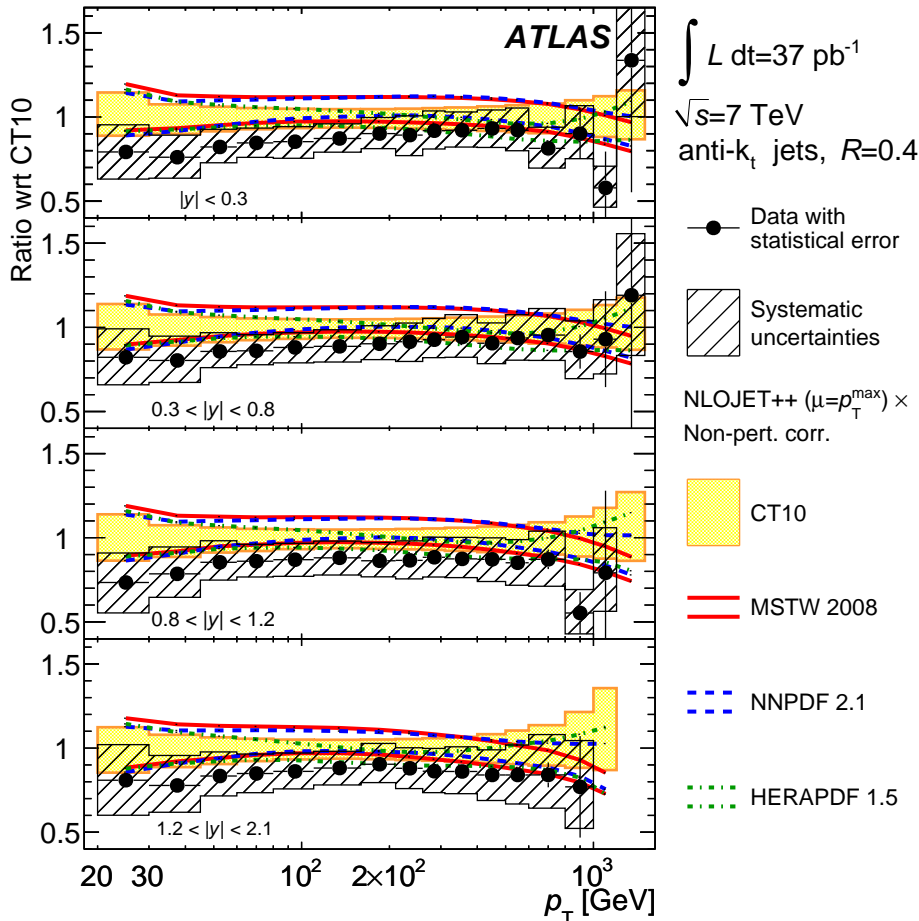


Figure 5.20: Inclusive jet double-differential cross section as a function of jet p_T in different central regions of $|y|$ for jets identified using the anti- k_t algorithm with $R = 0.4$. The theoretical error bands obtained by using different PDF sets (CT10, MSTW 2008, NNPDF 2.1, HERAPDF 1.5) are shown. The data points and the error bands are normalized to the theoretical predictions obtained by using the CT10 PDF set. Statistically insignificant data points at large p_T are omitted in the ratio.

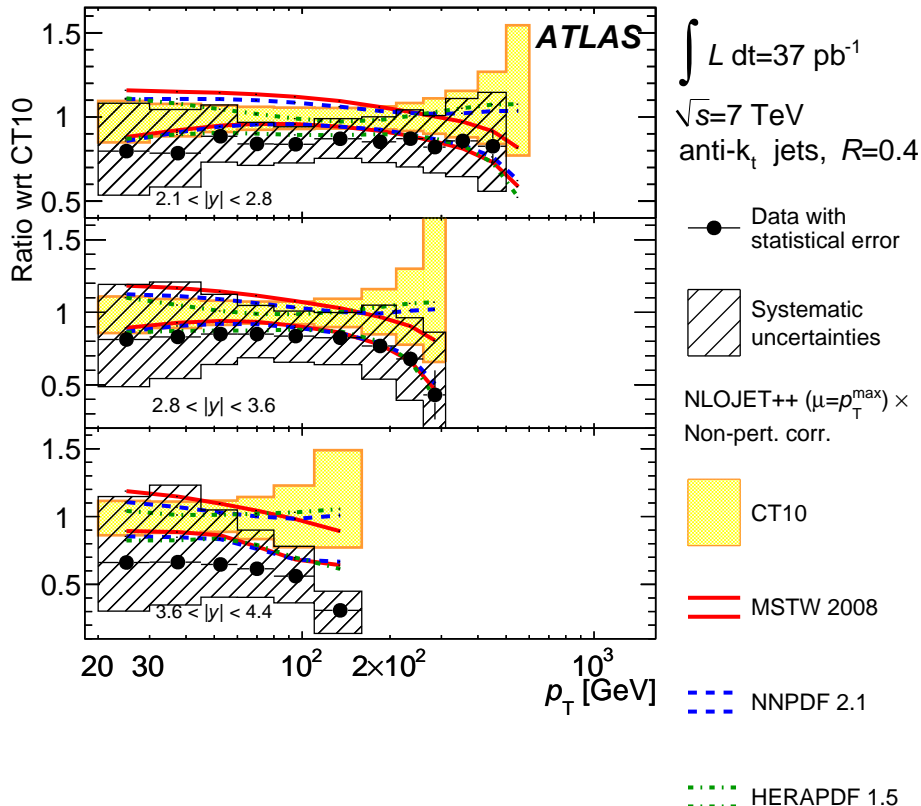


Figure 5.21: Inclusive jet double-differential cross section as a function of jet p_T in different forward regions of $|y|$ for jets identified using the anti- k_t algorithm with $R = 0.4$. The theoretical error bands obtained by using different PDF sets (CT10, MSTW 2008, NNPDF 2.1, HERAPDF 1.5) are shown. The data points and the error bands are normalized to the theoretical predictions obtained by using the CT10 PDF set. Statistically insignificant data points at large p_T are omitted in the ratio.

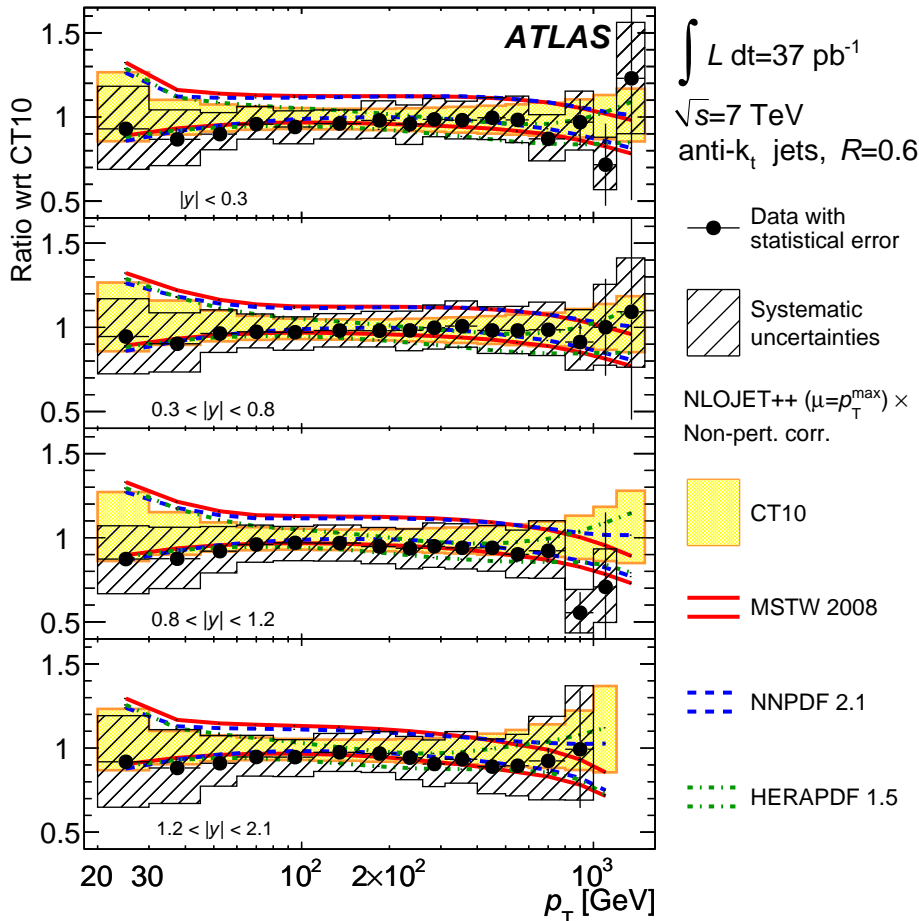


Figure 5.22: Inclusive jet double-differential cross section as a function of jet p_T in different central regions of $|y|$ for jets identified using the anti- k_t algorithm with $R = 0.6$. The theoretical error bands obtained by using different PDF sets (CT10, MSTW 2008, NNPDF 2.1, HERAPDF 1.5) are shown. The data points and the error bands are normalized to the theoretical predictions obtained by using the CT10 PDF set.

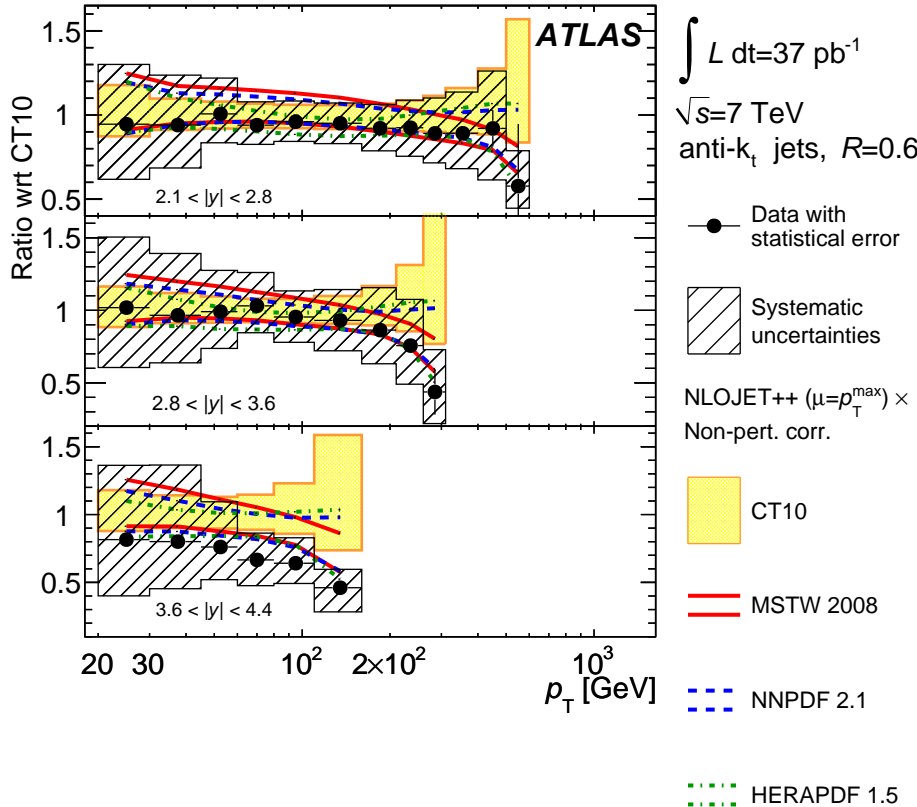


Figure 5.23: Inclusive jet double-differential cross section as a function of jet p_T in different forward regions of $|y|$ for jets identified using the anti- k_t algorithm with $R = 0.6$. The theoretical error bands obtained by using different PDF sets (CT10, MSTW 2008, NNPDF 2.1, HERAPDF 1.5) are shown. The data points and the error bands are normalized to the theoretical predictions obtained by using the CT10 PDF set.

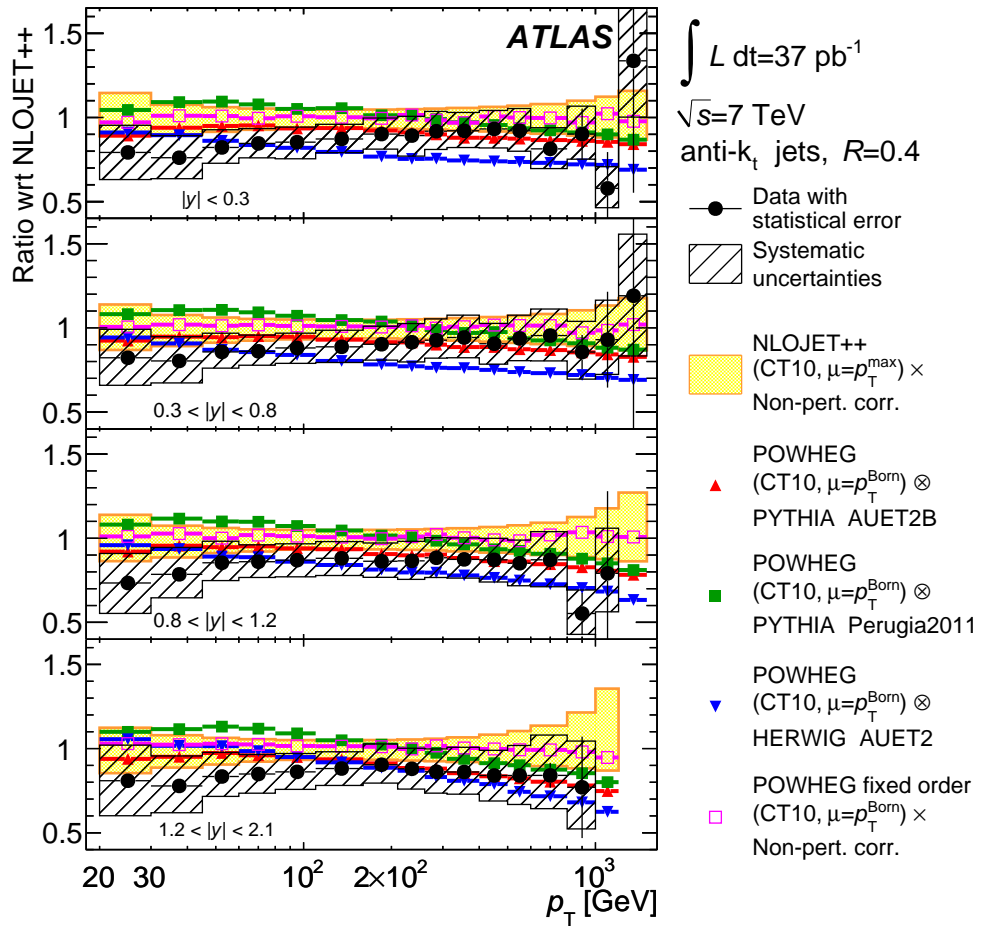


Figure 5.24: Inclusive jet double-differential cross section as a function of jet p_T in different regions of $|y|$ for jets identified using the anti- k_t algorithm with $R = 0.4$. The ratio of the Powheg predictions showered using either PYTHIA or HERWIG to the NLO predictions corrected for non-perturbative effects is shown. The ratio shows only the statistical uncertainty on the Powheg prediction, and can be compared to the corresponding data ratio. The total systematic uncertainty on the theory and measurement are indicated. The NLO pQCD prediction and the Powheg ME calculations use the CT10 PDF set. Statistically insignificant data points at large p_T are omitted in the ratio.

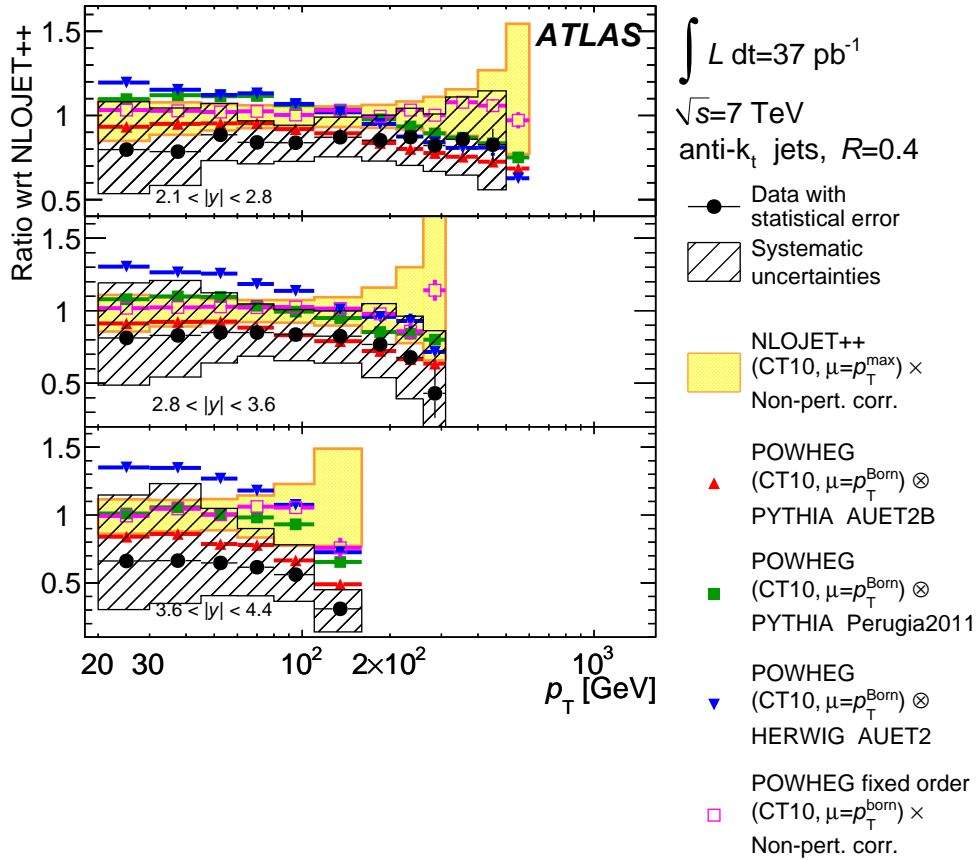


Figure 5.25: Inclusive jet double-differential cross section as a function of jet p_T in different forward regions of $|y|$ for jets identified using the anti- k_t algorithm with $R = 0.4$. The ratio of the Powheg predictions showered using either PYTHIA or HERWIG to the NLO predictions corrected for non-perturbative effects is shown. The ratio shows only the statistical uncertainty on the Powheg prediction, and can be compared to the corresponding data ratio. The total systematic uncertainties on the theory and measurement are indicated. The NLO pQCD prediction and the Powheg ME calculations use the CT10 PDF set.

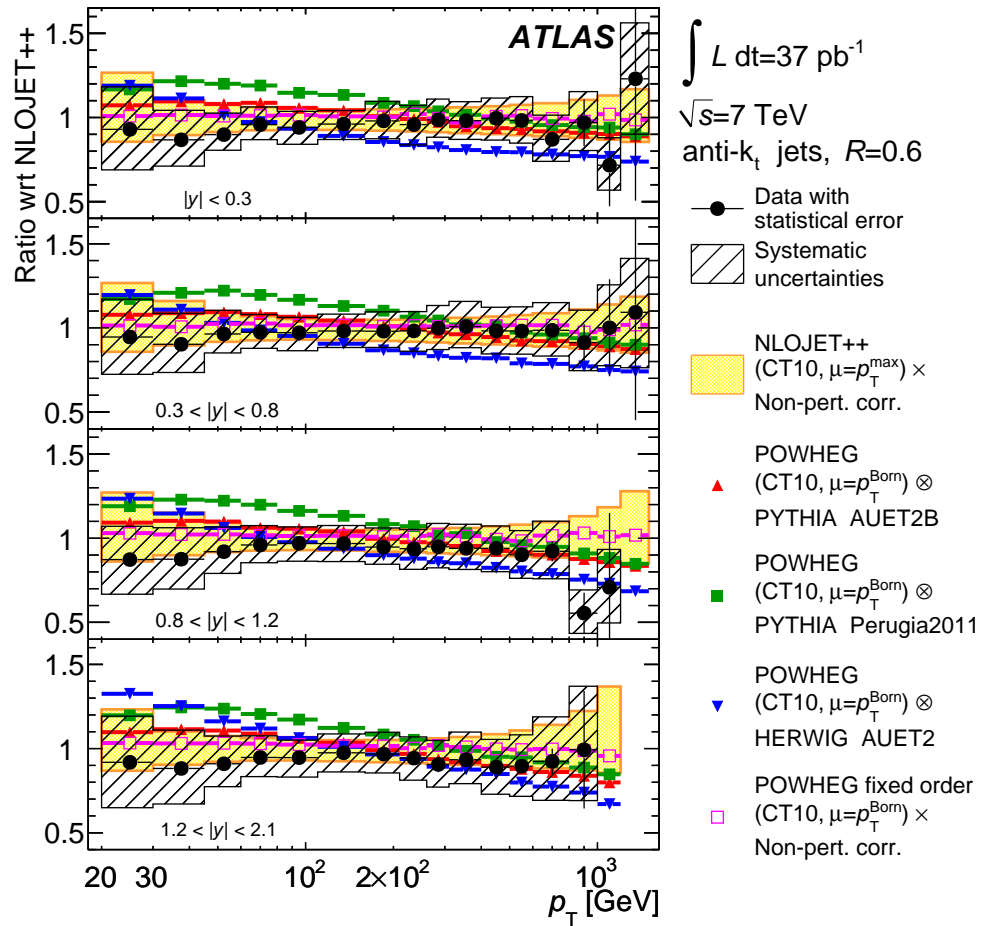


Figure 5.26: Inclusive jet double-differential cross section as a function of jet p_T in different regions of $|y|$ for jets identified using the anti- k_t algorithm with $R = 0.6$. The ratio of the Powheg predictions showered using either PYTHIA or HERWIG to the NLO predictions corrected for non-perturbative effects is shown. The ratio shows only the statistical uncertainty on the Powheg prediction, and can be compared to the corresponding data ratio. The total systematic uncertainties on the theory and measurement are indicated. The NLO pQCD prediction and the Powheg ME calculations use the CT10 PDF set. Statistically insignificant data points at large p_T are omitted in the ratio.

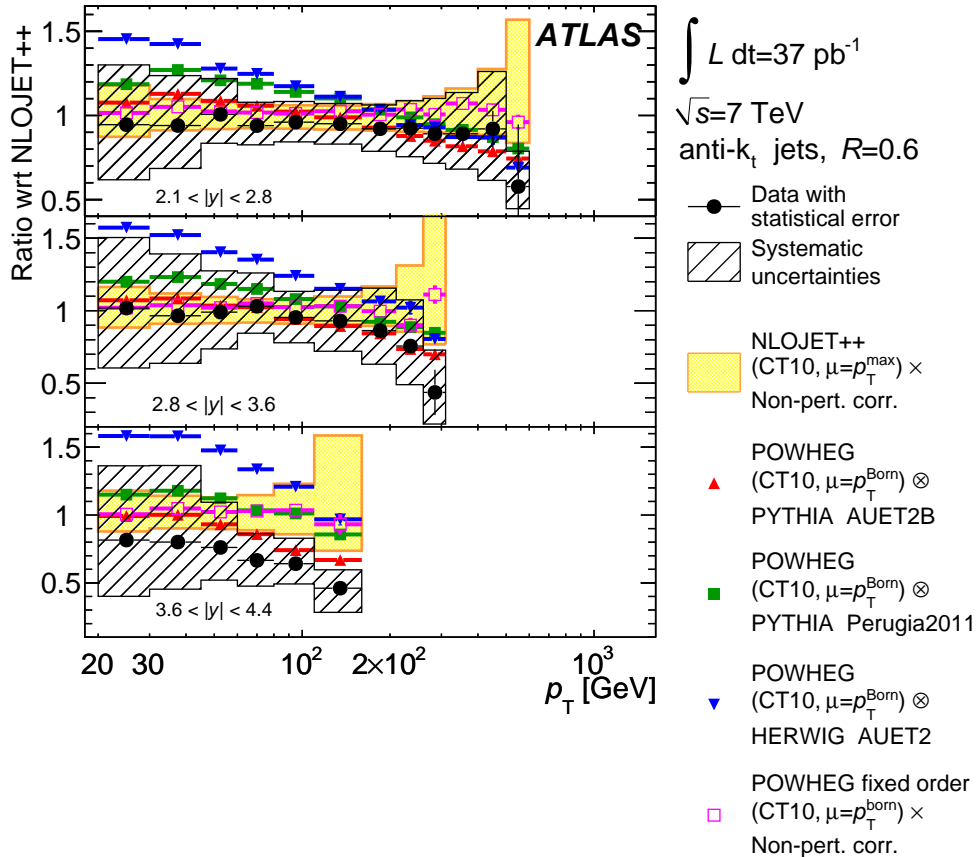


Figure 5.27: Inclusive jet double-differential cross section as a function of jet p_T in different forward regions of $|y|$ for jets identified using the anti- k_t algorithm with $R = 0.6$. The ratio of the Powheg predictions showered using either PYTHIA or HERWIG to the NLO predictions corrected for non-perturbative effects is shown. The ratio shows only the statistical uncertainty on the Powheg prediction, and can be compared to the corresponding data ratio. The total systematic uncertainties on the theory and measurement are indicated. The NLO pQCD prediction and the Powheg ME calculations use the CT10 PDF set.

CHAPTER 6

Conclusions

Cross section measurements have been presented for inclusive jets reconstructed with the anti- k_t algorithm using two values of the clustering parameter R (0.4 and 0.6). The inclusive jet production has been measured as a function of jet transverse momentum, in bins of jet rapidity. These results are based on the data sample collected with the ATLAS detector during 2010, which corresponds to $37.3 \pm 1.2 \text{ pb}^{-1}$ of integrated luminosity.

Two different sizes of the jet clustering parameter have been used in order to probe the relative effects of the parton shower, hadronisation, and the underlying event. The measurements have been corrected for all detector effects to the particle level so that they can be compared to any theoretical calculation. In this thesis, they have been compared to fixed order NLO pQCD calculations corrected for non-perturbative effects, as well as to parton shower Monte Carlos with NLO matrix elements. The latter predictions have only recently become available for inclusive jet production.

The results in this thesis present a number of significant experimental improvements with respect to the previous ATLAS publication on the same subject [[ATLAS Collaboration 2011k](#)], and to the other results obtained at other hadron colliders:

- The use of the full 2010 dataset extends the measurements to 1.5 TeV in jet transverse momentum, truly probing a large, new kinematic regime.
- The measurement has been expanded, using data acquired with minimum bias and forward jet triggers, to both the low- p_T region (down to jet transverse momentum of 20 GeV) and to the forward region (out to rapidities of $|y| = 4.4$). The forward region, in particular, has never been explored before with such precision at a hadron-hadron collider.
- High-precision measurements of the data collected during LHC beam position scans have allowed the uncertainty on the collected luminosity to be 3.4%.
- Improved understanding of the detector performance has reduced several systematic uncertainties, in particular those arising from the jet energy scale. The JES uncertainty has been reduced by up to a factor of two with respect to the JES used in the publication in Reference [[ATLAS Collaboration 2011k](#)]. In the central region ($|\eta| < 0.8$) the uncertainty is lower than 4.6% for all jets with $p_T > 20$ GeV, while for jet transverse momenta between 60 and 800 GeV the uncertainty is below 2.5%.

The experimental uncertainties achieved are similar in size to the theoretical uncertainties in some regions of phase space, thereby providing some sensitivity to different theoretical

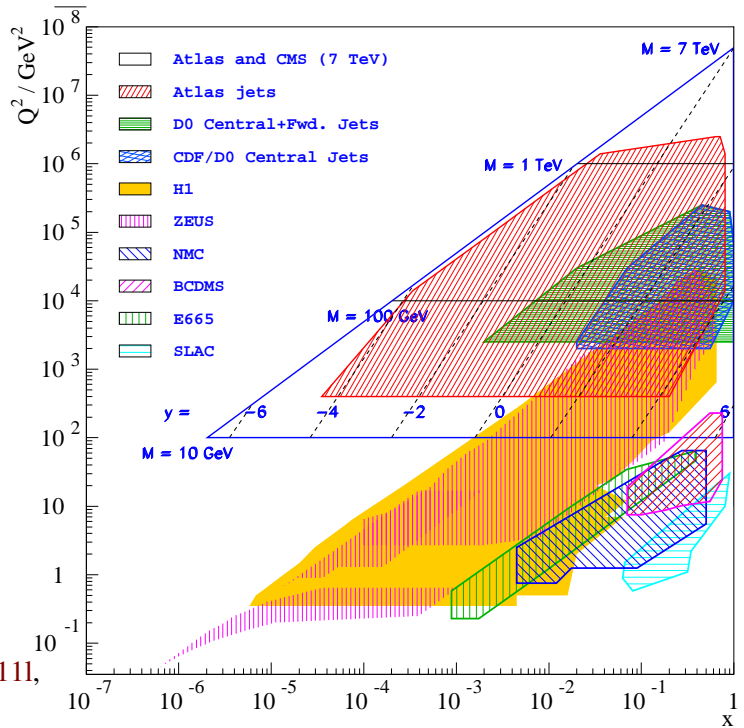


Figure 6.1: Region covered by the measurement of the inclusive jet cross section in the (x, Q^2) plane, compared with the regions covered by previous experiments. Figure taken from References [ATLAS Collaboration 2011], Glazov 2011].

predictions. A detailed study of the correlation on the systematics and statistical errors makes this result a solid measurement to be used in QCD fits.

Overall, the agreement of the NLO perturbative QCD predictions with the measurements extends over many orders of magnitude in cross section, up to 7 in the central region. Figure 6.1 shows the region in the (x, Q^2) plane covered by this measurement (labeled "Atlas jet"), compared with the total expected region at the LHC (labeled "Atlas and CMS (7 TeV)"), and the measured region in other previous experiments. As shown in this Figure, this measurement probes and may constrain the largely unexplored area of parton distribution functions at large x and high momentum transfer. The results reported here offer one of the most comprehensive tests of QCD ever performed.

APPENDIX A

Comparison of the 2010 Summer result and the complete 2010 data analysis

The measurement of the inclusive jet cross section presented in this thesis is the evolution of the first measurement of the inclusive jet production at the LHC ever public. The first cross section was publicly presented for the first time at ICHEP2010, and it was published few months later. The publication can be found in Reference [ATLAS Collaboration 2011k].

The analysis reported here profits of the higher available statistics at the end of 2010, and of the improved understanding of the systematics errors. On the other hand, this measurement overcomes the old results not only for the accuracy in the estimate of the cross section, but also in extending the covered phase-space.

The comparison of the phase- space covered by the old measurement, and the new one reported here, is shown in Figure A.1.

The new measurement, profiting of the higher statistics, covers regions at higher p_T . The regions at low- p_T and forward $|y|$ regions are extended to the reachable limits of the detector.

In Figure A.2, the old measurement reported in Reference [ATLAS Collaboration 2011k], is compared with the new one. From this plot, it is evident that the systematic errors decreased by a factor two, thanks to the improved understanding of the jet energy scale.

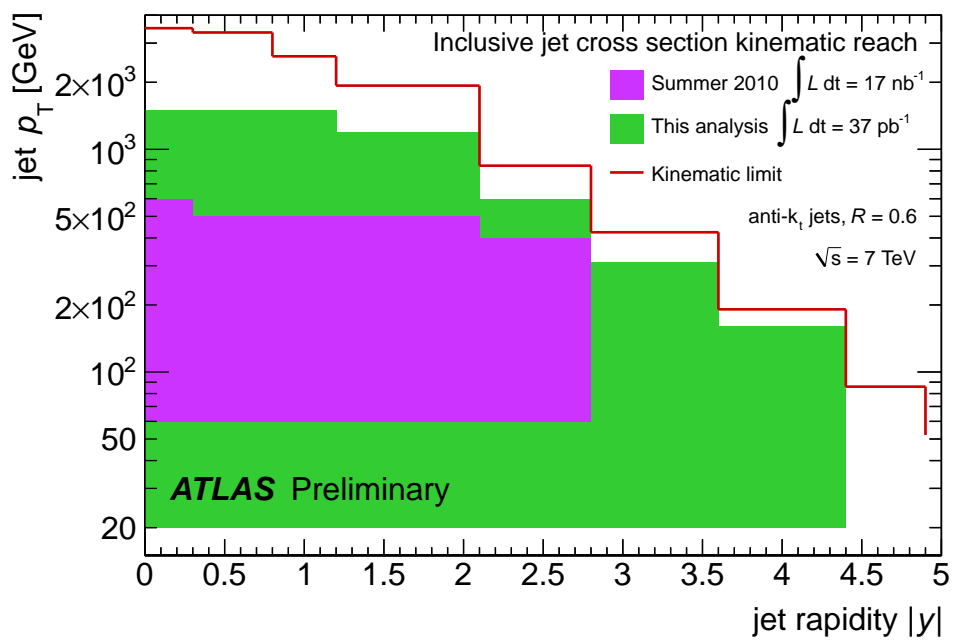


Figure A.1: Kinematic range in p_T and $|y|$ of the measurement of the inclusive jet cross section reported in this thesis, compared with the kinematic range reported in the Reference [ATLAS Collaboration 2011k].

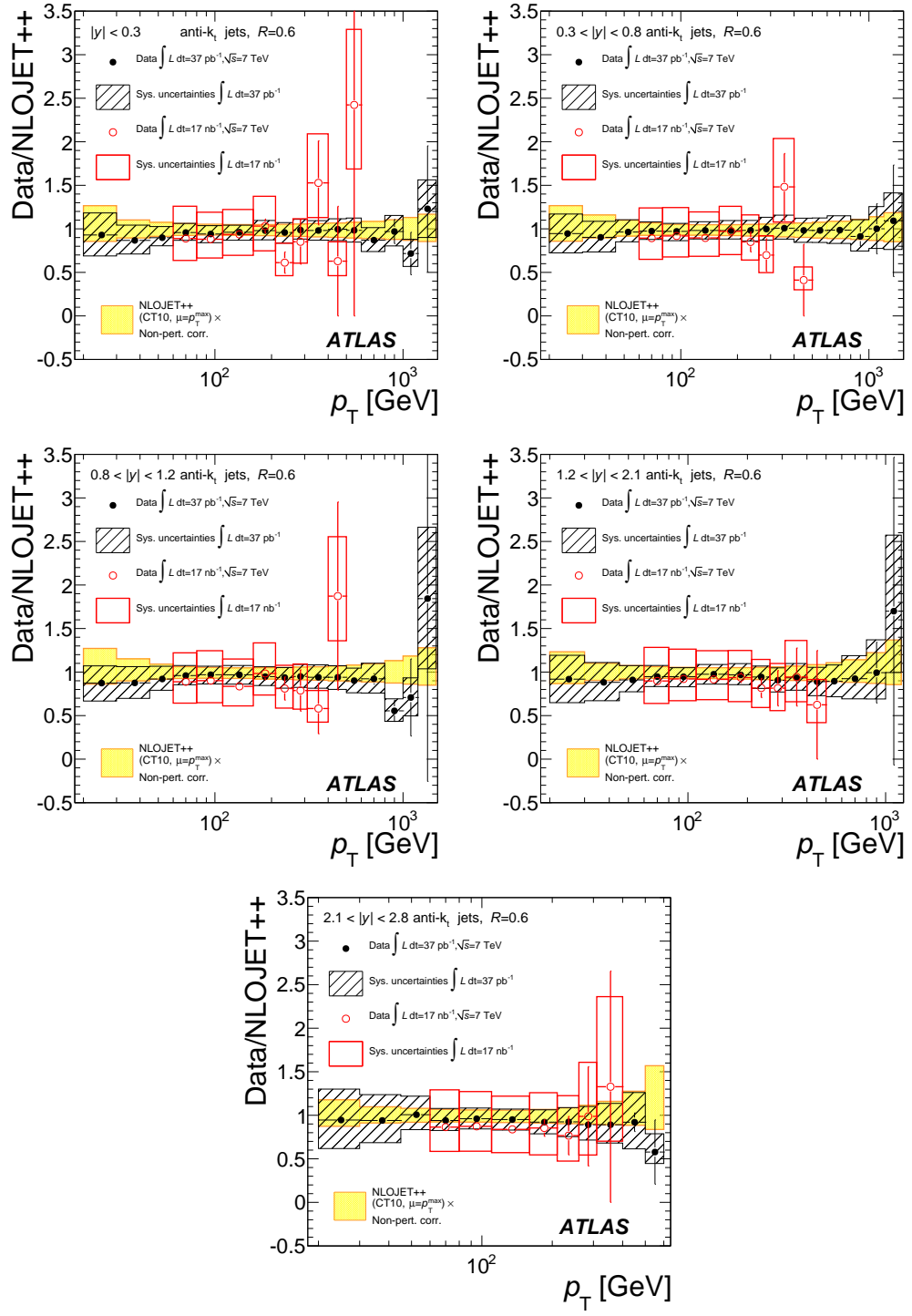


Figure A.2: Plot of the ratio between the measured cross section and the NLO fixed order prediction, corrected for the non-perturbative effects. The comparison of the accuracy of the measurement reported in this thesis, with the measurement reported in the Reference [ATLAS Collaboration 2011k] is shown.

APPENDIX B

Additional material to Chapter 2

This appendix contains additional material to Chapter 2.

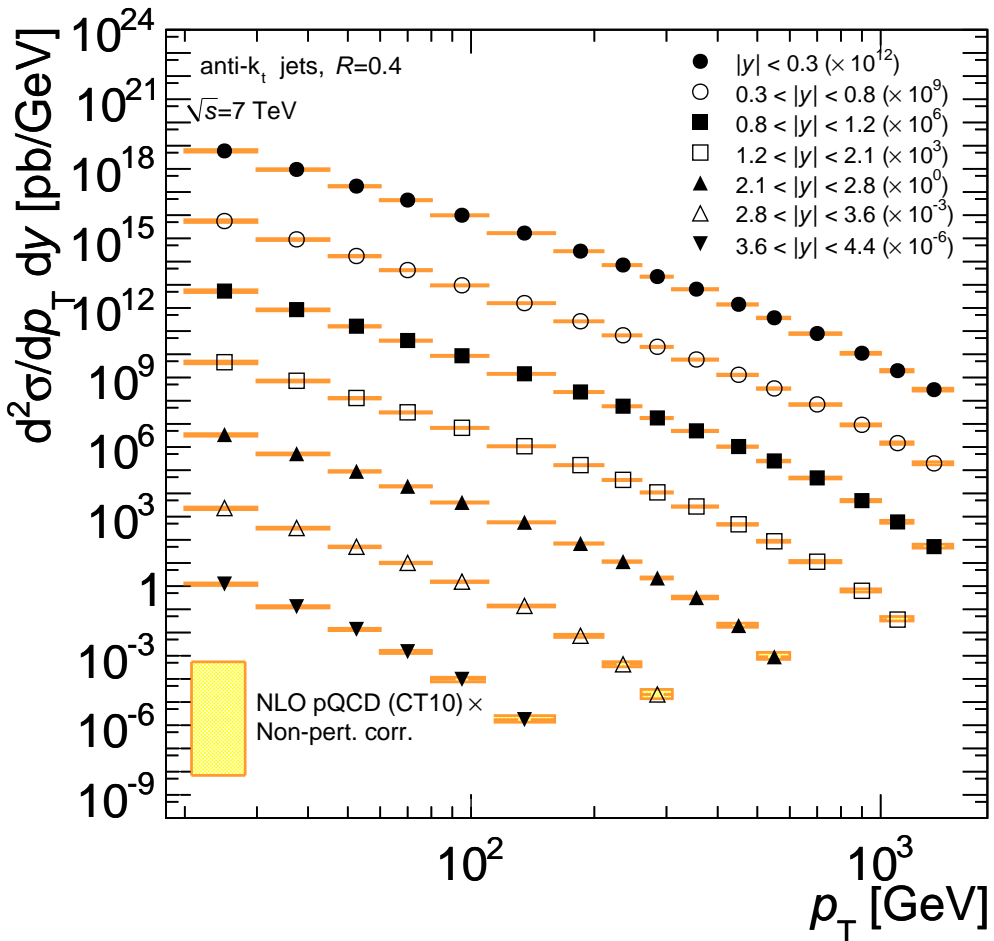


Figure B.1: Prediction for the inclusive jet cross section at $\sqrt{s} = 7$ TeV for the anti- k_t jet algorithm with $R = 0.4$. The theoretical prediction is derived by correcting with the non perturbative factors, the fixed order NLO calculation. To distinguish the cross section in the different rapidity regions, multiplicative factors have been used. The PDF used for the perturbative calculation are the CT10.

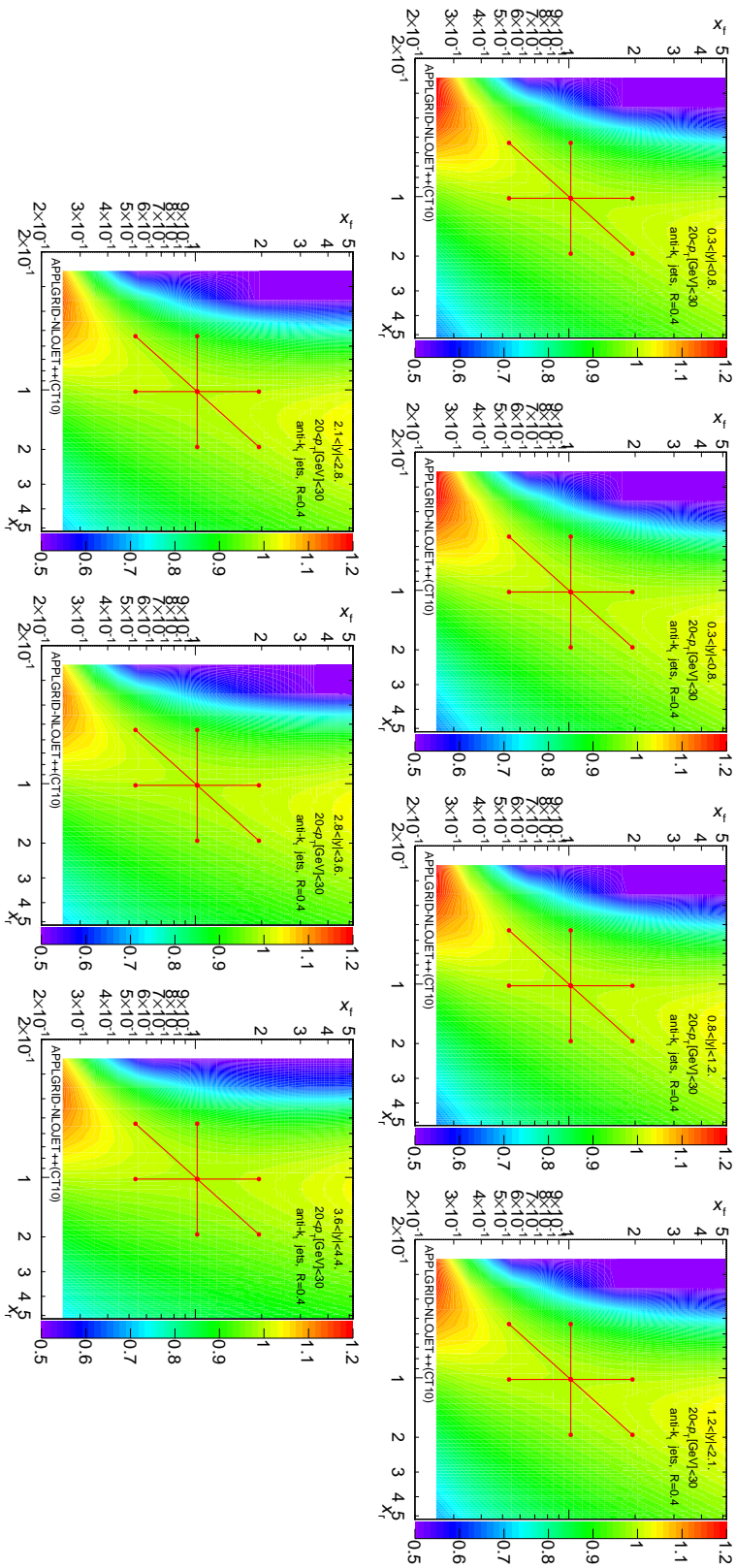


Figure B.2: Scale dependence for the inclusive jet cross section for the anti- k_t jet algorithm with $R = 0.4$, in the first bins in p_T of the measured jet cross in the different $|y|$ regions. The scale dependence, shown following the color scheme on the right, is normalized to the cross section in the point (1,1).

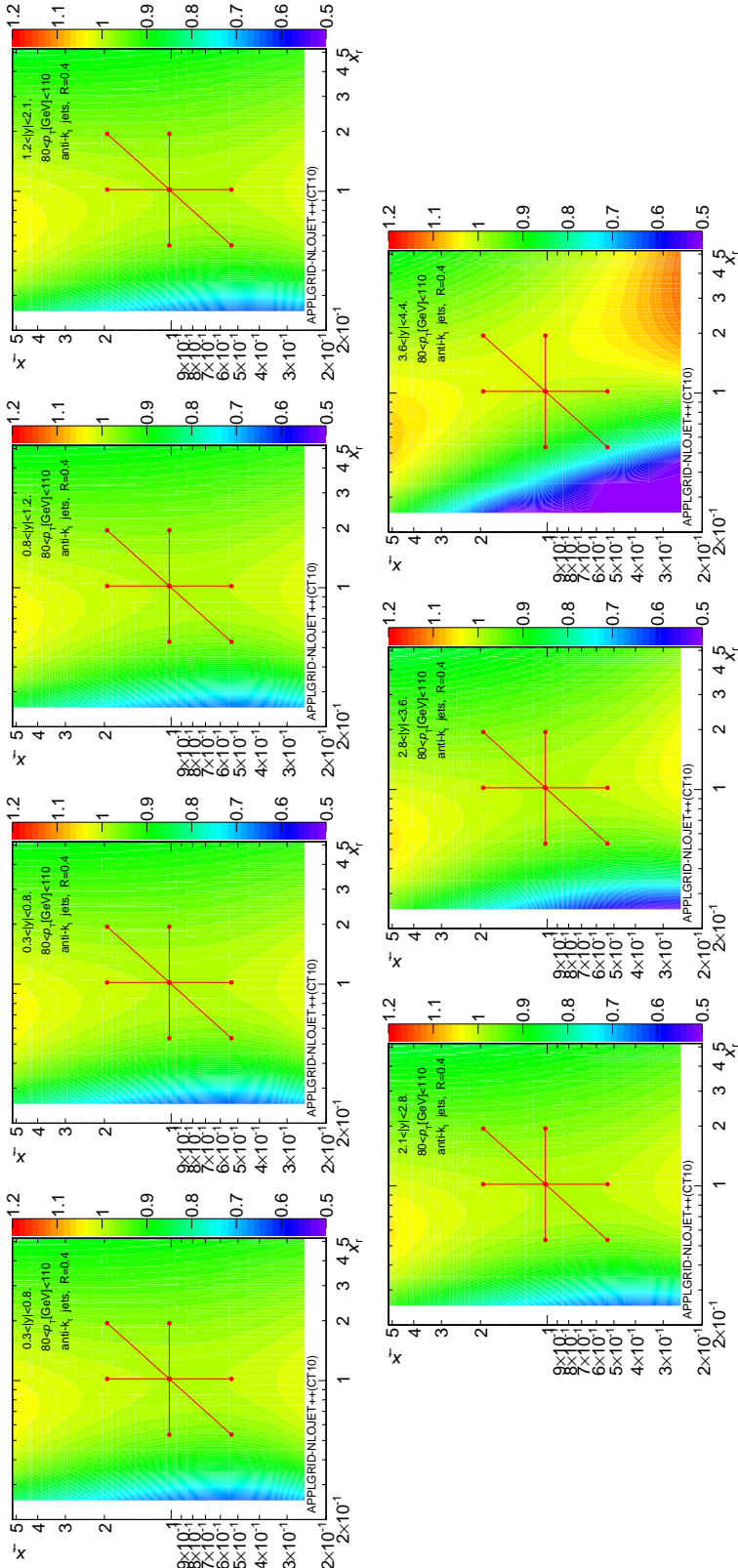


Figure B.3: Scale dependence for the inclusive jet cross section for the anti- k_t jet algorithm with $R=0.4$, in an intermediate bins in p_T (~ 100 GeV) of the measured jet cross section in the different $|y|$ regions. The scale dependence, shown following the color scheme on the right, is normalized to the cross section in the point (1,1).

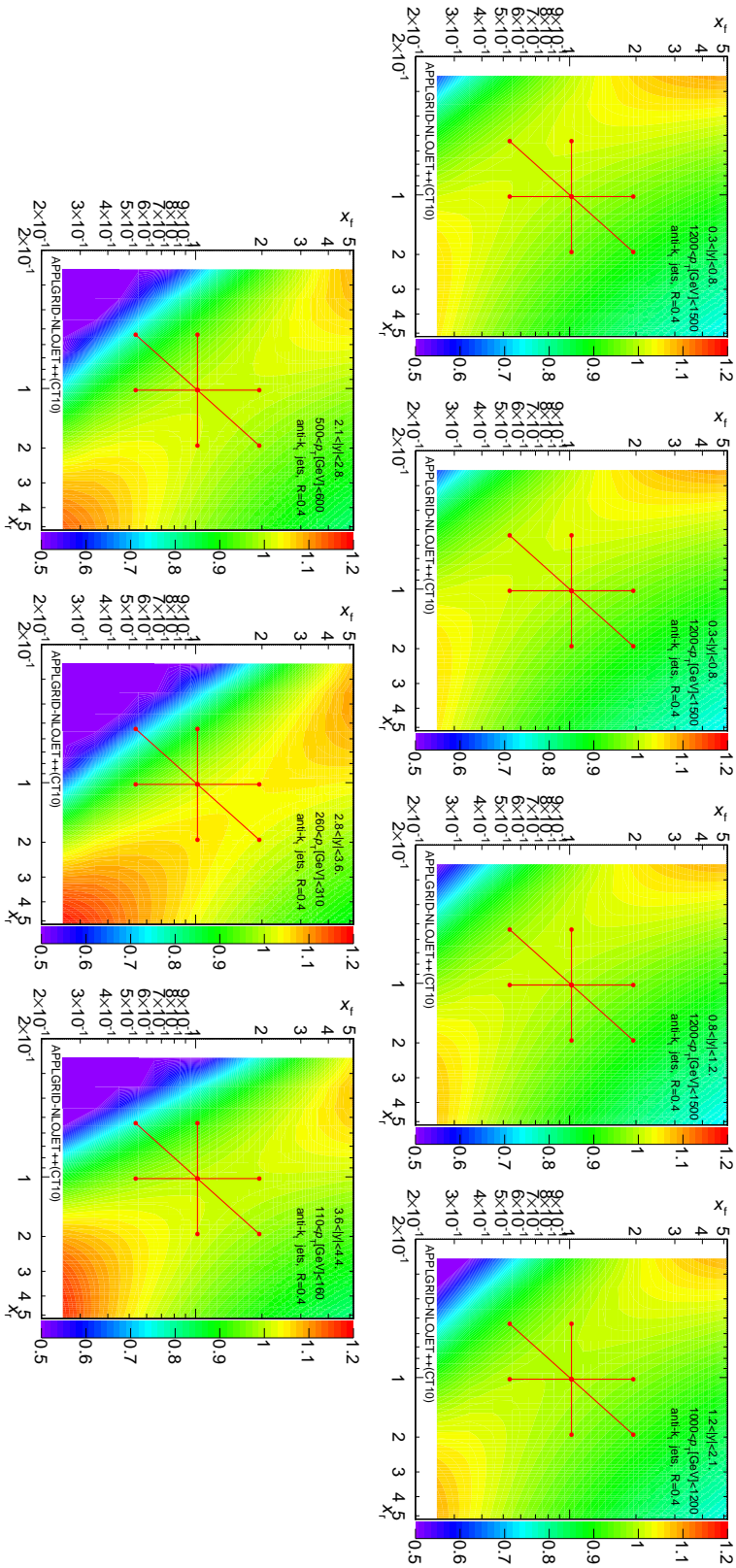


Figure B.4: Scale dependence for the inclusive jet cross section for the anti- k_t jet algorithm with $R=0.4$, in the last bins in p_T of the measured jet cross section, in the different $|y|$ regions. The scale dependence, shown following the color scheme on the right, is normalized to the cross section in the point (1,1).

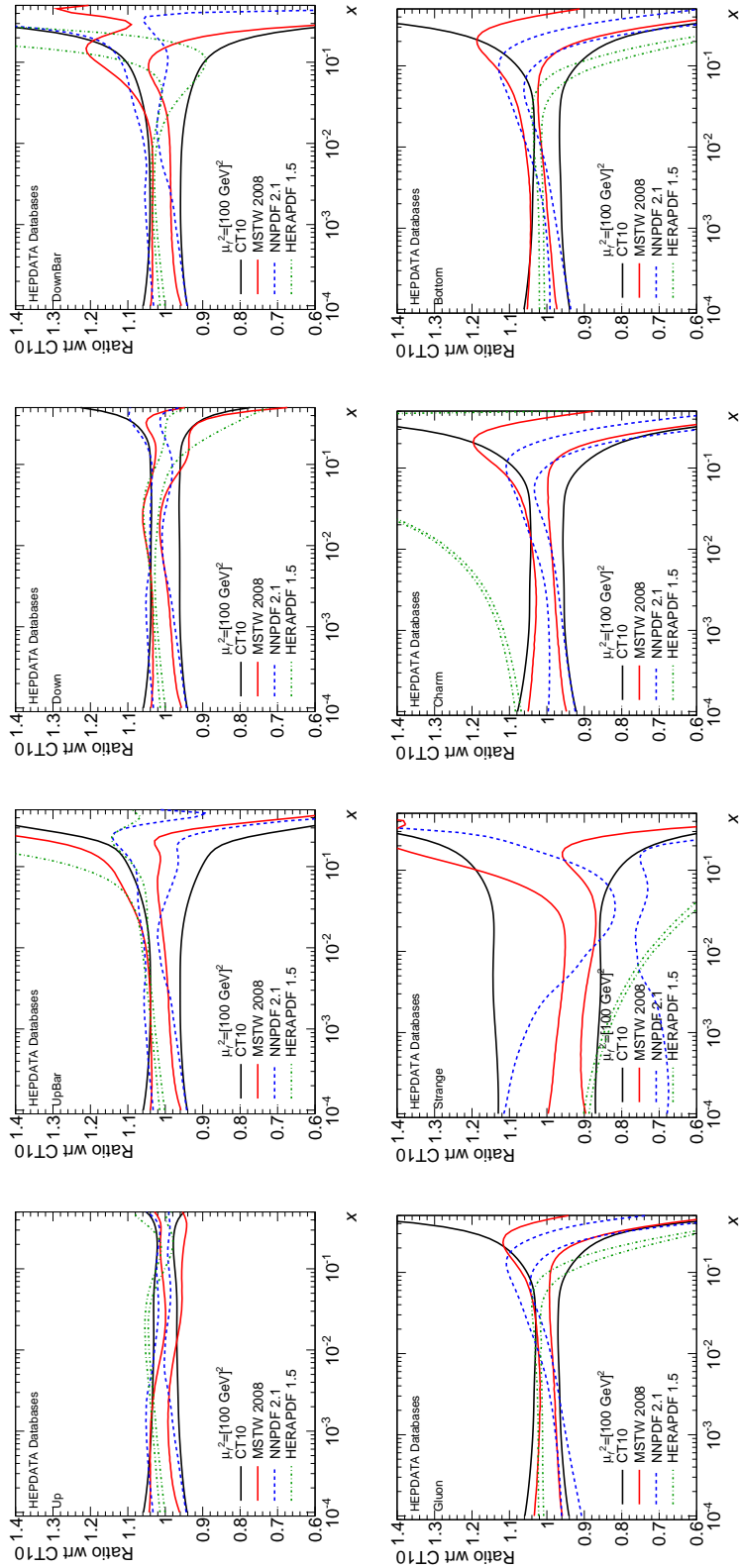


Figure B.5: Comparison of parton distribution functions in different PDF families: CT10, MSTW 2008, HERAPDF 1.5, NNPDF 2.1. Values extracted from Reference [<http://dmpdg.dur.ac.uk/>].

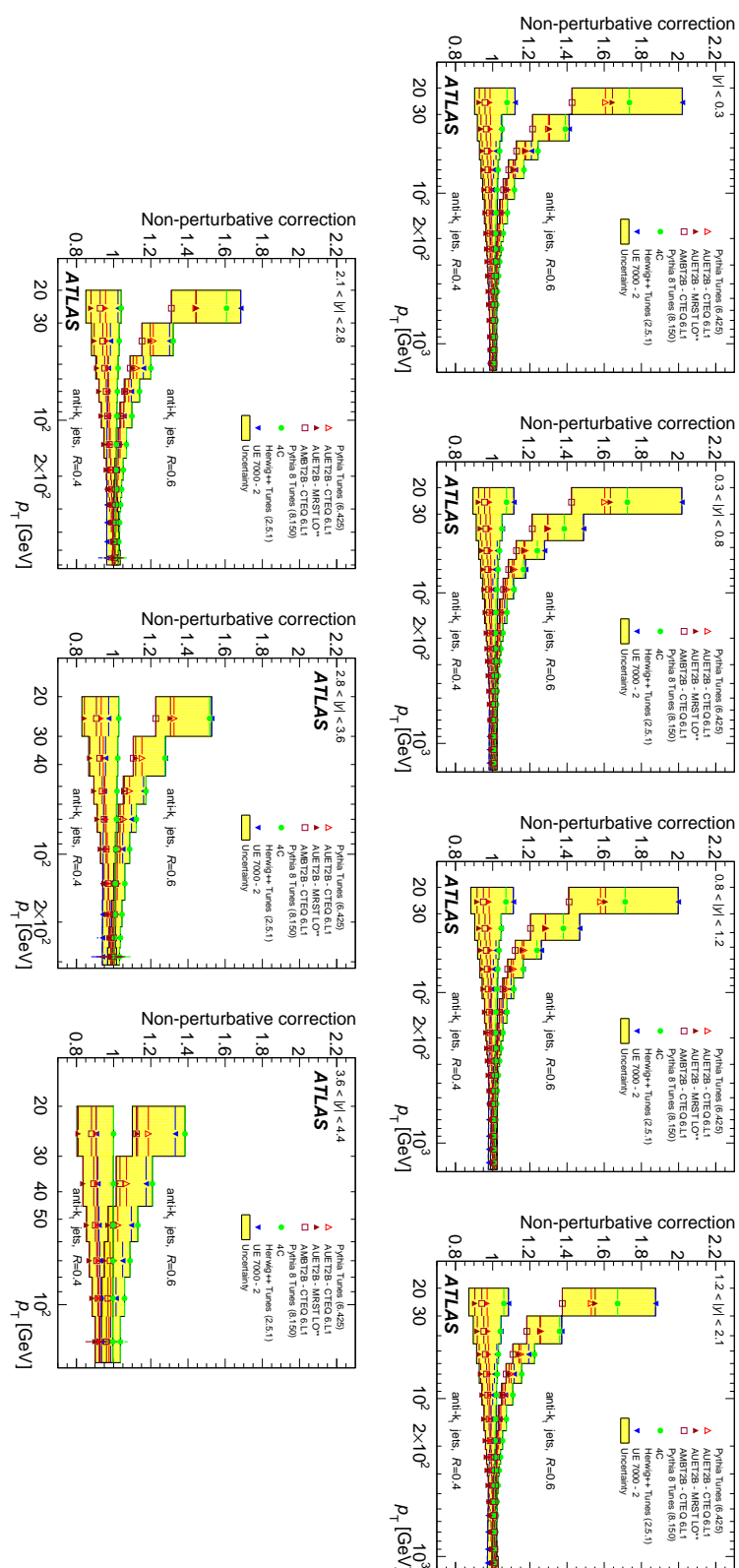


Figure B.6: Non-perturbative corrections, evaluated with different Monte Carlo generators and tunes for the inclusive jet cross section of anti- k_t jets with $R=0.4$ and $R=0.6$ in different rapidity regions.

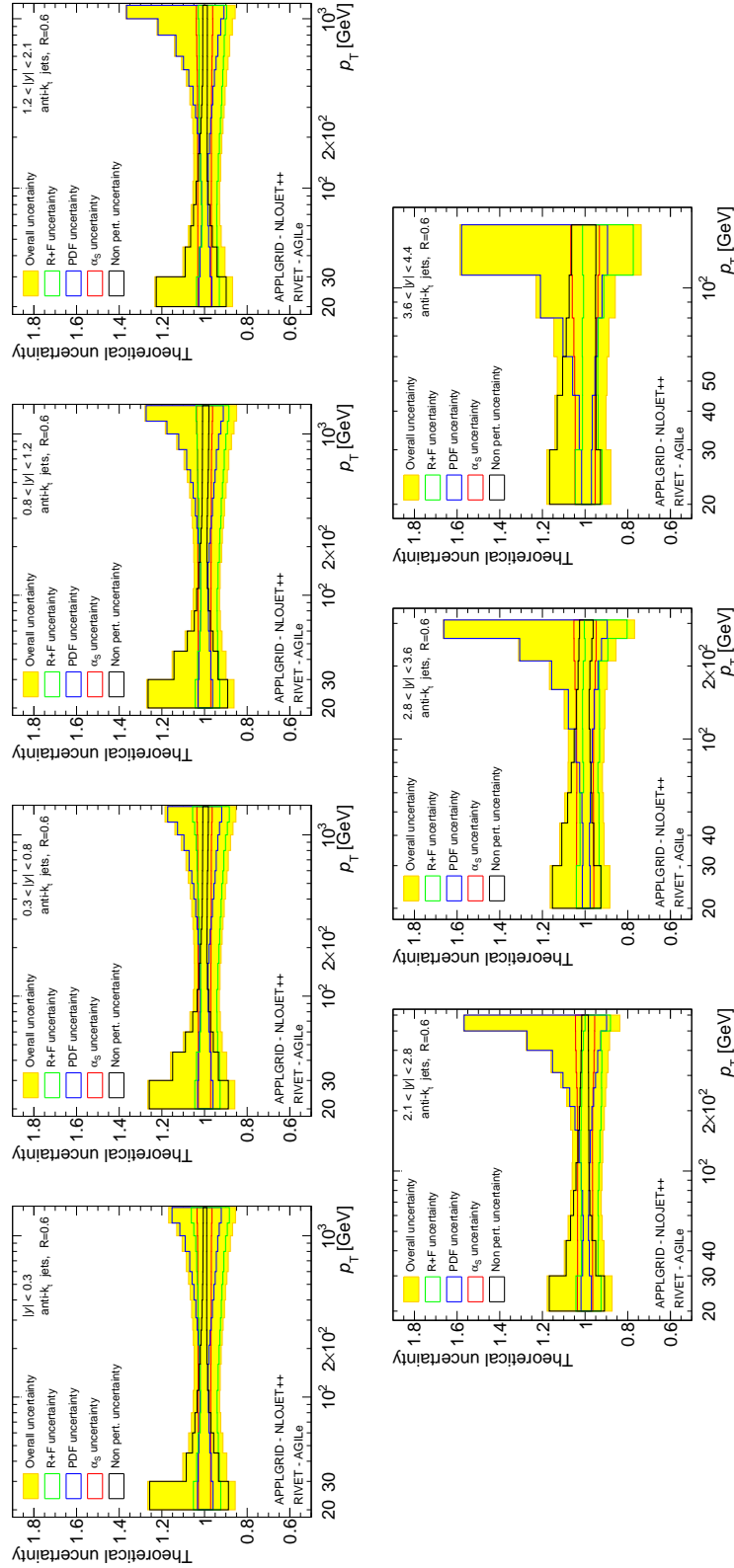


Figure B.7: Total uncertainty on the fixed order theoretical prediction for the different rapidity regions for the inclusive jet cross section of anti- κ_t jets with $R=0.6$. The different sub-components are shown in the different figures.

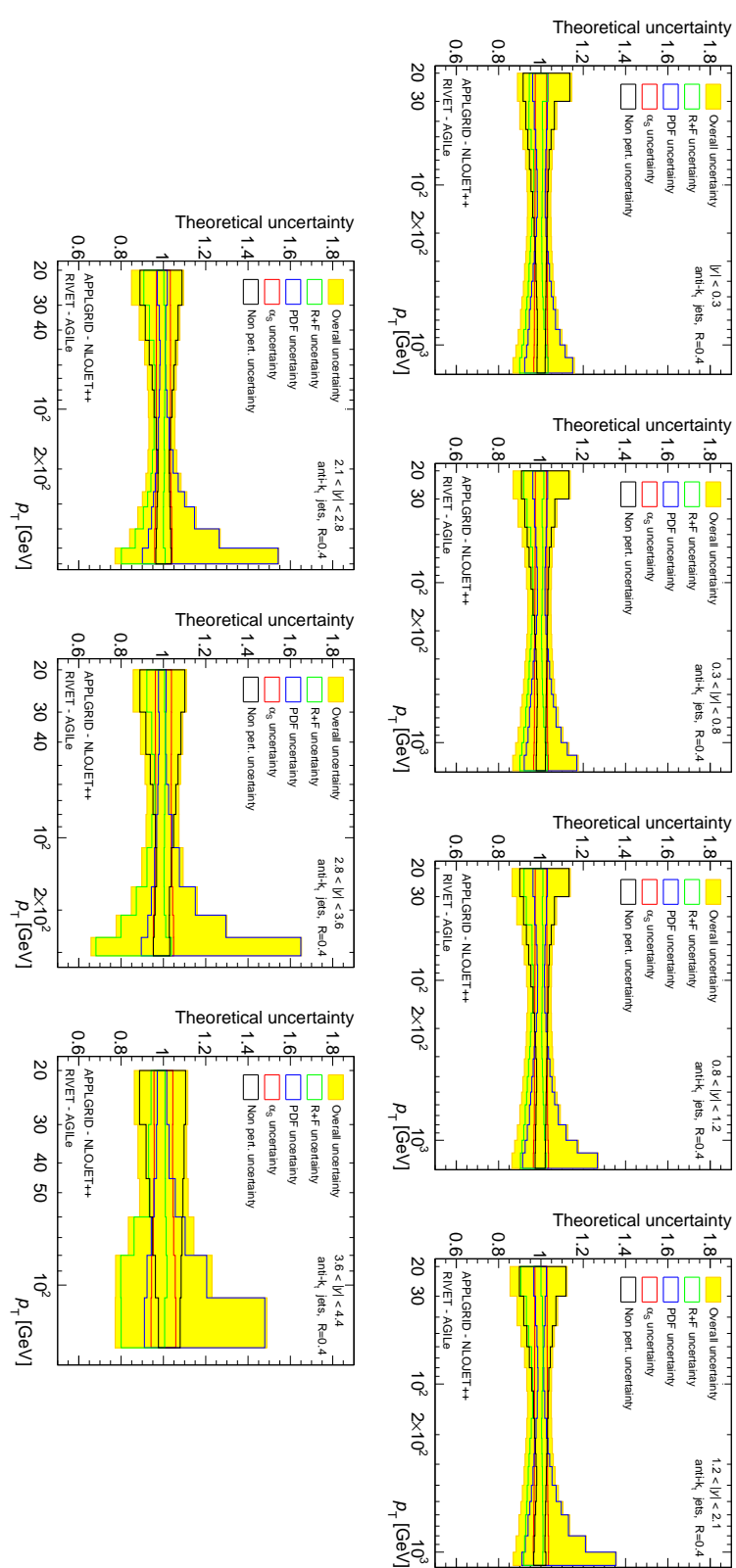


Figure B.8: Total uncertainty on the fixed order theoretical prediction for the different rapidity regions for the inclusive jet cross section of anti- k_t jets with $R=0.4$. The different sub-components are shown in the different figures.

APPENDIX C

Additional material to Chapter 4

This appendix contains additional material to Chapter 4.

C.1 Jet cleaning

The detailed list of variables and selection cuts described in Section 4.1 is the following:

- **Jets from noisy hadronic end-cap (HEC) calorimeter electronics:** a jet is rejected if:
 - the fraction of energy deposited in the HEC (HECf) is greater than one minus the HEC quality variable (HECQ). HECQ is the fraction of jet cells located in the HEC with a bad pulse shape compared to a reference shape;
 - the sum of all absolute values of cell energies below 0 GeV in a given jet (negE) is greater than 60 GeV. This has great discriminating power in rejecting jets reconstructed due to noise fluctuations.
- **Jets from noisy electromagnetic (EM) calorimeter electronics:** a jet is rejected if:
 - the fraction of energy deposited in the EM calorimeter (EMf) is greater than 0.9, the liquid argon calorimeter quality variable (LArQ) is greater than 0.8, and the jet is within $|\eta| < 2.8$. LArQ is the analogue of HECQ for the EM calorimeter.
- **Jets from non-collision background:**
a jet is rejected if:
 - the EMf variable is smaller than 0.05, the charged fraction (chf) is smaller than 0.1, and the jet is within $|\eta| < 2.0$. The chf variable is the fraction of the total jet p_T that is represented by the sum of the p_T of all tracks associated to a jet;
 - the absolute difference between the cell weighted time of the jets and the average event time (timing) is more than 10 ns;
 - the EMf variable is smaller than 0.05, and the jet is outside the tracking acceptance $|\eta| > 2.0$;
 - the EMf variable is greater than 0.95, the chf variable is smaller than 0.05, and the jet is within $|\eta| < 2.0$;
 - the maximal fraction of energy deposited in any one layer of the sampling calorimeter (fmax) is greater than 0.99.

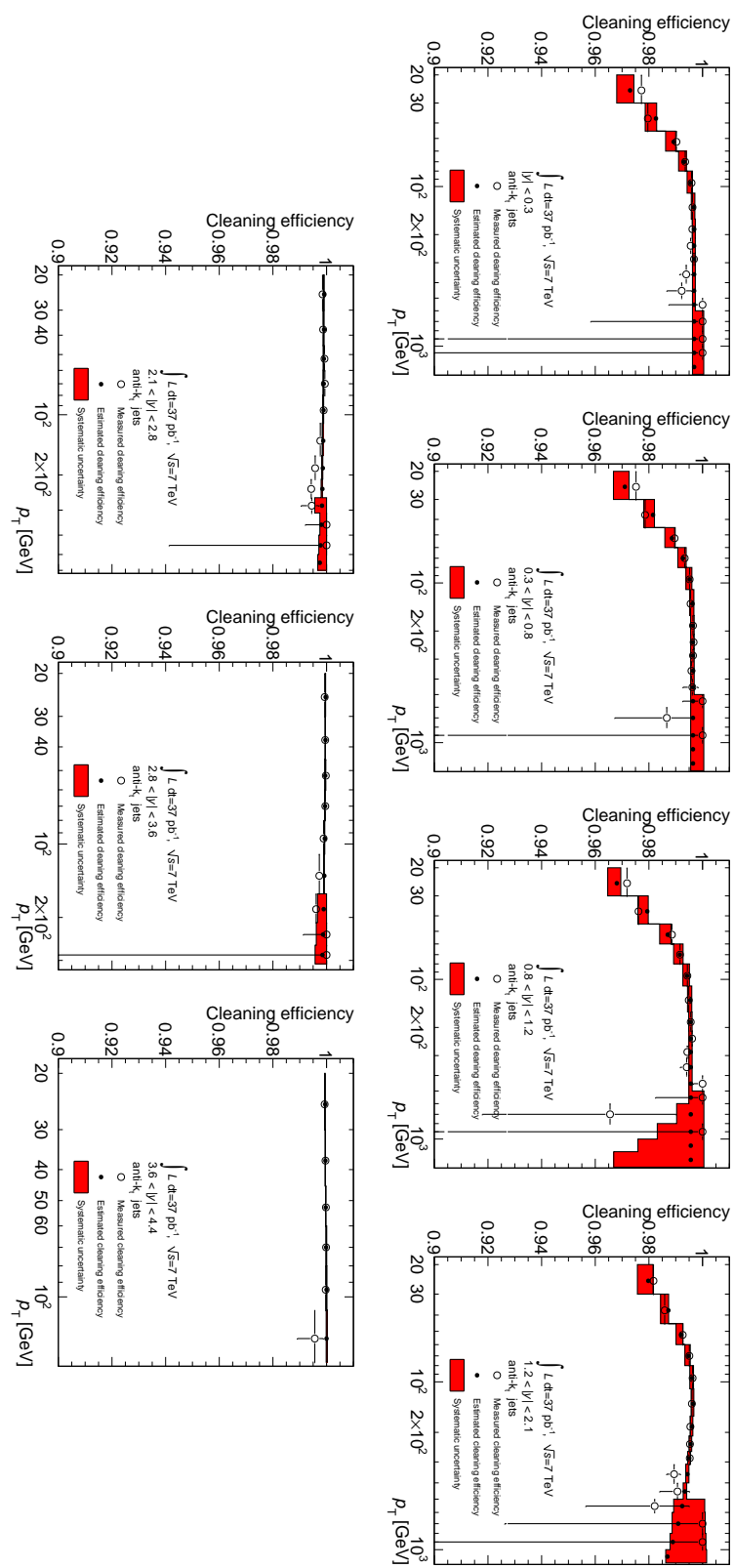


Figure C.1: Measured cleaning efficiencies in bins of p_T in different rapidity regions for the anti- k_t jets with $R=0.4$. The black dots are the result of a fit performed on measured values marked as white points. The red uncertainty band is the systematic uncertainty obtained from variations of the tag jet selection.

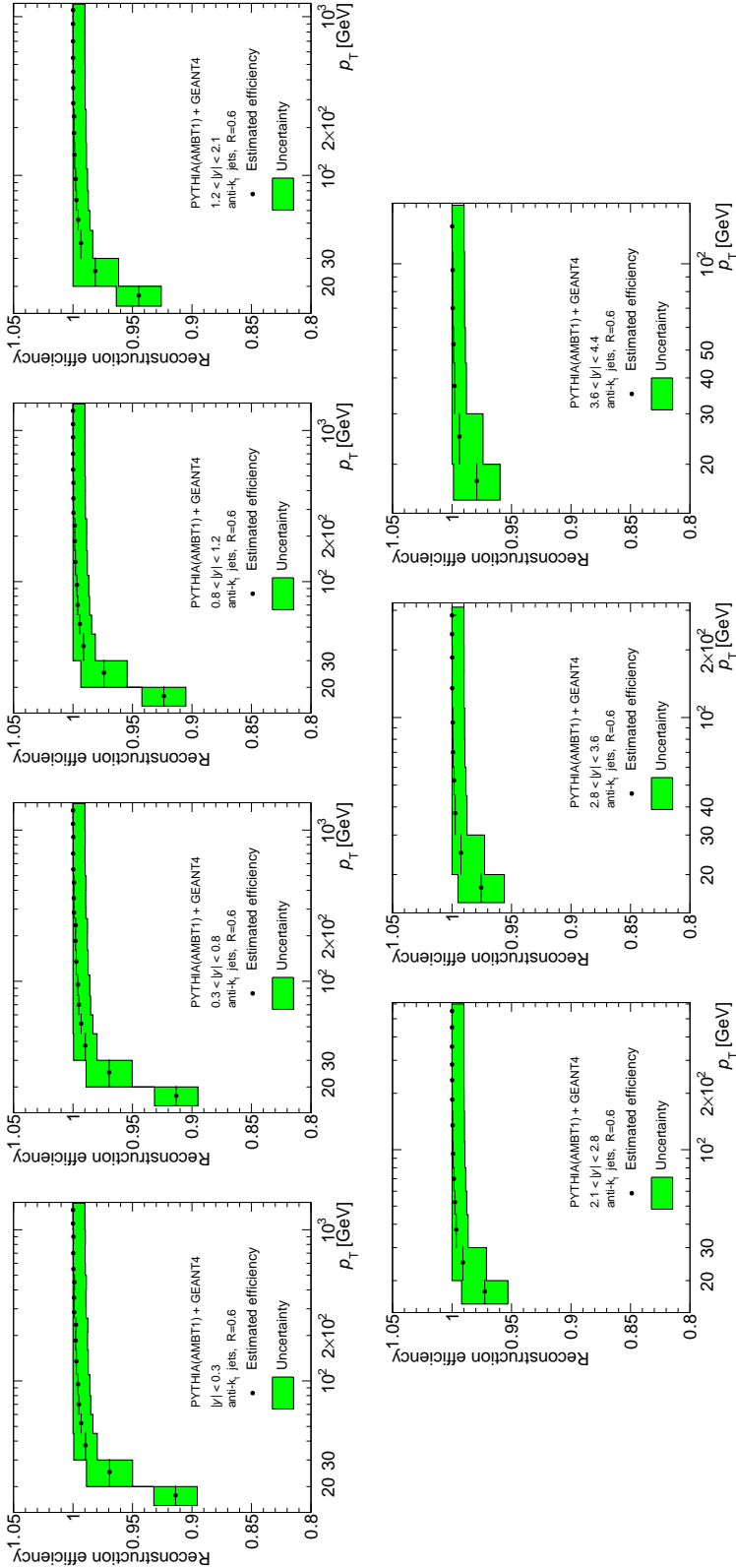


Figure C.2: Monte Carlo estimate of the jet reconstruction efficiencies for the anti- k_t with $R=0.6$ in different rapidity regions. The black dots are the estimate of the efficiency derived from the nominal Monte Carlo simulation. The green uncertainty band is a conservative estimate of the systematic uncertainty.

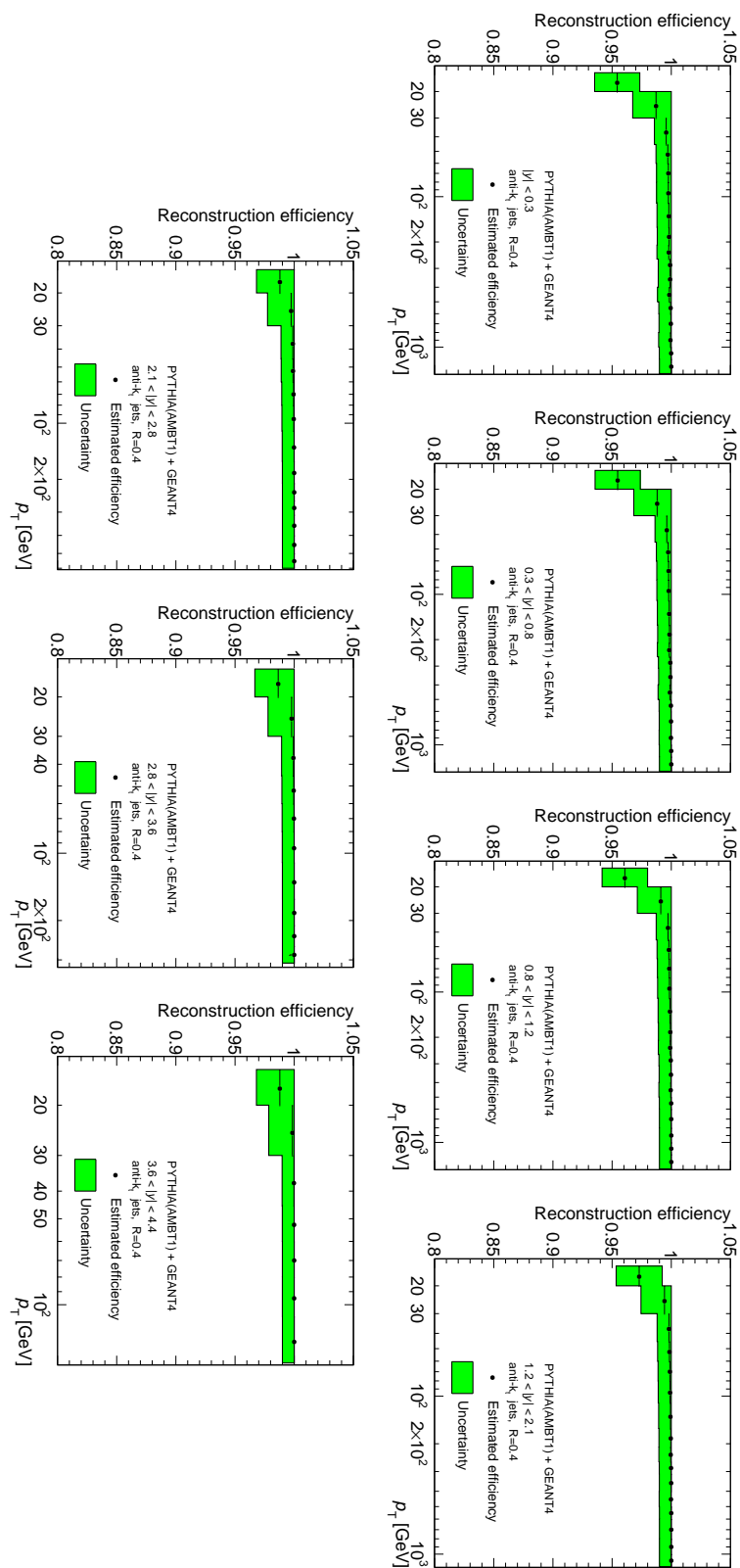


Figure C.3: Monte Carlo estimate of the jet reconstruction efficiencies for the anti- k_t with $R=0.4$ in bins of p_T in different rapidity regions. The black dots are the estimate of the efficiency derived from the nominal Monte Carlo simulation. The green uncertainty band is a conservative estimate of the systematic uncertainty.

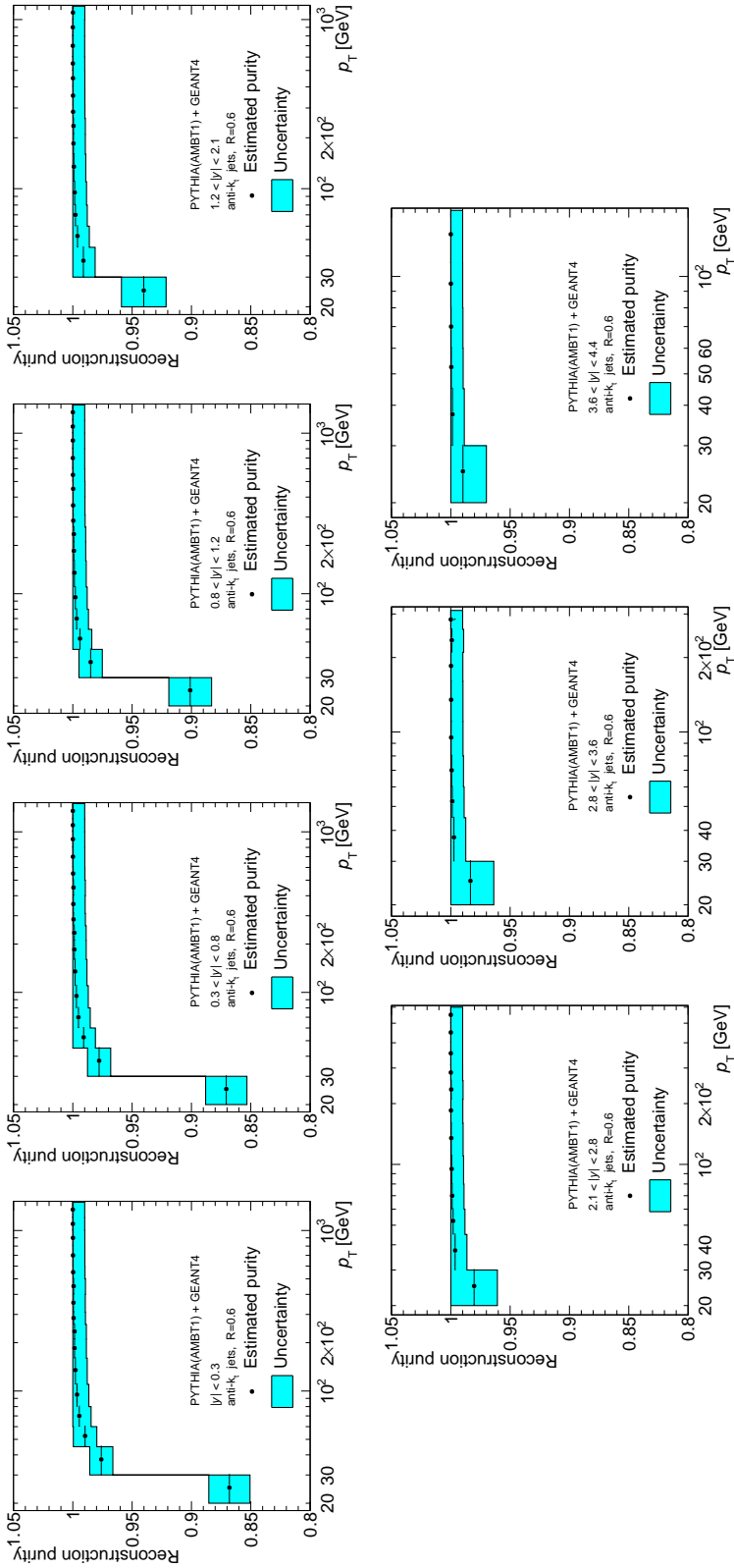


Figure C.4: Monte Carlo estimate of the jet reconstruction purity for the anti- k_t with $R=0.6$ in bins of p_T in different rapidity regions. The black dots are the estimate of the purity derived from the nominal Monte Carlo simulation. The cyan uncertainty band is a conservative estimate of the systematic uncertainty.

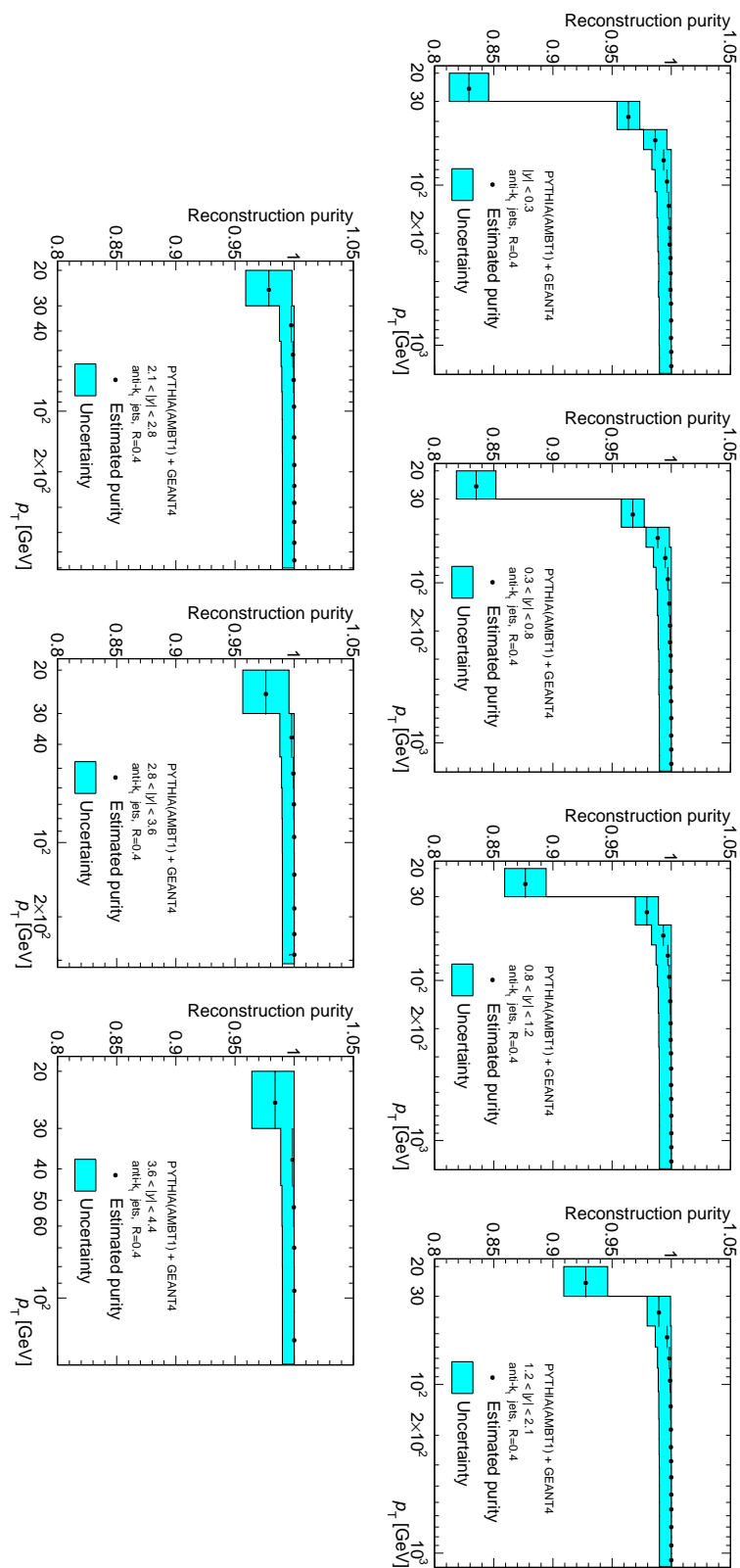


Figure C.5: Monte Carlo estimate of the jet reconstruction purity for the anti- k_t with $R=0.4$ in bins of p_T in different rapidity regions. The black dots are the estimate of the purity derived from the nominal Monte Carlo simulation. The cyan uncertainty band is a conservative estimate of the systematic uncertainty.

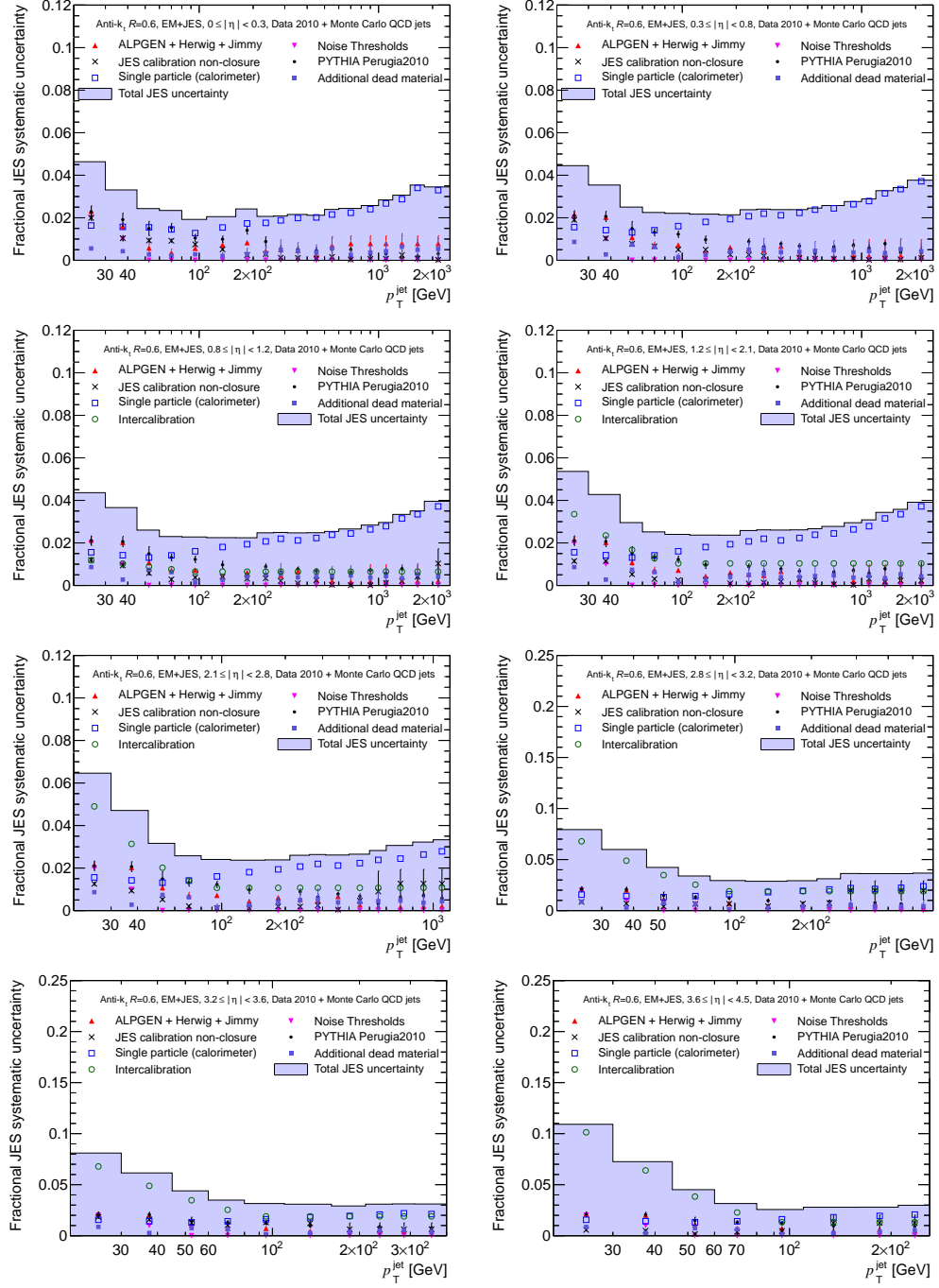


Figure C.6: Jet energy scale uncertainty in bins of p_T and y for the anti- k_t jets with $R=0.6$. The different components used to estimate the uncertainty are shown. Figures taken from Reference [Doglioni 2011a].

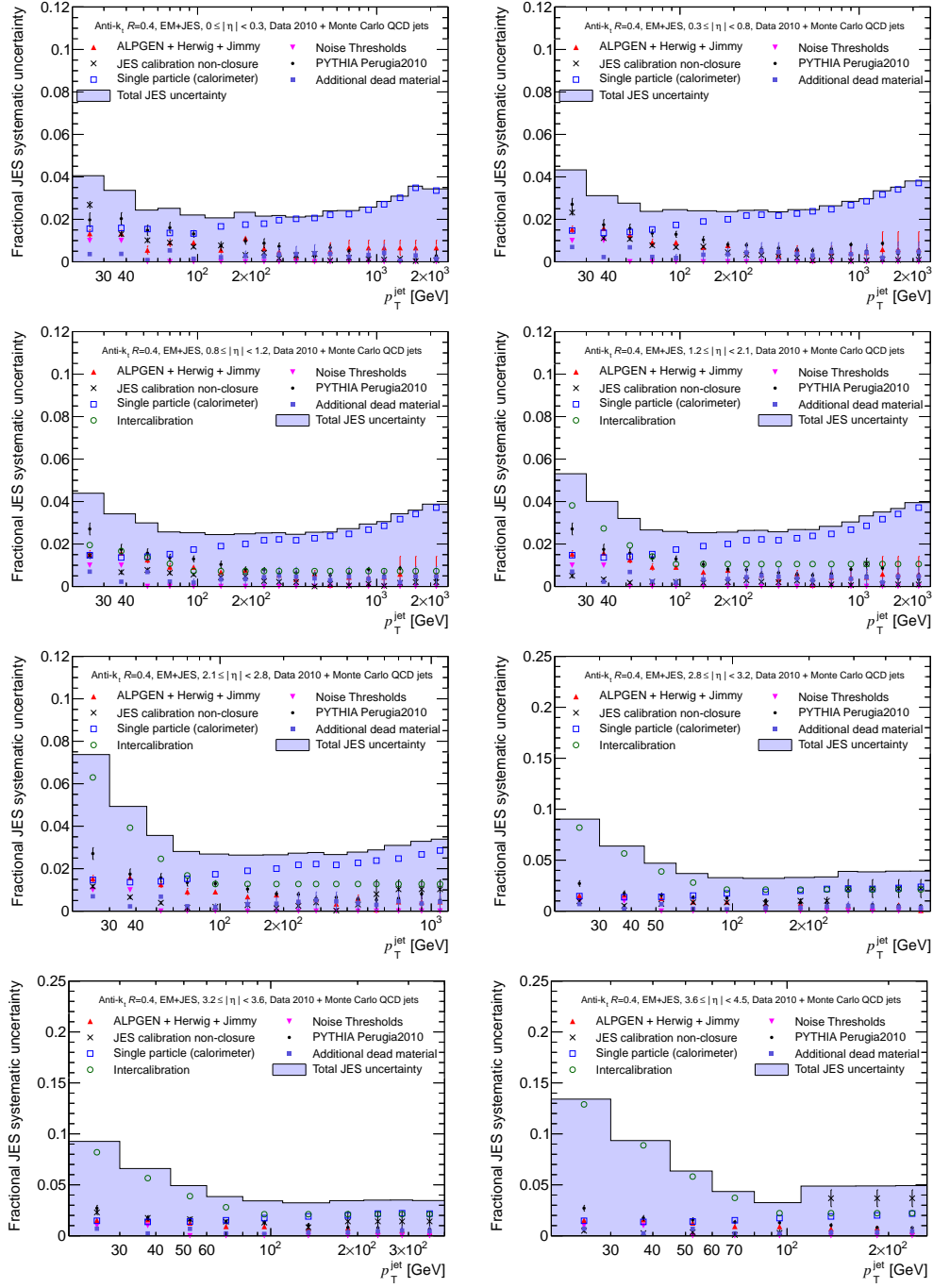


Figure C.7: Jet energy scale uncertainty in bins of p_T and y for the anti- k_t jets with $R=0.4$. The different components used to estimate the uncertainty are shown. Figures taken from Reference [Doglioni 2011a].

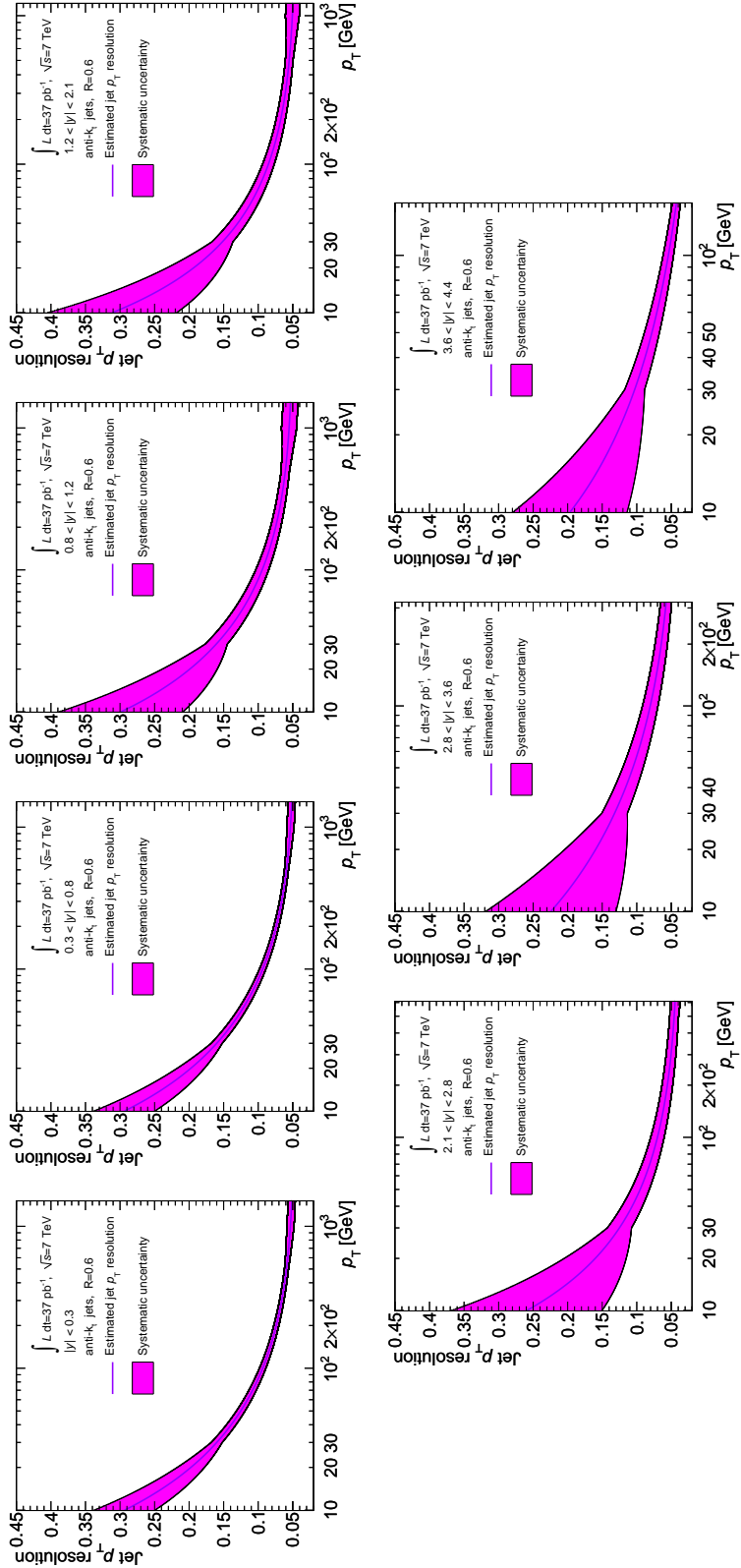


Figure C.8: Jet energy resolution, and its uncertainty, as a function of p_T in the different rapidity regions for anti- k_t jets with $R=0.6$.

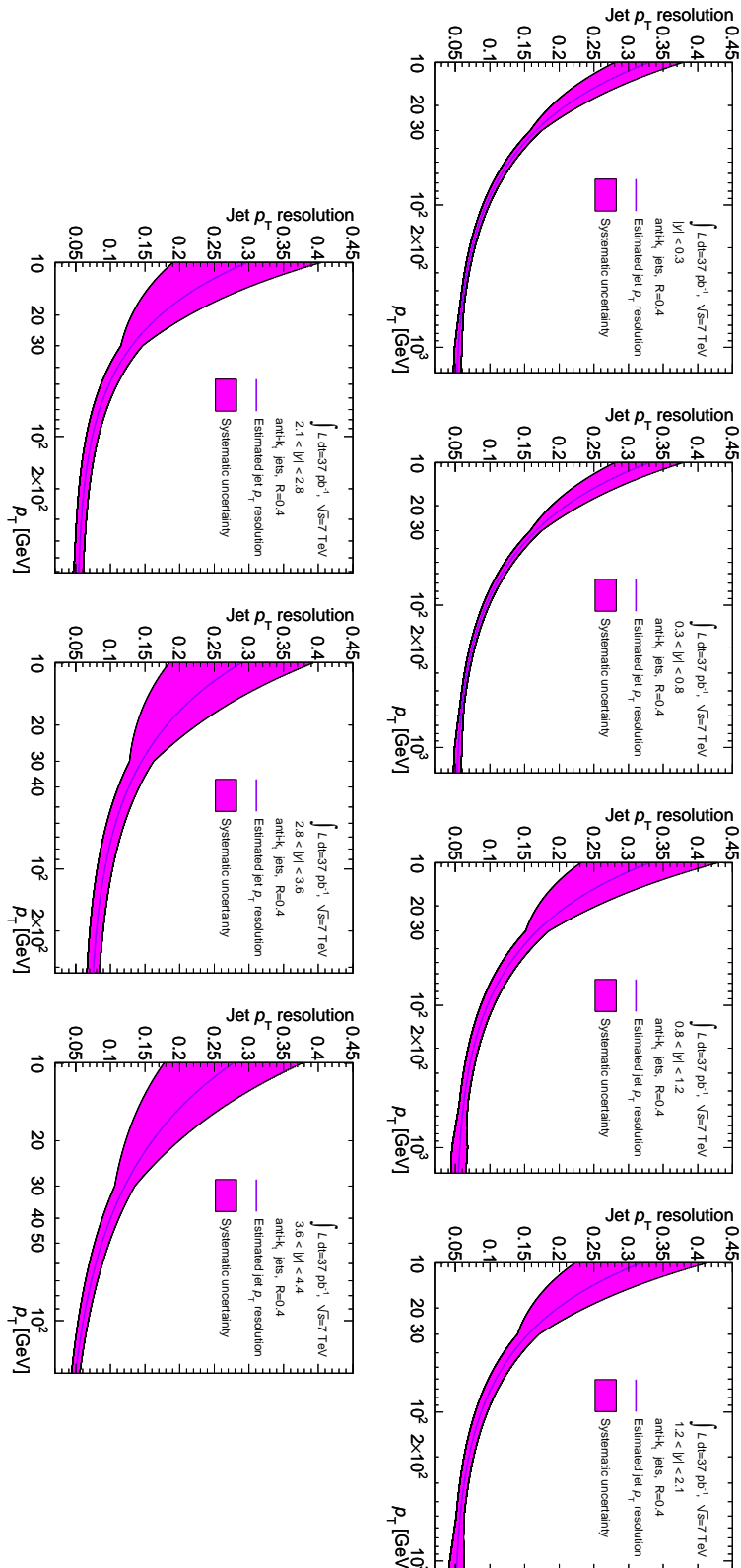


Figure C.9: Jet energy resolution, and its uncertainty, as a function of p_T in the different rapidity regions for anti- k_t jets with $R=0.4$.

APPENDIX D

Additional material to Chapter 5

This appendix contains additional material to Chapter 5.

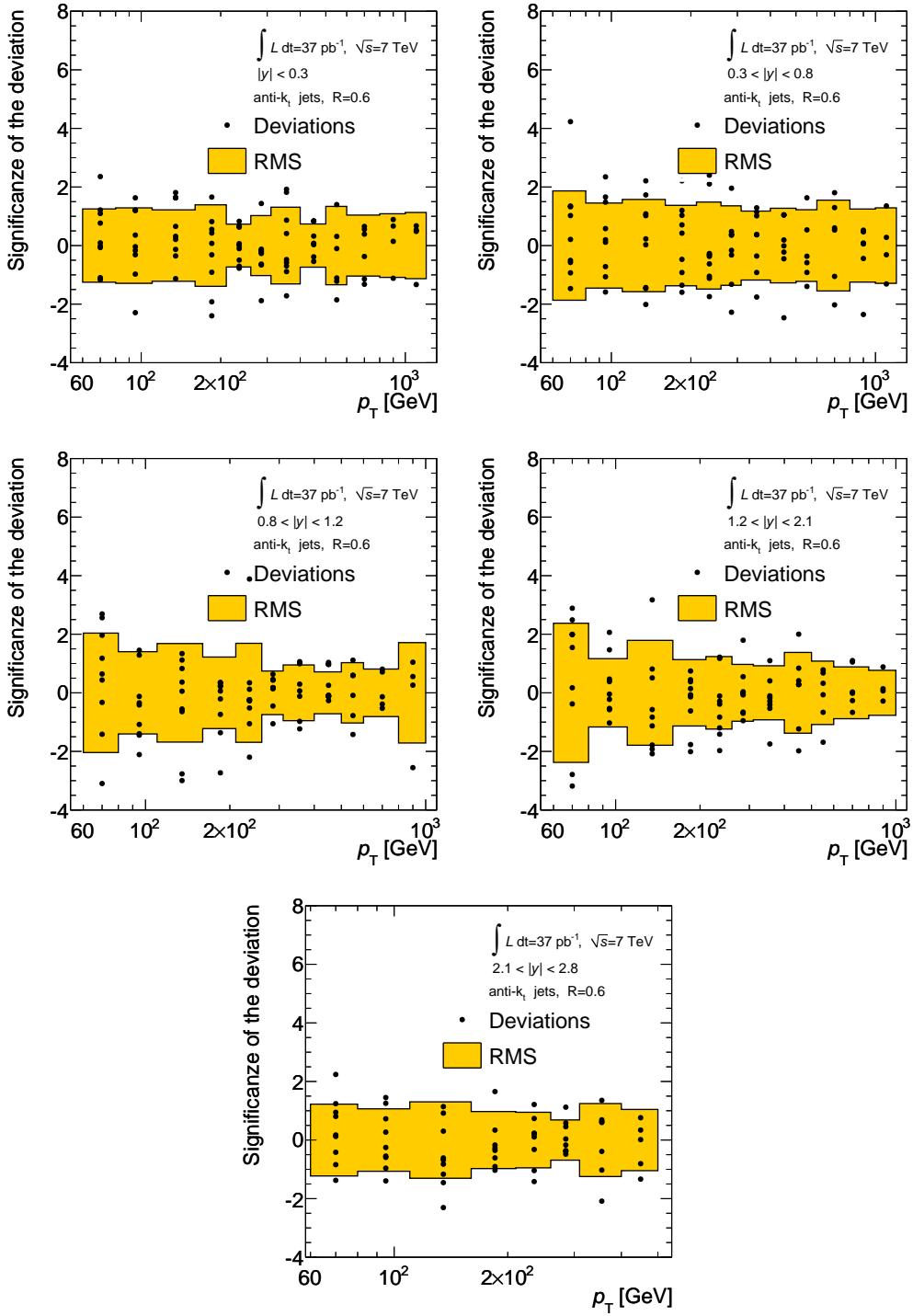


Figure D.1: Stability of the inclusive jet cross section measured in each period of data taking for the anti- k_t jets with $R=0.6$ in several rapidity regions. The cross section measured in each period is compared to the measurement performed on the complete statistics. Each point in the p_T bins shows the significance of the deviation of the measurement in each period, from the measurement done with the complete dataset. Only the statistical uncertainty is taken into account to define the significance. The yellow band is the RMS measured from the black points, which is expected to be at 1.

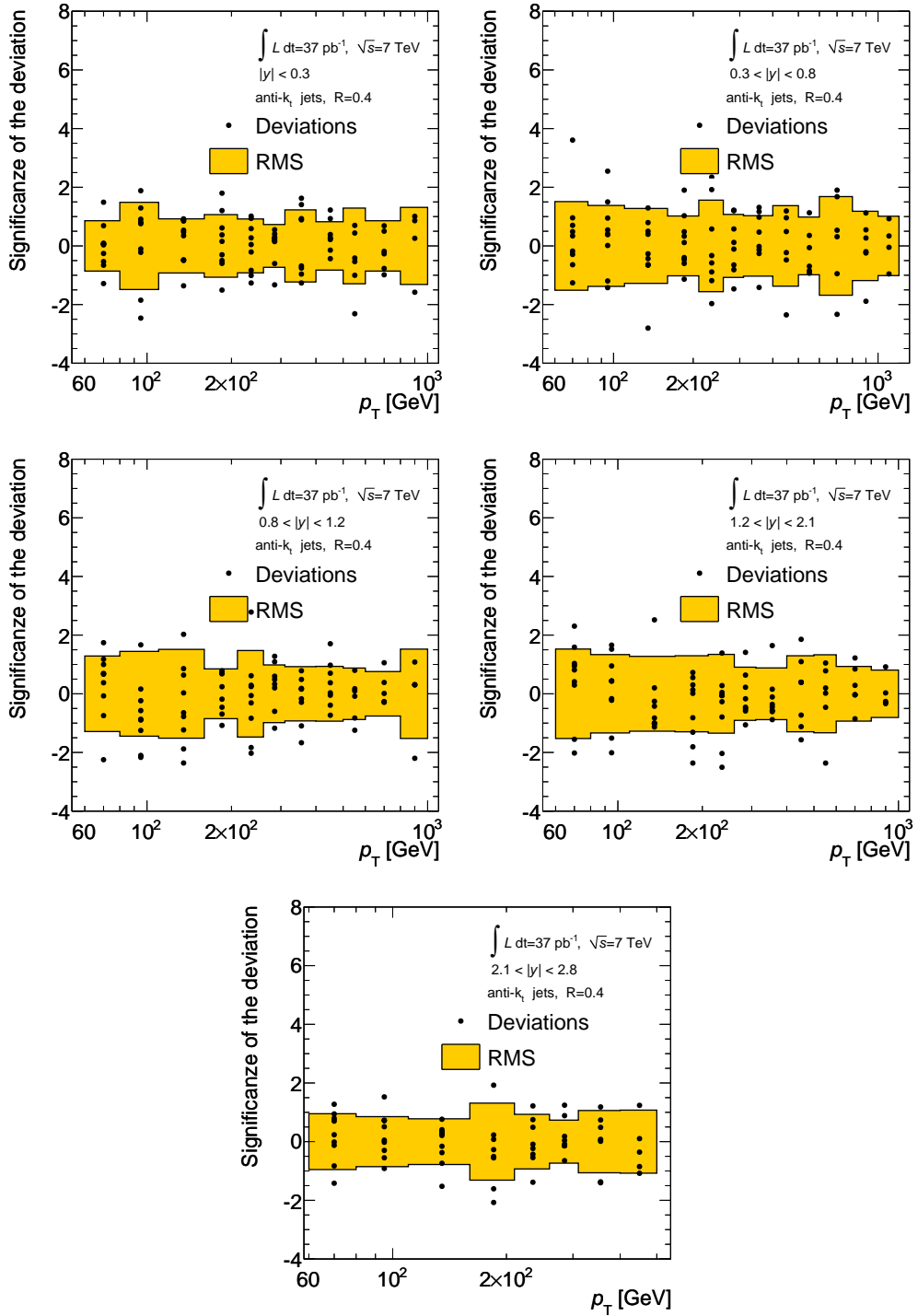


Figure D.2: Stability of the inclusive jet cross section measured in each period of data taking for the anti- k_t jets with $R=0.4$ in several rapidity regions. The cross section measured in each period is compared to the measurement performed on the complete statistics. Each point in the p_T bins shows the significance of the deviation of the measurement in each period, from the measurement done with the complete dataset. Only the statistical uncertainty is taken into account to define the significance. The yellow band is the RMS measured from the black points, which is expected to be at 1.

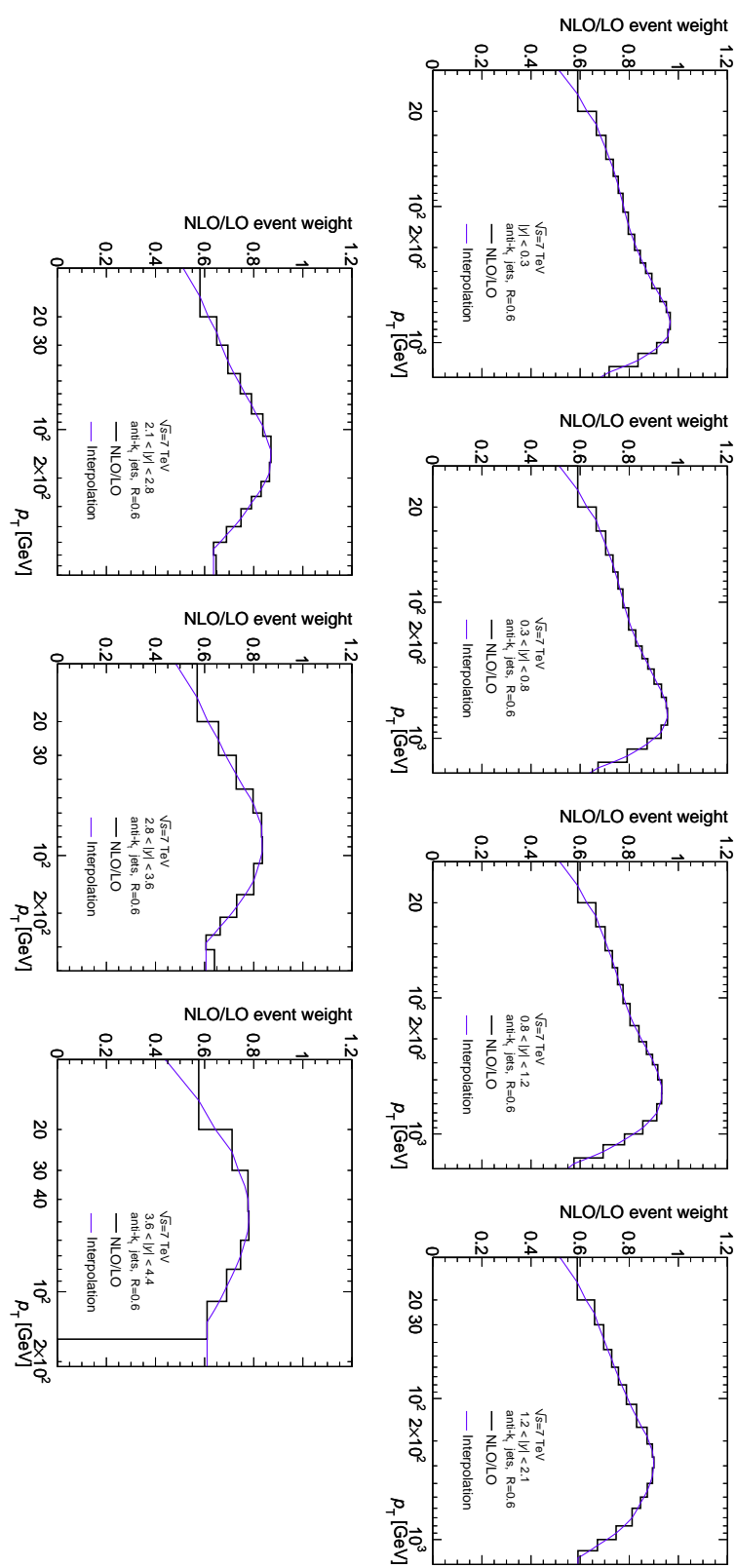


Figure D.3: Weights for the anti- k_t jets with $R=0.6$ used to correct for the difference in the shape of the Monte Carlo simulation due to the MRST 2007 LO* PDFs and to the missing NLO terms. These weights are used to improve the agreement between the Monte Carlo detector level shapes and the measured shape, to reduce the unfolding systematic errors, especially for the bin-by-bin unfolding.

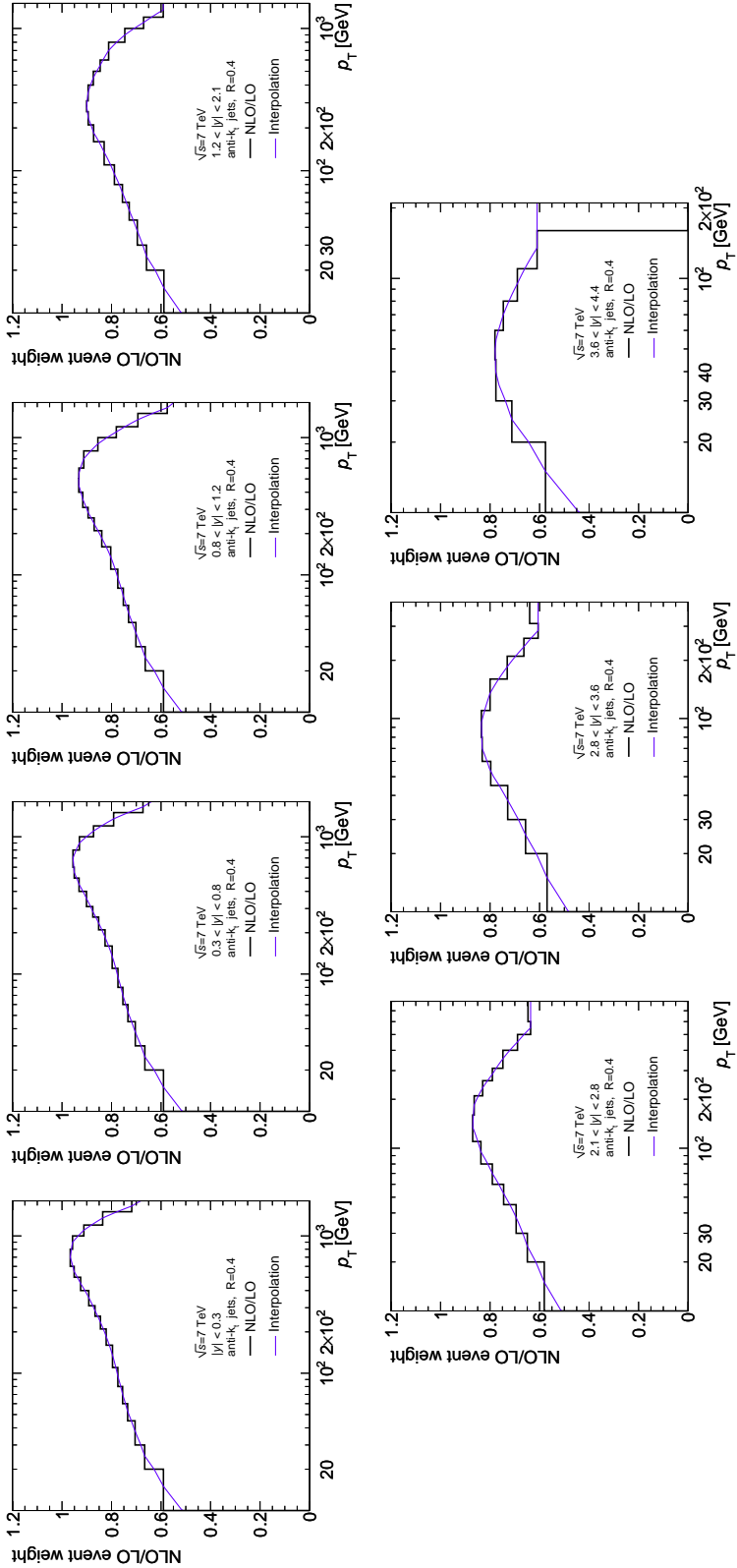


Figure D.4: Weights for the anti- k_t jets with $R=0.4$ used to correct for the difference in the shape of the Monte Carlo simulation due to the MRST 2007 LO* PDFs and to the missing NLO terms. These weights are used to improve the agreement between the Monte Carlo detector level shapes and the measured shape, to reduce the unfolding systematic errors, especially for the bin-by-bin unfolding.

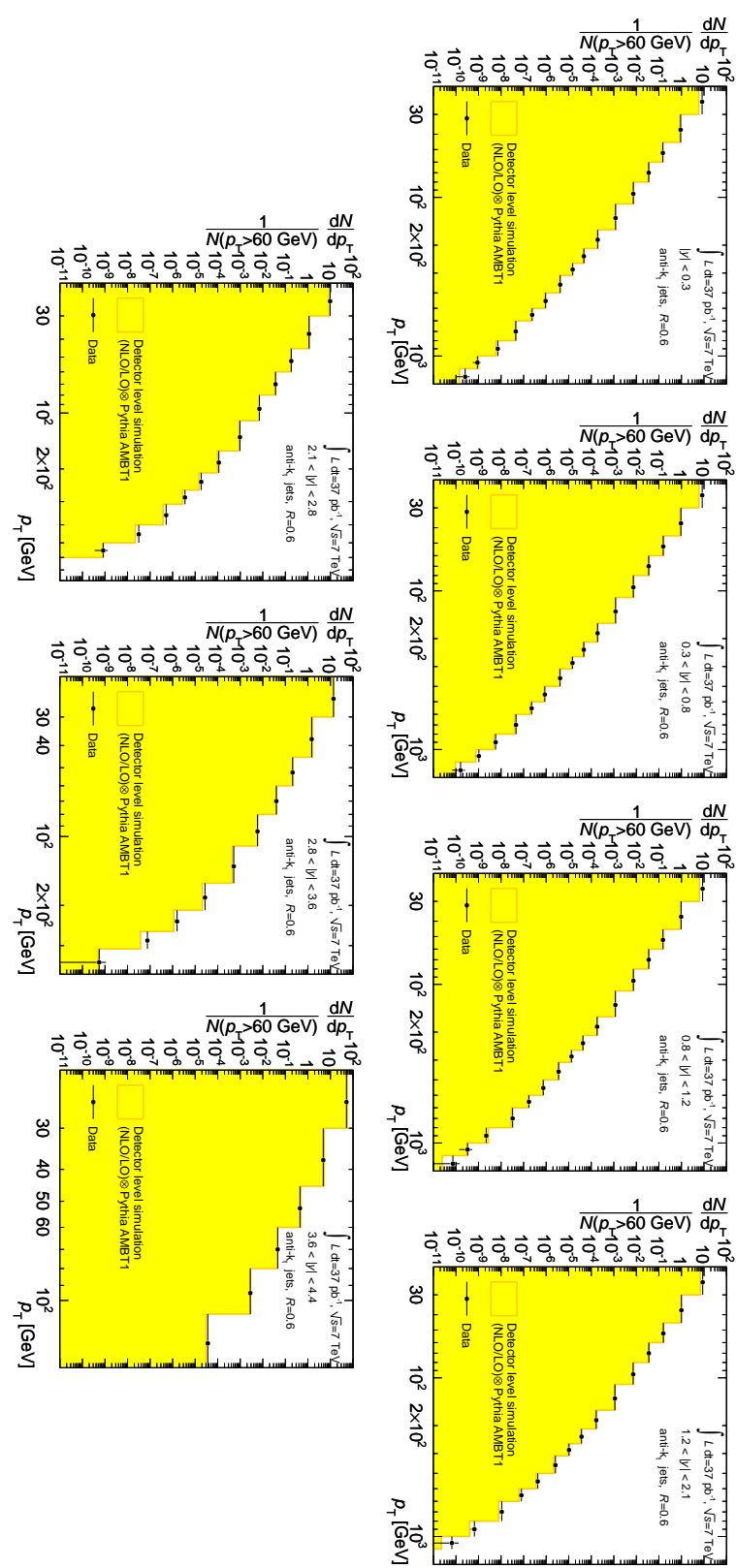


Figure D.5: Observed inclusive p_T distribution (black dots) for jets with $p_T > 20$ GeV in the different rapidity regions for anti- k_t jets with $R=0.6$. Only statistical uncertainties are included and the distributions are normalized to the integral from $p_T > 60$ GeV. The data are compared to Monte Carlo predictions, re-weighted for the NLO/LO coefficients.

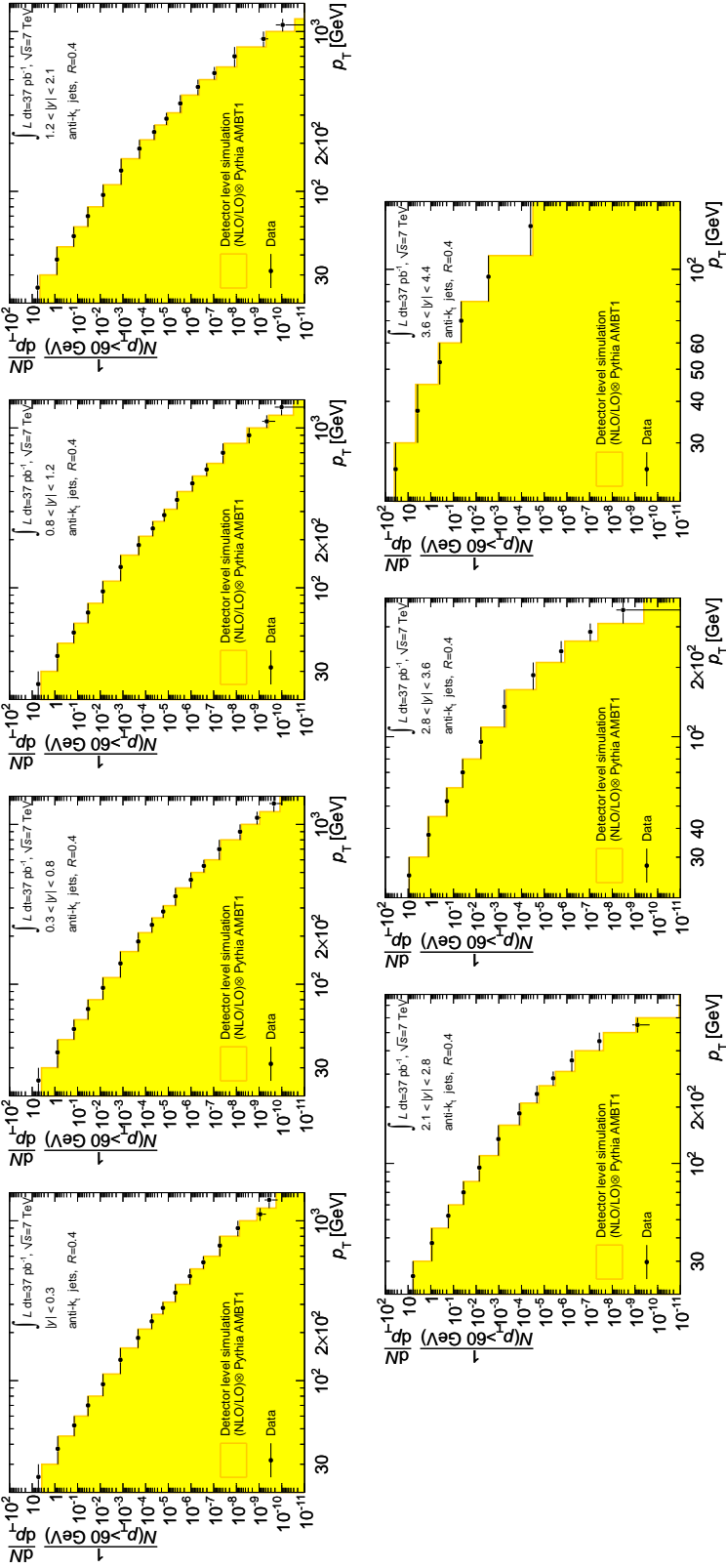


Figure D.6: Observed inclusive p_T distribution (black dots) for jets with $p_T > 20$ GeV in the different rapidity regions for anti- k_t jets with $R=0.4$. Only statistical uncertainties are included and the distributions are normalized to the integral from $p_T > 60$ GeV. The data are compared to Monte Carlo predictions, re-weighted for the NLO/LO coefficients.

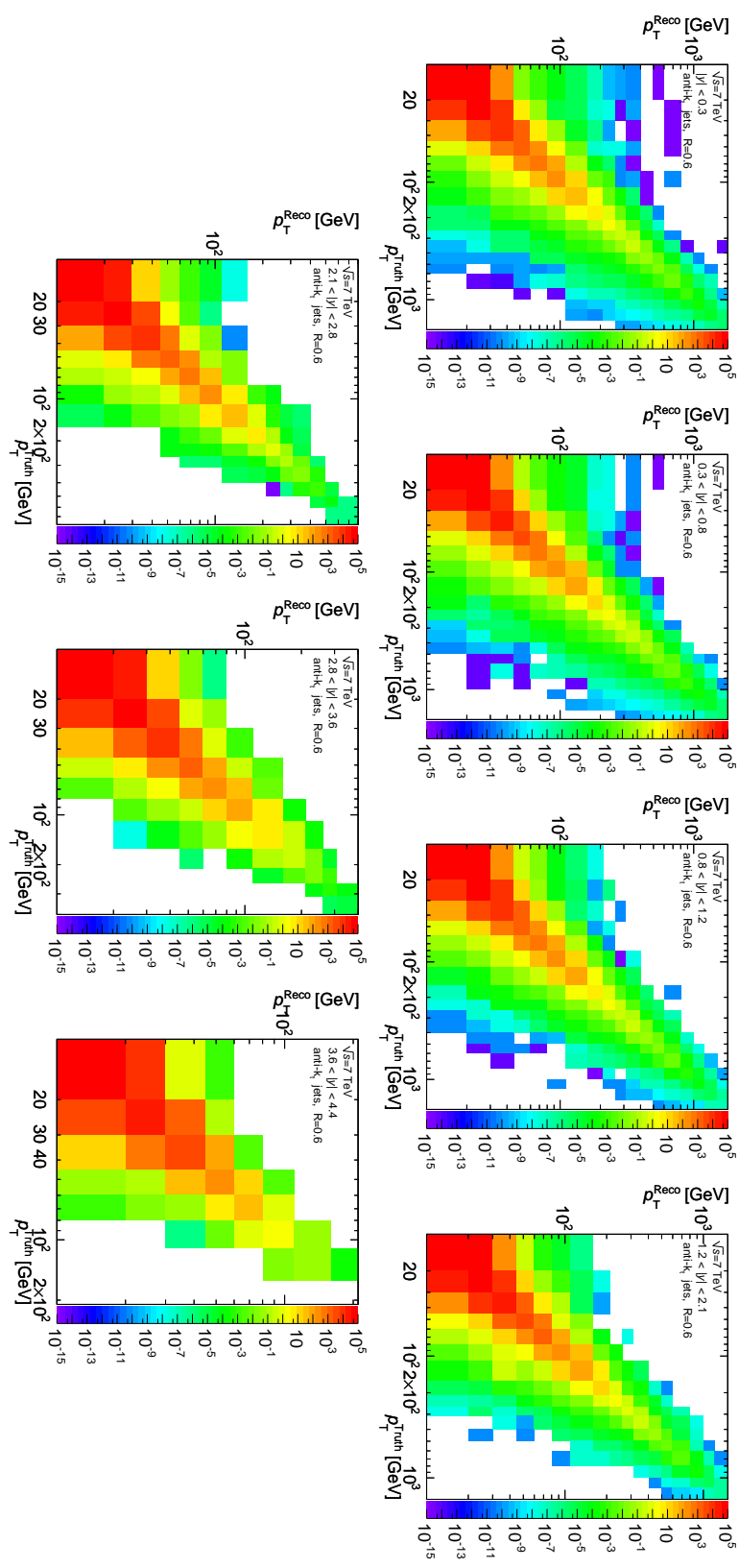


Figure D.7: Transfer matrices derived by matching the truth jets to the reconstructed jets with the geometrical requirement $\Delta R < 0.3$ for the anti- k_t jets with $R=0.6$ in all the rapidity regions.

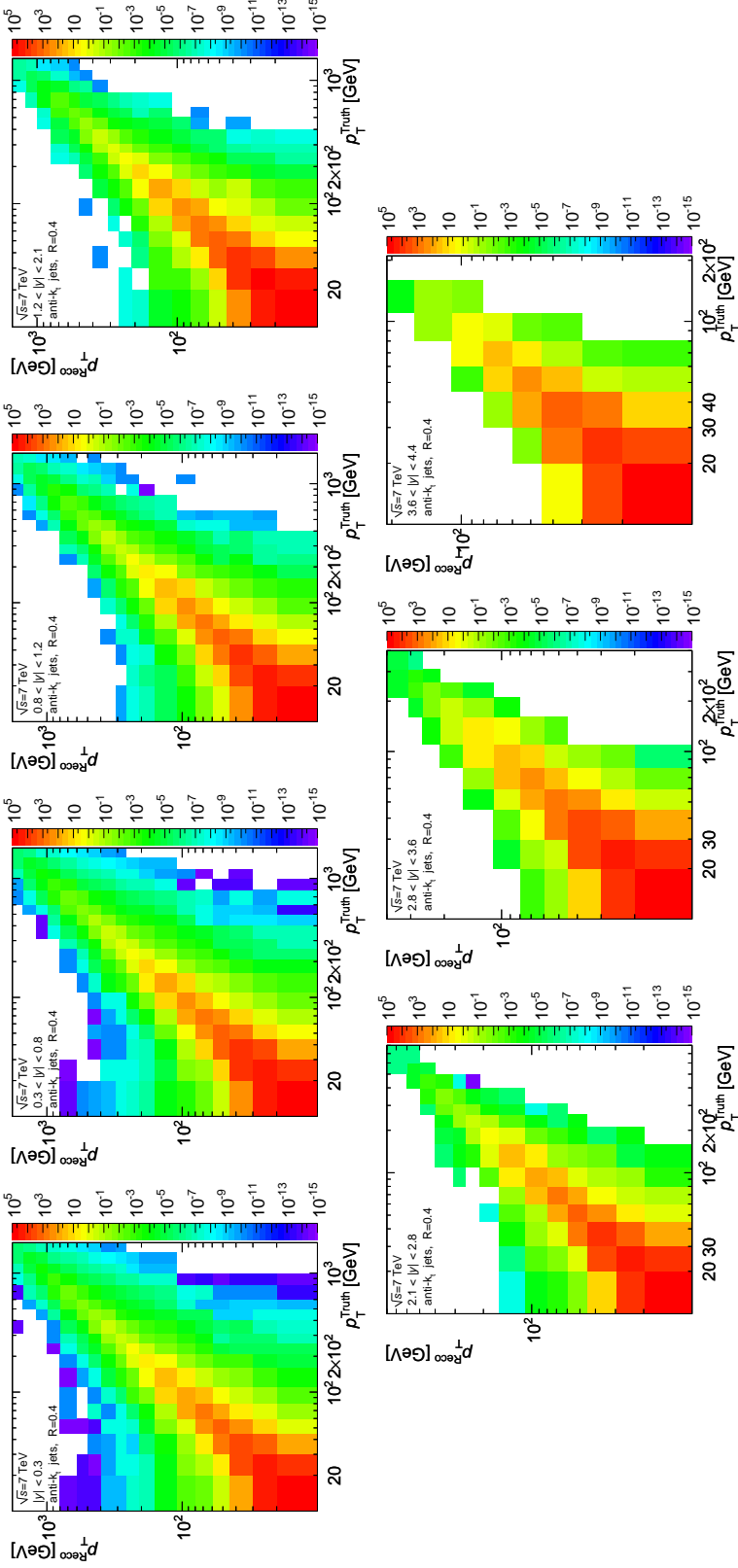


Figure D.8: Transfer matrices derived by matching the truth jets to the reconstructed jets with the geometrical requirement $\Delta R < 0.3$ for the anti- k_t jets with $R=0.4$ in all the rapidity regions.

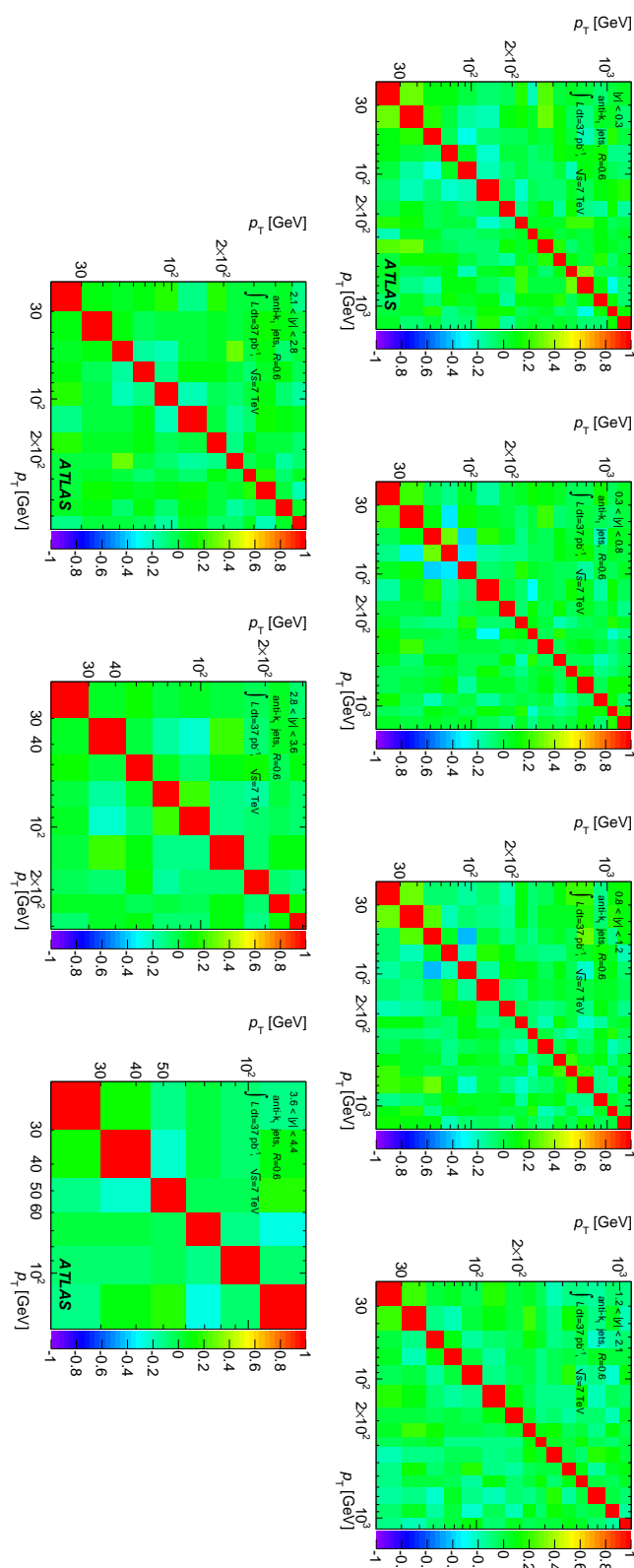


Figure D.9: Correlation of the statistical uncertainty of the inclusive jet cross section after the unfolding procedure. The results are shown for anti- k_t jets with $R = 0.6$ in all the rapidity regions.

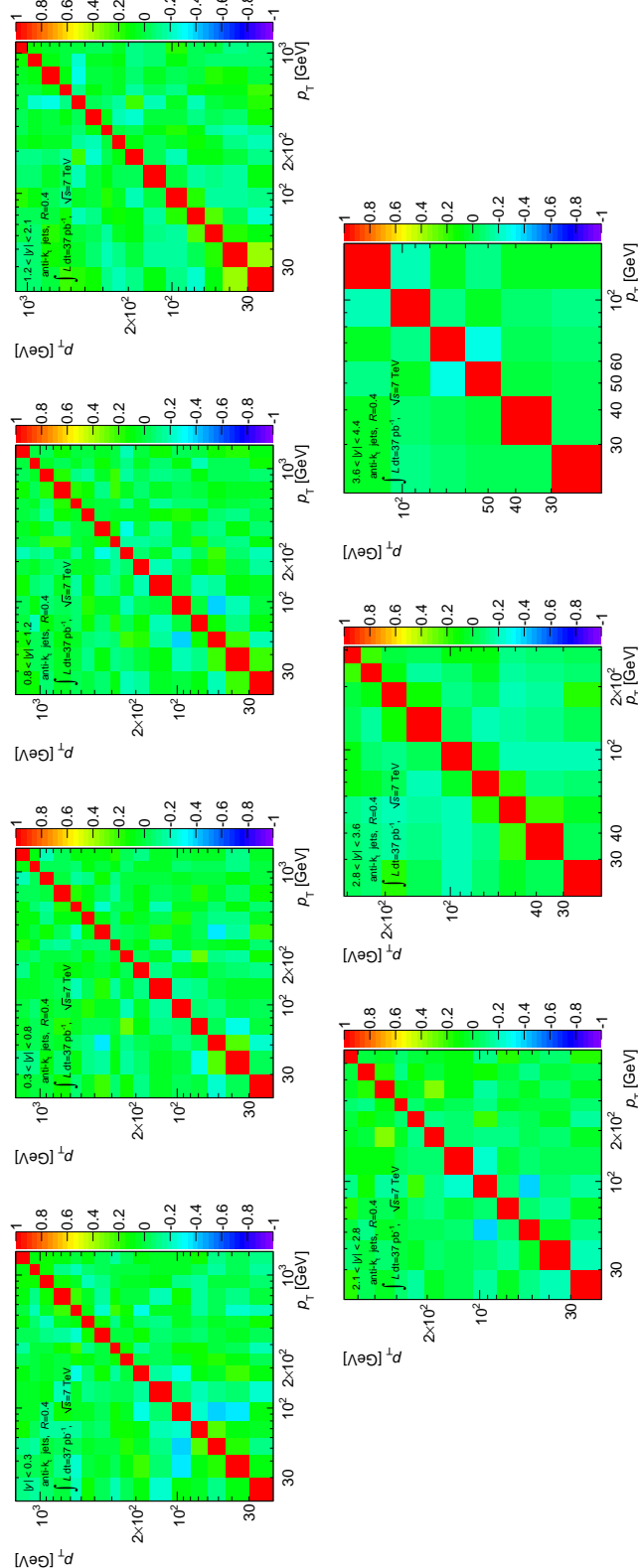


Figure D.10: Correlation of the statistical uncertainty of the inclusive jet cross section after the unfolding procedure. The results are shown for anti- k_t jets with $R = 0.4$ in all the rapidity regions.

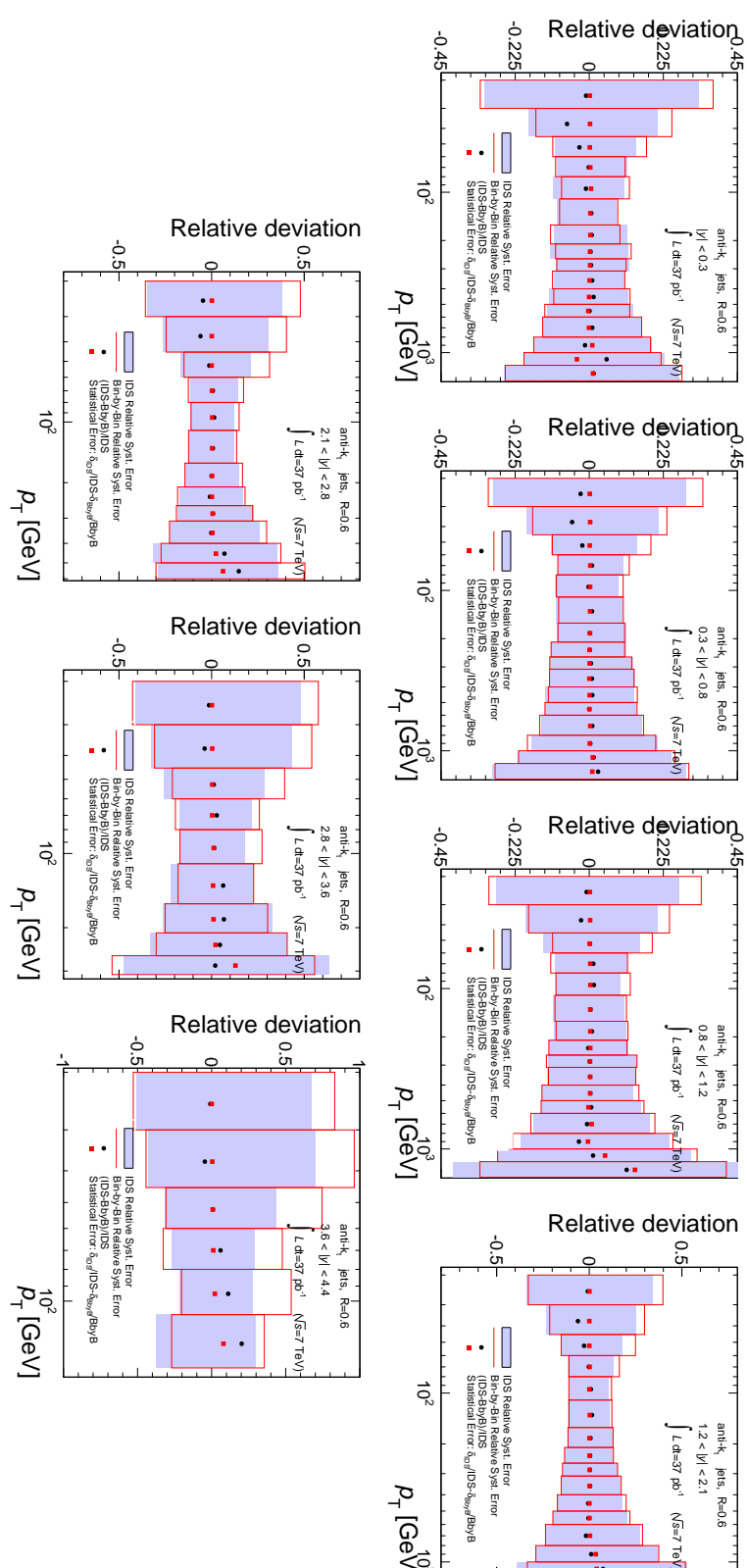


Figure D.11: Comparison of the unfolded cross section using the bin-by-bin and the IDS methods. The relative difference with respect to the final (IDS) result is plotted as a function of jet transverse momentum in black dots. Red dots show the difference of the relative statistical uncertainties obtained in the two method. The two bands show the total systematic uncertainty for the IDS, and for the bin-by-bin methods. Agreement is observed at the per cent level or better precision. The results are shown for anti- k_t jets with $R = 0.6$.

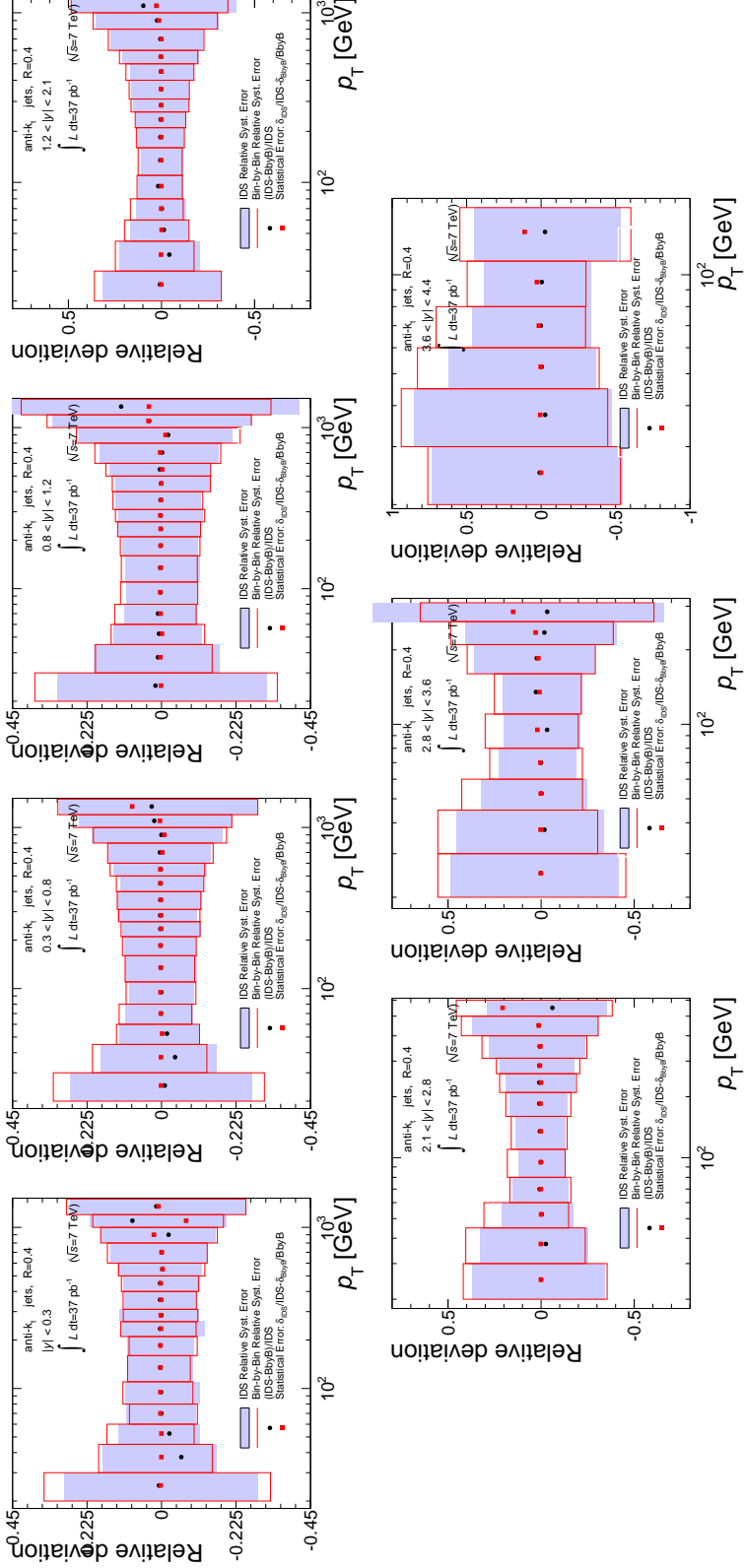


Figure D.12: Comparison of the unfolded cross section using the bin-by-bin and the IDS methods. The relative difference with respect to the final (IDS) result is plotted as a function of jet transverse momentum in black dots. Red dots show the difference of the relative statistical uncertainties obtained in the two method. The two bands show the total systematic uncertainty for the IDS, and for the bin-by-bin methods. Agreement is observed at the per cent level or better precision. The results are shown for anti- k_t jets with $R = 0.4$.

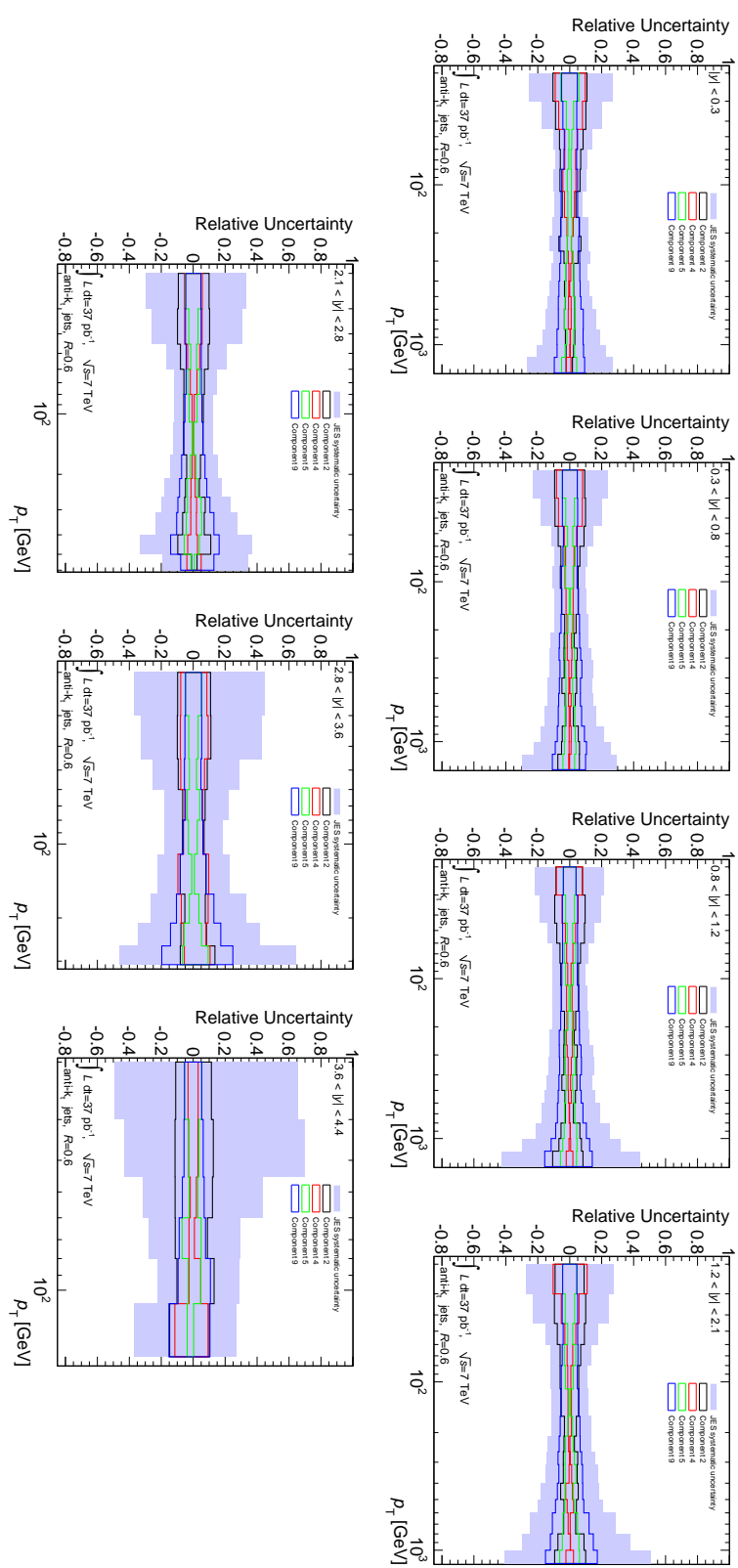


Figure D.13: The colored lines show the relative systematic uncertainty on the inclusive jet cross section measurement due to the various components of the jet energy scale uncertainty for anti- k_t jets with $R=0.6$ (SET 1). The association between the numbering and the meaning of each component is reported in Table 4.1. The light blue band shows the total uncertainty.

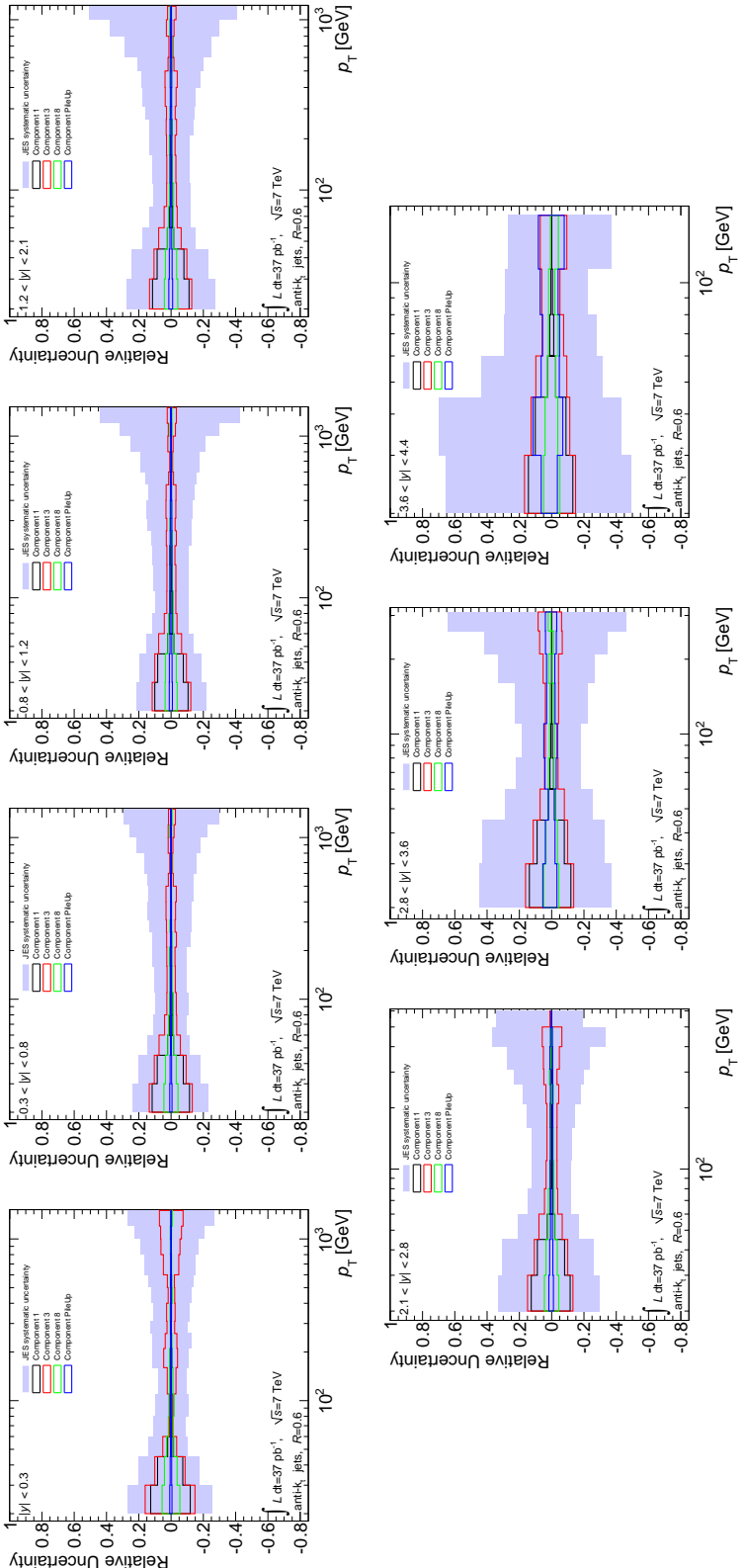


Figure D.14: The colored lines show the relative systematic uncertainty on the inclusive jet cross section measurement due to the various components of the jet energy scale uncertainty for anti- k_t jets with $R=0.6$ (SET 2). The association between the numbering and the meaning of each component is reported in Table 4.1. The light blue band shows the total uncertainty.

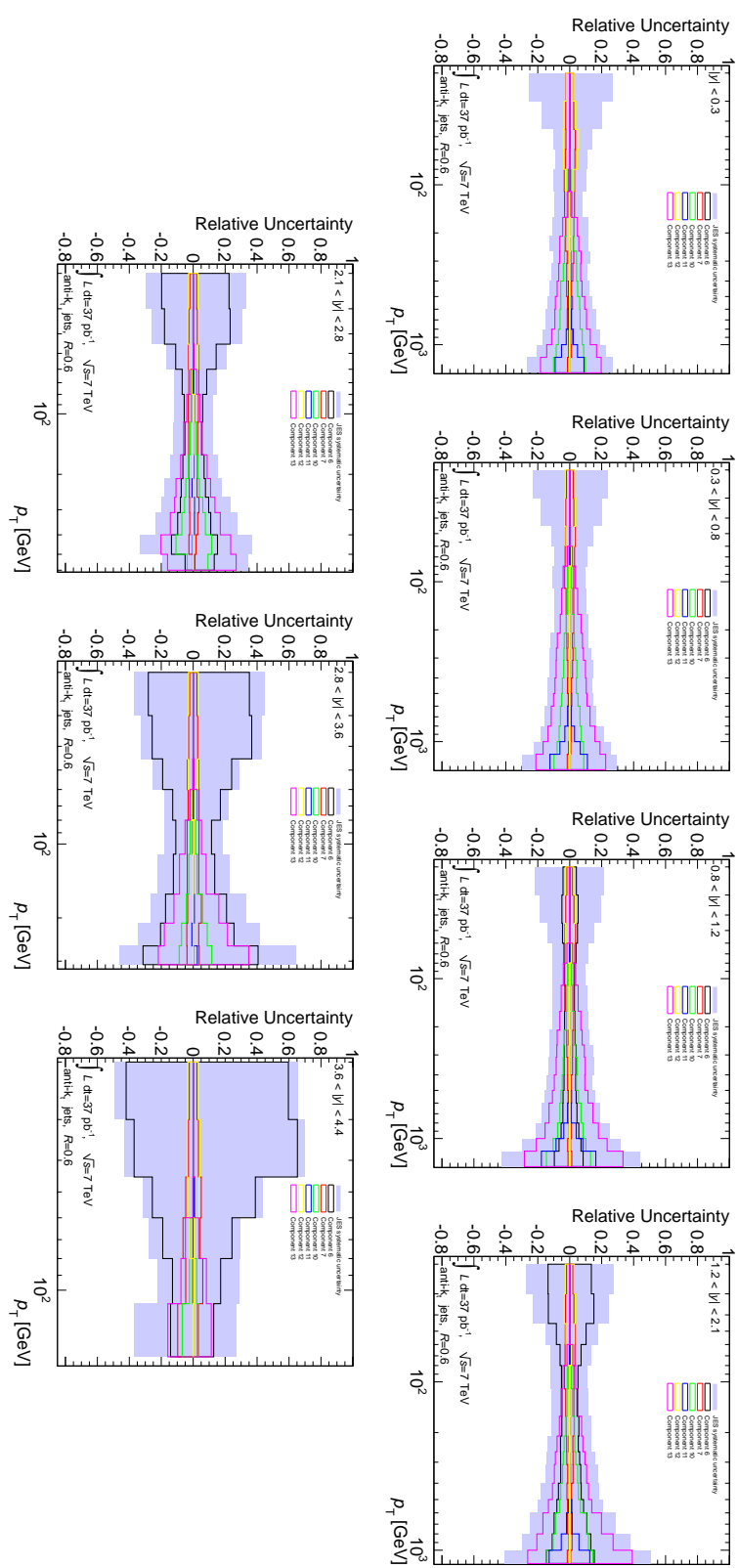


Figure D.15: The colored lines show the relative systematic uncertainty on the inclusive jet cross section measurement due to the various components of the jet energy scale uncertainty for anti- k_t jets with $R=0.6$ (SET 3). The association between the numbering and the meaning of each component is reported in Table 4.1. The light blue band shows the total uncertainty.

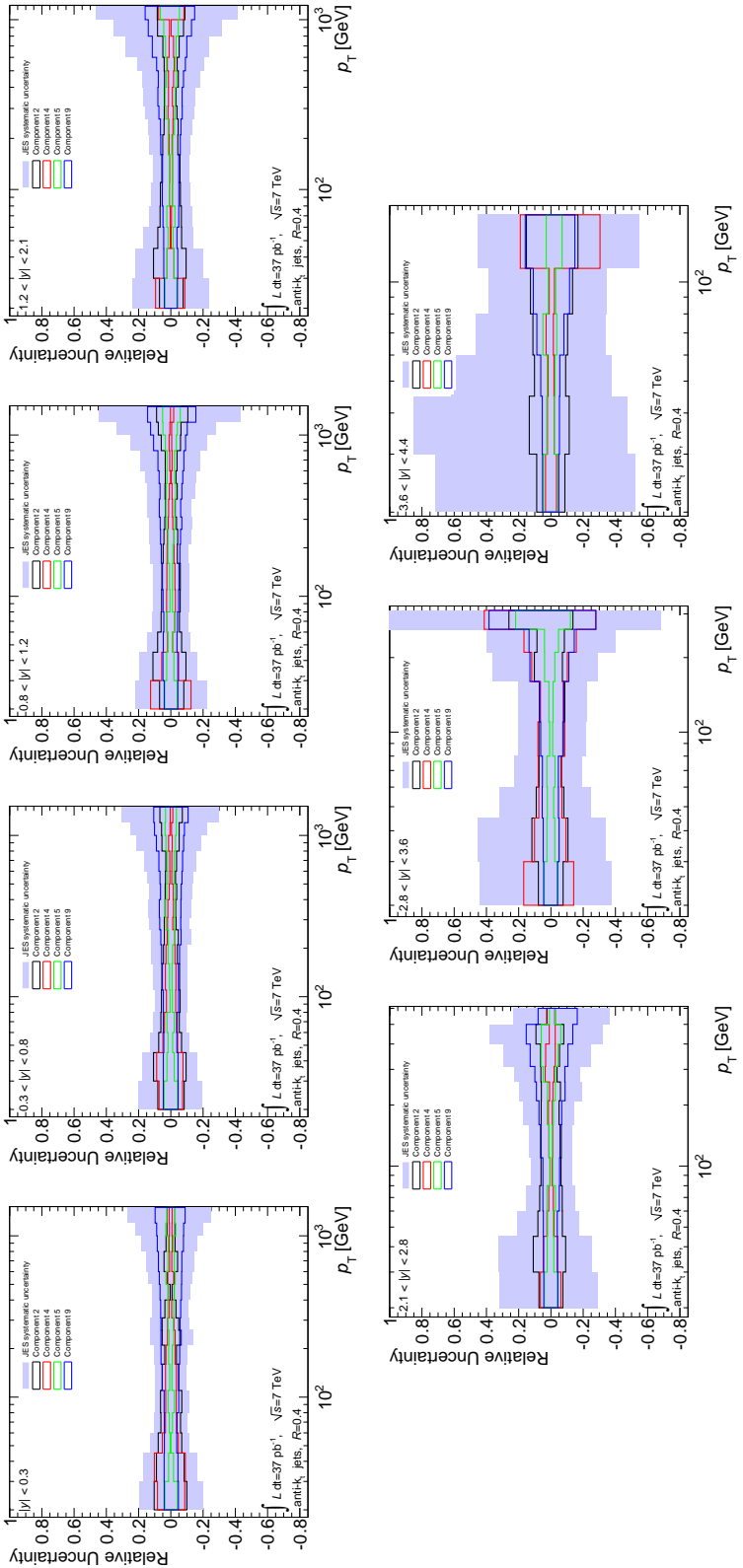


Figure D.16: The colored lines show the relative systematic uncertainty on the inclusive jet cross section measurement due to the various components of the jet energy scale uncertainty for anti- k_t jets with $R=0.4$ (SET 1). The association between the numbering and the meaning of each component is reported in Table 4.1. The light blue band shows the total uncertainty.

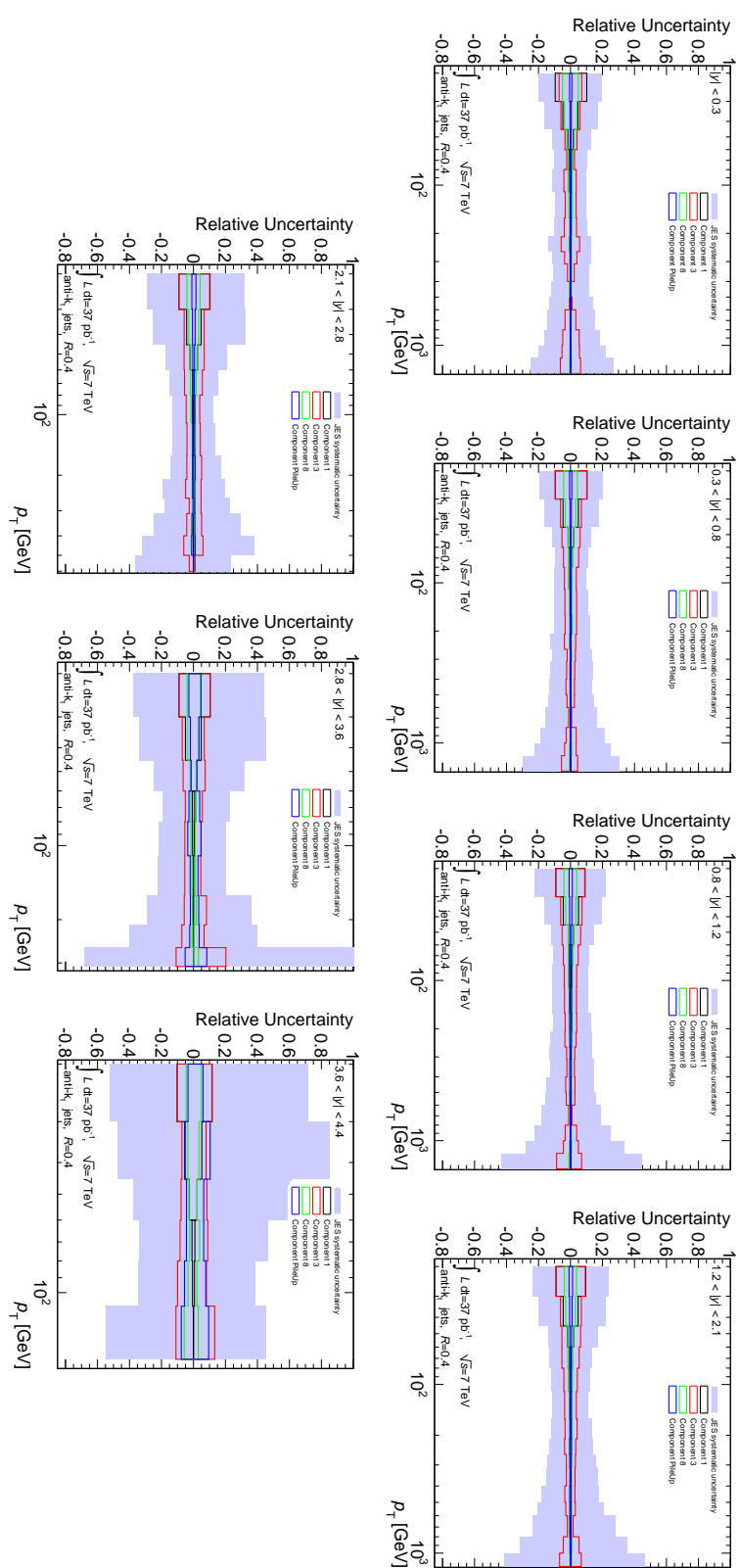


Figure D.17: The colored lines show the relative systematic uncertainty on the inclusive jet cross section measurement due to the various components of the jet energy scale uncertainty for anti- k_t jets with $R=0.4$ (SET 2). The association between the numbering and the meaning of each component is reported in Table 4.1. The light blue band shows the total uncertainty.

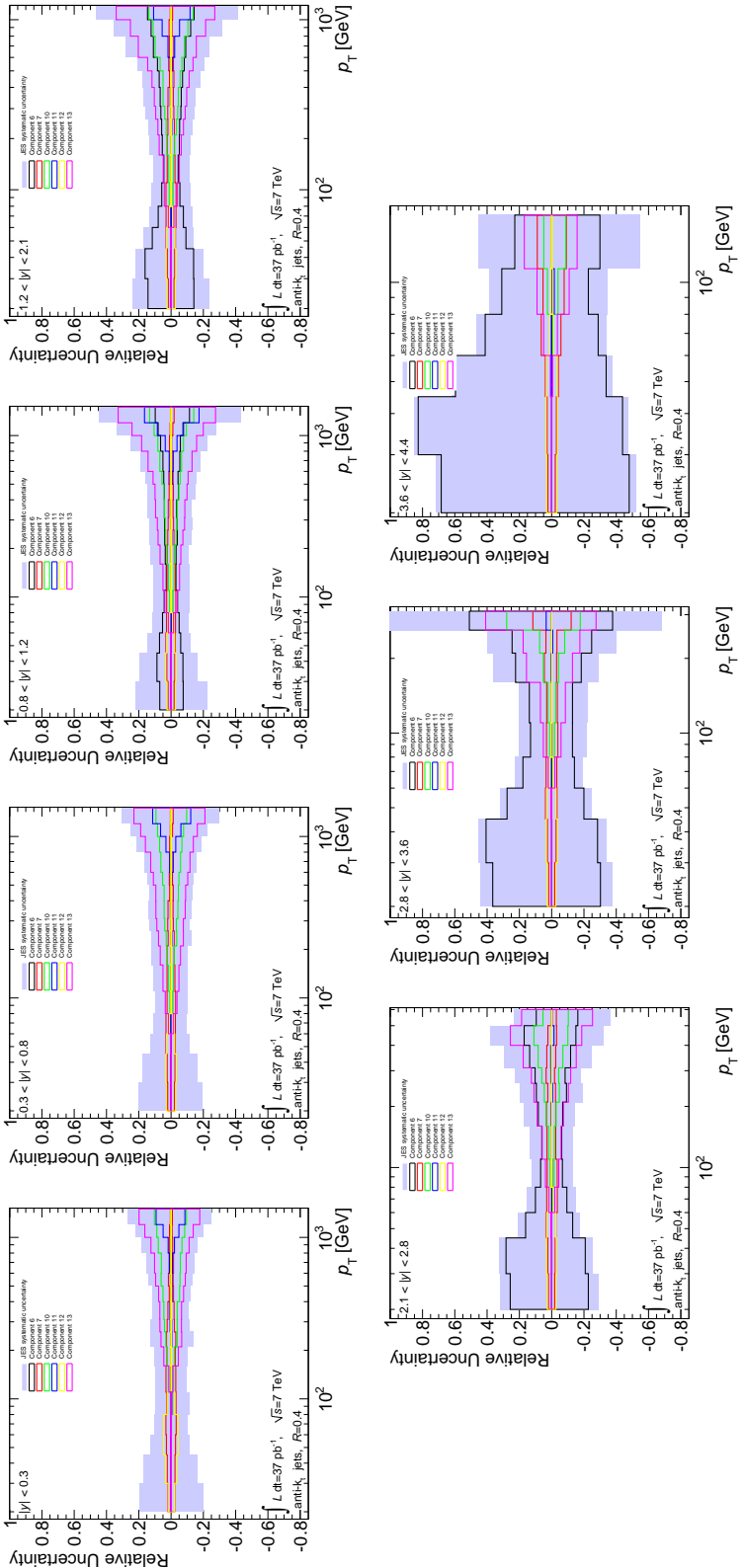


Figure D.18: The colored lines show the relative systematic uncertainty on the inclusive jet cross section measurement due to the various components of the jet energy scale uncertainty for anti- k_t jets with $R=0.4$ (SET 3). The association between the numbering and the meaning of each component is reported in Table 4.1. The light blue band shows the total uncertainty.

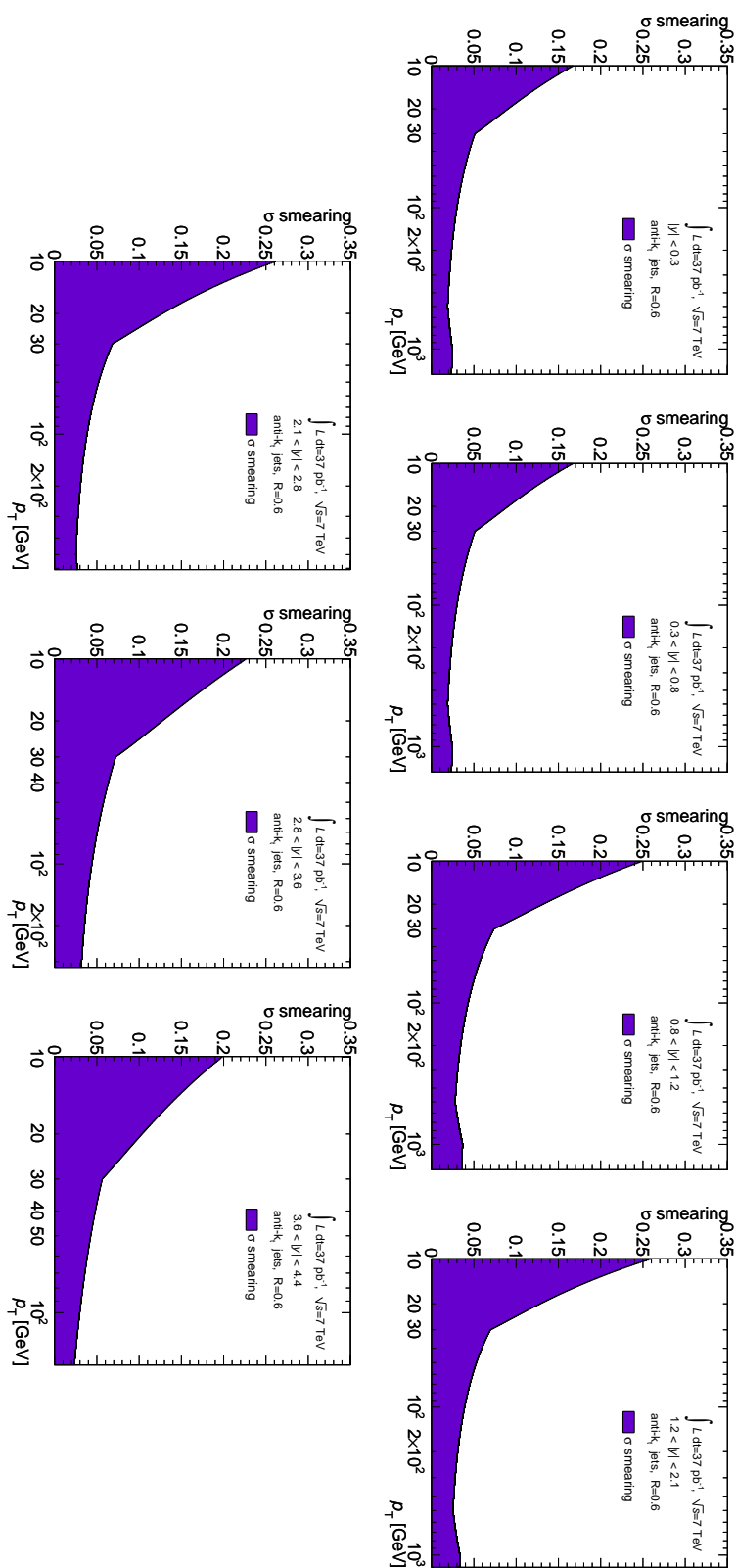


Figure D.19: Additional smearing applied to the Monte Carlo reconstructed jets to estimate the impact of the uncertainty on the jet energy resolution on the final inclusive jet cross section for anti- k_t jets with $R=0.6$.

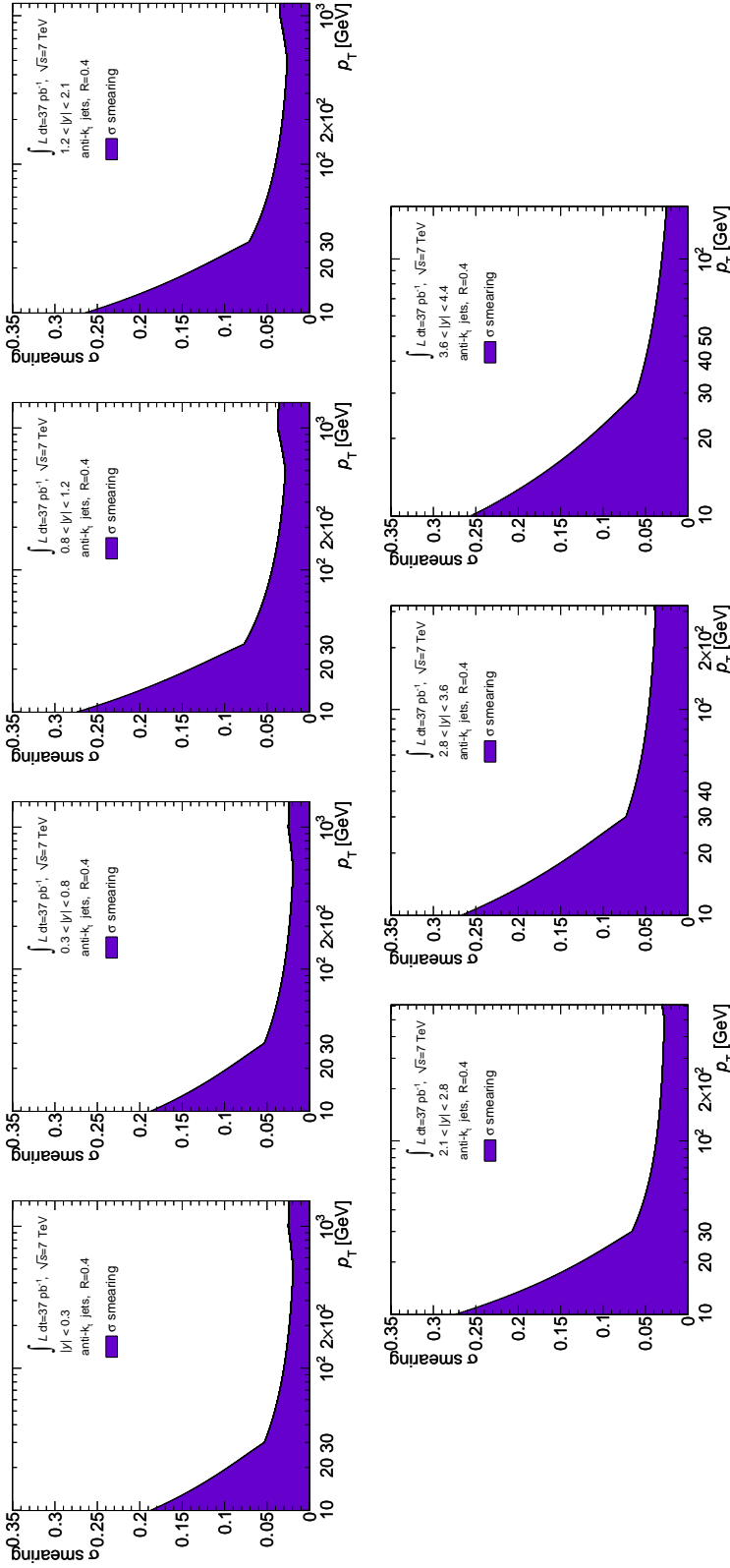


Figure D.20: Additional smearing applied to the Monte Carlo reconstructed jets to estimate the impact of the uncertainty on the jet energy resolution on the final inclusive jet cross section for anti- k_t jets with $R=0.4$.

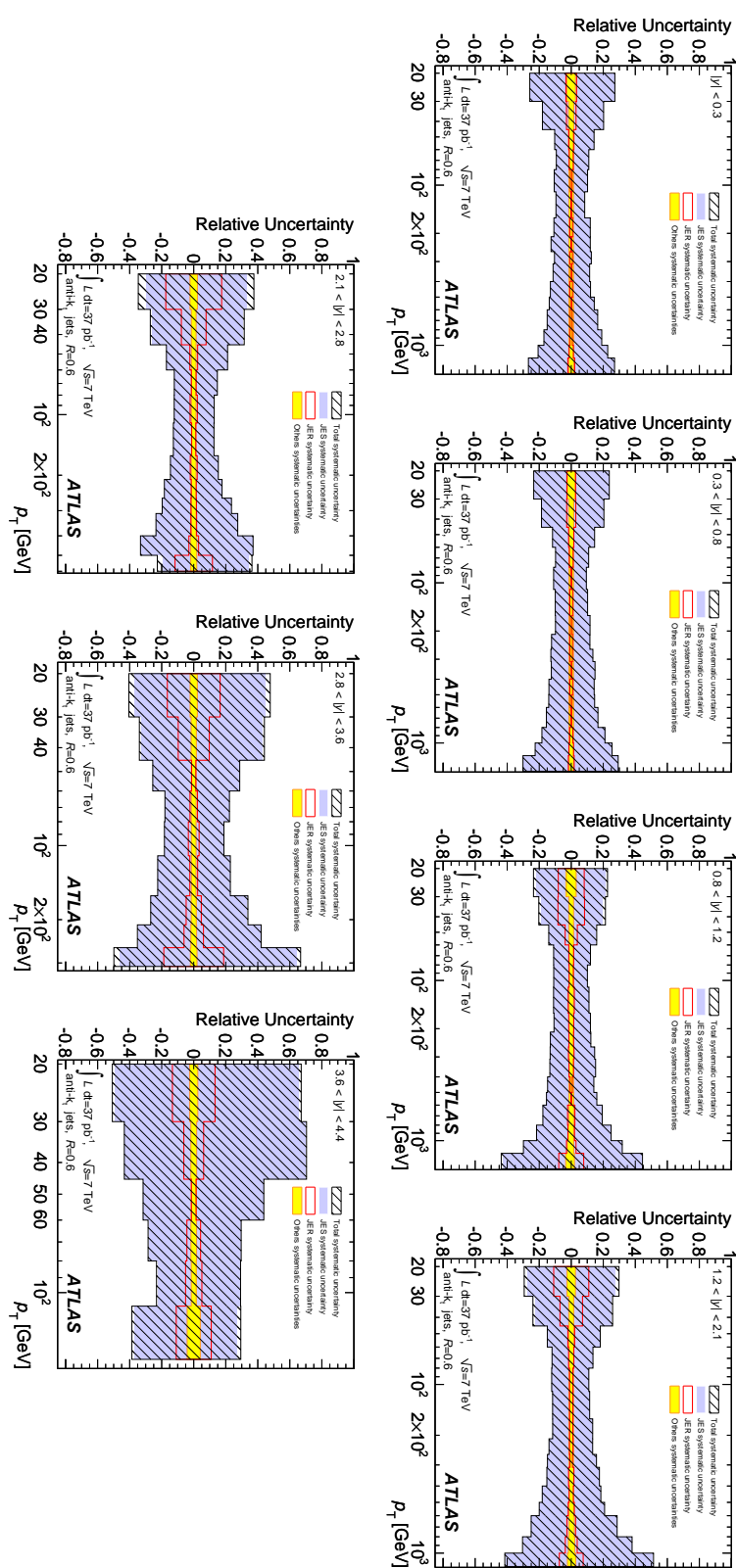


Figure D.21: Relative systematic uncertainty on the final inclusive jet cross section for anti- k_t jets with $R=0.6$. The contributions from the jet energy scale, the jet energy resolution and all the other sources are shown.

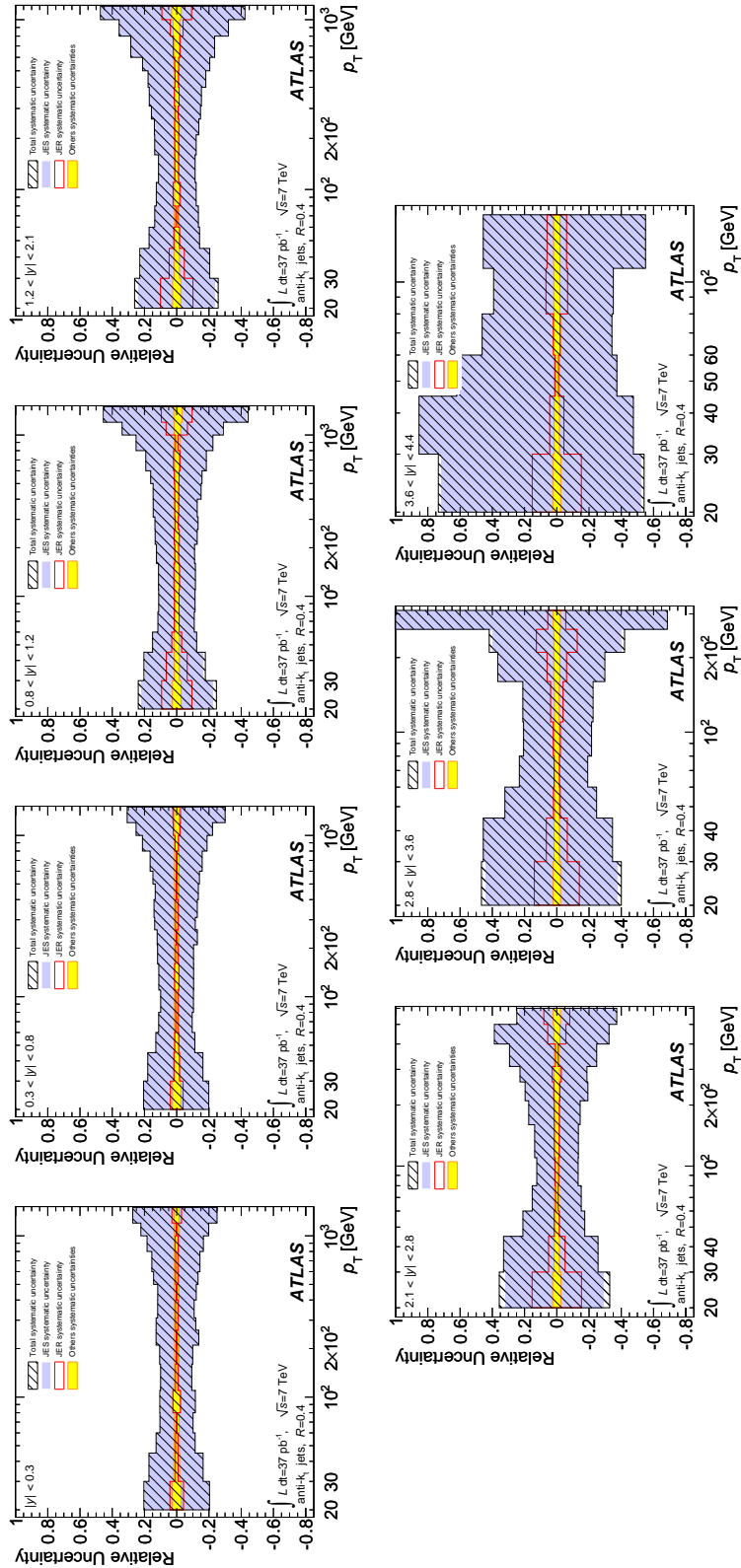


Figure D.22: Relative systematic uncertainty on the final inclusive jet cross section for anti- k_t jets with $R=0.4$. The contributions from the jet energy scale, the jet energy resolution and all the other sources are shown.

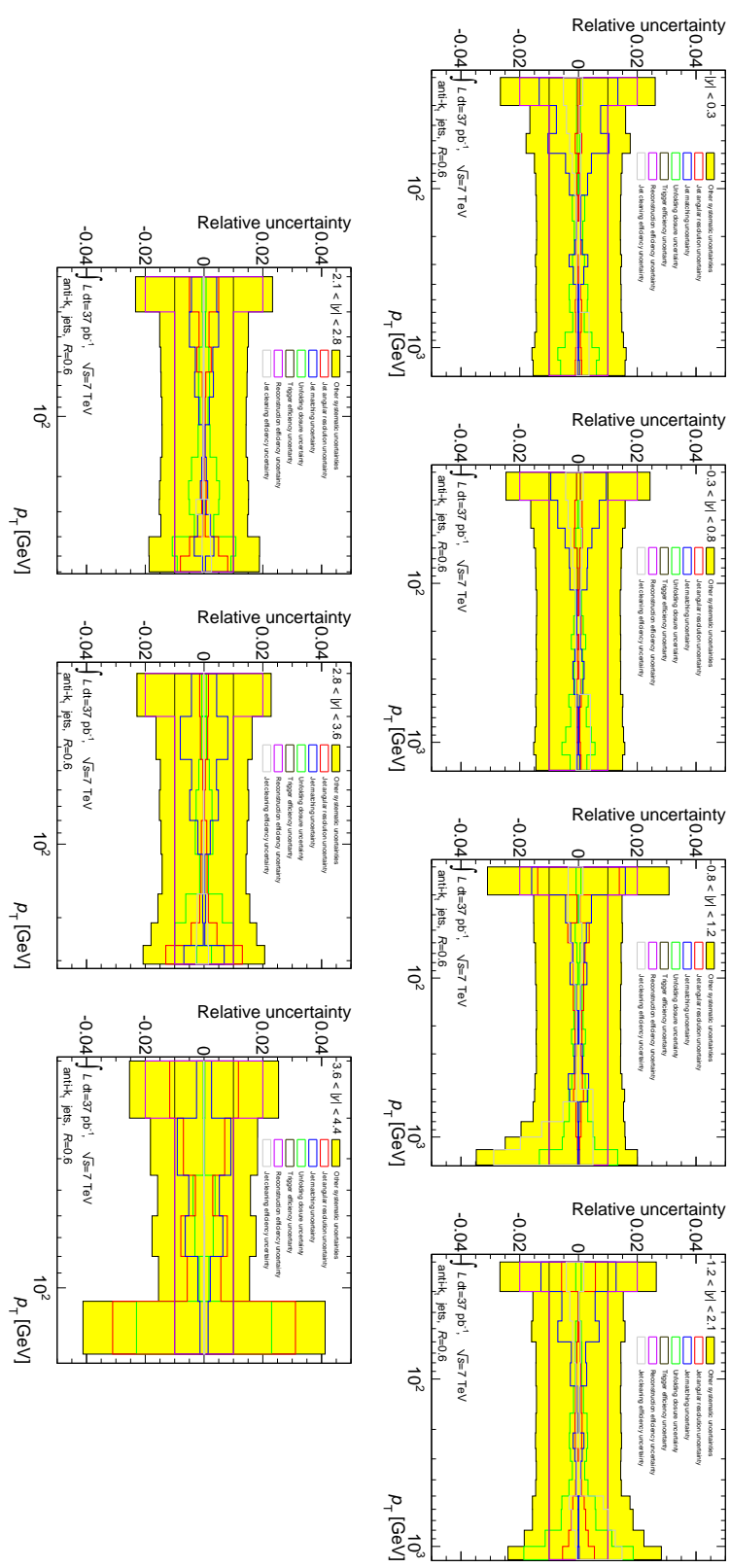


Figure D.23: Contributions of the sub-dominant sources on the relative systematic uncertainty on the final inclusive jet cross section for anti- k_t jets with $R=0.6$.

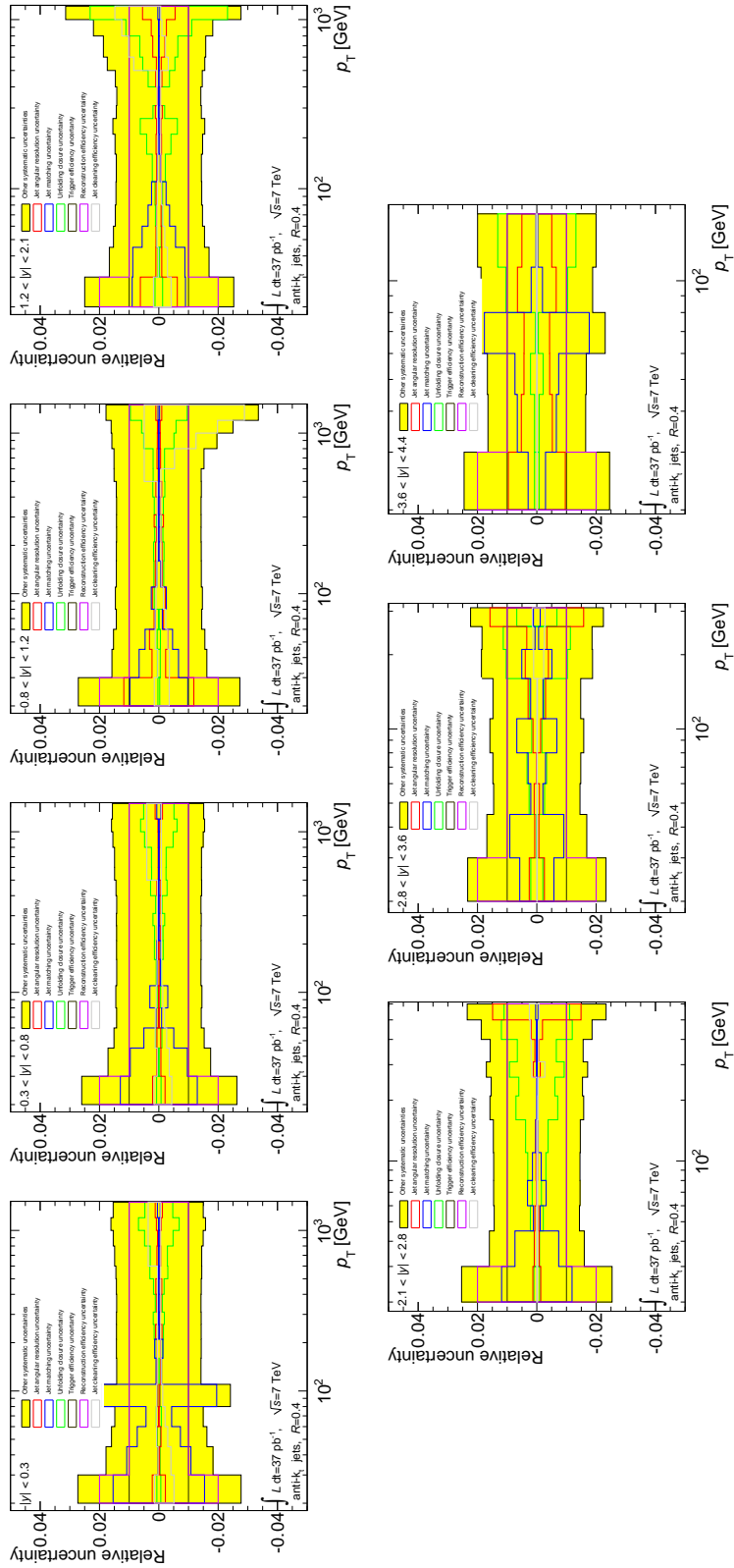


Figure D.24: Contributions of the sub-dominant sources on the relative systematic uncertainty on the final inclusive jet cross section for anti- k_t jets with $R=0.4$.

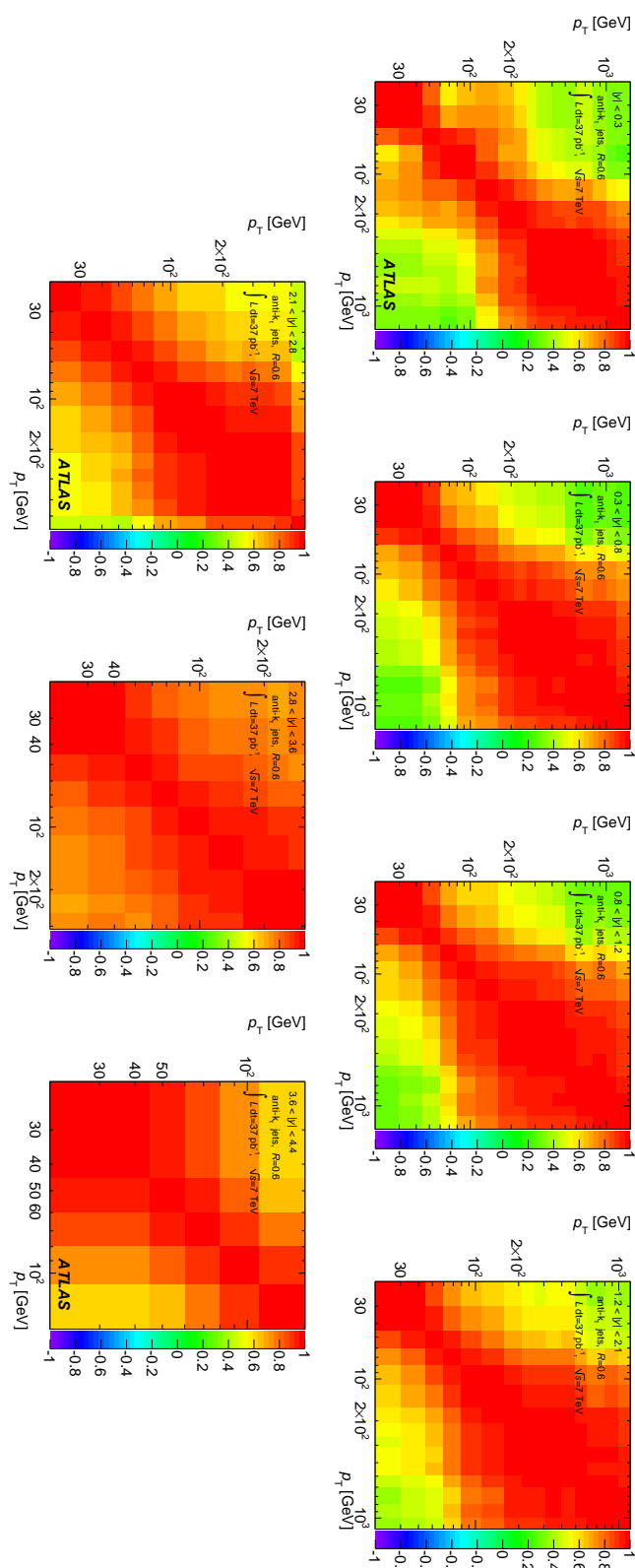


Figure D.25: Correlation of the systematic uncertainties of the inclusive jet cross section at the end of the unfolding procedure. The results are shown for anti- k_t jets with $R = 0.6$ in different slices of rapidity.

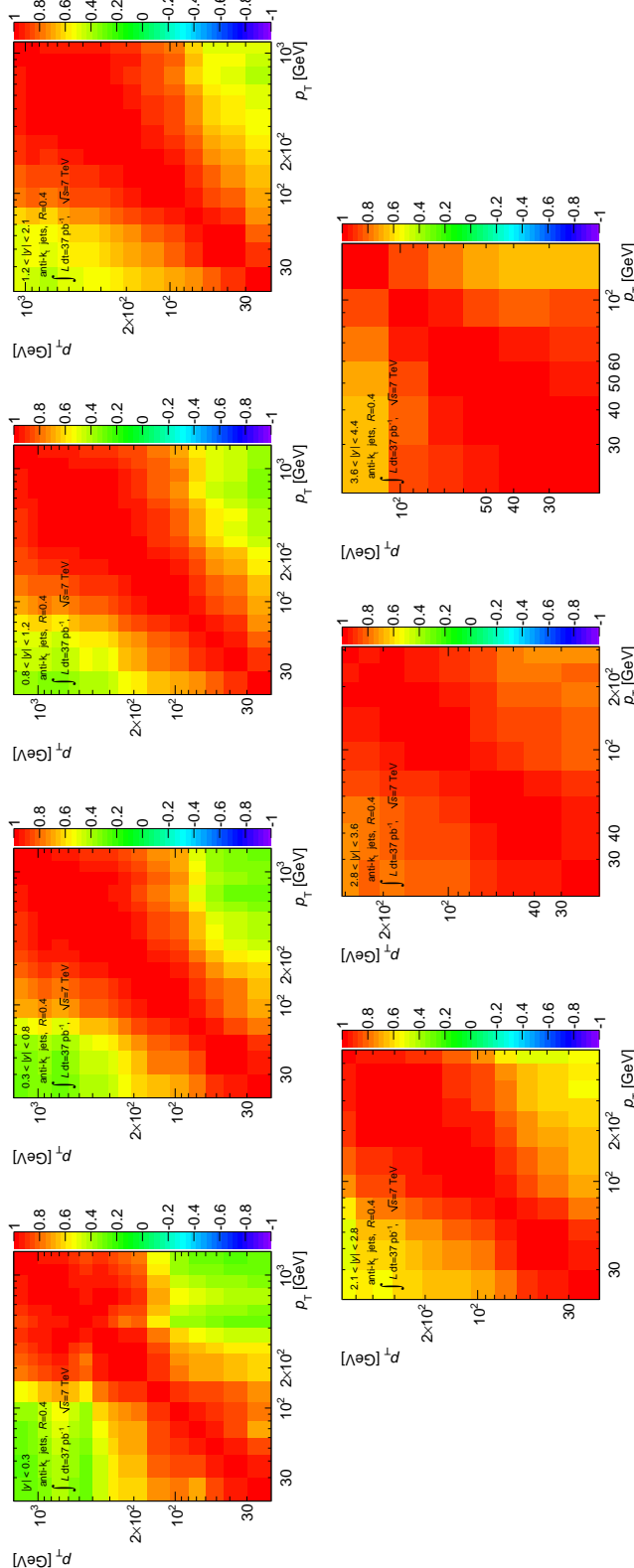


Figure D.26: Correlation of the systematic uncertainties of the inclusive jet cross section at the end of the unfolding procedure. The results are shown for anti- k_t jets with $R = 0.4$ in different slices of rapidity.

Bibliography

- [Abbott 2001] B. Abbott *et al.* *High $p(T)$ jets in anti- p p collisions at $s^{**}(1/2) = 630\text{-}GeV$ and $1800\text{-}GeV$.* Phys. Rev., vol. D64, page 032003, 2001. (Cited on page 99.)
- [Adragna 2009] P. Adragna *et al.* *Testbeam studies of production modules of the ATLAS Tile calorimeter.* Nucl. Instrum. Meth. A, vol. 606, pages 362–394, 2009. (Cited on page 55.)
- [Agostinelli 2003] S. Agostinelli *et al.* *GEANT4: A simulation toolkit.* Nucl. Instrum. Meth., vol. A506, pages 250–303, 2003. (Cited on pages 24, 80, 96 and 113.)
- [Aitchison 2003] I.J.R. Aitchison and A.J.G. Hey. *Gauge theories in particle physics: A practical introduction. Vol. 1: From relativistic quantum mechanics to QED.* 2003. (Cited on pages 27 and 29.)
- [Aitchison 2004] I.J.R. Aitchison and A.J.G. Hey. *Gauge theories in particle physics: A practical introduction. Vol. 2: Non-Abelian gauge theories: QCD and the electroweak theory.* 2004. (Cited on pages 27 and 29.)
- [Alioli 2010] Simone Alioli, Paolo Nason, Carlo Oleari and Emanuele Re. *A general framework for implementing NLO calculations in shower Monte Carlo programs: the POWHEG BOX.* JHEP, vol. 1006, page 043, 2010. (Cited on page 51.)
- [Alioli 2011a] Simone Alioli, Keith Hamilton, Paolo Nason, Carlo Oleari and Emanuele Re. *Jet pair production in POWHEG.* JHEP, vol. 04, page 081, 2011. (Cited on page 51.)
- [Alioli 2011b] Simone Alioli, Paolo Nason, Carlo Oleari and Emanuele Re. *Vector boson plus one jet production in POWHEG.* JHEP, vol. 01, page 095, 2011. (Cited on page 52.)
- [Amati 1979] D. Amati and G. Veneziano. *Preconfinement as a Property of Perturbative QCD.* Phys.Lett., vol. B83, page 87, 1979. (Cited on page 39.)
- [Andersson 1983] Bo Andersson, G. Gustafson, G. Ingelman and T. Sjöstrand. *Parton Fragmentation and String Dynamics.* Phys. Rept., vol. 97, pages 31–145, 1983. (Cited on page 39.)
- [A.Ribon 2010] A.Ribonet *et al.* *Status of Geant4 hadronic physics for the simulation of LHC experiments at the start of LHC physics program.* CERN-LCGAPP-2010-01, 2010. (Cited on pages 24 and 80.)
- [ATLAS Collaboration] ATLAS Collaboration. (Cited on pages 78, 80, 81 and 82.)
- [ATLAS Collaboration 1996a] ATLAS Collaboration. *ATLAS liquid-argon calorimeter: Technical Design Report.* 1996. (Cited on page 15.)

- [ATLAS Collaboration 1996b] ATLAS Collaboration. *ATLAS tile calorimeter: Technical Design Report*. 1996. (Cited on page 15.)
- [ATLAS Collaboration 1997a] ATLAS Collaboration. *ATLAS inner detector: Technical design report. Vol. 1.* 1997. (Cited on page 12.)
- [ATLAS Collaboration 1997b] ATLAS Collaboration. *ATLAS inner detector: Technical design report. Vol. 2.* 1997. (Cited on page 12.)
- [ATLAS Collaboration 1997c] ATLAS Collaboration. *ATLAS muon spectrometer: Technical Design Report*. 1997. distribution. (Cited on page 20.)
- [ATLAS Collaboration 1998] ATLAS Collaboration. *ATLAS level-1 trigger: Technical Design Report*. 1998. (Cited on page 21.)
- [ATLAS Collaboration 2003] ATLAS Collaboration. *ATLAS high-level trigger, data-acquisition and controls: Technical Design Report*. 2003. (Cited on page 21.)
- [ATLAS Collaboration 2008a] ATLAS Collaboration. *The ATLAS Experiment at the CERN Large Hadron Collider*. JINST, vol. 3, page S08003, 2008. (Cited on pages 5 and 12.)
- [ATLAS Collaboration 2008b] ATLAS Collaboration. *The ATLAS Forward Calorimeters*. JINST, vol. 3, page P02010, 2008. (Cited on page 20.)
- [ATLAS Collaboration 2009a] ATLAS Collaboration. *Discovering heavy particles decaying into single boosted jets with substructure using the kT algorithm*. Rapport technique ATL-PHYS-PUB-2009-076; ATL-COM-PHYS-2009-262, CERN, Geneva, May 2009. (Cited on page 37.)
- [ATLAS Collaboration 2009b] ATLAS Collaboration. *Expected Performance of the ATLAS Experiment - Detector, Trigger and Physics*. 2009. (Cited on pages 12, 37 and 58.)
- [ATLAS Collaboration 2009c] ATLAS Collaboration. *Overview and Performance Studies of Jet Identification in the Trigger System*. 2009. Pg. 697 in Expected Performance of the ATLAS Experiment - Detector, Trigger and Physics. (Cited on page 24.)
- [ATLAS Collaboration 2009d] ATLAS Collaboration. *Reconstruction of High Mass $t\bar{t}$ Resonances in the Lepton+Jets Channel*. Rapport technique ATL-PHYS-PUB-2009-081; ATL-COM-PHYS-2009-255, CERN, Geneva, May 2009. (Cited on page 37.)
- [ATLAS Collaboration 2009e] ATLAS Collaboration. *Local Hadronic Calibration*. Rapport technique ATL-LARG-PUB-2009-001, CERN, Geneva (Switzerland), January 2009. (Cited on page 65.)

- [ATLAS Collaboration 2010a] ATLAS Collaboration. *Study of energy response and resolution of the ATLAS barrel calorimeter to hadrons of energies from 20 to 350 GeV*. ATL-TILECAL-PUB-2009-007, <http://dx.doi.org/10.1016/j.nima.2010.04.054>, 2010. (Cited on page 82.)
- [ATLAS Collaboration 2010b] ATLAS Collaboration. *Characterization of Interaction-Point Beam Parameters Using the pp Event-Vertex Distribution Reconstructed in the ATLAS Detector at the LHC*. Rapport technique ATLAS-CONF-2010-027, CERN, Geneva, May 2010. (Cited on page 15.)
- [ATLAS Collaboration 2010c] ATLAS Collaboration. *Charged-particle multiplicities in pp interactions at $\sqrt{s} = 900$ GeV measured with the ATLAS detector at the LHC*. Phys. Lett., vol. B688, pages 21–42, 2010. (Cited on page 104.)
- [ATLAS Collaboration 2010d] ATLAS Collaboration. *Charged particle multiplicities in pp interactions at $\sqrt{s} = 900$ GeV and 7 TeV in a diffractive limited phase-space measured with the ATLAS detector at the LHC and new PYTHIA6 tune*. ATLAS-CONF-2010-031, 2010. (Cited on page 112.)
- [ATLAS Collaboration 2010e] ATLAS Collaboration. *Charged-particle multiplicities in pp interactions measured with the ATLAS detector at the LHC*. 2010. Accepted by New J Phys. (Cited on pages 41, 80 and 87.)
- [ATLAS Collaboration 2010f] ATLAS Collaboration. *Combined performance studies for electrons at the 2004 ATLAS combined test-beam*. JINST, vol. 5, page P11006, 2010. (Cited on page 55.)
- [ATLAS Collaboration 2010g] ATLAS Collaboration. *In-situ pseudo-rapidity intercalibration to evaluate jet energy scale uncertainty and calorimeter performance in the forward region*. ATLAS-CONF-2010-055, 2010. (Cited on page 85.)
- [ATLAS Collaboration 2010h] ATLAS Collaboration. *Jet energy resolution and reconstruction efficiencies from in-situ techniques with the ATLAS Detector using proton-proton collisions at a center-of-mass energy $\sqrt{s} = 7$ TeV*. ATLAS-CONF-2010-054, 2010. (Cited on page 74.)
- [ATLAS Collaboration 2010i] ATLAS Collaboration. *Performance of primary vertex reconstruction in proton-proton collisions at $\sqrt{s} = 7$ TeV in the ATLAS experiment*. Rapport technique ATLAS-CONF-2010-069, CERN, Geneva, Jul 2010. (Cited on page 15.)
- [ATLAS Collaboration 2010j] ATLAS Collaboration. *Readiness of the ATLAS Liquid Argon Calorimeter for LHC Collisions*. Eur.Phys.J., vol. C70, pages 723–753, 2010. (Cited on page 15.)
- [ATLAS Collaboration 2010k] ATLAS Collaboration. *Readiness of the ATLAS Tile Calorimeter for LHC collisions*. Eur.Phys.J., vol. C70, pages 1193–1236, 2010. (Cited on page 15.)

- [ATLAS Collaboration 2010l] ATLAS Collaboration. *Response of the ATLAS calorimeters to single isolated hadrons produced in proton–proton collisions at a center-of-mass energy of $\sqrt{s} = 900$ GeV.* ATLAS-CONF-2010-017, 2010. (Cited on page 78.)
- [ATLAS Collaboration 2010m] ATLAS Collaboration. *The ATLAS Inner Detector commissioning and calibration.* Eur.Phys.J., vol. C70, pages 787–821, 2010. * Temporary entry *. (Cited on page 12.)
- [ATLAS Collaboration 2010n] ATLAS Collaboration. *The ATLAS Simulation Infrastructure.* Eur. Phys. J., vol. C70, pages 823–874, 2010. (Cited on pages 24, 80 and 113.)
- [ATLAS Collaboration 2011a] ATLAS Collaboration. *ATLAS Calorimeter Response to Single Isolated Hadrons and Estimation of the Calorimeter Jet Scale Uncertainty.* ATLAS-CONF-2011-028, 2011. (Cited on pages 78, 79, 81, 82, 83 and 84.)
- [ATLAS Collaboration 2011b] ATLAS Collaboration. *ATLAS tunes of PYTHIA 6 and PYTHIA 8 for MC11.* ATL-PHYS-PUB-2011-009, 2011. (Cited on page 41.)
- [ATLAS Collaboration 2011c] ATLAS Collaboration. *Determination of the jet energy measurement uncertainty using photon-jet events in proton-proton collisions at $\sqrt{s} = 7$ TeV.* ATLAS-CONF-2011-031, 2011. (Cited on page 94.)
- [ATLAS Collaboration 2011d] ATLAS Collaboration. <https://twiki.cern.ch/twiki/bin/view/AtlasPublic/JetResolutionPreliminaryResults>. 2011. (Cited on page 59.)
- [ATLAS Collaboration 2011e] ATLAS Collaboration. *In-situ jet energy scale and jet shape corrections for multiple interactions in the first ATLAS data at the LHC.* ATLAS-CONF-2011-030, 2011. (Cited on pages 56 and 77.)
- [ATLAS Collaboration 2011f] ATLAS Collaboration. *In-situ pseudorapidity intercalibration for evaluation of jet energy scale uncertainty using dijet events in proton-proton collisions at $\sqrt{s} = 7$ TeV.* ATLAS-CONF-2011-014, 2011. (Cited on page 85.)
- [ATLAS Collaboration 2011g] ATLAS Collaboration. *Jet energy measurement with the ATLAS detector in proton-proton collisions at $\sqrt{s} = 7$ TeV in 2010.* Rapport technique, Aug 2011. Paper in preparation. (Cited on page 70.)
- [ATLAS Collaboration 2011h] ATLAS Collaboration. *Jet energy scale and its systematic uncertainty in proton-proton collisions at $\sqrt{s} = 7$ TeV in ATLAS 2010 data.* ATLAS-CONF-2011-032, 2011. (Cited on pages 57, 75, 77, 83, 89, 96 and 120.)
- [ATLAS Collaboration 2011i] ATLAS Collaboration. *Luminosity Determination in pp Collisions at $\text{sqrt}(s)=7$ TeV Using the ATLAS Detector at the LHC.* Eur.Phys.J., vol. C71, page 1630, 2011. (Cited on page 108.)

- [ATLAS Collaboration 2011j] ATLAS Collaboration. *Measurement of inclusive jet and dijet cross sections in proton-proton collision data at 7 TeV centre-of-mass energy using the ATLAS detector.* ATLAS-CONF-2011-047, 2011. (Cited on page 3.)
- [ATLAS Collaboration 2011k] ATLAS Collaboration. *Measurement of inclusive jet and dijet cross sections in proton-proton collisions at 7 TeV centre-of-mass energy with the ATLAS detector.* Eur. Phys. J., vol. C71, page 1512, 2011. (Cited on pages 1, 3, 145, 147, 148 and 149.)
- [ATLAS Collaboration 2011l] ATLAS Collaboration. *Measurement of inclusive jet and dijet production in pp collisions at $\sqrt{s}=7$ TeV using the ATLAS detector.* Rapport technique ATL-COM-PHYS-2011-1118, CERN, Geneva, Aug 2011. Paper in preparation. Publication draft on inclusive jet and dijet cross-section measurements using the full 2010 dataset. (Cited on page 146.)
- [ATLAS Collaboration 2011m] ATLAS Collaboration. *New ATLAS event generator tunes to 2010 data.* ATL-PHYS-PUB-2011-008, 2011. (Cited on page 41.)
- [ATLAS Collaboration 2011n] ATLAS Collaboration. *Probing the jet energy measurement at the TeV-scale with the multi-jet balance technique in proton-proton collisions at $\sqrt{s} = 7$ TeV with the ATLAS detector.* ATLAS-CONF-2011-029, 2011. (Cited on pages 94 and 97.)
- [ATLAS Collaboration 2011o] ATLAS Collaboration. *Updated Luminosity Determination in pp Collisions at $\sqrt{s} = 7$ TeV using the ATLAS Detector.* ATLAS-CONF-2011-011, 2011. (Cited on pages 108 and 109.)
- [Bagnaia 1984] P. Bagnaia et al. *Measurement of Jet Production Properties at the CERN anti- p p Collider.* Phys.Lett., vol. B144, page 283, 1984. (Cited on page 99.)
- [Bahr 2008a] M. Bahret et al. *Herwig++ 2.3 Release Note.* 2008. (Cited on page 38.)
- [Bahr 2008b] M. Bahret et al. *Herwig++ Physics and Manual.* Eur. Phys. J., vol. C58, pages 639–707, 2008. (Cited on pages 41, 49, 51 and 87.)
- [Ball 2010] Richard D. Ballet et al. *A first unbiased global NLO determination of parton distributions and their uncertainties.* Nucl. Phys., vol. B838, pages 136–206, 2010. (Cited on page 46.)
- [Bassetto 1980] A. Bassetto, M. Ciafaloni and G. Marchesini. *Inelastic Distributions and Color Structure in Perturbative QCD.* Nucl.Phys., vol. B163, page 477, 1980. (Cited on page 39.)
- [Benedikt 2004] (Ed.) Benedikt M., (Ed.) Collier P., (Ed.) Mertens V., (Ed.) Poole J. and (Ed.) Schindl K. *LHC Design Report. 3. The LHC injector chain.* 2004. (Cited on page 5.)
- [Bethke 2009] Siegfried Bethke. *The 2009 World Average of alpha(s).* Eur.Phys.J., vol. C64, pages 689–703, 2009. (Cited on pages 30 and 31.)

- [Brooijmans 2008] Gustaaf H. Brooijmans *et al.* *New Physics at the LHC: A Les Houches Report. Physics at Tev Colliders 2007 – New Physics Working Group.* 2008. (Cited on page 37.)
- [Bruning 2004a] (Ed.) Bruning O., (Ed.) Collier P., (Ed.) Lebrun P., (Ed.) Myers S., (Ed.) Ostojic R.*et al.* *LHC Design Report. 1. The LHC Main Ring.* 2004. (Cited on page 5.)
- [Bruning 2004b] (Ed.) Bruning O., (Ed.) Collier P., (Ed.) Lebrun P., (Ed.) Myers S., (Ed.) Ostojic R.*et al.* *LHC Design Report. 2. The LHC infrastructure and general services.* 2004. (Cited on page 5.)
- [Buckley 2010a] Andy Buckley *et al.* *Rivet user manual.* 2010. (Cited on page 49.)
- [Buckley 2010b] Andy Buckley, Hendrik Hoeth, Heiko Lacker, Holger Schulz and Jan Eike von Seggern. *Systematic event generator tuning for the LHC.* Eur. Phys. J., vol. C65, pages 331–357, 2010. (Cited on page 41.)
- [Buttar 2008] C. Buttar, J. D’Hondt, M. Kramer, G. Salam, M. Wobischet *et al.* *Standard Model Handles and Candles Working Group: Tools and Jets Summary Report,* 2008. (Cited on page 43.)
- [Butterworth 1996] J. M. Butterworth, Jeffrey R. Forshaw and M. H. Seymour. *Multiparton interactions in photoproduction at HERA.* Z. Phys., vol. C72, pages 637–646, 1996. (Cited on pages 41, 51 and 87.)
- [Butterworth 2002] J. M. Butterworth, B. E. Cox and Jeffrey R. Forshaw. *WW scattering at the CERN LHC.* Phys. Rev., vol. D65, page 096014, 2002. (Cited on page 37.)
- [Butterworth 2007] J. M. Butterworth, John R. Ellis and A. R. Raklev. *Reconstructing sparticle mass spectra using hadronic decays.* JHEP, vol. 05, page 033, 2007. (Cited on page 37.)
- [Cacciari] M. Cacciari, G. P. Salam and G. Soyez. *FastJet package.* (Cited on pages 37 and 43.)
- [Cacciari 2006] Matteo Cacciari and Gavin P. Salam. *Dispelling the N^3 myth for the k_t jet-finder.* Phys. Lett., vol. B641, pages 57–61, 2006. (Cited on pages 37 and 43.)
- [Cacciari 2008] M. Cacciari, G.P. Salam and G. Soyez. *The anti- k_t jet clustering algorithm.* JHEP, vol. 0804, page 063, 2008. (Cited on pages 37 and 43.)
- [Carli 2010] T. Carli *et al.* *A posteriori inclusion of parton density functions in NLO QCD final-state calculations at hadron colliders: The APPLGRID Project.* Eur. Phys. J., vol. C66, pages 503–524, 2010. (Cited on page 44.)
- [Catani 1993] S. Catani, Yuri L. Dokshitzer, M. H. Seymour and B. R. Webber. *Longitudinally invariant $K(t)$ clustering algorithms for hadron hadron collisions.* Nucl. Phys., vol. B406, pages 187–224, 1993. (Cited on page 37.)

- [Cleland 1992] W.E. Cleland and E.G. Stern. *Signal processing for liquid ionization calorimeters*. 1992. (Cited on page 18.)
- [Cojocaru 2004] C. Cojocaruet al. *Hadronic calibration of the ATLAS liquid argon end-cap calorimeter in the pseudorapidity region $1.6 < |\eta| < 1.8$ in beam tests*. Nucl. Instrum. Meth. A, vol. 531, no. 3, pages 481 – 514, 2004. (Cited on pages 55 and 82.)
- [Collaboration 2010] ATLAS Collaboration. *Measurement of the response of the ATLAS liquid argon barrel calorimeter to electrons at the 2004 combined test-beam*. Nucl. Instrum. Meth., vol. A614, pages 400–432, 2010. (Cited on page 55.)
- [Corcella 2001] G. Corcellaet al. *HERWIG 6.5: an event generator for Hadron Emission Reactions With Interfering Gluons (including supersymmetric processes)*. JHEP, vol. 01, page 010, 2001. (Cited on page 38.)
- [Corcella 2002] G. Corcellaet al. *HERWIG 6.5 Release Note*. 2002. (Cited on pages 41, 51 and 87.)
- [Dissertori 2010] G. Dissertori and G.P. Salam. *Quantum Chromodynamics*. J.Phys.G, vol. G37, page 075021, 2010. Pg. 114 in Review of particle physics. (Cited on pages 2 and 30.)
- [Doglioni 2011a] C Doglioni. *Private Communicartion*, June 2011. (Cited on pages 90, 165 and 166.)
- [Doglioni 2011b] C Doglioni, P Francavilla, P Loch, K Perez and RA Vitillo. *Design of the Jet Performance Software for the ATLAS Experiment at LHC*. Rapport technique ATL-SOFT-PROC-2011-037, CERN, Geneva, Feb 2011. (Cited on page 2.)
- [Dowler 2002] B. Dowleret al. *Performance of the ATLAS hadronic end-cap calorimeter in beam tests*. Nucl. Instrum. Meth., vol. A482, pages 94–124, 2002. (Cited on page 82.)
- [Ellis 1993] Stephen D. Ellis and Davison E. Soper. *Successive combination jet algorithm for hadron collisions*. Phys. Rev., vol. D48, pages 3160–3166, 1993. (Cited on page 37.)
- [Ellis 1996] R. Keith Ellis, W. James Stirling and Brian R. Webber. QCD and collider physics, volume 8. Cambridge Monogr. Part. Phys. Nucl. Phys. Cosmol., 1 édition, 1996. (Cited on page 33.)
- [Ferro-Luzzi 2011] M. Ferro-Luzzi. *LHC 2010 OPERATION - AS VIEWED FROM THE EXPERIMENTS*. 2011. Chamonix 2011 LHC Performance Workshop. (Cited on page 8.)
- [Forte 2010] Stefano Forte, Eric Laenen, Paolo Nason and Juan Rojo. *Heavy quarks in deep-inelastic scattering*. Nucl. Phys., vol. B834, pages 116–162, 2010. (Cited on page 46.)

- [Francavilla 2011] P Francavilla, S Baker, G Brown, M Campanelli, T Carli, V Cavasinni, R Chislett, C Doglioni, S Eckweiler, E Feng, D Gillberg, E Hughes, J Huston, G Jones, J Keung, P Krieger, H Li, B Malaescu, C Meyer, F Mueller, M Oreglia, K Perez, J Pilcher, A Pilkington, J Poveda, J Robinson, C Roda, N Ruthmann, B Salvachua, S Shimizu, P Starovoitov, T Sumida, K Terashi, P Thompson, F Vives, M Vujicic, S L Wu and S Yanush. *Measurement of inclusive jet and dijet production in pp collisions at $\sqrt{s}=7$ TeV using the ATLAS detector.* Rapport technique ATL-COM-PHYS-2011-738, CERN, Geneva, Jun 2011. Supporting documentation for the inclusive jet and dijet publication using the full 2010 dataset. (Cited on page 126.)
- [Frixione 2002] Stefano Frixione and Bryan R. Webber. *Matching NLO QCD computations and parton shower simulations.* JHEP, vol. 06, page 029, 2002. (Cited on page 51.)
- [Frixione 2007] Stefano Frixione, Paolo Nason and Carlo Oleari. *Matching NLO QCD computations with Parton Shower simulations: the POWHEG method.* JHEP, vol. 11, page 070, 2007. (Cited on page 51.)
- [Frixione 2010] Stefano Frixione, Fabian Stoeckli, Paolo Torrielli, Bryan R. Webber and Chris D. White. *The MC@NLO 4.0 Event Generator*, 2010. (Cited on page 51.)
- [Fullana 2005] E Fullana et al. *Optimal Filtering in the ATLAS Hadronic Tile Calorimeter.* Rapport technique ATL-TILECAL-2005-001. ATL-COM-TILECAL-2005-001. CERN-ATL-TILECAL-2005-001, CERN, Geneva, 2005. (Cited on page 19.)
- [Gillberg 2011] D Gillberg. *Private Communicartion*, September 2011. (Cited on page 92.)
- [Glazov 2011] A Glazov. *Private Communicartion*, October 2011. (Cited on page 146.)
- [Gupta 1997] Rajan Gupta. *Introduction to lattice QCD: Course.* pages 83–219, 1997. (Cited on page 30.)
- [H1 and ZEUS Collaborations] H1 and ZEUS Collaborations. *HERAPDF 1.5.* H1prelim-10-142, ZEUS-prel-10-018. (Cited on page 46.)
- [Hoche 2011] Stefan Hoche, Frank Krauss, Marek Schonherr and Frank Siegert. *Automating the POWHEG method in Sherpa.* JHEP, vol. 1104, page 024, 2011. (Cited on page 51.)
- [Hocker 1996] Andreas Hocker and Vakhtang Kartvelishvili. *SVD approach to data unfolding.* Nucl. Instrum. Meth., vol. A372, pages 469–481, 1996. TSVDUnfold implementation by K. Tackmann et al. (Cited on page 115.)
- [Hoeche 2009] Stefan Hoeche, Frank Krauss, Steffen Schumann and Frank Siegert. *QCD matrix elements and truncated showers.* JHEP, vol. 05, page 053, 2009. (Cited on page 38.)

- [<http://durpdg.dur.ac.uk/>] <http://durpdg.dur.ac.uk/>. *The Durham HepData Project*. (Cited on pages 32, 48 and 155.)
- [Lai] H-L. Lai *et al.* *Uncertainty induced by QCD coupling in the CTEQ-TEA global analysis of parton densities*. (Cited on page 48.)
- [Lai 2010] Hung-Liang Lai *et al.* *New parton distributions for collider physics*. Phys. Rev., vol. D82, page 074024, 2010. (Cited on pages 32 and 44.)
- [Lendermann 2009] Victor Lendermann *et al.* *Combining Triggers in HEP Data Analysis*. Nucl. Instrum. Meth., vol. A604, pages 707–718, 2009. (Cited on page 110.)
- [Lönnblad 1992] Leif Lönnblad. *ARIADNE version 4: A Program for simulation of QCD cascades implementing the color dipole model*. Comput. Phys. Commun., vol. 71, pages 15–31, 1992. (Cited on page 38.)
- [Malaescu 2011] Bogdan Malaescu. *An Iterative, Dynamically Stabilized (IDS) Method of Data Unfolding*, 2011. (Cited on page 115.)
- [Mangano 2003] Michelangelo L. Mangano, Mauro Moretti, Fulvio Piccinini, Roberto Pittau and Antonio D. Polosa. *ALPGEN, a generator for hard multiparton processes in hadronic collisions*. JHEP, vol. 07, page 001, 2003. (Cited on pages 41 and 87.)
- [Marchesini 1981] G. Marchesini, L. Trentadue and G. Veneziano. *SPACE-TIME DESCRIPTION OF COLOR SCREENING VIA JET CALCULUS TECHNIQUES*. Nucl.Phys., vol. B181, page 335, 1981. (Cited on page 39.)
- [Martin 2009] A. D. Martin, W. J. Stirling, R. S. Thorne and G. Watt. *Parton distributions for the LHC*. Eur. Phys. J., vol. C63, pages 189–285, 2009. (Cited on pages 46 and 112.)
- [Meddahi 2011] M. Meddahi. *LHC operation: experience from 2010 and plans for 2011*. 2011. ATLAS Week, 28 February - 4 March 2011. (Cited on page 8.)
- [Nadolsky] Pavel Nadolsky. *Nuisance parameters in the PDF analysis*. Presentation at PDF4LHC Meeting, Oct 23, 2009. (Cited on page 91.)
- [Nagy 2003] Zoltan Nagy. *Next-to-leading order calculation of three jet observables in hadron hadron collision*. Phys. Rev., vol. D68, page 094002, 2003. (Cited on page 44.)
- [Nason 2004] Paolo Nason. *A new method for combining NLO QCD with shower Monte Carlo algorithms*. JHEP, vol. 11, page 040, 2004. (Cited on page 51.)
- [Nason 2007] Paolo Nason. *MINT: a Computer Program for Adaptive Monte Carlo Integration and Generation of Unweighted Distributions*, 2007. (Cited on page 52.)

- [Olness 2010] Fredrick I. Olness and Davison E. Soper. *Correlated theoretical uncertainties for the one-jet inclusive cross section*. Phys.Rev., vol. D81, page 035018, 2010. (Cited on page 46.)
- [Pinfold 2008] J. Pinfold *et al.* *Performance of the ATLAS liquid argon endcap calorimeter in the pseudorapidity region $2.5 < |\eta| < 4.0$ in beam tests*. Nucl. Instrum. Meth. A, vol. 593, pages 324–342, 2008. (Cited on page 55.)
- [Pumplin 2002] J. Pumplin *et al.* *New generation of parton distributions with uncertainties from global QCD analysis*. JHEP, vol. 07, page 012, 2002. (Cited on page 91.)
- [Ruehr 2009] Frederik Ruehr. *TeV Jets at ATLAS - A Probe for New Physics*. Rapport technique, PhD thesis at the Joint Faculties for Natural Sciences and Mathematics of the Ruperta Carola University of Heidelberg, Germany, 2009. (Cited on page 95.)
- [S. D. Ellis 2001] J. Huston S. D. Ellis and M. Tonnesmann. *On building better cone jet algorithms*. 2001. (Cited on page 63.)
- [Salam 2007] Gavin P. Salam and Gregory Soyez. *A practical Seedless Infrared-Safe Cone jet algorithm*. JHEP, vol. 05, page 086, 2007. (Cited on page 36.)
- [Salam 2009] Gavin P. Salam. *Towards Jetography*. 2009. (Cited on page 36.)
- [Salam 2010] Gavin P. Salam. *Elements of QCD for hadron colliders*. 2010. (Cited on page 30.)
- [Salvachua 2009] B. Salvachua, S. Chekanov and J. Proudfoot. *Comparison of MC based Jet Energy Scales applied after H1 calibration*, ATL-PHYS-INT-2009-050, Apr 2009. (Cited on page 58.)
- [Schwartz] M. Schwartz. to appear in proceedings of Les Houches 2009. (Cited on page 38.)
- [Seymour 1998] M. H. Seymour. *Jet shapes in hadron collisions: Higher orders, resummation and hadronization*. Nucl. Phys., vol. B513, pages 269–300, 1998. (Cited on pages 36 and 60.)
- [Sherstnev 2008] A. Sherstnev and R.S. Thorne. *Different PDF approximations useful for LO Monte Carlo generators*, 2008. (Cited on page 112.)
- [Sjostrand 2006] Torbjorn Sjostrand, Stephen Mrenna and Peter Z. Skands. *PYTHIA 6.4 Physics and Manual*. JHEP, vol. 0605, page 026, 2006. (Cited on pages 38, 41, 49, 80 and 87.)
- [Sjostrand 2008] Torbjorn Sjostrand. *Pythia 8 Status Report*. 2008. (Cited on pages 38 and 49.)
- [Skands 2009] Peter Z. Skands. *The Perugia Tunes*, 2009. (Cited on page 41.)
- [Skands 2010] Peter Zeiler Skands. *Tuning Monte Carlo Generators: The Perugia Tunes*. Phys. Rev., vol. D82, page 074018, 2010. (Cited on page 41.)

Acknowledgments

The last four years of activities in the ATLAS Pisa group and in the ATLAS Collaboration were really intensive and constructive. I had the possibility to do different activities and to experience different aspects of the high energy physics.

In this long period project, which started well before the beginning of the Ph.D. studies, I had always a strong encouragement from Chiara Roda. She is the advisor of this thesis, and I consider her as a mentor, who knew how to transform my enthusiasms in a real passion, and my curiosities in real concrete skills. I had most of the inspiring discussion with her, which deeply guided me in the different activities in these years.

These activities are possible thanks to the ATLAS Pisa group. Thanks to the strong support of the group, I had the possibility to play an important role in the ATLAS measurement described in the thesis, and in other important aspects of the experiment. I would like to thank in particular Vincenzo Cavasinni, for the really instructive discussions and for the support, especially in the last months; and Tarcisio (Nino) Del Prete: it is always really interesting to discuss with him, learning new things.

The group of Pisa had some changes in the last years. I start thanking the "old quard": Iacopo Vivarelli Andrea Dotti, Giulio Usai, and Francesca Sarri. Being introduced to the high energy physics, and to the ATLAS experiment by you was really an honor.

In the last years, I had alway the help of Zinonos Zinonas, Michele Cascella, Vincent Giangioffe, and Roberto Vitillo, who encourage me in this project. All of them put up with me, sharing the projects, the office, (sometime the apartment),... Having their help was really necessary to complete the Ph.D.

In the last two years, a new group of people joined the ATLAS Pisa group, guided by Paola Giannetti, and Mauro Dell'Orso. Their feedbacks, coming from deep experiences in hadron colliders, were a real precious gift to this project.

The ATLAS Collaboration was an amazing group where to move the first steps in high energy physics. In particular, there are at least three groups I would like to thank: the TileCal group, JetEtMiss group, and the Standard Model/QCD/Inclusive jet and dijet cross section group.

I spent the last months as coordinator of the TileCal operations, and this was an honor, and I would like to thanks the Tile community, in particular Ana Maria Henriques Correia, Oleg Solovyanov, Belen Salvachua, Maria Fiascaris and Claudio Santoni for their fundamental help and support in these months.

An important part of this thesis has been possible thank to the JetEtMiss working group. I am really glad to thank Tancredi Carli, always a guide on the measurement and calibration of jets, who helped me with really good advices and discussions. And I thank Peter Lock. He deeply contributed to my preparation, and I am really glad because I had the opportunity to work with him in several occasions.

The third working group to thank is the Standard Model/QCD/ Inclusive Jet Cross section. In these years, the Standard Model working group and the QCD working group had very enlightened conveners, such as Kevin Einsweiler, Jonathan Butterworth, Koji Terashi and Mario Campanelli. In particular, Jonathan Butterworth played a fundamental role in several aspects of this analysis, by guiding, for instance, the inclusive jet cross

section group to the publication of the first jet cross section measurement at the LHC.

The inclusive jet cross section group was a really positive group. Several of the results in this thesis have been possible only with the hard work of this group. I need to thank all of my colleges/friends in this group. My deepest thanks go to all of them, and to all the people who contributed to the inclusive jet cross section measurement. I am glad to list some of them. A crucial role has been played by Kerstin Perez. We started the discussions on the inclusive jet cross section a couple of years ago, and our experience on this measurement has grown in parallel. Thanks a lot, Kerstin. A huge contribution on the jet energy scale uncertainty in the inclusive jet cross section comes from Dag Gillberg, Miro Vujicic, Caterina Doglioni. Caterina and Dag were fundamental in most of the discussions on the inclusive jet cross section measurement. It was a pleasure to participate to their discussions. I would like to thanks Felix Miller, for the plot of the integrated luminosity in the different bins of the measurements, and to Nils Ruthmann for his studies on the jet cleaning. They participated, to several checks and stability studies, fundamental to have a solid measurement. The revolution on the detector unfolding was possible thanks to the experience of Bogdan Malaescu, and Shima Shimizu. Thanks for this really important contribution. A really deep discussion on the theoretical calculations was necessary to establish a good and solid prediction. I thanks the contribution from Pavel Starovoitov, Serguei Yanush, Graham Jones and Joy Huston. Thanks to Peter Thomson and Chris Meyer, for their studies on the trigger for the inclusive jet cross section. And finally I thank Eric Feng. We had a lot of discussions in these years on our measurement.

I was really lucky in the last years. Not only I had the possibility to closely follow the detector activities, but also to have really inspiring discussions with some of the prominent Monte Carlo experts and QCD experts. It was an honor, and I am really glad to thanks them. In particular, the discussions at CERN with Mike Seymour, and in Lund with Torbjorn Sjostrand and Leif Lonnblad during the MCnet project. This was one of the most interesting periods in my Ph.D.

I am glad to thanks the authors of Powheg, in particular Paolo Nason, Carlo Oleari, Simone Alioli and Emanuele Re. Their help in using Powheg, and the discussions in the last months were really really precious. I would really thanks Matteo Cacciari and Gavin Salam. Their works are always inspiring me, and their lectures on jets deeply encouraged me in investigating the performances of the different jet definitions. A special thanks goes to the organizers and participants of the 2009 and 2011 Les Houches Workshop "Physics at the TeV scale". The discussions, especially with Peter Loch, Gavin Salam, Jon Butterworth, Peter Skands and Joey Huston were really nice, and useful for this thesis.

Infine, vorrei ringraziare la mia famiglia e i miei amici, che hanno avuto il coraggio di sopportare la mia lontanza, le mie assenze, le mie mancanze.... Alcuni di loro hanno avuto la "sfortuna" di divedere l'appartamento a Pisa, a Saint Genis o a Gex con me (Domenico, Stefano, Fabio, Marta, Iacopo, Andrea, Riccardo, Vincent, Giuseppe). Senza il loro aiuto, questi anni sarebbero stati meno interessanti. Vorrei poi ringraziare Matteo Volpi, per gli interessanti mesi trascorsi in Svizzera - (con qualche imprevisto ad Aprile - io almeno una chiave USB l'ho avuta indietro dalla polizia svizzera - sto ancora sperando per il laptop). Ma soprattutto, voglio ringraziare due persone che in questi anni, anche se da lontano, ho sempre sentito vicinissime: Carlo, Franca, senza la vostra forza, e le vostre parole, questo

non ci sarebbe.

Grazie.

Measurement of the inclusive jet cross section in the ATLAS detector at the LHC

Abstract: The measurement of the inclusive jet cross section is one of the test of perturbative quantum chromo-dynamics par excellence. The inclusive jet cross section presented in this thesis is measured with the ATLAS detector at the Large Hadron Collider (LHC). The double-differential inclusive jet cross section has been measured in bin of transverse momentum p_T and rapidity $|y|$. It measures the cross sections for anti- k_t jet with resolution parameter $R = 0.4$ and $R = 0.6$ for $20 \text{ GeV} < p_T < 1500 \text{ GeV}$, and for $-4.4 < y < 4.4$, which is the wider range reached so far at hadron collider. The total recorded integrated luminosity L in 2010, used in this analysis, is almost 37 pb^{-1} .

Four distinctive features make this measurement one of the more extensive and detailed tests of the jet physics at hadron colliders:

- (a) the measurement can profit of the unprecedented collision intensity and center-of-mass energy of $\sqrt{s} = 7 \text{ TeV}$ provided by the Large Hadron Collider, overcoming the highest measured jet energies in previous experiments;
- (b) the wide solid angle coverage of the ATLAS experiment allow the measurement of the cross section in uncharted angular regions;
- (c) the quality of the ATLAS measurement of jets at low energies allow the extension of the cross section measurement to really low energy;
- (d) the jet cross section profits of the new anti- k_t jet definition developed in the last couple of years, which overcame most of the problems of the previous definitions.

Keywords: Large Hadron Collider, LHC, ATLAS, QCD, Jets, cross-section
